DESIGN AND SYNTHESIS OF NOVEL POROUS TITANIA, CARBON, AND SILICA NANOMATERIALS FOR CATALYSIS AND ENVIRONMENTAL REMEDIATION

By

TAO ZHANG

A dissertation submitted to the

Graduate School-New Brunswick

Rutgers, The State University of New Jersey

In partial fulfillment of the requirements

For the degree of

Doctor of Philosophy

Graduate Program in Chemical and Biochemical Engineering

Written under the direction of

Tewodros Asefa

And approved by

_____

_____

_____

_____

New Brunswick, New Jersey

May 2020

ABSTRACT OF THE DISSERTATION

DESIGN AND SYNTHESIS OF NOVEL POROUS TITANIA, CARBON, AND SILICA NANOMATERIALS FOR CATALYSIS AND ENVIRONMENTAL REMEDIATION

By

TAO ZHANG

Dissertation Director

Prof. Dr. Tewodros Asefa

Nanocatalysts have attracted considerable research attention due to their tunable physical and chemical properties. In this dissertation, several synthetic strategies have been developed to prepare novel porous nanocatalysts for various applications, including photocatalytic carbon dioxide reduction, photocatalytic degradation of pollutants, and electrocatalytic hydrazine oxidation reaction.

In chapter 1, a brief introduction is first given regarding the current status and latest developments of novel nanoporous catalysts, including titania, silica, and carbon-based nanomaterials. The applications of these nanocatalysts including photocatalysis, electrocatalysis, and energy storage and conversion are summarized. Future challenges and prospects are also discussed.

In chapter 2, a simple template-free synthetic route is employed to prepare highly crystalline mesoporous titanium dioxides. The resulting materials are shown to serve as highly active photocatalysts for the conversion of carbon dioxide reduction with water into hydrocarbon

fuels. The formation of nanoporous structure and the maintaining of anatase phase during hydrolysis-calcination synthetic route are found to be critical for the desired catalytic activity and their roles are discussed in detail.

In chapter 3, a series of metallic copper-decorated nanoporous titanium dioxide materials with different loadings of Cu are synthesized by in situ hydrolysis of Sn^{2+}-grafted titanium glycolate microspheres in the presence of Cu^{2+} ions. With the optimal amount of deposited Cu species, the material exhibits the highest photocatalytic activity toward carbon dioxide reduction thanks to the optimized structural features, the increased visible-light absorption and the enhanced separation of photogenerated electron-hole pairs.

In chapter 4, small vacancy-rich anatase nanoparticles is prepared by mesoporous carbon-assisted synthesis, by taking advantage of the pores of a polymer-derived nanoporous carbon as a hard template to hydrolyze and condense a titania precursor. The titania/carbon composite material exhibits unprecedented "blinking" property under an electron beam without decaying for an extended period of time. After being extracted from the carbon template, the vacancy-rich anatase nanoparticles show an exceptional electron trapping ability with long lived electron-hole pairs. As an example, the material is demonstrated to be an efficient photocatalyst for reduction of carbon dioxide with water into hydrocarbons.

In chapter 5, besides of being used as template, the above-mentioned polyaniline-derived mesoporous carbon is employed as supporting material for copper nanoparticles. The inclusion of copper nanoparticles into nanoporous carbon are found to reduce the overpotential and increase the current density of the electrocatalytic hydrazine oxidation reaction. The synthetic method can be extended for the development of other non-noble metal-based electrocatalysts.

Chapter 4 and chapter 5 have successfully demonstrated that colloidal silica nanoparticles with different sizes can serve as hard templates to prepare carbon materials with controlled porosity and large surface area. By employing the same idea, this synthetic strategy is extended to synthesize mesoporous graphitic carbon nitride materials in chapter 6. Besides the size of the colloidal silica nanoparticles, the initial melamine-to-silica template ratio are also found to be crucial for the formation of graphitic carbon nitride with desirable surface are and porosity. After decoration with copper nanoparticles, the composite material shows excellent photocatalytic activity for degradation of tartrazine yellow dye.

Lastly, protonated polyaniline is functionalized onto the surface of mesoporous silica nanomaterial SBA-15. The resulting composite material possesses high surface area and ideal surface properties for the adsorption of anionic dyes Orange G from wastewater and has a significantly higher adsorption capacity compared with the conventional emeraldine salt of polyaniline. Modeling studies are also carried out to further analyze the adsorption properties of the material. This work could encourage further research on porous inorganic/polymer hybrid nanomaterials for various applications.

In summary, this dissertation presents a few novel synthetic strategies for fabrication of nanostructured titania, carbon and silica materials and demonstrates their potential applications in the fields of photocatalytic carbon dioxide reduction, electrocatalytic hydrazine oxidation reaction, photocatalytic degradation of tartrazine yellow dye and removal of organic dye Orange G from wastewater.

DEDICATIONS

Dedicated to my parents,

Xiaopin Zhang and **Zhemin Yang**.

And

My wife, **Weiming (Isabelle) Wang**.

ACKNOWLEDGEMENT

I would first like to thank my supervisor, Dr. Tewodros (Teddy) Asefa, for his valuable advices and support throughout my graduate study. Besides research, he is also a fantastic mentor with great personality. I deeply appreciate him for being a good mentor guiding me on the right path and helping me grow into my potential. This dissertation would not have been possible without his guidance and continuous help.

I want to thank my committee members, Dr. Nina Shapley, Dr. George Tsilomelekis, Dr. Alexei Tyryshkin for spending time reviewing and providing insightful suggestions on my thesis.

I am also grateful to my collaborators, Dr. Jingxiang Low and his advisor Dr. Jiaguo Yu of Wuhan University of Technology, for their continuous help with the measurement of photocatalytic activity.

I would also like to thank the co-authors for their valuable help and discussion of all the projects that I have worked with.

Many thanks to all my current and past group members for supporting my research projects as well as hanging out together, especially Dr. Xiaoxi Huang, Dr. Katherine Koh, Dr. Vitor Almeida, Dr. Taís Larissa Silva, Dr. Anandarup Goswami, Dr. Yuying Meng, Dr. Yan Liu, Viktor Dubovoy and Maricely Ramírez -Hernández.

My deepest gratitude goes to my loving and supportive wife, Weiming (Isabelle), who has made extraordinary sacrifices to let me achieve this milestone. Thank you for always being there for me.

Finally, I would like to express much thanks to my beloved parents for encouraging and supporting me to study aboard and chase my dreams!

TABLE OF CONTENTS

Chapter 1

Introduction to Nanostructured Catalysis

1.1 Nanomaterials and Nanocatalysts

Nanoscience and nanotechnology are the fields of science and technology that study nanomaterials (e.g., nanoparticles, nanowires, nanoporous materials and nanostructured materials) with length between 1-100 nm in, at least, one dimension and apply them in various science fields including chemistry, biology, engineering, and physics. Not surprisingly, they have attracted considerable attention over the last two decades and brings huge opportunities for the development and commercialization of nanomaterials.

Nanomaterials are materials composed of organic, inorganic or their mixtures with sizes in the nanoscale region. They can be further classified into natural nanomaterials, incidental nanomaterials and engineered nanomaterials based on their origin.[1,2] Nanomaterials are not always synthetic, naturally occurring or produced nanomaterials, such as volcanic ashes, sand, dust, biological materials, and inorganic nanocomposites that are produced by combustion, abrasion, oxidation or bioreduction, have been existed for billions of years and are commonly found in soils, waters and atmosphere. Some of these nanomaterials are widely applied in medicine, agriculture, cosmetics, waste removal and other fields of technology and engineering.[2] It has undoubtedly stimulated the research on engineered nanomaterials, which are intentionally produced by humans and have significant impact on our daily life.

The enhanced performance of nanomaterials over their bulk counterparts heavily rely on their tunable chemical, physical and electrical properties, such as size, shape, composition, structure, surface area, porosity and conductivity, which generally vary as a function of their sizes and shapes. These unique features allow them to be used in numerous applications including biotechnology, environmental remediation, electronics, sensing, batteries, renewable energy storage and conversion as well as catalysis.

Among many of their applications, catalysis is of great importance. Rationally designed and synthesized nanocatalysts possessing large surface area, optimal structure, ideal surface properties, suitable electronic states and thus excellent catalytic activity, selectivity can potentially fill the gap between homogeneous and heterogeneous catalysts. In addition, the fast development of nanocatalysts also offers us a potential solution address the current energy crisis and helps achieve a sustainable energy future.

Top-down synthesis and bottom-up synthesis are the most widely used synthetic approaches to prepare nanocatalysts. In order to create large surface area and proper porous structures, bottom-up synthetic approaches have its advantages over top-down synthetic strategies since various hard and/or soft templates can be employed to create such nanoporous structures within the nanocatalysts.

Besides their size, surface area and porous structure, the performance of nanocatalysts is dependent on their chemical composition, crystal structure, surface properties, structure defects and magnetic properties. As a result, the rapidly growing of nanocatalysts in recent years cannot happen without the fast development of different characterization methods. For example, N_2 porosimetry is necessary to measure the surface area and porosity of the nanocatalysts. Microscopic techniques such as transmission electron microscopy (TEM and HRTEM), scanning

electron microscopy (SEM) and atomic force microscopy (AFM) are important to provide information of their size, morphology, porosity, and crystal structures. X-ray based techniques such as X-ray diffraction (XRD), X-ray photoelectron spectroscopy and X-ray absorption spectroscopy (XAS) are extensively used for determining the crystalline structure, grain size, lattice parameters, crystal phase and surface chemical compositions. Inductively coupled plasma mass spectrometry (ICP-MS) can provide accurate information of the elemental composition of nanocatalysts.[3] With the proper combination, these techniques can complement each other and provide more detailed and accurate information for better evaluation and improvement of nanocatalysts.

1.2. Photocatalysts and Photocatalysis

The overexploitation and depletion of fossil fuel reserves (*e.g.*, coal, petroleum and natural gas) have caused global energy crisis and raised concerns about global climate change. Finding renewable energy sources such as solar energy, hydropower, geothermal, wind and biomass energy to replace or reduce the use of finite fossil fuels is urgently needed in order to achieve a sustainable energy future. Among the above-mentioned renewable energy sources, solar energy is considered as the ultimate renewable energy considering the long-predicted lifetime of the Sun. The utilization of solar energy heavily depends on how to efficiently harvest and transfer the energy from the light. Inspired by natural photosynthesis, the first experiment to study whether "light and light alone" can enable chemical reactions was carried out by Giacomo Ciamician in 1901.[4] Later in 1911, the term "photocatalysis" first appeared in literatures where it was referred to Prussian blue bleaching by ZnO as photocatalyst under illumination.[5] Photocatalysis (*e.g.*, photosynthesis by plants, photosynthesis by microalgae and photocatalysis by heterogeneous or homogeneous molecule

photocatalysts) is based on the ability of photocatalysts, which can simultaneously adsorb both photons and reactants and trigger the subsequent catalytic reaction.[4] Photocatalyst is defined by the international Union of Pure and Applied Chemistry (IUPAC) as " a catalyst able to produce, upon absorption of light, chemical transformations of the reaction partners. The excited state of the photocatalyst repeatedly interacts with the reaction partners forming reaction intermediates and regenerates itself after each cycle of such interactions."[6]

In recent years, heterogeneous photocatalysis has received considerable research attention since it provides a potential solution to solve many important energy and environmental concerns in a sustainable manner.[7] For example, photocatalysis have shown great promise in CO_2 reduction, water splitting and pollutant degradation. Although inspired by natural photosynthesis, an energetically uphill reaction, it is worth noting that the currently widely used term "photocatalysis" generally refers to both thermodynamically downhill ($\Delta G < 0$) reactions such as pollutant degradation and thermodynamically uphill ($\Delta G > 0$) reactions such as conversion of CO_2 into hydrocarbon fuels or water splitting (**Figure 1.1**).[4] In both cases, the solar energy is a critical driving force for the successful chemical transformations.[8] Compared with thermodynamically downhill reactions, thermodynamically uphill reactions generally require a more detailed design of the photocatalysts for higher light absorption and charge separation efficiency.[4,6,8]

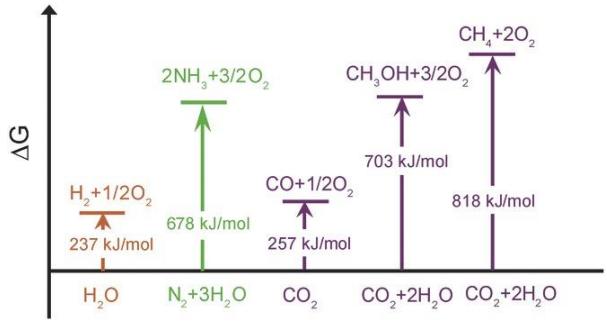

Figure 1.1. Energy diagrams of representative thermodynamically uphill reactions. Reproduced with permission from Ref. [4]. Copyright 2017 Wiley-VCH.

Similar to many other heterogeneous catalytic reactions, heterogeneous photocatalysis can be carried out in different media, including gas phase, aqueous phase and pure organic liquid phase. The overall process may be described by five steps: 1) the transfer of reactants to the surface of photocatalysis, 2) the adsorption of reactants, 3) redox reactions on the surface of photocatalysis, 4) desorption of products, and 5) removal of the products form the interface region, where the photocatalytic reaction occurs at the third step.[9] When semiconducting solid materials (*e.g.*, TiO_2, ZnO, ZrO_2, CeO_2, CdS, ZnS, Fe_2O_3, Cu_2O, Bi_2WO_6, g-C_3N_4 and Ta_2O_5) are employed as photocatalysts, the redox reaction step can be further divided into four important steps: 1) the generation of electron-hole pairs by absorption of photon energy equal to or greater than the band gap (E_g) of the semiconductors, where the electrons in the valence band (VB) are transferred to the conduction band (CB), leaving the positively charged holes in the VB, 2) the separation of photogenerated electron-hole pairs, 3) the migration of electron-hole pairs to the surface of photocatalysts, and 4) the utilization of photogenerated electron-hole pairs for surface reduction and oxidation reaction, respectively (**Figure 1.2**).[10]

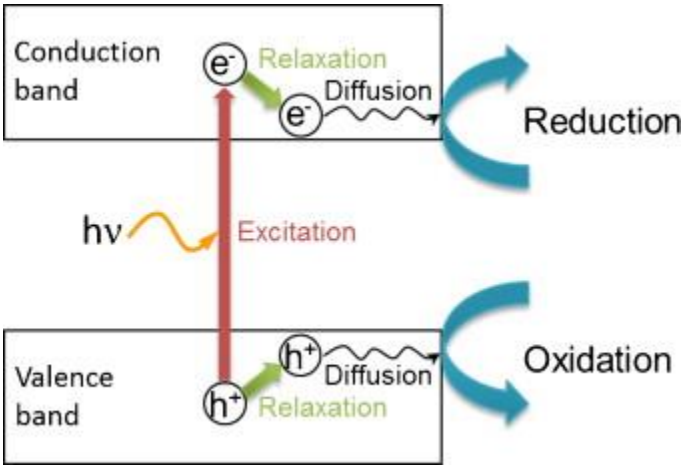

Figure 1.2. Schematic illustration of the formation of photogenerated charge carriers upon absorption of light. Reproduced with permission from Ref. [10]. Copyright 2012 Elsevier.

The oxidation and reduction powers of semiconductor-based photocatalysts depend on three critical aspects: 1) a proper width of the band gap that can adsorption light irradiation, 2) the positions of conduction band and valence band of the semiconductor must be greater than the corresponding potentials of the redox reactions (thermodynamic requirement), and 3) an efficient charge separation efficiency (kinetics requirement).[7] Many strategies have been proposed to promote the charge separation efficiency, including creating Schottky junction between deposited metal nanoparticles and semiconductor, fabricating Type II heterojunctions and all solid-state Z-scheme junctions (**Figure 1.3**).[7]

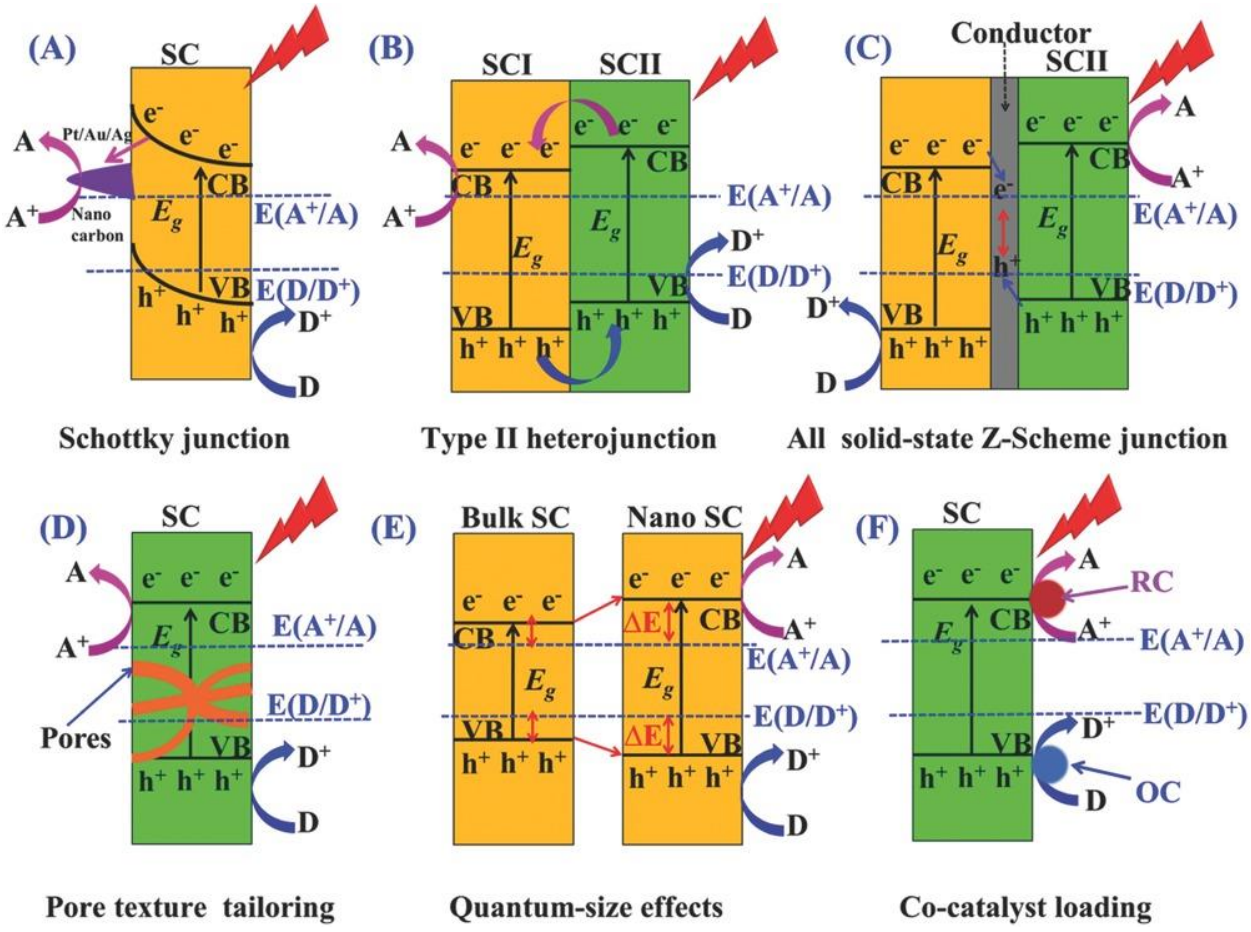

Figure 1.3. Schematic energy band models of typical engineering modification strategies for tackling kinetics challenges: A) Schottky junction; B) Type II heterojunction; C) all solid-state Z-

scheme junction; D) pore texture tailoring; E) quantum-size effects; and F) co-catalysts loading. SC, semiconductor; ΔE, over-potential for the corresponding reactions. Reproduced with permission from Ref. [7]. Copyright 2016 Wiley-VCH.

Among various candidates for photocatalysis, TiO_2 is almost the only suitable material for industrial use at present and probably in the future because it is not only stable, environment friendly and cost-effective, but also possesses suitable conduction and valence band positions that can trigger various reduction and oxidation reactions.[5] In natural, TiO_2 usually exists in three different polymorphs, anatase, rutile and brookite. Rutile is the most stable phase of TiO_2, while anatase and brookite are metastable phases and can be transformed to rutile by high temperature treatment. Although the anatase has a larger band gap (3.2 eV) than that of rutile (3.0 eV), which reduces the light that can be absorbed, the photocatalytic activity of anatase is generally found to be superior than rutile. This can be possibly attributed to its high surface adsorption capacity and indirect band gap that result in lower charge carrier recombination rate.

Scientific studies on TiO_2 can be traced by to the early 20^{th} century. For example, TiO_2 was found to be active for photobleaching of dyes in 1938.[11] In 1956, Mashio et al. compared the photocatalytic activities of various TiO_2 powders, including twelve types of commercial anatase and there types of rutile for the autooxidation of solvents and the simultaneous formation of H_2O_2 under ambient conditions.[12] Then in 1960s, Fujishima first investigated n-type TiO_2 as a semiconductor electrode for photocatalysis of water under UV light irradiation due to its sufficiently positive valence band edge to oxidize water to oxygen. There are many factors that can impact the photocatalytic performance of TiO_2-based photocatalysis, such as size, surface area, pore size, crystallinity, exposed surface facet and charge separation efficiency. Numerous research

efforts have been spent in synthesis, modification and understanding the fundamental principles of TiO_2 based photocatalysts in order to achieve high photocatalytic efficiencies.

1.3. Electrocatalysts and Electrocatalysis

Electrocatalysts are specific types of homogeneous or heterogeneous catalysts that function at the surfaces of electrodes to facilitate redox reactions, help with the transfer of electrons between electrodes and reactants, or accelerate electrochemical reactions/processes. Electrocatalysts are key in the development and operations of various energy technologies, including energy conversion and energy storage systems.

To generate fuels (*e.g.*, with water electrolyzers, which utilize electricity and produce H_2 from H_2O) or to produce electricity from fuels (e.g., with fuel cells, which generate electricity by consuming H_2 and O_2), it is important to use active (or energy efficient) electrocatalysts. Unlike enzymes (natural catalysts), which can operate at near equilibrium redox potentials, electrocatalysts generally require certain overpotentials to overcome the kinetic barriers of the electrochemical reactions, without which electrolyzers and fuel cells require high energy to operate, or their efficiency is low.[13] With the right catalysts, water electrolyzers, for example, can produce H_2 (a green energy carrier) with minimal CO_2 emission; they are thus helpful in meeting sustainable energy goals in future. Electrolyzers can produce H_2 with efficiencies in the range of 60-90% (which can be lower than the energy efficiency of batteries, i.e., 80-90%).[14] In the case of fuel cells (e.g., PEMFCs), the energy conversion efficiency can be lower, with a value of 35-40%.[14] The primary cause of such low efficiency is the high overpotentials that the electrocatalysts require to run reactions over them in these energy devices. Since the kinetic barriers associated with these reactions can be overcome by improving the activities of the electrocatalysts, the design and

synthesis of electrocatalysts with optimized physical, chemical and electrical properties for achieving efficient redox reactions are of paramount importance for the renewable energy systems mentioned above.

Among many types of fuel cells, including: 1) proton exchange membrane fuel cells (PEMFCs), 2) alkaline fuel cells (AFCs), 3) phosphoric acid fuel cells (PAFCs), 4) molten carbonate fuel cells (MCFCs), 5) solid oxide fuel cells (SOFCs) and 6) direct methanol fuel cells (DMFCs).[15-19]. Direct hydrazine fuel cells (DHFCs) are of particular interest, especially due to their high theoretical cell voltages and clean emission. Research on DHFCs began in the 1960s, and has since increasingly continued,[20] especially as different viable membranes (e.g., anion- and cation-exchange membranes) for DHFCs and safe storage methods for hydrazine have been developed.[21,22] The first DHFCs were designed to run by using O_2 as oxidizer, for which the overall reaction of hydrazine electrooxidation can be written as $N_2H_4 + O_2 \rightarrow N_2 + 2H_2O$ $E^{\circ}_{cell} = 1.56$ V.[21] Given the sluggish kinetics of the oxygen reduction reaction (ORR) at the cathode, as well as the relative inconvenience associated with using fuel cells operating with O_2 or air in some applications, DHFCs that work using H_2O_2 (which is liquid under ambient condition) as oxidant, also called hydrazine/H_2O_2 fuel cells (DHHPFC), were later considered, for which the corresponding reaction can be written as $N_2H_4 + 2H_2O_2 \rightarrow N_2 + 4H_2O$ $E^{\circ}_{cell} = 2.13$ V. Besides their ability to offer much higher open-circuit voltage (OCV) per unit molecule of hydrazine, DHHPFCs are more amenable for use than direct hydrazine/O_2 fuel cells (DHOFCs), especially for running mobile systems in outer space and underwater environments (**Figure 1.4**).[23-26] Despite the progress made on DHFCs, the actual OCVs given off by many of them are still much lower than their theoretically expected OCVs, partly because the hydrazine oxidation reaction (HzOR) has inherently large activation barrier and thus consumes a large amount of energy. Thus, the design

and synthesis of advanced electrocatalysts that can lower this activation barrier and help hydrazine efficiently undergo electrocatalysis at the anode electrode remains at the heart of achieving successful electrochemical energy conversion with DHFCs.

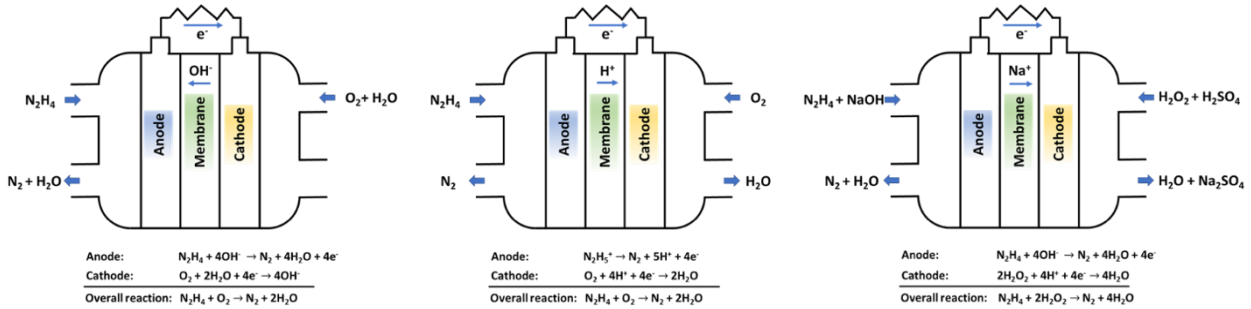

Figure 1.4. Schematic illustration of the reactions at the electrodes and the working mechanisms of DHFC in alkaline medium, DHFC in acidic medium, and DHHPFC in alkaline medium. Reproduced with permission from Ref. [26]. Copyright 2018 Wiley-VCH.

1.4. Recent Development of Titania and Carbon Nanomaterials and Their Application in Renewable Energy

1.4.1. Titanium Dioxide Based Nanomaterials for Photocatalytic CO_2 Reduction

CO_2 is a chemical stable compound and requires substantial energy input for cleaving the carbon oxygen bonds (bond enthalpy of C=O is +805 kJ/mol).[27] There are few routes of lowering CO_2 level in atmosphere including pumping CO_2 into the ocean or under the ground. However, such methods not only require significant energy input and raises environmental concerns, but also do not provide a sustainable solution. In contrast, photocatalytic conversion of CO_2 into hydrocarbon fuels using the abundant photoenergy provides a promising approach to solve the problem. In order to achieve the photocatalytic CO_2 reduction in the presence of reductant (*e.g.*,

H_2O, an electron source), the CB and VB levels of the semiconductors must be more negative and positive than the CO_2 reduction potential and H_2O oxidation potential, respectively. The band gap structures of several types of semiconductors and the standard redox potentials of several products from CO_2 reduction are shown in **Figure 1.5** and **Table 1.1**, respectively.[7,28]

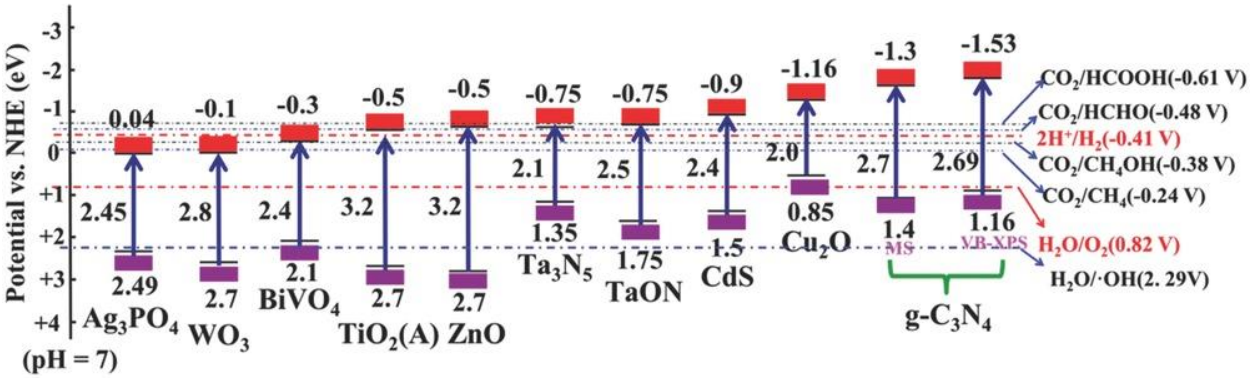

Figure 1.5. Schematic illustration of the band structures of several typical semiconductors. Reproduced with permission from Ref. [7]. Copyright 2016 Wiley-VCH.

Table 1.1. Listed the standard redox potentials of different products from CO_2 reduction with the potentials vs. normal hydrogen electrode (NHE) at pH = 7 in aqueous solution at 25 ˚C and 1 atm. Reproduced with permission from Ref. [28]. Copyright 2018 The Royal Society of Chemistry.

Equation	Reaction	E^0(V) *vs.* NHE at pH = 7
1	$CO_2 + e^- \rightarrow CO_2^-$	-1.9
2	$CO_2 + 2H^+ + 2e^- \rightarrow CO + H_2O$	-0.53
3	$CO_2 + 2H^+ + 2e^- \rightarrow HCOOH$	-0.61
4	$CO_2 + 4H^+ + 4e^- \rightarrow HCHO + H_2O$	-0.48
5	$CO_2 + 6H^+ + 6e^- \rightarrow CH_3OH + H_2O$	-0.38
6	$CO_2 + 8H^+ + 8e^- \rightarrow CH_4 + 2H_2O$	-0.24
7	$2CO_2 + 9H^+ + 12e^- \rightarrow C_2H_5OH + 3H_2O$	-0.33
8	$2H+ + 2e^- \rightarrow H_2$	-0.41

Photocatalytic CO_2 reduction using semiconducting TiO_2 photocatalyst generally involves four steps: 1) surface adsorption of CO_2 , 2) generation of electron-hole pairs by adsorbing photon energy equal to or greater than the gap, 3) separation and migration of the photogenerated electron-

hole pairs to the surface of TiO_2, and 4) the electrons react with CO_2 and H^+ to produce hydrocarbon fuels while the holes react with H_2O to produce O_2.[29] In reality, step 4 in photocatalytic CO_2 reduction is relatively complicated, which starts from the cleavage of the O=C=O bond and formation of different intermediates.[30,31] The reduction products can be CO, CH_4, CH_3OH, HCHO, HCOOH or C_2H_5OH depending on the reduction power of the photocatalysts. Three possible reduction mechanisms have been proposed by a few research groups and summarized in **Table 1.2**.[30]

Table 1.2. Summary of reaction mechanism studies on photocatalytic CO_2 reduction. Reproduced with permission from Ref. [30]. Copyright 2018 Elsevier.

Mechanism I	Mechanism II	Mechanism III
$2CO_2 \rightarrow 2CO + O_2$	$2CO_2 + 4H^{\cdot} \rightarrow 2HCOOH + O_2$	$CO_2 + e^- \rightarrow CO_2^{\cdot}$
$2CO \rightarrow 2C^{\cdot} + O_2$	$HCOOH + 2H^{\cdot} \rightarrow HCOH + H_2O$	$CO_2^{\cdot} + H^{\cdot} \rightarrow OC^{\cdot}H + OH^-$
$2C^{\cdot} + H^{\cdot} \rightarrow CH_3OH$	$HCOH + 2H^{\cdot} \rightarrow CH_3OH$	$OC^{\cdot}H + OC^{\cdot}H \rightarrow HOCCOH$
$CH^{\cdot} + H^{\cdot} \rightarrow CH_2^{\cdot}$	$CH_3OH + H^{\cdot} \rightarrow CH_3^{\cdot}$	$HOCCOH + 4H^{\cdot} \rightarrow CH_3COH$
$CH_2^{\cdot} + H^{\cdot} \rightarrow CH_3^{\cdot}$	$CH_3^{\cdot} + H^{\cdot} \rightarrow CH_4$	$CH_3COH + H^{\cdot} \rightarrow CH_3^{\cdot} + CO$
$CH_3^{\cdot} + H^{\cdot} \rightarrow CH_4$	$CH_3^{\cdot} + CH_3^{\cdot} \rightarrow C_2H_6$	$CH_3^{\cdot} + H^{\cdot} \rightarrow CH_4$
$CH_3^{\cdot} + OH \rightarrow CH_3OH$		

Pristine TiO_2 generally suffers from fast electron-hole recombination and its reduction potentials are below certain CO_2 reduction potentials. Therefore, to improve the photocatalytic CO_2 reduction efficiency, it is necessary to modify the physicochemical properties (*e.g.*, optical and electronic properties) of TiO_2 with increased surface area, reduced band gap and suppressed electron-hole recombination. Up to date, numerous modification or combination methods have been developed according to these steps, respectively.

Porous TiO_2 with large surface area and negative surface charge, which greatly increases the density of active adsorption sites for TiO_2 has been fabricated by either template or template-free synthesis to improve the CO_2 adsorption ability of TiO_2. Such increased number of active

surface sites are beneficial for the photocatalytic CO_2 reduction. Synthesis of TiO_2 with different morphology/porosity, such as 1) 0D spherical nanoparticles, 2) 1D nanowires, nanotubes and nanorods, 3) 2D nanosheet, and 4) 3D porous films, porous fibers and hollow spheres or complex hierarchical morphologies combining different types of porous structure is critical in terms of improving the catalytic performance.

For example, porous TiO_2 materials can be synthesized by template-free and templated approaches (**Figure 1.6**).[32] Each method has its own advantages. Template-free method is a facial way to fabricate TiO_2 with different porosity and large surface area. The porosity and surface area can be tuned by adjusting the synthetic conditions and composition. Sol-gel synthesis, based on hydrolysis and polycondensation of various molecular titanium precursors, offers a facile strategy to control the porosity and properties of the obtained TiO_2 materials. For example, Konishi et al. fabricated multiscale porous TiO_2 monoliths in template-free conditions by combining a sol-gel process and phase separation.[33] The size of the macropores can be well-controlled by changing the start ratio of titanium n-propoxide, HCl, H_2O, and FA.

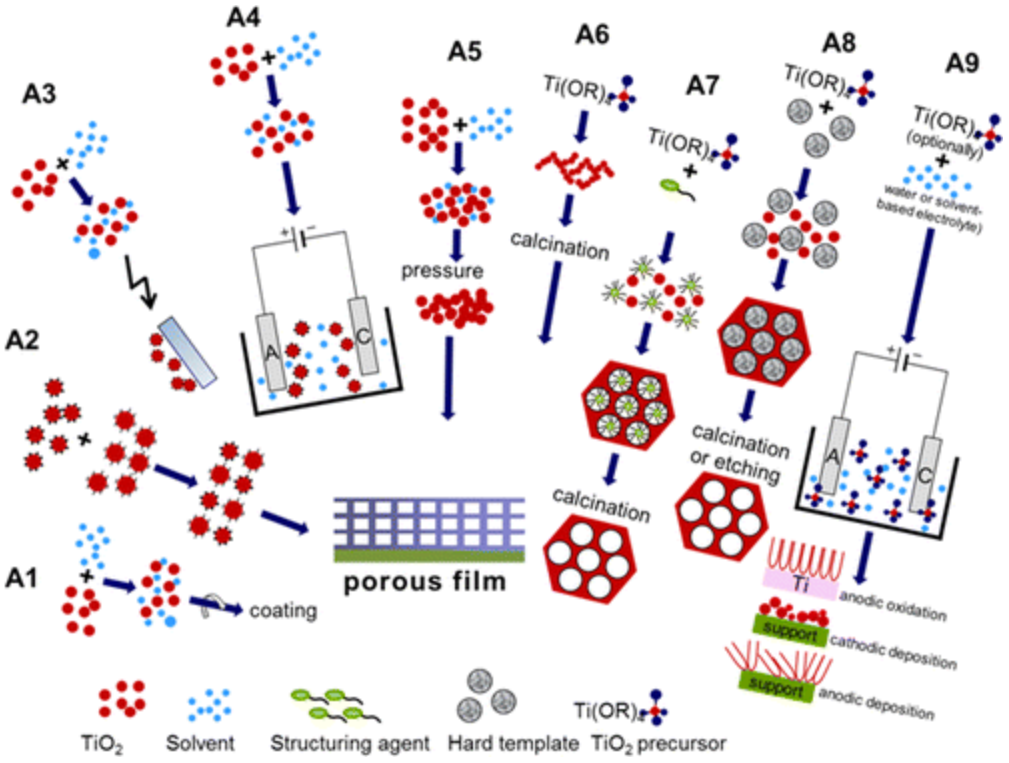

Figure 1.6. Overview of different synthetic strategies of porous titania films. Reproduced with permission from Ref. [32]. Copyright 2014 American Chemical Society.

Compared with template-free method, templated approaches provide new possibilities for controlling the porosity, surface area, structure and crystallinity of TiO_2 by using well-defined hard/soft template to guide the formation of porous structure. Considering the high hydrolysis and condensation rates of titanium precursors, it is necessary to regulate the rates in order to effectively match the cooperative assembly process with the template.[34] Yang et al. first reported the synthesis of mesoporous TiO_2 via a nonhydrolytic evaporation-induced self-assembly (EISA) method using $TiCl_4$ and Pluronic P123 as precursor and structure-directing agent, respectively.[35] The hydrolysis and condensation rates were well controlled since no water is involved during the reaction. The resulting material possessed high surface area well-ordered mesoporous structure. It is worth noting that when soft templated is involved in the synthesis, the collapse of porous structure of TiO_2 during the template removal and crystallization should also be carefully monitored. This

potential shortage of using soft template can be overcame by using hard template or nanocasting method (*e.g*., colloidal silica, mesoporous silica and carbon nanoparticles), which allows the preparation of porous TiO_2 with large porosity, high thermal stability and crystallinity.

Owing to its wide bandgap (3.2 eV for anatase), TiO_2 can only absorbs UV-light, which represents only 5% of the total solar energy that reaches Earth. Developing visible light active TiO_2 photocatalyst through band gap engineering (*e.g*., doping and compositing), which allows the absorption of the main part of solar spectrum or even interior lighting, is one of the exciting research areas. Many surface modification strategies, including impurity doping, metal doping, self-doping or defect engineering have been employed to reduce the band gap of TiO_2 and enhance the light harvesting efficiency. The precise control of the distribution dopants and dopant induced electronic states while maintaining the porous structure of TiO_2 is the current challenge associated with doping. Asahi et al. developed $TiO_{2-x}N_x$ that showed improved photocatalytic activity for photodegradation of methylene blue and gaseous acetaldehyde over undoped TiO_2 under visible light.[36] UV-Vis absorption spectra of $TiO_{2-x}N_x$ shows the optical absorption edge extended to *ca*. 600 nm compared with pure TiO_2 (**Figure 1.7**). The incorporation of nitrogen into TiO_2 lattice is responsible for the narrowing of band gap. In another example, oxygen vacancy rich TiO_2 was prepared by hydrogen plasma treatment.[37] The electron spin resonance (EPR) measurement showed a symmetrical, sharp signal at g = 2.004, which is only detected for plasma-treated TiO_2, indicating the presence of electrons trapped on oxygen vacancies (**Figure 1.8**). The absorption edge of plasma-treated TiO_2 was found to shift to *ca*. 600 nm, indicating the material is visible light active. The enhanced visible light activity of plasma-treated TiO_2 for NO removal is attributed to the presence of oxygen vacancy between the conduction and valence bands.

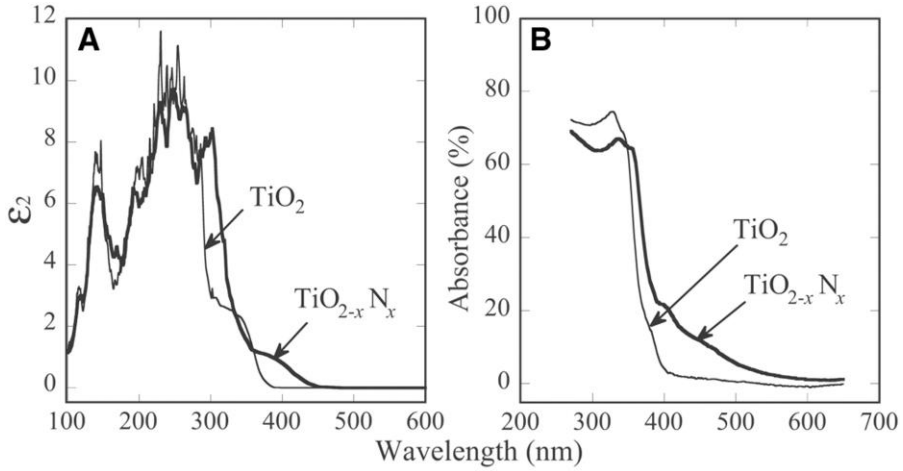

Figure 1.7. Optical properties of $TiO_{2-x}N_x$ (thick lines) compared with TiO_2 (thin lines). (A) Calculated imaginary parts of the dielectric functions, which are averaged over three (x, y, and z) polarization vectors. (B) Experimental optical absorption spectra of $TiO_{2-x}N_x$ and TiO_2 films. Reproduced with permission from Ref. [36]. Copyright 2001 The American Association for the Advancement of Science.

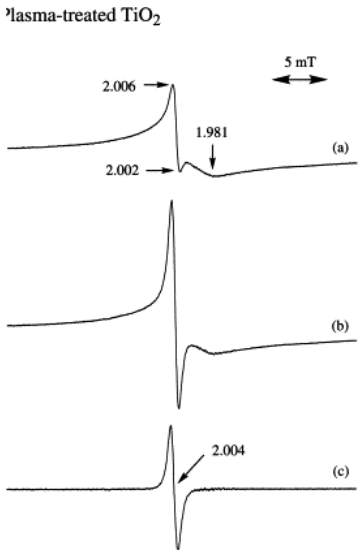

Figure 1.8. ESR spectra of plasma-treated TiO_2 under (a) the dark condition, (b) >475 nm light irradiation for 5 min, and (c) corresponds to spectrum in (b)-spectrum in (a). Reproduced with permission from Ref. [37]. Copyright 2000 Elsevier.

Furthermore, instead of migrating and participating in the surface redox reaction, the photogenerated electron-hole pairs tend to recombine with each other and generate less favored heat energy. The separation efficiency could be potentially improved by introducing co-catalysts such as metal nanoparticles or carbon-based materials on to the surface of TiO_2 that can serve as electron sink or electron trap to capture photogenerated electrons and holes.[38] For example, Schottky barrier will form when noble metals (e.g., Au, Pt and Pt) are in contact with TiO_2 due to their different Fermi levels, which favors the separation of photogenerated electron and hole pairs and will thus enhance the photocatalytic performance.[39] Recently, constructing TiO_2-based heterojunction photocatalysts (e.g., conventional type-II, p-n, non-p-n, Z-scheme, and surface heterojunction) by combining TiO_2 with another semiconductors with matched electronic band structures is another research hotspot (Figure 1.3).[28,30] The well-defined heterojunction between TiO_2 and the other semiconductor can synergistically enhance the light harvesting and the electron-hole pair separation and thereby the photocatalytic performance.

1.4.2. Graphitic Carbon Nitride-Based Nanomaterials for Pollutant Remediation

Graphitic carbon nitride (g-C_3N_4) is a polymeric semiconductor with excellent physicochemical stability and tunable electronic structures. The advantage of g-C_3N_4 over TiO_2 is it possesses a small bandgap of *ca*. 2.7 eV, with conduction band at *ca*. -1.1 V and valence band at *ca*. 1.6 V vs. normal hydrogen electrode, allowing it to serve as a visible light driven photocatalyst (**Figure 1.9**).[40,41]

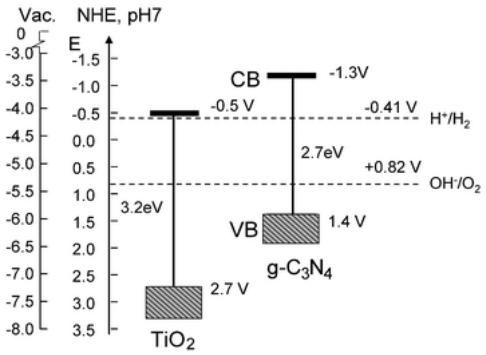

Figure 1.9. The band gap structure comparison of g-C_3N_4 with titanium dioxide (TiO_2, anatase). Reproduced with permission from Ref. [41]. Copyright 2012, Royal Society of Chemistry.

Since g-C_3N_4 is only composed of carbon and nitrogen, it can be prepared by thermal condensation of cheap carbon and nitrogen-rich feedstocks such as cyanamide, dicyandiamide, urea, thiourea, and melamine (**Figure 1.10**). Moreover, its physicochemical properties can be controlled by molecular-level modification and surface engineering.

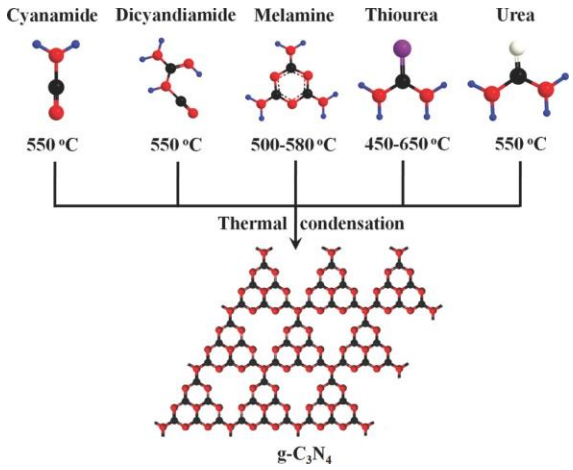

Figure 1.10. Schematic illustration of the main routes for the synthesis of g-C_3N_4 by condensation of cyanamide, dicyandiamide, melamine, thiourea and urea; the color code used in chemical structures: C, black; N, red; H, blue; S, purple; O, white. Reproduced with permission from Ref. [40]. Copyright 2015 Wiley-VCH.

The discovery of g-C_3N_4 can be traced back to the 1830s, its application for heterogeneous catalyst was not explored until 2006 and it was only recently utilized as visible-light photocatalyst for water splitting in 2009. Since this pioneering work, g-C_3N_4 has received considerable research attention in various fields including water splitting, CO_2 reduction, organic syntheses, bacterial disinfection, supercapacitors, air purification, hydrogen evolution and pollutant degradation.[40] For example, g-C_3N_4 has been widely applied for photocatalytic degradation of various contaminants, such as methyl orange, rhodamine B and methylene blue. The removal of residue pharmaceutical and personal care products, including ciprofloxacin, fluoroquinolones and indomethacin are also investigated.[42,43] Electron spin resonance (ESR) and reactive species scavenging experiments have indicated that the superoxide anion radical, photogenerated holes, and hydroxyl radical are generally identified as reactive species responsible for the photodegradation activity.

Although the theoretical specific surface area of monolayer g-C_3N_4 is predicted to be 2500 $m^2\ g^{-1}$, the direct polymerization of nitrogen-rich precursors generally results in low surface area (below 10 $m^2\ g^{-1}$). In addition, bulk/pure g-C_3N_4 suffers from fast charge-hole recombination, which compromises its visible light utilization efficiency and practical application. Various attempts, such as sonication and/or thermal-assisted exfoliation of bulk g-C_3N_4, templating synthesis, elemental doping, molecular doping and building g-C_3N_4-based nanocomposite have been utilized to optimize the specific surface area and electronic structure of g-C_3N_4, respectively.

It is found that the active sites and charge separation efficiency of g-C_3N_4 can be easily tuned by constructing various nanostructure (*e.g.*, hollow structures, porous structures, nanoflakes, and 3D followers). Not surprisingly, the most widely used method to prepare mesoporous g-C_3N_4 with uniform pore structure involves physically rigid or soft template (*e.g.*, nanoporous silica, colloidal silica nanospheres and Pluronic P123). Zhang et al. loaded cyanamide molecules into the

pores of SBA-15 by applying sonication and vacuum. The resulting g-C_3N_4 showed ordered mesoporous structure with high surface area (517 m^2 g^{-1}) and large pore volume (0.49 cm^3 g^{-1}) (**Figure 1.11**).[44] Furthermore, mesoporous g-C_3N_4 with tunable pore sizes can be prepared by using silica nanospheres with various sizes.

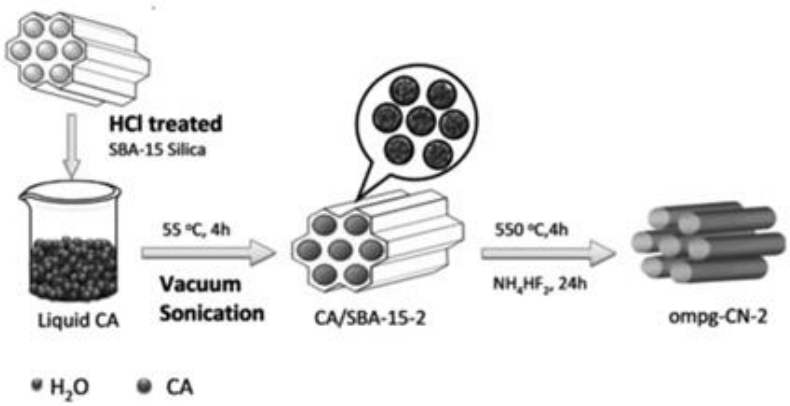

Figure 1.11. Illustration of the preparation of ordered mesoporous g-C_3N_4 using SBA-15 as hard template. CA stands for cyanamide. Reproduced with permission from Ref. [44] Copyright 2013, Wiley-VCH.

Another attractive strategy to prepare porous g-C_3N_4 is template-free synthesis. For example, Wu et al. prepared nanocage-like 3D porous g-C_3N_4 with high surface area and nitrogen defects via a template-free route.[45] The more exposed catalytic active sites and the improved charge transfer and separation efficiency render the resulting porous g-C_3N_4 with higher photocatalytic activity compared with pristine g-C_3N_4 (**Figure 1.12**).

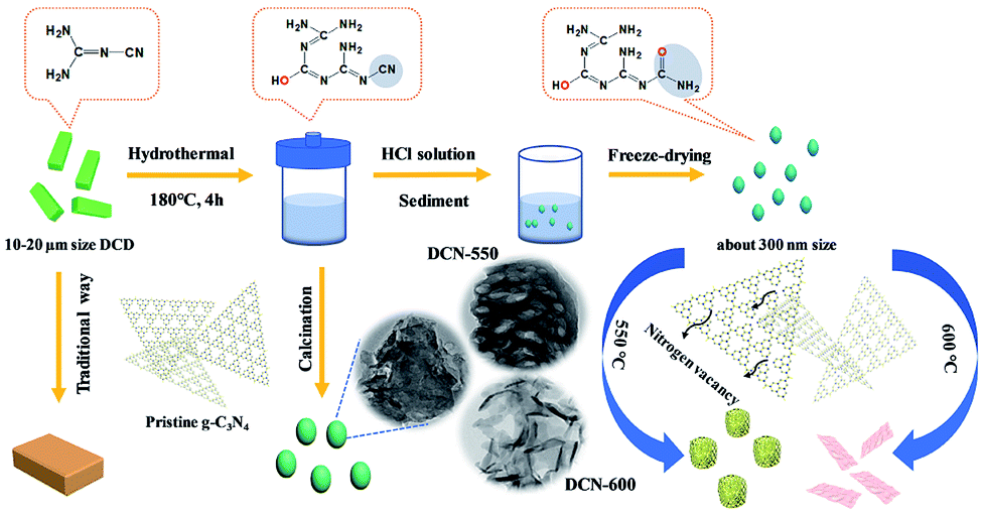

Figure 1.12. Schematic illustration for the synthetic process of nanocage-like carbon nitride. Reproduced with permission from Ref. [45]. Copyright 2019, Royal Society of Chemistry.

Besides designing various nanostructures, engineer the bandgap of g-C_3N_4 and couple g-C_3N_4 with other functional materials to build g-C_3N_4-based nanocomposites are also effective ways to enhance its photocatalytic performance because of the boosted charge separation efficiency. Doping g-C_3N_4 with either non-metal elements (*e.g.*, B, F, S, and I) or metal elements (*e.g.*, Fe, Mn, Co, Ni, Cu, Pt and Pd) are the most popular strategy to modify its electronic structure. The substitution of C or N atoms by non-metal doping or the insertion of metal ions into the framework of g-C_3N_4 generally result in a narrowed bandgap, which enhances the visible light absorption. The unique electronic structure of g-C_3N_4 also allows it to be coupled with various functional materials (e.g., noble metals, metal oxides and graphene). Six primary systems (the g-C_3N_4 based metal-free heterojunction, the g-C_3N_4/single metal oxide (metal sulfide) heterojunction, g-C_3N_4/composite oxide, the g-C_3N_4/halide heterojunction, g-C_3N_4/noble metal heterostructures, and the g-C_3N_4 based complex system) of g-C_3N_4 based nanocomposite have been designed based on the photocatalytic mechanism and process.[46] The resulting nanocomposite systems enable

enhanced light absorption, charge separation, and transportation, which significantly promote the subsequent photocatalytic reactions.

Among various photocatalytic applications of g-C_3N_4, the removal of organic dyes from industrial wastewater is of great importance since most of the dyes are toxic and resistant against normal biodegradation under aerobic conditions.[41] Xu et al. developed porous g-C_3N_4 nanosheets (PCNS) using a two-step template-free approaches including hydrothermal treatment and a thermal etching process.[47] The resulting nanosheet exhibit an average thickness of 2 nm, a pore volume of 0.61 cm^3 g^{-1} and a surface area of 190.1 m^2 g^{-1}. Its photocatalytic performance toward methylene blue degradation is significantly enhanced when compared with bulk g-C_3N_4 due to the mesoporous structure, which renders the material with greater number of surface active sites, improved charge transfer efficiency and enhanced charge separation efficiency. Furthermore, electron spin resonance (ESR) analysis revealed that the photogenerated electrons can efficiency reduce the adsorbed O_2 into $\cdot O_2^-$, which serves as reactive specie for the MB degradation. In another example, MoS_2 nanosheets were coupled into the porous g-C_3N_4 to form MoS_2/C_3N_4 heterostructures using a facile ultrasonic chemical method.[48] The coupled MoS_2 resulted in improved light harvesting and charge separation efficiency of the electron-hole pairs, which led to the enhanced photocatalytic performance toward the degradation of Rhodamine B (RhB) and methyl orange (MO) dyes under visible light irradiation (420-780 nm) compared with bare carbon nitride. The direct hole oxidation is found to play a significant role in the photocatalytic degradation reactions.

1.4.3. Heteroatom-Doped Carbons for Electrocatalytic Hydrazine Oxidation Reaction

Porous carbon nanomaterials possess high surface area and various porous structures have been widely used for adsorption, chemical synthesis, fuel cells, catalyst supports and catalysts.[49] The synthesis of porous carbon with uniform pore sizes with proper chemical-physical properties deserves significant attention. There are generally two popular synthetic strategies used to prepared porous carbon with uniform pore sizes: 1) hard-templating synthesis, which involves using physically rigid nanostructured materials such as silica and zeolites, 2) soft-templating synthesis, which utilizes soft template such as surfactants as pore forming agent to tailor the porosity of the materials. The general synthetic procedure involves 1) prepare the carbon precursor/template composite, 2) carbonization/pyrolysis, and 3) removal of templates.

Besides control structure and morphologies, doping carbon materials with heteroatoms (B, N, O, F, P, S, I, etc.) can induce structural distortions and charge-density and electronic-structure modulation in carbon materials and direct affect the catalytic performance.[50] As a result, heteroatom-doped carbon materials possess advanced physical, chemical and electronic properties have been utilized in many catalytic applications such as hydrogen evolution reaction (HER), oxygen evolution reaction (OER), oxygen reduction reaction (ORR), carbon dioxide reduction reaction (CO_2RR) and hydrazine oxidation reaction (HzOR). Apart from catalysis, heteroatom doped carbon materials can also be used in batteries, sensors and capacitors.

Among various heteroatom-doped carbon materials, nitrogen doping is the most popular and effective way to tailor the properties of carbons. The enhanced catalytic activity is believed to mainly originate from four nitrogen configurations: pyrrolic N, pyridinic N, quaternary/graphitic N and N oxides of pyridinic N (**Figure 1.13**).[51]

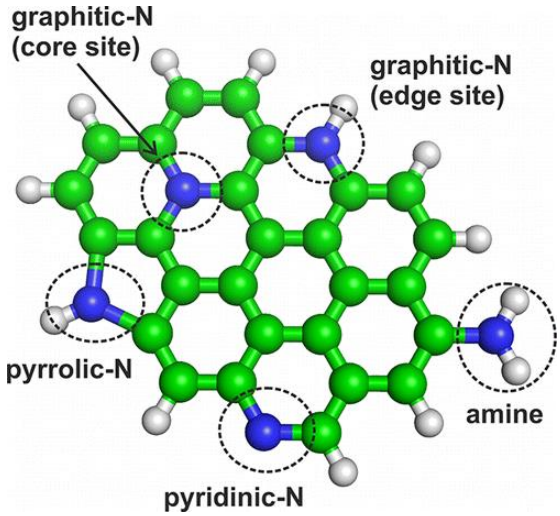

Figure 1.13. Common types of N-doping/functionalization in nitrogen doped carbon dots. Green, blue, and gray represent carbon, nitrogen, and hydrogen atoms, respectively. Reproduced with permission from Ref. [51]. Copyright 2015, American Chemical Society.

Many researchers consider pyridinic N and graphitic N as the primary sites for the excellent catalytic performance for HER, OER, ORR and HzOR. For example, polypyrrole-derived N- and O-codoped mesoporous carbons were prepared by polymerization of pyrrole inside the channel pores of diamine-functionalized SBA-15 and subsequent pyrolysis and removal of the silica template.[52] It is found that the higher pyrolysis temperature favors the formation of graphitic N at the expense of pyridinic N. More importantly, the HzOR electrocatalytic activity of the materials increased with the pyrolysis temperature, indicating graphitic N are more responsible for the electrocatalytic activity.

In terms of electrocatalytic CO_2RR, the nitrogen dopants can break the charge neutrality of carbon and induce charge redistribution. Pyridinic N, pyrrolic N and graphitic N are proposed to serve active site for conversion of CO_2. For example, pyridinic N has a low free energy barrier, which helps the formation of COOH, a key intermediate that limit the overall CO_2RR.[53] Liu et al.

synthesized 3D nitrogen-doped nanoribbon networks with controllable types and contents of nitrogen dopants. It is unraveled that the pyridinic N sites are active sites in the CO_2 reduction since it promotes the CO_2 adsorption, *COOH formation and *CO removal (**Figure 1.14**).[54]

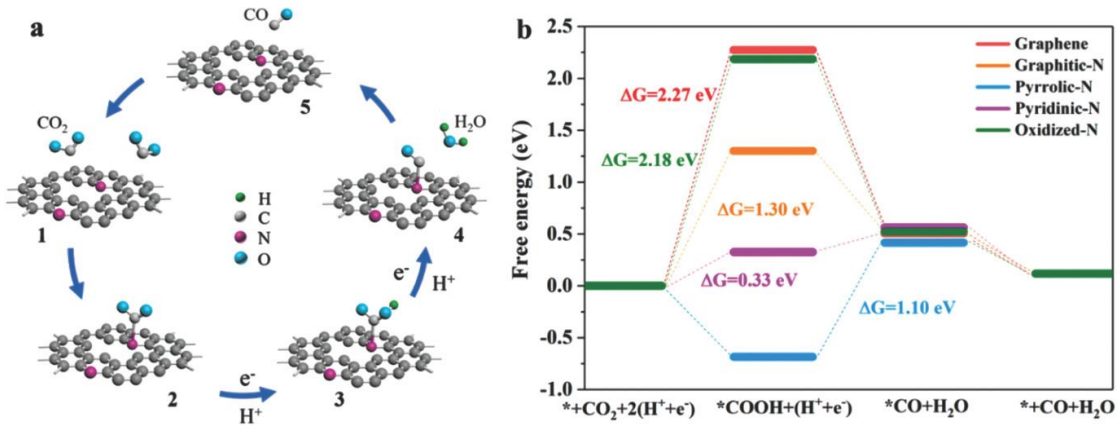

Figure 1.14. Illustration of the carbon dioxide reduction reaction (CRR) processes on nitrogen-doped graphene nanoribbon networks (N-GRW) catalysts. b) Free energy diagram of CRR on various N-GRW catalysts. Reproduced with permission from Ref. [54] Copyright 2018, Wiley-VCH.

Moreover, the heteroatom dopants in the carbon structure can be used to anchor metal nanoparticles preventing them from dissolution, corrosion and agglomeration by creating a strong and beneficial catalyst-support interaction and subsequently enhance the composite materials' catalytic performance and stability. For example, nitrogen doping can 1) modify the growth kinetics of metal particles during deposition, resulting in nanosized particles with good dispersion, 2) modify the electronic structure of the deposited metal particles and thus improve the intrinsic catalytic activity.[55] For example, Cu clusters with size less than 5 nm and single Cu atoms were supported on N-doped mesoporous carbon supports, which was 7 times smaller than that of the particles grown on N-free carbon supports.[56] More importantly, the deposited Cu nanoparticles

were stable even after reacting at 600 K, which can be attributed to the strong interaction of Cu species with the edge pyridinic N atoms. Not surprisingly, the resulting supported material showed enhanced activity for hydrogen production form formic acid decomposition.

Despite the recent progresses on different heteroatom-doped carbon materials and much studies on their electrocatalytic applications for CO_2RR, ORR, OER, HER, only little attention has been paid to their potential application for HzOR. Hydrazine can be electrooxidized into N_2 under acidic and alkaline conditions, according to the following two reactions, respectively:[21,57] $N_2H_5^+ \rightarrow N_2 + 5H^+ + 4e^-$ (acidic) and $N_2H_4 + 4OH^- \rightarrow N_2 + 4H_2O + 4e^-$ (alkaline). Besides these electrochemical (Faradaic) reaction pathways, competing catalytic oxidative decomposition (non-Faradaic) pathways are also reported for hydrazine, especially when noble and non-noble metal catalysts are present: $N_2H_4 \rightarrow N_2 + 2H_2$; $3N_2H_4 \rightarrow N_2 + 4NH_3$.[58-60] Hydrazine can also undergo hydrolysis as: $N_2H_4 + H_2O \rightarrow N_2H_5^+ + OH^-$. Because this reaction produces OH^- ions, hydrazine makes the pH of an aqueous reaction media alkaline, and this pH change, in turn, may affect its own catalytic oxidation or the performances of various electrocatalysts during HzOR. Given these complex reaction pathways, which hydrazine can undergo and the various intermediates and products (*e.g.*, N_2, H_2, NH_3) it can generate, the total number of electrons involved in the reaction may need to be carefully examined and the products may have to be closely monitored using online mass spectrometry during studies of HzOR.[58]

The ability of heteroatom-doped carbons to electrocatalyze HzOR was first demonstrated by Silva et al.[61] The materials, N-doped carbon nanoneedles (CNNs), were synthesized from CeNWs using core-shell synthetic strategy. The materials had nanoneedle morphology and a higher density of heteroatom dopants (*ca*. 9% N), predominantly in pyridinic form, as analyzed by XPS. In addition, they had a high proportion of edge planes in their structures as indicated by micro-Raman

spectral analysis. These, in turn, make the CNNs exhibit high electrocatalytic activity toward HzOR, with an onset potential at ca. 0.15 V (vs. SCE) for 10 mM hydrazine solution. The catalytic effect of trace Fe residue that may be present in CNNs, at density below the detection limit of XPS, was indirectly checked by measuring the HzOR electrocatalytic activity of two control materials synthesized by intentionally adding Fe^{3+} ions to the CNNs or by treating the CNNs with HNO_3 solution to dissolve and remove accessible, soluble Fe impurities. No difference among the three materials in terms of electrocatalytic activity was observed, indicating that the electrocatalytic activity of CNNs toward HzOR was most likely due to their N dopants, or more specifically, their pyridinic species and high proportion of edge planes created by the presence of heteroatom dopants.

While this work demonstrated for the first time that N-doped carbons can be a promising alternative materials to conventional noble metals to electrocatalyze HzOR, the potential at which it did so was still far from the thermodynamic value of the reaction (-0.38 vs. NHE). Thus, other precursors and synthetic approaches are urgently needed in order to find more catalytically active heteroatom-doped carbon-based materials for HzOR.

1.5. Summary and Outlook

In this section, fundamental aspects of photocatalytic CO_2 reduction, photocatalytic pollutant degradation and electrocatalytic hydrazine oxidation mechanism have been discussed. The importance and benefits of using nanostructured materials for improving the efficiency of the above-mentioned reactions have also been elaborated. Many efforts over the past few years have been focused on developing such materials with optimized physical and chemical properties by various advanced synthetic strategies. The development of advanced analytical techniques provides valuable insight for further understanding the mechanism by monitoring the catalysis in

action and in turn guides the design of the materials. It is clear that significant progress have been made in the field of nanoscience and nanotechnology, which shows great promising for solving the worldwide demand for energy and achieving a sustainable future.

Despite the significant advancements, there are still many challenges that limit the practical application of nanomaterials. In terms of TiO_2 based photocatalytic CO_2 reduction, large scale synthesis of porous TiO_2 with maximum exposed active sites using template-free synthetic strategies is highly desired. Design TiO_2 with good charge separation efficiency, high crystallinity, large surface area and good thermal stability and thus enhanced photocatalytic activity is also critical. Furthermore, recent studies confirm that the photocatalytic activity of TiO_2 is related to its defect disorder.[62] Therefore, using defect engineering to prepare defective rich TiO_2 is another promising technique to maximize its performance for the generation of solar fuels. In the following sections, I attempt to provide a few promising strategies to prepare TiO_2 with these desired properties and further improve their photocatalytic performance. In addition to TiO_2, g-C_3N_4 and heteroatom doped carbon materials with advanced structures and optimized properties are also prepared. Their performance toward photocatalytic pollutant degradation and electrocatalytic hydrazine oxidation are also measured.

Rational design and synthesis of efficient catalysts for the generation of energy or removal of pollutants is crucial for achieving a sustainable future. I hope the studies conducted in this work will shed some light on this field and encourage further investigations on developing practical catalysts for CO_2 reduction, pollutant degradation and hydrazine oxidation for fuel cells.

1.6. Reference

1. Griffin, S.; Masood, M. I.; Nasim, M. J.; Sarfraz, M.; Ebokaiwe, A. P.; Schäfer, K.-H.; Keck, C.; Jacob, C. *Antioxidants*, **2018**, *7*, 3-24.
2. Hochella, M. F. Jr.; Mogk, D. W.; Ranville, J.; Allen, I. C.; Luther, G. W.; Marr, L. C.; McGrail, B. P.; Murayama, M.; Qafoku, N. P.; Rosso, K. M.; Sahai, N.; Schroeder, P. A.; Vikesland, P.; Westerhoff, P.; Yang, Y. *Science*, **2019**, *363*, 1414-1423.
3. Mourdikoudis, S.; Pallares, R. M.; Thanh, N. T. K. *Nanoscale*, **2018**,*10*, 12871-12934.
4. Zhu, S., Wang, D. *Adv. Energy Mater*., **2017**, *7*, 1700841-1700864.
5. Hashimoto, K.; Irie, H.; Fujishima, A. *Jpn. J. Appl. Phys.*, **2005**, *44*, 8269-8285.
6. Osterloh, F. E. *ACS Energy Lett*., **2017**, *2*, 445-453.
7. Li, X.; Yu, J.; Wageh, S.; Al-Ghamdi, A. A.; Xie, J. *Small*, **2016**, *12*, 6640-6696.
8. Takanabe, K. *ACS Catal.*, **2017**, *7*, 8006-8022
9. Herrmann, J.-M. *Catal. Today*, **1999**, *53*, 115-129.
10. Nakata, K,; Fujishima. *J. Photoch. Photobio. C.*, **2012**, *13*, 169-189.
11. Doodeve, C. F.; Kitchener, J. A. *Trans. Faraday Soc.*, **1938**, *34*, 902-908.
12. Kato,S.; Mashio, F. *Abtr. Book Annu. Meet. Chemical Society of Japan*, **1956**, 223-225.
13. Stamenkovic, V. R.; Strmcnik, D.; Lopes, P. P.; Markovic, N. M. Nat. Mater., **2016**, *16*, 57-69.
14. Duan, H.; Wang, D.; Li, Y. *Chem. Soc. Rev*., **2015**, *44*, 5778-5792.
15. Wang, S.; Jiang, S. P. *Natl. Sci. Rev*., **2017**, *4*, 163-166.
16. Kirubakaran, A.; Jain, S.; Nema, R. K. *Renew. Sust. Energ. Rev*., **2009**, *13*, 2430-2440.
17. Acres, G. J. K.; Frost, J. C.; Hards, G. A.; Potter, R. J.; Ralph, T. R.; Thompsett, D.; Burstein, G. T.; Hutchings, G. J. *Catal. Today*, **1997**, *38*, 393-400.

18. Wang, Y.; Chen, K. S.; Mishler, J.; Cho, S. C.; Adroher, X. C. *Appl. Energ*., **2011**, *88*, 981-1007.

19. Yuan, W.; Tang, Y.; Yang, X.; Wan, Z. *Appl. Energ*., **2012**, *94*, 309-329.

20. Rees, N. V.; Compton, R. G. *Energy Environ. Sci.*, **2011**, *4*, 1255-1260.

21. Serov, A.; Kwak, C. *Appl. Catal., B* **2010**, *98*, 1-9.

22. Asazawa, K.; Yamada, K.; Tanaka, H.; Oka, A.; Taniguchi, M.; Kobayashi, T. *Angew. Chem. Int. Ed*., **2007**, *46*, 8024-8027.

23. Yan, X.; Meng, F.; Xie, Y.; Liu, J.; Ding, Y. *Sci. Rep*., **2012**, *2*, 941-947.

24. Feng, G.; Kuang, T.; Li, P.; Han, N.; Sun, M.; Zhang, G.; Sun, X. *Adv. Sci*., **2017**, *4*, 1600179-1600184.

25. Lao, S. J.; Qin, H. Y.; Ye, L. Q.; Liu, B. H.; Li, Z. P. *J. Power Sources*, **2010**, *195*, 4135-4138.

26. Zhang, T.; Asefa, T. *Adv. Mater.*, **2019**, *31*, 1804394-1804420.

27. Ola, O.; Maroto-Valer, M. M. *J. Photoch. Photobio. C.*, **2015**, *24*, 16-42.

28. Wei, L.; Yu, Ch.; Zhang, Q.; Liu, H.; Wang, Y. *J. Mater. Chem. A*, **2018**, *6*, 22411-2243

29. Low, J.; Cheng, B.; Yu, J.; *Appl. Surf. Sci.*, **2017**, *382*, 656-686.

30. Shehzad, N.; Tahir, M.; Johari, K.; Murugesan, T.; Hussain, M. *J. CO_2 Util.*, **2018**, *26*, 98-122.

31. Liu, L.; Zhao, H.; Andino, J. M.; Li, Y. *ACS Catal*., **2012**, *2*, *8*, 1817-1828

32. Fattakhova-Rohlfing, D.; Zaleska, A.; Bin, T. *Chem. Rev.*, **2014**, *114*, 19, 9487-9558.

33. Konishi, J.; Fujita, K.; Nakanishi, K.; Hirao, K. *Chem. Mater*., **2006**, *18*, *25*, 6069-6074

34. Li, W.; Wu, Z.; Wang, J.; Elzathry, A. A.; Zhao, D. *Chem. Mater.*, **2014**, *26*, 1, 287-298

35. Yang, P.; Zhao, D.; Margolese, D. I.; Chmelka, B. F.; Stucky, G. D. *Nature*, 1998, *396*, 152-155.

36. Asahi, R.; Morikawa, T.; Ohwaki, T.; Aoki, K.; Taga, Y. *Science*, **2001**, *293*, 269-271.

37. Nakamura, I.; Negishi, N.; Kutsuna, S.; Ihara, T.; Sugihara, S.; Takeuch, K. *J. Mol. Catal*., **2000**, *161*, 205-212.

38. Sakthivel, S.; Shankar, M. V.; Palanichamy, M.; Arabindoo, B.; Bahnemann, D. W.; Murugesan, V. *Water Res*., **2004**, *13*, 3001-3008.

39. Zhang, Z.; Yates, J. Y. Jr. *Chem. Rev*., **2012**, *112*, 5520-5551

40. Cao, S.; Low, J.; Yu, J.; Jaroniec, M. *Adv. Mater*., **2015**, *27*, 2150-2176.

41. Cui, Y.; Ding, Z.; Liu, P.; Antonietti, M.; Fu, X.; Wang, X. *Phys. Chem. Chem. Phys*., **2012**, *14*, 1455-1462.

42. Wang, F.; Peng, Y.; Chen, P.; Wang, Y.; Su, Y.; Zhang, Q.; Zeng, Y.; Xie, Z.; Liu, H.; Liu, Y.; Lv, W.; Liu, G. *Appl. Catal. B-Environ*., **2018**, *227*, 114-122.

43. Wang, F.; Chen, P.; Feng, Y.; Xie, Z.; Liu, Y.; Su, Y.; Zhang, Q.; Wang, Y.; Yao, K.; Yao, K.; Lv, W.; Liu, G. *Appl. Catal. B-Environ*., **2017**, *207*, 103-113.

44. Zhan, J.; Guo, F.; Wang, X. *Adv. Funct. Mater*., **2013**, *23*, 3008-3014.

45. Wu, M.; Gong, Y.; Nie, T.; Zhang,J.; Wang, R.; Wang, H.; He, B. *J. Mater. Chem. A*, **2019**, *7*, 5324-5332.

46. Zhao, Z.; Sun, Y.; Dong, F. *Nanoscale*, **2015**, *7*, 15-37.

47. Xu, J.; Wang, Z.; Zhu, Y. *ACS Appl. Mater. Interfaces*, **2017**, *9*, 27727-27735.

48. Li, Q.; Zhang, N.; Yang, Y.; Wang, G.; Ng. D. H. L. *Langmuir*, **2014**, *30*, 29, 8965-8972.

49. Lee, J.; Kim, J. *Adv. Mater*., **2006**, *18*, 2073-2094.

50. Paraknowitsch, J. P.; Thomas, A. *Energy Environ. Sci.*, **2013**, *6*, 2839-2855.

51. Sarkar, S.; Sudolská, M.; Dubecký, M.; Reckmeier, C. J.; Rogach, A. L.; Zbořil, R.; Otyepka, M. *J. Phys. Chem. C*, **2016**, *120*, 1303-1308.

52. Meng, Y.; Zou, X.; Huang, X.; Goswami, A.; Liu, Z.; Asefa, T. *Adv. Mater*., **2014**, *26*, 6510-6516.

53. Cui, H.; Guo, Y.; Guo, L.; Wang, L.; Zhou, Z.; Peng, Z. *J. Mater. Chem. A*, **2018**, *6*, 18782-18793.

54. Liu, S.; Yang, H.; Huang, X.; Liu, L.; Cai, W.; Gao, J.; Li, X.; Zhang, T.; Huang, Y.; Liu, B. *Adv. Funct. Mater*., **2018**, *28*, 1800499-1800455.

55. Zhou, Y.; Neyerlin, K.; Olson, T. S.; Pylypenko, S.; Bult, J.; Dinh, H. N.; Gennett, T.; Shao, Z.; O'Hayre, R. *Energy Environ. Sci*., **2010**, *3*, 1437-1446.

56. Bulushev, D. A.; Chuvilin, A. L.; Sobolev, V. I.; Stolyarova, S. G.; Shubin, Y. V.; Asanov, I. P.; Ischenko, A. V.; Magnani, G.; Riccco, M.; Okotrub, A. V.; Bulusheva, L. G. *J. Mater. Chem*., A, **2017**, *5*, 10574-10583.

57. Krittayavathananon, A.; Srimuk, P.; Lunawuthi, S.; Sawangphruk, M. *Anal. Chem*., **2014**, *86*, 12272-12278.

58. Sanabria-Chinchilla, J.; Asazawa, K.; Sakamoto, T.; Yamada, K.; Tanaka, H.; Strasser, P. *J. Am. Chem. Soc*., **2011**, *133*, 5425-5431.

59. Zhang, P.X.; Wang, Y. G.; Huang, T.; G.; Zhang, T.; Wu, G. S.; Li, J. *Catal. Today*, **2011**, *165*, 80-88.

60. He, L.; Huang, Y.; Wang, A.; Wang, X.; Chen, X.; Delgado, J. J.; Zhang, T. *Angew, Chem.* **2012**, *124*, 6295-6298

61. Silva, R.; Al-Sharab, J.; Asefa, T. *Angew. Chem., Int. Ed*. **2012**, *51*, 7171-7175.

62. Nowotny, J.; Alim, M. A.; Bak, T.; Idris, M. A.; Ionescu, M.; Prince, K.; Sahdan, M. Z.; Sopian, K.; Teridi, M. A. M.; Sigmund, W. *Chem. Soc. Rev*., **2015**, *44*, 8424-8442.

Chapter 2

Mesoporous TiO_2 Comprising Small, Highly Crystalline Nanoparticles for Efficient CO_2 Reduction by H_2O

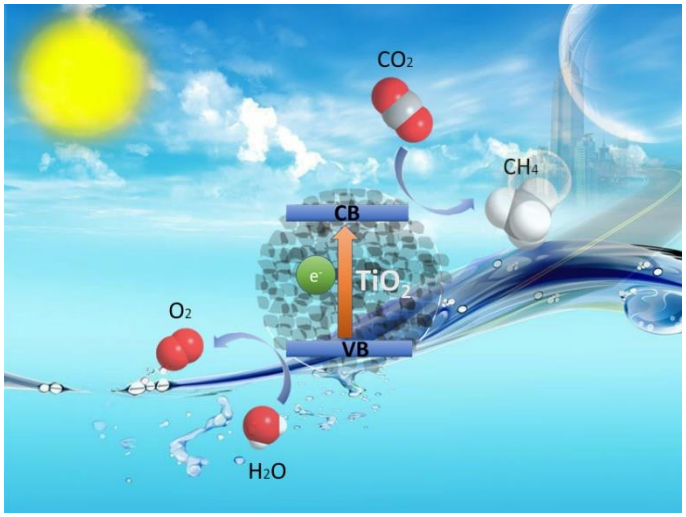

2.1. Overview

The conversion of CO_2 into hydrocarbon fuels with H_2O using low-cost photocatalysts can offer a sustainable route to meet some of our energy needs, besides being able to contribute to the solutions of global warming. In this work, a series of highly crystalline mesoporous titanium dioxide (TiO_2) photocatalysts are synthesized *via* a simple template-free synthetic method. The synthesis involves preparation of titanium glycolate microspheres (TGMs), then hydrolysis of the TGMs in boiling water under ambient pressure, and finally calcination of the products in air. The hydrolysis step is found to play a crucial role in the formation of TiO_2 microspheres comprising a network of small anatase grains. The hydrolysis of the TGMs is also found to considerably inhibit the possible phase transformation of anatase to rutile during the subsequent high-temperature

crystallization process. The resulting materials have good crystallinity and efficient charge carrier separation capabilities as well as large specific surface areas, and thus large density of accessible catalytically active sites. These unique structural features enable these materials to exhibit high photocatalytic activities for the conversion of CO_2 with H_2O into hydrocarbon fuels (CH_4), and with much better catalytic performances than the commercial photocatalyst Degussa P25 TiO_2.

2.2. Introduction

The fast-growing global economy currently relies heavily on increased consumption of fossil fuels ranging from coal, petroleum and nature gas to shale oil and shale gas. However, the continued increased energy demand and usage worldwide cannot be met indefinitely with our depleting fossil fuel reserves. Besides, burning fossil fuels has already generated a large amount of the greenhouse gas CO_2 and is causing serious climate change.[1] Although many methods including pumping CO_2 into the ocean or under the ground have been considered to mitigate these problems, many of them not only require substantial energy but also raise safety concerns and are unable to provide long-term solutions.[1,2] One sustainable route to potentially address these issues is by photocatalytically recycling CO_2 back into hydrocarbon fuels over efficient photocatalysts using solar energy.[3-6]

Among many photocatalysts applicable to CO_2 recycling processes, titanium dioxide (TiO_2) deserves a special attention because it is inexpensive, chemically stable and environmentally friendly.[7] TiO_2 is, however, inherently poor photocatalyst. TiO_2's photocatalytic activity has been shown to improve by tailoring its crystal phase and increasing its surface area, porosity and crystallinity.[8,9] In the case of crystal phases of TiO_2, anatase is usually more photocatalytically active and more preferable than rutile due to its more negative conduction band

position, which results in higher reduction potential and lower charge carrier recombination rate.[3,9] Generally, improving crystallinity in TiO_2 through high temperature calcination can effectively reduce the density of structural defect sites, which can otherwise function as recombination centres for photogenerated electron-hole pairs or compromise charge carrier separations in the material.[10,11] However, thermal treatment can also induce an undesired phase transition from the more photocatalytically active anatase to the less active photocatalyst rutile. Furthermore, if the material is nanoporous, thermal treatment can simultaneously make the porous structure collapse and the catalytically active sites become less accessible. Although soft and hard templating methods have been utilized to synthesize TiO_2 materials with improved crystallinity, thermal stability and mesoporosity,[12-14] facile and practical synthetic routes that can lead to highly crystalline TiO_2 composed of anatase are still required.

To this end, we here report a template-free synthetic route that produces highly crystalline mesoporous TiO_2 materials composed of small grains of anatase nanoparticles that show high photocatalytic activity for CO_2 reduction with H_2O into hydrocarbon fuels. Of note, the synthesis involves only simple hydrolysis and calcination synthetic procedures. The structures, properties and catalytic activities of the materials and their corresponding control materials are also investigated and included in the work.

2.3. Experimental Section

2.3.1. Chemicals and Reagents.

Titanium(IV) *n*-butoxide (TBO), ethylene glycol (EG) and acetone were purchased from Sigma-Aldrich. Anhydrous ethanol was obtained from Fisher Scientific. The chemicals and

reagents were all used as received without further purification. Distilled water was used throughout the experiments.

2.3.2. Synthesis of Titanium Glycolate Microspheres (TGMs).

Titanium glycolate microspheres (TGMs) were synthesized at room temperature by following a previously reported synthetic method.[15,16] First, TBO (2 mL) was mixed with EG (50 mL) and the two were stirred together for 4 h to form titanium glycolate. The solution was then poured into another solution containing acetone (170 mL) and water (2 mL), and the resulting solution was stirred for 60 min. A white solid product, which was produced in the solution, was recovered *via* centrifugation. It was then washed 3 times with ethanol (40 mL) and let to dry at 60 °C, resulting in TGMs.

2.3.3. Calcination-Assisted Synthesis of TiO_2 Materials (TiO_2-(C@*T*)).

The TGMs (300 mg) obtained above were converted into TiO_2 by calcining them in air at different temperatures (500, 650 or 800 °C) in a temperature-programmable tube furnace as follows. The samples were kept in the furnace, and the temperature was raised from room temperature to one of the desired temperatures (*i.e*., 500, 650 or 800 °C) with a ramp of 5 °C min^{-1} and kept at that temperature for 2 h. The furnace was then let to cool down to room temperature. The final materials were denoted as TiO_2-(C@*T*)), where *T* represents the final calcination temperature in °C used to make each material. Unless mentioned otherwise, the default calcination time is 2 h.

2.3.4. Hydrolysis-Assisted Synthesis of TiO_2 Material (TiO_2-(H)).

Here the TGMs were converted into TiO_2 by refluxing them in boiling water for 24 h. The solid product was collected *via* centrifugation of the solution. It was washed several times with

water (40 mL) and then ethanol (40 mL), and finally let to dry at 60 °C. The final product was denoted as TiO_2-(H), in which H represents the hydrolysis treatment. For comparative studies, TiO_2 materials were synthesized with the same synthetic procedure but using different hydrolysis times (5 min, 15 min, 30 min, or 2 h). The resulting materials were denoted as TiO_2-(H(*t*)), where *t* represents the hydrolysis time. Unless mentioned otherwise, the default hydrolysis time is 24 h; hence, TiO_2-(H(*24h*)) is the same as TiO_2-(H) hereafter.

2.3.5. Synthesis of TiO_2 Materials via Hydrolysis followed by Calcination (TiO_2-(H+C@*T*).

Samples from the above-prepared TiO_2-(H) material (300 mg in each case) were taken and subjected to calcination at different temperature (500, 650 or 800 °C) for 2 h, after raising the temperature from room temperature to the desired temperature at a ramp of 5 °C min^{-1}. The resulting materials were denoted as TiO_2-(H+C@*T*), where *T* indicates the final calcination temperature in °C. For comparison, samples of TiO_2-(H) were calcined at 500 °C for prolonged times (4, 8, 12 or 16 h), after raising the temperature from room temperature to 500 °C at a ramp of 5 °C min^{-1}. The resulting materials here were denoted as TiO_2-(H+C@500-*t*), where *t* represents the calcination time. Unless mentioned otherwise, the default calcination time, *t*, is 2 h; hence, hereafter TiO_2-(H+C@500-*2h*) is denoted as TiO_2-(H+C@500) and the other materials are all accompanied with calcination time.

2.3.6. Characterizations.

Transmission electron microscope (TEM) images of the materials were taken with a Topcon 002B TEM instrument operating at 200 kV. Field emission scanning electron microscope (FESEM) images were acquired using a Zeiss Sigma Field Emission SEM. The surface areas and pore properties of the materials were determined by N_2 porosimetry using liquid N_2 (at -196 °C)

and a Micromeritics Tristar-3000 instrument (Micromeritics, USA). Before each measurement, the samples were degassed at 80 °C for 8 h under a flow of N_2 gas to remove any possible guest species adsorbed on the samples' surfaces. Based on the adsorption-desorption isotherm data, the surface areas and pore size distributions of the materials were calculated using the Brunauer-Emmett-Teller (BET) method and the Barrett-Joyner-Halenda (BJH) method, respectively. X-ray diffraction (XRD) patterns of the materials were obtained using a Philip XPert diffractometer operating with Cu Kα radiation as the X-ray source. The XRD diffraction patterns were recorded in the 2θ range between 15 and 80 ° with a step size (2θ) of 0.02 ° and at a scanning rate of 0.6 ° min^{-1}. The UV-Vis diffuse reflectance spectra (UV-Vis DRS) of the materials were acquired with a Lambda 950 spectrophotometer (PerkinElmer) over a spectral range of 250 to 800 nm. Thermogravimetric analyses (TGA) of the materials were done using a PerkinElmer TGA7 instrument at a heating rate of 5 °C min^{-1} in a flow of air at 20 mL min^{-1}. The photocurrent and electrochemical impedance measurements were performed on CHI660C (CHI, China) standard three-electrode electrochemical analyzer. The prepared samples (cut into 1 cm^2), Pt wire and Ag/AgCl were used as working electrode, counter electrode and reference electrode, respectively. Low power UV-LED (3 W, 365 nm) was used as light source and Na_2SO_4 aqueous solution was used as an electrolyte during the measurements.

2.3.7. Photocatalytic Reduction of CO_2.

A 200 mL-size home-made Pyrex reactor was used to perform the photocatalytic CO_2 reduction over the TiO_2 materials at room temperature and at atmospheric pressure, as in our previous reports.[7,17-19] Typically, prior to the test, 50 mg of the TiO_2 material was mixed with 10 mL of deionized water, and the mixture was poured into the reactor. The mixture was then ultrasonically dispersed for 30 min, and the solvent in it was allowed to evaporate at 80 °C for 2

h. After a thin film of the solid sample formed on the bottom of the reactor, the reactor was sealed off. In order to create anaerobic conditions in the reactor, the air in it was removed by blowing N_2 gas into the reactor for 30 min. The reactants used as a source of carbon (*viz.* CO_2) and hydrogen (*viz.* H_2O) were generated *in situ* by letting $NaHCO_3$ (0.1 g, which was added into the reactor before sealing it off) and 2 M sulfuric acid (0.3 mL which was purged into the reactor using a syringe) react for 30 min, before turning on the light irradiation. A 300 W simulated solar Xe arc lamp was positioned 10 cm above the photocatalytic reactor and used as the source of light. After 1 h of light irradiation, 1 mL of the gas sample was taken from the reactor and analyzed by gas chromatograph (GC-2014C, Shimadzu, Japan) equipped with a flame ionization detector (FID). Blank experiments were also performed without the presence of CO_2 in the reactor and/or without exposing the reactor to irradiation. These experiments allowed us to check if any of the products could be generated without photocatalytic processes and without the presence of CO_2.

2.4. Results and Discussion

The synthetic procedures that were employed to make the TiO_2 materials and their corresponding control materials are depicted in **Scheme 2.1** and also described in detail in the Experimental section above. First, the precursors, titanium glycolate microspheres (also denoted as TGMs), were synthesized by letting titanium(IV) *n*-butoxide (TBO) react with ethylene glycol (EG), and then mixing the reaction product with a solution containing acetone and water at room temperature.[7,15] The resulting TGMs were then subjected to either calcination at different temperature (500, 650 or 800 °C) or hydrolysis in boiling water under ambient pressure. The resulting materials were named as TiO_2-(C@*T*) and TiO_2-(H(*t*)), respectively, in which "*T*" represents the temperature in °C at which the materials were calcined, and "C" and "H" indicate

the calcination and hydrolysis treatments, respectively, and *t* indicates the hydrolysis time. The TiO_2-(H) material (or TiO_2-(H(*24h*)) that was hydrolyzed for 24 h was further treated with an additional calcination step (500, 650 or 800 °C), giving materials labeled as TiO_2-(H+C@*T*), where "*T*" here represents the final calcination temperature in °C.

The structures of TiO_2-(C@*T*), TiO_2-(H) and TiO_2-(H+C@*T*) and their precursors (*i.e.*, TGMs) were first examined with a transmission electron microscope (TEM). The results clearly showed that the morphologies of the materials depended highly on the synthetic procedures applied to make them (**Figure 2.1 and Figure 2.2**). The TGMs showed spherical shape with a diameter of *ca*. 400 nm with relatively smooth surfaces and non-porous structures (**Figure 2.1a and Figure 2.2a**). The TiO_2-(C@*T*) materials, which were obtained by calcination, also for the most part showed spherically-shaped non-porous particles (**Figure 2.1b-d**). However, compared with the TGMs, the particles in the latter appeared to be shrunk, with their sizes decreasing from *ca*. 400 nm to *ca*. 250 nm (**Figure 2.2a-d**). This was due to the loss of ethylene glycolate groups from the TGMs as well as the condensation of surface hydroxyl groups in the materials during the high temperature calcination. Meanwhile, the particles in TiO_2-(H), which were obtained by treating TGMs in boiling water for 24 h, had porous frameworks composed of closely packed nanosized grains with sizes of *ca*. 400 nm (**Figures 2.1e, 2.2e and 2.3**). Furthermore, the particles maintained similar spherical structures and sizes as their precursors (*i.e.*, TGMs).

Scheme 2.1. Schematic illustration of the synthesis of TiO_2 materials/photocatalysts using different synthetic routes and conditions.

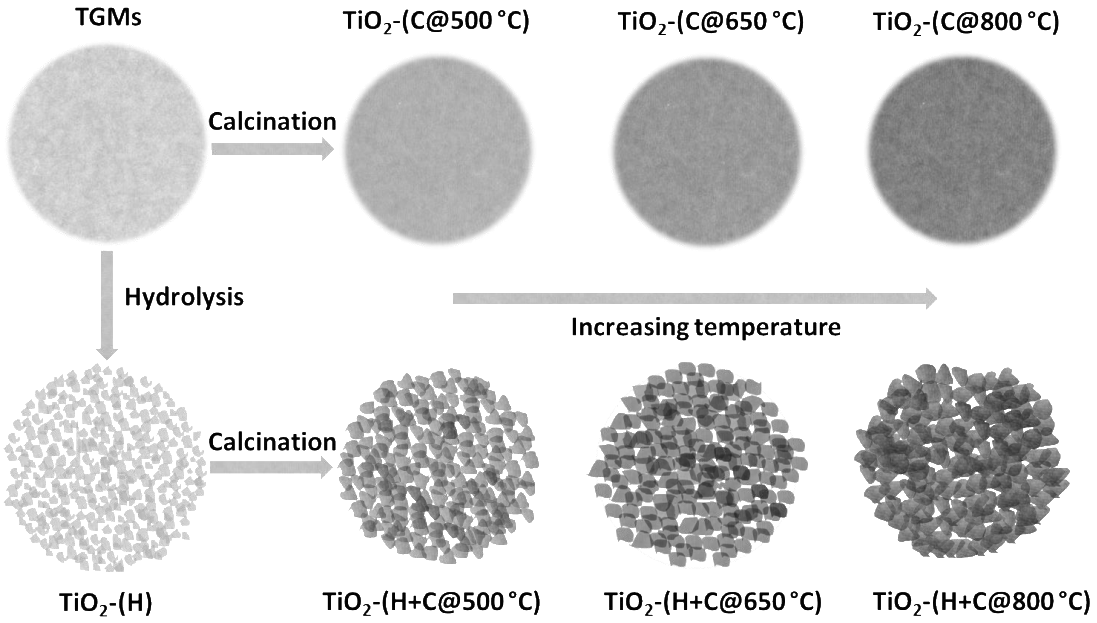

The TEM images of TiO_2-(H+C@*T*), the materials obtained by subjecting the hydrolyzed material TiO_2-(H) to calcination at 500, 650 or 800 °C (*i.e.*, TiO_2-(H+C@500 °C), TiO_2-(H+C@650 °C) and TiO_2-(H+C@800 °C), respectively), were also acquired (**Figure 2.1 and 2.2**). Their sizes again decreased with the increase in the calcination temperature, namely *ca*. 400, 300 and 250 nm for TiO_2-(H+C@500 °C), TiO_2-(H+C@650 °C) and TiO_2-(H+C@800 °C), respectively. The particles in TiO_2-(H+C@500 °C) and TiO_2-(H+C@650 °C) showed similar mesoporous structures as those in TiO_2-(H), except that the crystal grains in the former were slightly bigger and formed more closely packed structures (**Figure 2.1e-g and Figure 2.2e-g**). However, TiO_2-(H+C@800 °C) showed more aggregated crystal grains with compromised porous structure, although the particles still had spherical morphology (**Figure 2.1h and Figure 2.2h**). It is worth adding here that the sizes of the particles decreased when a relatively lower amount of

TBO (0.55 mL) and a relatively higher amount of acetone (510 mL) were used to make the TiO_2 materials, under otherwise similar synthetic procedure and condition.[20] The material made from this precursor through hydrolysis followed by calcination at 500 °C, denoted TiO_2-(H+C@500 °C)-300 nm, has particles with a diameter of *ca*. 300 nm (*cf*. the corresponding original material TiO_2-(H+C@500 °C) has particles with an average diameter of *ca*. 400 nm) (**Figures 2.4**) (see also **Figure 2.7** and other results below).

Based on the above TEM results, it could be said that the synthetic procedures employed to make the TiO_2 materials had significant impacts on the structures and morphologies of the particles formed in them. To further investigate the effect of the synthetic conditions on the surface areas and pore structures of the materials, the materials were analyzed by N_2 porosimetry (**Figure 2.5, 2.6** and **Table 2.1**). The TiO_2-(C@*T*) materials that were directly obtained by subjecting the TGMs to calcination could be seen to have highly aggregated crystal grains. This could be why these materials all showed non-porous structure with small surface area and pore volume (**Figure 2.5, 2.6** and **Table 2.1**). On the other hand, the N_2 adsorption-desorption isotherm of TiO_2-(H) showed a type IV isotherm with a type H2 hysteresis loop, which is characteristic of mesoporous materials. Among the materials synthesized and studied here, TiO_2-(H) showed the highest surface area (*ca*. 200 m^2/g). It also had a narrow pore size distribution, centered at *ca*. 6.8 nm. So, the hydrolysis route used to make TiO_2-(H) was evidently important in the formation of nanoporous structures inside the material.

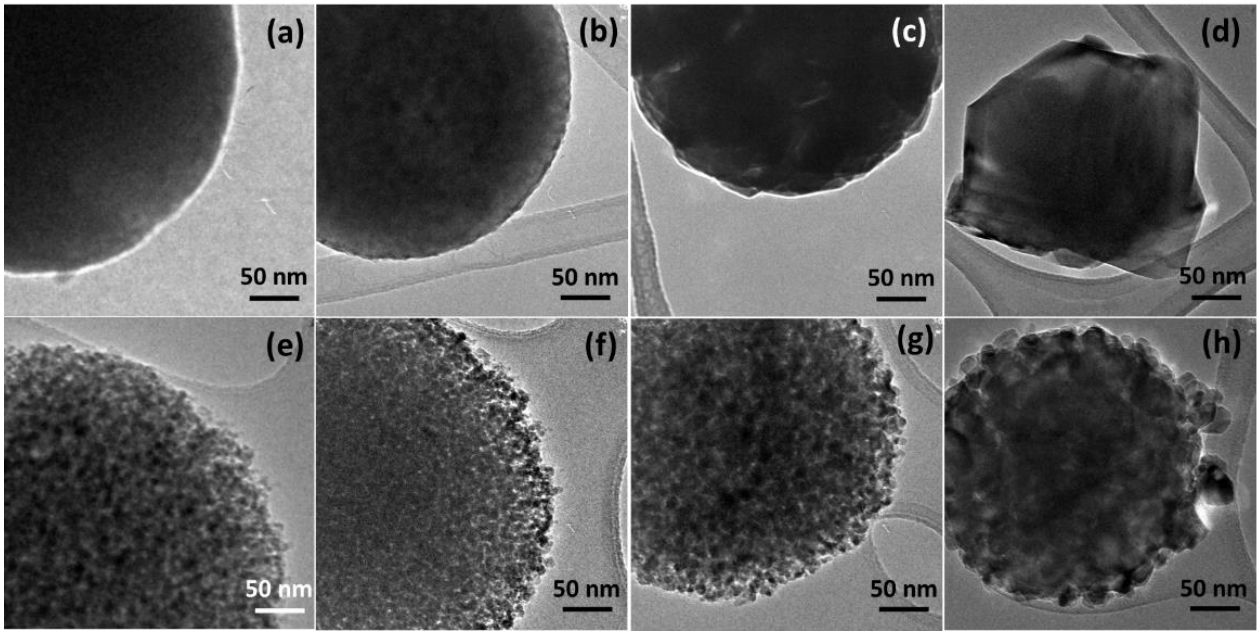

Figure 2.1. TEM images of TiO_2 microparticles derived from TGMs using different synthetic routes and conditions: (a) a TGM, (b) a TiO_2-(C@500 °C), (c) a TiO_2-(C@650 °C), (d) a TiO_2-(C@800 °C), (e) a TiO_2-(H), (f) a TiO_2-(H+C@500 °C), (g) a TiO_2-(H+C@650 °C), and (h) a TiO_2-(H+C@800 °C) particle. The images show the sizes as well as the differences in the edge structures of the particles formed in the materials.

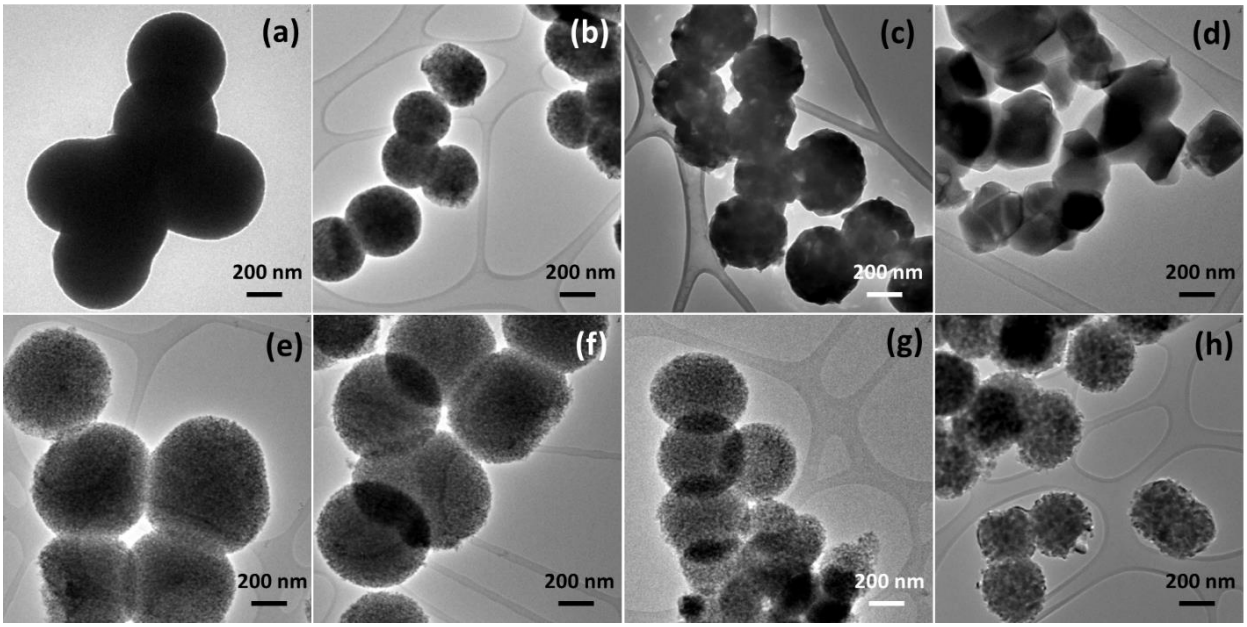

Figure 2.2. TEM image of (a) TGMs and TEM images of TiO_2 particles derived from TGMs by applying different synthetic conditions: (b) TiO_2-(C@500 °C), (c) TiO_2-(C@650 °C), (d) TiO_2-(C@800 °C), (e) TiO_2-(H), (f) TiO_2-(H+C@500 °C), (g) TiO_2-(H+C@650 °C), and (h) TiO_2-(H+C

Figure 2.3. SEM image of TiO_2-(H) material. The image shows that TiO_2-(H) particles have uniform sizes.

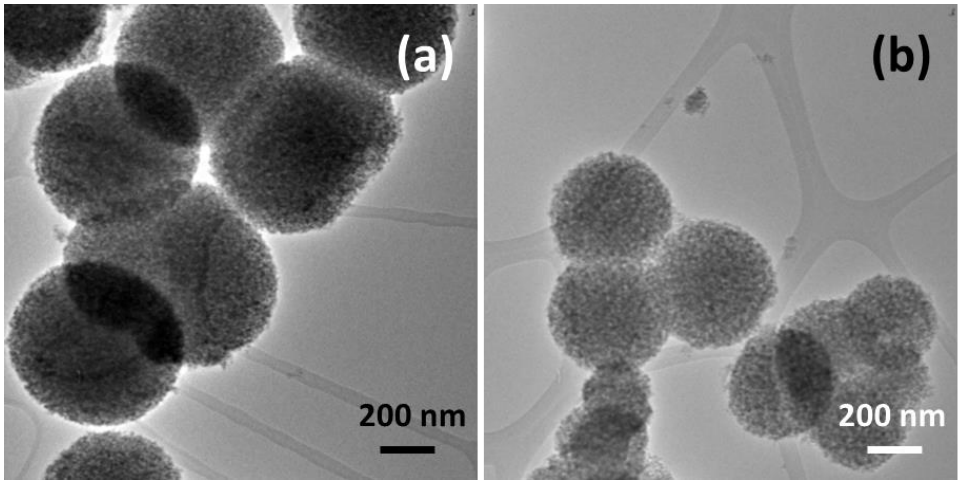

Figure 2.4. Comparison of TEM images of (a) TiO_2-(H+C@500 °C) and (b) TiO_2-(H+C@500 °C)-300 nm. The average size of the particles in the former is about 400 nm and the average size of the particles in the latter is about 300 nm. The latter material is synthesized by using a relatively lower amount of TBO (0.55 mL) and a relatively higher amount of acetone (510 mL), under otherwise similar synthetic procedure and synthetic condition as the one used to make TiO_2-(H+C@500 °C). Other characterization results and catalytic properties of the later material are provided below (**Figure 2.7, Table 2.2** and **Figure 2.18** below).

As mentioned earlier, high-temperature treatment can improve the crystallinity, and thereby the photocatalytic performances of TiO_2 materials.[10,11] However, it can also cause the aggregation of crystal grains and the degradation of porous structures in the materials, which can in turn compromise the materials' photocatalytic activities (*e.g.*, by reducing the accessible catalytic active sites as well as the mass transport pathways for reactants, intermediates and products in the materials). In light of this conundrum, it is of great importance to figure out the possible impact that high temperature treatment may have on the structures and porosity of such materials and to determine the optimal synthetic conditions that produce the most effective

photocatalyst. Hence, the structures of all the materials obtained above by different synthetic routes were further probed before testing their catalytic activities.

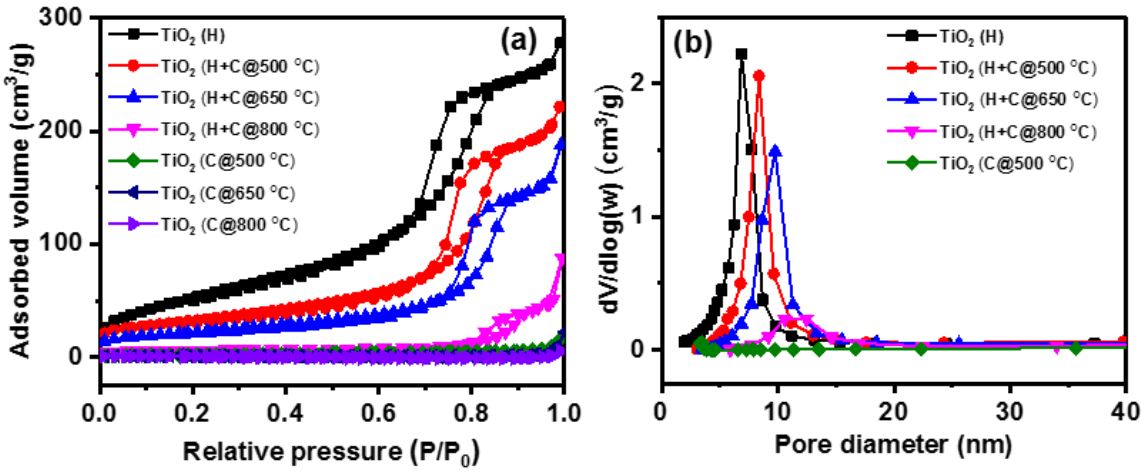

Figure 2.5. (a) N_2 adsorption-desorption isotherms of TiO_2 materials synthesized by using different synthetic procedures and (b) their corresponding pore size distributions.

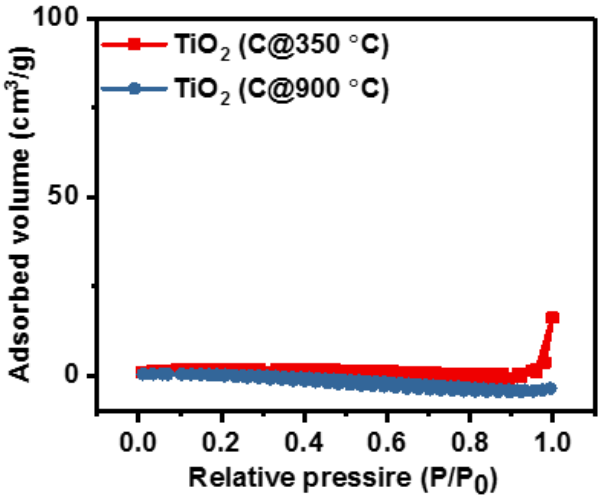

Figure 2.6. N_2 adsorption-desorption isotherms of TiO_2-(C@350 °C) and TiO_2-(C@900 °C) materials.

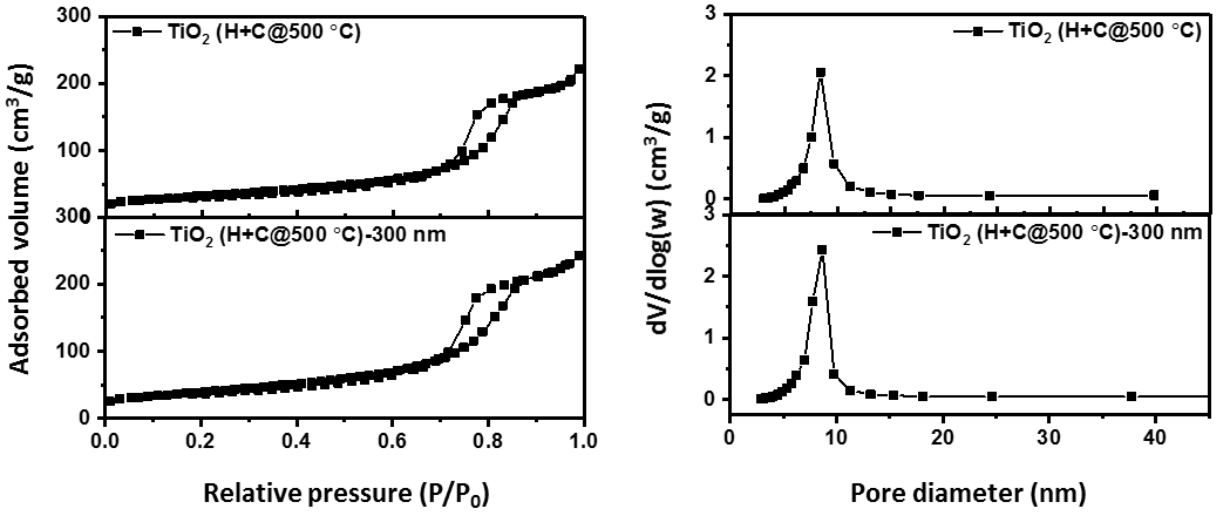

Figure 2.7. (Left panel) N_2 adsorption-desorption isotherms of TiO_2-(H+C@500 °C) and TiO_2-(H+C@500 °C)-300 nm and (right panel) their corresponding pore size distributions. Their surface areas and pore structures are analyzed by N_2 porosimetry and compared with one another. TiO_2-(H+C@500 °C)-300 shows a slightly higher BET surface area (134 m^2/g) compared with TiO_2-(H+C@500 °C) (which has a surface area of 126 m^2/g). The higher surface area in the former is most likely due to its smaller particle sizes (see **Figure 2.4** above). The average pore sizes in both materials are found to be about the same (*ca*. 8.3 and 8.5 nm).

Just like TiO_2-(H), TiO_2-(H+C@*T*) materials displayed a type IV isotherm with a type H2 hysteresis loop, indicating the existence of mesoporous structures in them. The surface area of TiO_2-(H+C@500 °C), TiO_2-(H+C@650 °C) and TiO_2-(H+C@800 °C) gradually decreased as the calcination temperature used to make them was increased; however, unlike the other calcined materials discussed above (*i.e*., TiO_2-(C@*T*) materials), these three materials all possessed relatively high BET surface areas (126, 78 and 29 m^2/g, respectively) (**Table 2.1**). These results clearly indicated that the hydrolysis process employed before calcination was indirectly helpful in the formation of the nanoporous structure inside TiO_2-(H) particles obtained from TGMs as well

as maintaining the resulting nanoporous structure upon high-temperature treatment. Moreover, based on additional experiments, the materials were found to maintain their porous structure even after being subjected to high-temperature calcination for prolonged times. For example, when the TiO_2-(H) material was calcined at 500 °C for 4, 8, 12 or 16 h in order to study its thermal stability, the resulting materials all showed similar BET surface areas and pore volumes as the material obtained by calcination at the same temperature but for 2 h (TiO_2-(H+C@500 °C(2h)) (see **Figure 2.8** and **Table 2.3**). This indicated that the mesoporous structure in these materials could survive the calcination treatment (*cf.*, the TiO_2-(C@*T*) materials obtained by calcination were not nanoporous). Quantitative results of the N_2 porosimetry analysis of all the materials are compiled in **Table 2.1**, **Table 2.2** and **Table 2.3**.

Table 2.1. Structural and crystallographic properties of some of the TiO_2 materials.[a]

TiO_2 materials or catalysts	Structure			Crystallinity	
	BET surface area (m^2/g) [b]	Average pore size (nm) [b]	Pore volume (cm^3/g) [b]	Phase [c]	Crystal size (nm) [d]
TiO_2-(H)	200	6.8	0.44	A	5.8
TiO_2(H+C@500°C)	126	8.3	0.35	A	7.9
TiO_2(H+C@650°C)	78	9.7	0.29	A	11.1
TiO_2(H+C@800°C)	29	10.5	0.14	A + R	20.7; 26.6 [e]
TiO_2(C@500°C)	3	-	0.01	A + R	13.5; 20.9 [e]
TiO_2(C@650°C)	3	-	0.02	A + R	30.4; 37.3 [e]
TiO_2(C@800°C)	2	-	-	R	37.7

[a] TiO_2-(H+C@*T*) and TiO_2-(C@*T*) materials were obtained by calcining TiO_2-(H) and TGMs at desired temperature, respectively, at the desired temperature *T* for 2 h (the default calcination time). [b] Obtained from the desorption branch of N_2 adsorption/desorption isotherms using the BET

method. [c] A and R represent anatase and rutile, respectively. [d] Measured by XRD using the Scherrer equation. [e] The two values correspond to the crystallite sizes of A and R, respectively.

Table 2.2. Structural properties and photocatalytic activities of TiO_2-(H+C@500 °C) and TiO_2-(H+C@500 °C)-300 nm.

Samples	Structure			Rate of production of CH_4 (μmol g^{-1} h^{-1})
	BET surface area (m^2/g)	Average pore size (nm) [a]	Pore volume (cm^3/g) [a]	
TiO_2-(H+C@500°C)	126	8.3	0.35	12.5
TiO_2-(H+C@500°C)-300 nm	134	8.5	0.33	13.2

[a] Measured from the desorption branch of N_2 adsorption/desorption isotherms.

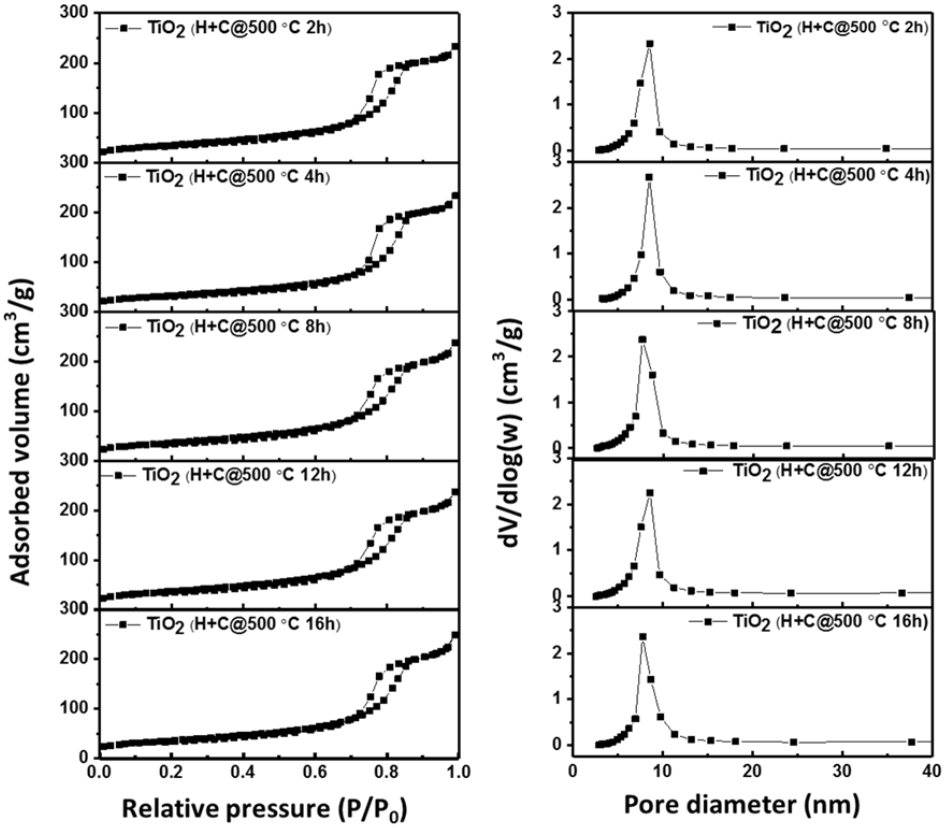

Figure 2.8. (Left panel) N_2 adsorption-desorption isotherms of TiO_2-(H+C@500 °C(*t*)) materials, which are calcined at 500 °C for different periods of time and (right panel) their corresponding pore size distributions.

Table 2.3. BET surface area, average pore size, and pore volume of TiO_2-(H+C@500 °C(*t*)) materials, which are calcined at 500 °C for different periods of times. [a]

TiO_2 Materials	Calcination time (h)	BET surface area (m^2/g) [b]	Average pore size (nm) [b]	Pore volume (cm^3/g) [b]
TiO_2(H+C@500°C(*t*))	2 [b]	123	8.5	0.35
	4	118	8.5	0.36
	8	129	8.1	0.39
	12	130	8.6	0.37
	16	127	8.2	0.39

[a] Measured by N_2 porosimetry. [b] This material is the same as TiO_2(H+C@500°C).

To study the effect of hydrolysis and calcination on the phase composition, crystallinity and crystallite size in the materials synthesized under different reaction conditions, a series of XRD measurements was performed. First, the effects of hydrolysis temperature and time on the XRD patterns of the materials were investigated. When TGMs were treated at 40 °C and 70 °C, they remained relatively stable and gave no crystalline TiO_2 (**Figure 2.9**). However, when they were treated under at 100 °C, they were gradually transformed into crystalline TiO_2 (or anatase) and fully became TiO_2 over longer hydrolysis times (**Figure 2.10**). Specifically, the characteristic diffraction peaks of anatase at 2θ of 25.4°, 38.0°, 48.1°, 54.2° and 62.7°, which could be ascribed to the (101), (004), (200), (105), and (204) planes of anatase (JCPDS: 21-1272), respectively, were increasingly observed in the XRD patterns of the materials hydrolyzed for longer periods. Meanwhile, when TiO_2-(H) materials were synthesized (at 100 °C) with hydrolysis times of 30 min or more (*i.e.*, TiO_2-(H(*t*)) materials, where "*t*" ≥ 30 min), they became crystalline, showing sharp diffraction peaks corresponding to anatase in their XRD patterns (**Figure 2.10**). Subjecting the materials to hydrolysis for more than 2 h did not, however, result in any more notable improvement in the peak intensities in the XRD patterns or the crystallinity of the materials

compared with the one obtained with 2 h-long hydrolysis. The mechanism by which TGMs transform into TiO_2 microparticles was previously proposed.[21] First, the outer shell of TGMs will undergo hydrolysis. The co-presence of TGM and TiO_2, which have different density, results in some cracks on the outer shell. This allows water to penetrate into the structure and react further with the inner part of TGMs as illustrated in **Scheme 2.2**.[21] With the prolonged hydrolysis time, the small crystalline TiO_2 clusters could gradually grow into interconnected crystalline TiO_2 nanoparticles. The conversion of TGM to TiO_2 during this hydrolysis treatment was corroborated by thermogravimetric analysis (TGA) (**Figure 2.11**). The TGA curve of TiO_2-(H) showed only *ca*. 7% weight loss, which is due to the condensation of the surface hydroxyl groups, and no significant weight loss between 100 - 300 °C and 400 - 500 °C. On the other hand, the TGA of TGMs showed weight losses between 100 - 300 °C and 400 - 500 °C corresponding to the removal of physisorbed water and ethylene glycol, and the degradation and removal of chemically bonded ethylene glycolate units and any other possible residual organic groups (butoxy groups), respectively.[15]

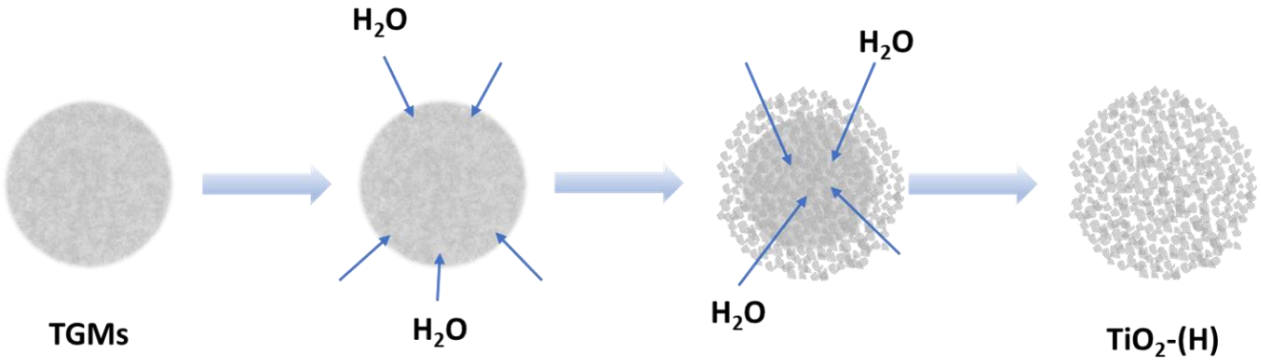

Scheme 2.2. Proposed mechanism of formation of TiO_2-(H) from TGMs through hydrolysis.

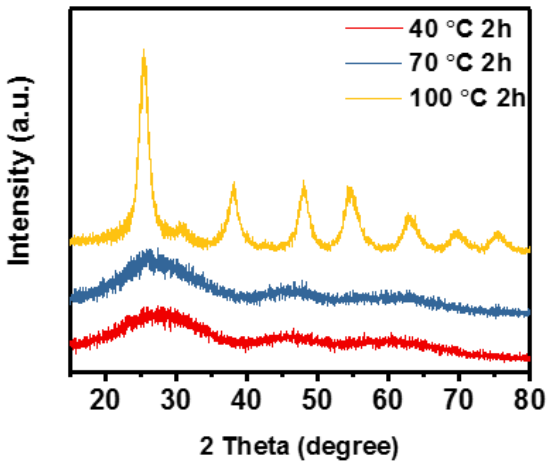

Figure 2.9. XRD patterns of mesoporous TiO_2 microparticles obtained by hydrolyzing TGMs at different temperatures for 2 h.

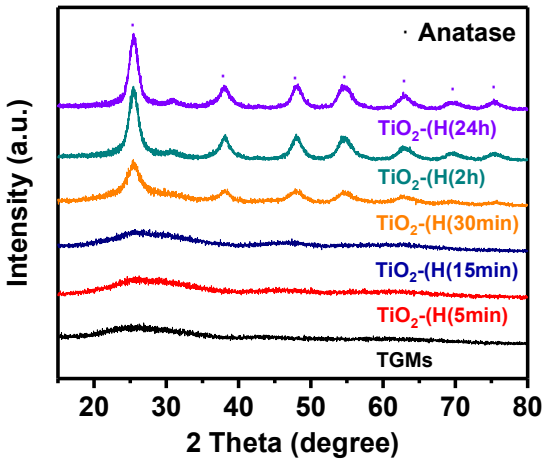

Figure 2.10. XRD patterns of mesoporous TiO_2 microparticles obtained by hydrolyzing TGMs at 100 °C for different periods of time. The one for TGM is also displayed for comparison.

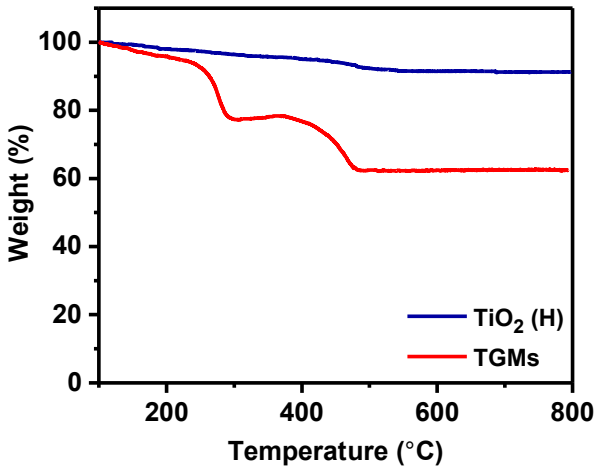

Figure 2.11. TGA curves of TGMs and TiO_2-(H).

When TiO_2-(H) (the material obtained by hydrolyzing TGMS for t = 24 h or TiO_2-(H(*24 h*)) was subjected to calcination at 500 °C, 650 °C and 800 °C, some notable differences in XRD patterns among the materials could be noted (**Figure 2.12**). First, compared with the anatase peaks in the XRD pattern of TiO_2-(H), the corresponding peaks in the XRD patterns of TiO_2-(H+C@500 °C) and TiO_2-(H+C@650 °C) appeared sharper, indicating that the latter materials were more crystalline and that the calcination treatment increased the crystallinity of the materials. Second, after calcination at 500 °C and 650 °C, anatase was still seen as the dominant phase in the XRD patterns of calcined materials. However, when a higher calcination temperature (800 °C) was used, rutile phase was also present, as peaks at 2θ of 27.5°, 36.2°, 41.3°, 44.2°, and 56.8°, which correspond to the (110), (101), (111), (210), and (220) phases of rutile (JCPDS: 21-1276), respectively, were observed in the XRD pattern of the material. Interestingly, note that the TiO_2 materials obtained directly by calcining TGMs (*i.e.*, TiO_2-(C@*T*) materials) without pre-subjecting them to hydrolysis remained amorphous at 350 °C, formed rutile phase at 500 °C and completely became rutile above 800 °C (**Figures 2.12 and 2.13**). Overall, the XRD results clearly revealed

that the hydrolysis step applied on the amorphous TGMs helped not only the anatase phase to form but also made it to remain largely intact even when the materials were treated at high temperature. In other words, the hydrolysis step performed prior to calcination significantly helped the materials to resist the possible phase transformation of anatase to rutile during subsequent high-temperature treatments.

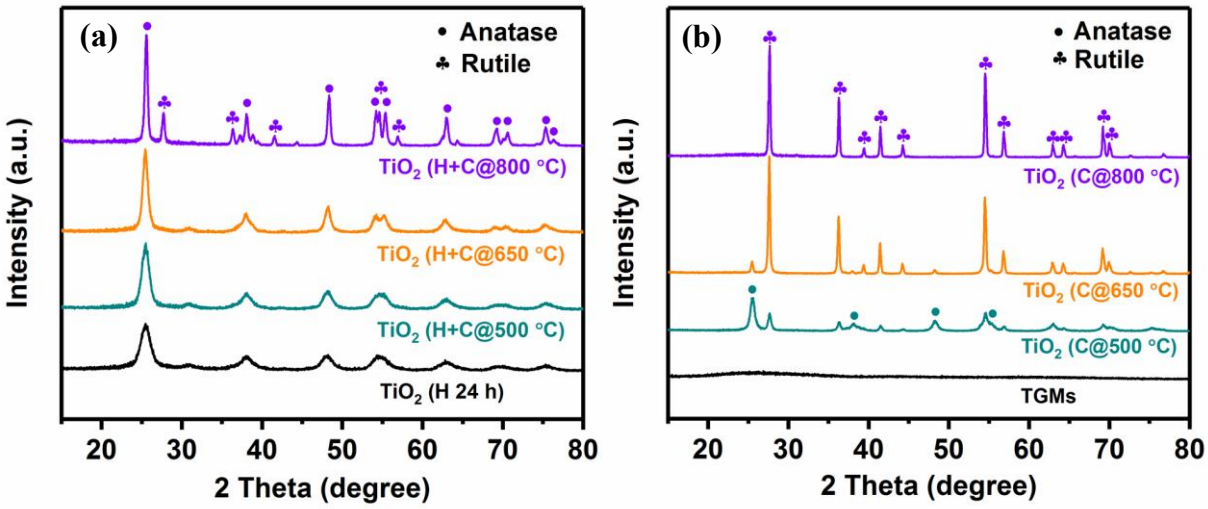

Figure 2.12. (a) XRD patterns of TiO_2-(H+C@*T*) materials obtained by calcining TiO_2-(H) at different temperature, *T*, and (b) XRD patterns of TiO_2-(C@*T*) materials obtained by calcining TGMs at different temperature, *T*.

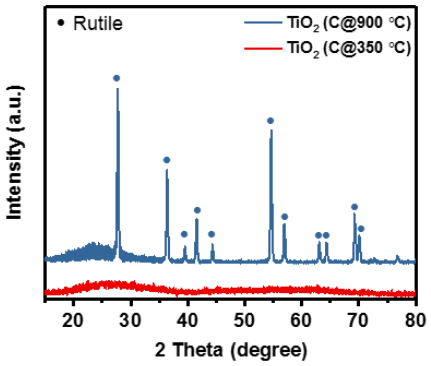

Figure 2.13. XRD patterns of TiO_2-(C@350 °C) and TiO_2-(C@900 °C) materials.

The crystallite sizes in the materials were determined based on the strongest anatase (101) and rutile (110) peaks using the Scherrer equation ($d = 0.89\lambda/\beta \cos\theta$, where d, λ, β and θ are the crystallite size, the wavelength of the X-ray radiation, the full width at half-maximum of the peaks in radians and the diffraction angle, respectively). The results, summarized in **Table 2.1**, showed that the average crystallite size of anatase particles in the hydrolyzed TiO_2-(H) material were *ca*. 5.8 nm. After being calcined for 2 h at 500 °C or 650 °C, the average crystallite sizes slightly increased, to *ca*. 7.9 and *ca*. 11.1 nm (for TiO_2-(H+C@500 °C) and TiO_2-(H+C@650 °C)), respectively. The materials treated at 800 °C (TiO_2-(H+C@800 °C)) showed both anatase and rutile phases, with their crystal sizes averaging at *ca*. 20.7 and *ca*. 26.6 nm, respectively.

It is generally accepted that the thermodynamic stability of crystalline TiO_2 depends on its crystal size.[22,23] When the crystal size of TiO_2 exceeds *ca*. 35 nm, rutile is a more thermodynamically stable phase than anatase, whereas the crystal size is below *ca*. 11 nm, anatase is more stable.[22,23] So, the 5.8 nm-in-size anatase crystal grains that were produced from the hydrolysis of TGMs and that led to the formation of stable porous frameworks were likely the reason that TiO_2-(H+C@*T*) materials resisted full transformation into rutile during high-temperature calcination. On the other hand, the dense TiO_2-(C@*T*) materials obtained from the TGMs by direct calcination and that are composed of bigger anatase particles could easily undergo this phase transformation completely.

Meanwhile, TiO_2-(H) was found to have mesoporous structure, based on the TEM images and the N_2 porosimetry results described above. The small spaces between the anatase grains in it, which were created during hydrolysis, were able to limit the potential aggregation of the crystallites at elevated temperatures.[18,24] Hence, the particles in TiO_2-(H+C@500 °C) and TiO_2-(H+C@650 °C) grew only slightly compared with those in TiO_2-(H). The highest temperature used

in our studies, 800 °C, however, led to substantial sintering of the grains of anatase and bigger particles. This, in turn, made some of the anatase crystallites to transform into rutile during calcination of the material at this temperature.

Meanwhile, when amorphous TGMs were directly converted into TiO_2-(C@*T*) by calcination, their interconnected structures/networks easily aggregated and resulted in bigger crystals (**Table 2.1**). Not surprisingly, the rutile phase started to appear in these materials even when they were calcined at 500 °C, and it was the only phase in the material that was calcined at 800 °C (**Figure 2.12b**). Furthermore, the crystal sizes of anatase in the materials grew from 13.5 to 30.4 nm when the calcination temperature was increased from 500 to 650 °C. Anatase was no longer observed in the material calcined at 800 °C because the higher temperature made the crystallites to increase in size and thereby easily and fully transform into rutile. This means, without the pre-hydrolysis step, direct calcination of TGMs made the crystal grains of TiO_2-(C@*T*) to aggregate and form solely bigger rutile particles with non-porous structures and extremely low surface areas. So, overall the XRD results clearly proved that the hydrolysis step considerably inhibited the growth of anatase grains, limiting their possible transformation into rutile in subsequent high-temperature calcination. Besides, it helped the materials to retain relatively large surface area and pore volume.

The UV-Vis diffuse reflectance spectra (DRS) of the different TiO_2 materials were measured in the range from 250 to 800 nm (**Figure 2.14**). Furthermore, the band gap energy (E_g) of the materials was estimated (**Table 2.4**) by using the reflectance data and the transformed Kubelka-Munk equation:[25] $[F(R) \cdot hv]^{0.5} = A(hv - E_g)$, where $F(R) = \alpha = (1-R)^2/2R$, hv is the incident photon energy, E_g is the band gap energy, A is constant, whose value depends on the transition probability, and R is the percentage of reflected light. The results indicated that when

the calcination temperature was increased from 500 to 800 °C, the absorption edges shifted towards higher wavelength and the corresponding band gap decreased from 3.21 to 3.04 eV. For example, the absorption band of TiO_2-(H+C@650 °C) was red shifted compared with that of TiO_2-(H+C@500 °C) and the corresponding band gap of TiO_2-(H+C@650 °C) ($E_g = 3.17$) was slightly lower than that of TiO_2-(H+C@500 °C) ($E_g = 3.21$). The lowest band gap observed for TiO_2-(H+C@800 °C) ($E_g = 3.04$) can be attributed to the presence of rutile phase in it.[26] Interestingly, the band gap energy of TiO_2-(H) ($E_g = 3.19$) was slightly lower than that of TiO_2-(H+C@500 °C) ($E_g = 3.21$); this can be explained in terms of the density of hydroxyl groups on the surface of TiO_2-(H), which can introduce new energy levels in the intra-band space in it.[26] After calcination at 500 °C in air of TiO_2-(H) (that means, upon making TiO_2-(H+C@500 °C)), the amount of surface hydroxyl groups in the material becomes significantly less, resulting in a slightly higher band gap TiO_2-(H+C@500 °C) (compared with that of TiO_2-(H)).

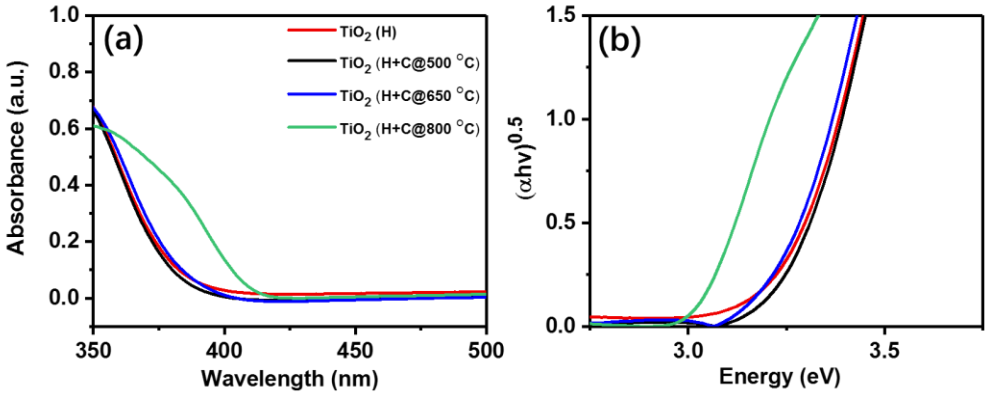

Figure 2.14. (a) UV-Vis diffuse reflectance spectra (DRS) of TiO_2-(H) and TiO_2-(H+C@*T*) materials and (b) the corresponding plots of the transformed Kubelka-Munk function versus the energy of the light.

Table 2.4. Band gap values of TiO_2-(H) and TiO_2-(H+C@*T*) materials. [a]

Sample name	TiO_2-(H)	TiO_2-(H+C@500 °C)	TiO_2-(H+C@650 °C)	TiO_2-(H+C@800 °C)
Band gap	3.19	3.21	3.17	3.04

[a] Estimated from Kubelka-Munk equation.

The transient photocurrent spectra were recorded to evaluate the separation efficiency of the photoinduced electron-hole pairs forming in the photocatalysts (**Figure 2.15**). It is widely documented that the separation efficiency of photoinduced charge carriers is directly related to the intensity of photoinduced current: a higher efficiency of charge carrier separation leads to a higher photocurrent.[27-29] **Figure 2.15a** shows the transient photocurrent responses of different TiO_2 materials during several on-off cycles. The photocurrent increased sharply when the light was switched on, and immediately returned to the initial state when the light was turned off, indicating irradiation of light was essential for generating the photocurrent in the materials. TiO_2-(H+C@*T*) materials all exhibited higher photocurrent than TiO_2-(H), suggesting that the charge separation efficiency could be enhanced by improving the crystallinity, or reducing structural defect sites, in the material. Among the TiO_2-(H+C@*T*) materials, TiO_2-(H+C@650 °C) exhibited the highest photocurrent, which suggests that the material has the highest charge separation efficiency.

Additionally, electrochemical impedance spectra (EIS) Nyquist plots have been obtained to further assess the charge separation efficiency and the charge transfer processes of the photogenerated electron-hole pairs in the materials. Generally, a smaller semicircle in EIS reflects a higher charge separation efficiency.[27-29] As shown in **Figure 2.15b**, TiO_2-(H+C@650 °C) exhibits the smallest semicircle in EIS, indicating once again that it shows the best performances in charge carrier separation and charge carrier mobility.

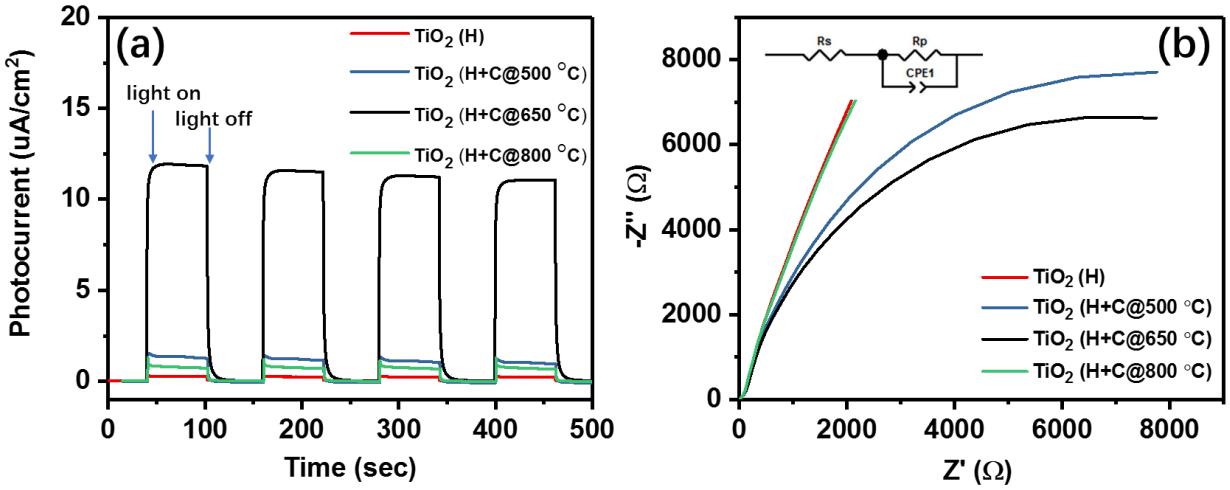

Figure 2.15. (a) Transient photocurrent responses and (b) Electrochemical impedance spectra (EIS) of TiO_2-(H+C@*T*) materials obtained by calcining TiO_2-(H) at different temperature.

Owing to their intrinsic properties, such as high specific surface area, mesoporous structure, high crystallinity as well as enhanced charge separation efficiency, the TiO_2-based materials synthesized here could be anticipated to serve as photocatalysts for various reactions.[2,3,14,30] Continuing on our previous line of work, the photocatalytic properties of the TiO_2 materials for reduction of CO_2 by H_2O into hydrocarbon fuels were investigated.[7,17-19] Comparative results of the photocatalytic activities of the materials toward CO_2 reduction are provided in **Figure 2.17**. As expected, no hydrocarbon products were detected in the absence of either CO_2 or light irradiation despite the presence of the TiO_2 materials in the reactor. Moreover, even when CO_2, H_2O and light (300 W simulated solar Xe arc lamp) were present, TiO_2-(C@*T*) materials (the materials synthesized without hydrolysis treatment) did not function well as photocatalyst, giving only negligible amount of hydrocarbon products. However, under the same reaction condition, the material obtained by hydrolysis (TiO_2-(H)) as well as those obtained by hydrolyzed plus calcination (TiO_2-(H+C@*T*)) yielded a hydrocarbon product, CH_4, with different rates depending on the synthetic condition and calcination temperature employed to make them. The rate of

production of CH_4 over TiO_2-(H) was 2.99 µmol/g^{-1} h^{-1}, and the value increased to 12.55 µmol g^{-1} h^{-1} and 14.75 µmol g^{-1} h^{-1} for TiO_2-(H+*C*@500 °C) and TiO_2-(H+C@650 °C), respectively. This means the photocatalytic activity of TiO_2-(H+C@*T*) materials increased when the calcination temperature was increased from 500 °C to 650 °C. But, the rate of production of CH_4 decreased to 6.75 µmol g^{-1} h^{-1} when the calcination temperature was further increased for TiO_2-(H+C@800 °C). Nevertheless, all the materials, including the relatively weakly performing ones, exhibited much higher photocatalytic activity compared with the commercial Degussa P25 TiO_2, which was used as a reference here and which produced CH_4 only at 0.38 µmol g^{-1} h^{-1} under the same photocatalytic reaction condition.

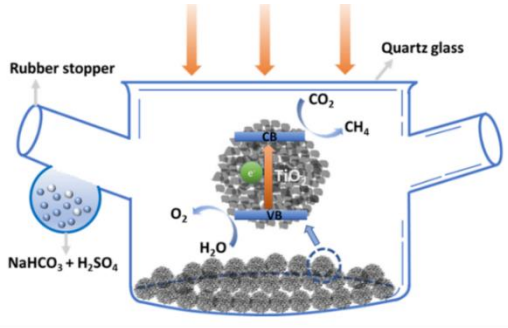

Figure 2.16. Schematic illustration of the photoreactor used for photocatalytic tests.

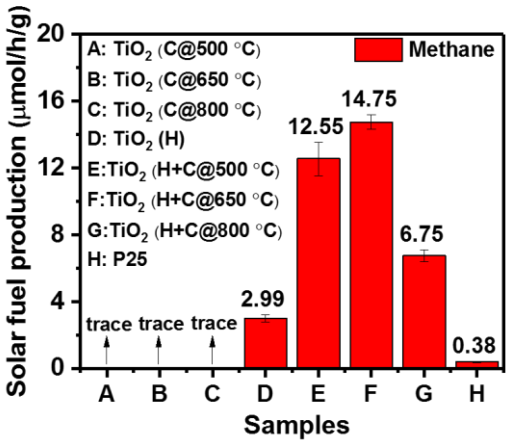

Figure 2.17. Rates of production of CH_4 over different TiO_2 materials or photocatalysts that are synthesized using different synthetic routes and conditions.

Perhaps not surprisingly, the above results clearly indicated that the rate of production of CH_4 by photocatalysis over the TiO_2 materials was significantly affected by the materials' structures and composition (*e.g.*, crystallinity, surface area and charge separation efficiency). The negligible catalytic activity exhibited by TiO_2-(C@*T*) materials could easily be accounted by their extremely low surface areas and non-porous structures, which obviously could result in less exposed catalytic active sites and diffusion pathways for reactants and products. On the other side, the hydrolysis step applied on amorphous TGMs helped with the formation of the mesoporous structures as well as the photoactive anatase grains in the TiO_2 materials. Thanks to these structure advantages, the resulting material, TiO_2-(H), exhibited much higher photocatalytic activity than TiO_2-(C@*T*) materials.

It is generally accepted that increasing crystallinity in TiO_2 material can reduce the density of structural defect sites, which can serve as electron trapping sites between the conduction band and valence band, or as recombination centers of the photogenerated charge carriers.[10,24,31] As can be seen in Figure 5a, the inclusion of a subsequent calcination step after hydrolysis significantly improved the crystallinity of TiO_2-(H) while letting it largely maintain its photoactive anatase phase. Not surprisingly, the transient photocurrent results as well as the EIS measurements both indicated that TiO_2-(H+C@*T*) materials exhibited higher charge separation efficiency than TiO_2-(H) (**Figure 2.15**). These must have been the reason why the TiO_2-(H+C@*T*) materials showed improved photocatalytic activity for CO_2 reduction compared with TiO_2-(H), which has relatively lower crystallinity and ability to carry out charge separation. More specifically, the rates of CH_4 production over TiO_2-(H) (2.99 μmol g^{-1} h^{-1}), TiO_2-(H+C@500 °C) (12.55 μmol g^{-1} h^{-1}) and TiO_2-(H+C@650 °C) (14.75 μmol g^{-1} h^{-1}) were in line with the transient photocurrent and EIS results. In addition, compared with the particles in TiO_2-(H), the crystal sizes of the anatase particles in

TiO_2-(H+C@500 °C) and TiO_2-(H+C@650 °C) were slightly bigger. This resulted in improved structural necking between TiO_2 grains in the latter, and thus better charge transport at grain boundaries and improved spatial separations over these materials.[18,32] So, the increased crystal sizes could also be beneficial for facilitating charge delocalization.[9] However, after reaching 800 °C (TiO_2-(C+H@800 °C)), the photocatalytic activity of the material got compromised, giving a CH_4 production rate of only 6.75 µmol g^{-1} h^{-1}. This can be explained in terms of its inferior charge separation efficiency (**Figure 2.15**) and significantly lower surface area (29 m^2/g) compared with TiO_2-(H+C@500 °C) and TiO_2-(H+C@650 °C) (126 and 78 m^2/g, respectively), which results in less available active catalytic sites. This was corroborated by the fact that the material prepared with smaller amount of TBO with respect to acetone (TiO_2-(H+C@500 °C)-300 nm), which showed higher surface area than TiO_2-(H+C@500 °C), exhibited a slightly higher rate for production of CH_4 during photocatalytic CO_2 reduction (**Figure 2.18**).

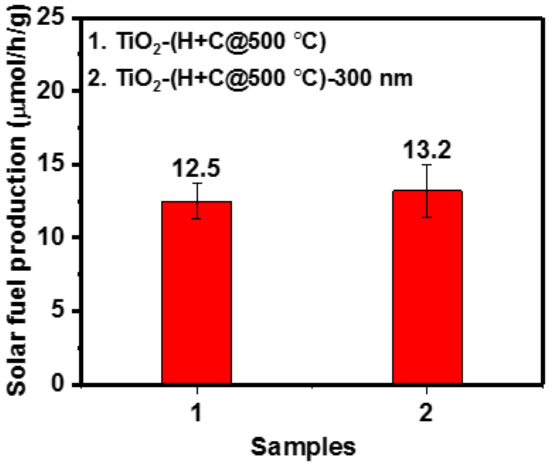

Figure 2.18. Rates of production of CH_4 from photocatalytic reduction of CO_2 with H_2O over TiO_2-(H+C@500 °C) and TiO_2-(H+C@500 °C)-300 nm materials.

The stability of the catalysts was tested by recovering TiO_2-(H+C@650 °C) after reaction and then evaluating its photocatalytic activity in four reaction cycles. The rates of generation of

CH_4 over this photocatalyst did not decrease after being reused, indicating its good stability (see **Figure 2.19**). Its TEM image after the stability test also showed no obvious change in the structures of its particles (**Figure 2.20**). The surface area and average pore size of the spent catalyst were found to be 74 m^2/g and 9.2 nm, respectively, which are close to those of the fresh sample (78 m^2/g and 9.7 nm) (**Figure 2.21** and **Table 2.5**). Moreover, the XRD analysis revealed that there was no phase change in the material after serving as catalyst, and the crystallite size of anatase in it remained similar to that in the original material (see **Figure 2.22** and **Table 2.5**). Based on the above experimental results, it can be said that TiO_2-(H+C@650 °C) remains stable during photocatalytic activity and the morphology and structure of the particles in it remain unchanged after reusing it in, at least, four reaction cycles.

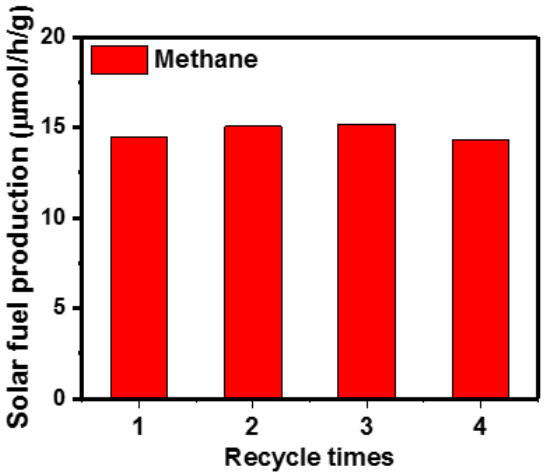

Figure 2.19. Rates of production of CH_4 during 1 h-long photocatalytic CO_2 reduction over TiO_2-(H+C@650 °C) in four reaction cycles.

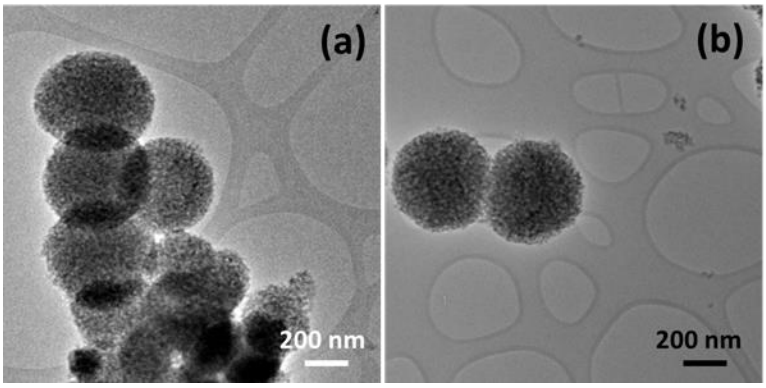

Figure 2.20. TEM image of (a) a fresh TiO_2-(H+C@650 °C) and (b) a TiO_2-(H+C@650 °C) material after photocatalytic stability test in four reaction cycles.

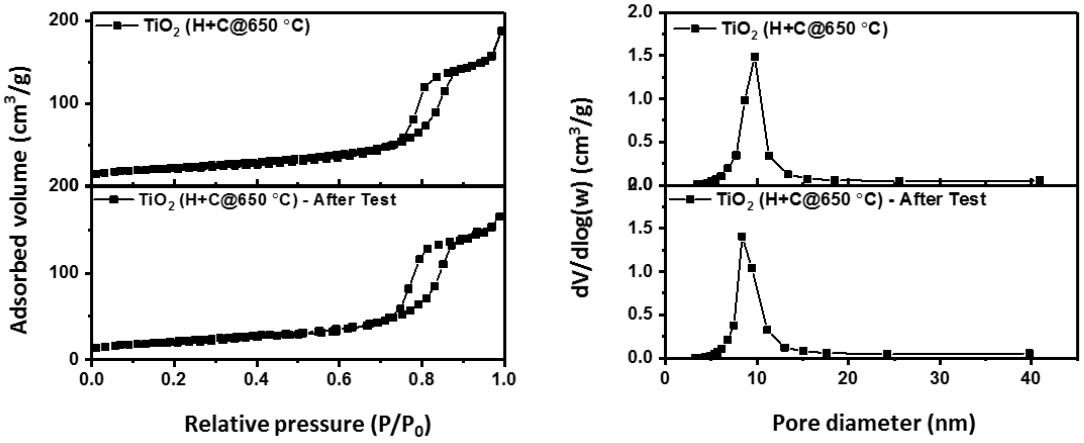

Figure 2.21. (Left panel) N_2 adsorption-desorption isotherms of a fresh TiO_2-(H+C@650 °C) material and a TiO_2-(H+C@650 °C) material after photocatalytic stability test in four reaction cycles, and (right panel) their corresponding pore size distributions.

Table 2.5. Structural and crystallographic properties of TiO_2-(H+C@650 °C) before and after photocatalytic stability test in four reaction cycles.

Samples	Structure			Crystallinity	
	BET surface area (m^2/g) [a]	Average pore size (nm) [a]	Pore volume (cm^3/g) [a]	Phase [b]	Crystal size (nm) [c]
TiO_2(H+C@650°C) (Original material)	78	9.7	0.29	A	11.1
TiO_2(H+C@650°C)-after test	74	9.2	0.30	A	11.8

[a] Measured from the desorption branch of N_2 adsorption/desorption isotherms. [b] A and R represent anatase and rutile, respectively. [c] Measured by XRD using the Scherrer equation.

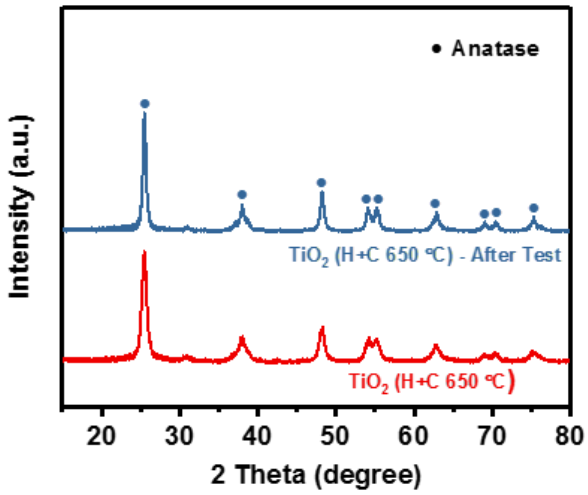

Figure 2.22. XRD patterns of a fresh TiO_2-(H+C@650 °C) material and a recycled TiO_2-(H+C@650 °C) material after four cycles of photocatalytic stability tests.

2.5. Conclusions

In summary, we have developed a simple, template-free hydrolysis-calcination synthetic route that can produce a series of highly crystalline porous TiO_2 microparticles or photocatalysts containing large surface area and predominantly anatase phase. The hydrolysis step was found to be instrumental for the formation of nanoporous structures and small anatase grains in the materials. Upon further calcination, the materials became more crystalline while, for the most part, maintaining their anatase phase and reasonably high surface area and porosity. The enhanced crystallinity along with the closely packed grains enabled the materials to serve as efficient photocatalysts for CO_2 reduction with H_2O under simulated solar light. The present work can inspire others to explore new synthetic methods that can lead to mesoporous TiO_2 with well

controlled morphology, pure phase, crystallinity as well as enhanced charge separation efficiency, which are important factors to help this material find advanced applications in areas including photovoltaics, catalysis, fuel cells and batteries.

2.6. Reference

1. Goeppert, A.; Czaun, M.; Jones, A.-P.; Prakash, G. K. S; Olah, G. A. *Chem. Soc. Rev*., **2014**, *43*, 7995-8048.
2. Habisreutinger, S. N.; Schmidt-Menda, L.; Stolarczyk, J. K. *Angew. Chem. Int. Ed.*, **2013**, *52*, 7372-7408.
3. Ma, Y.; Wang, X.; Jia, Y.; Chen, X.; Han, H., Li, C. *Chem. Rev*., **2014**, *114*, 9987-10043.
4. Fang, B.; Xing, Y.; Bonakdarpour, A.; Zhang, S.; Wilkinson, D. P. *ACS Sustainable Chem. Eng.*, **2015**, *3*, 2381-2388.
5. Su, J.; Vayssieres. L. *ACS Energy Lett*., **2016**, *1*, 121-135.
6. Protti, S.; Albini, A.; Serpone, N. *Phys. Chem. Chem. Phys.*, **2014**, *16*, 19790-19827.
7. Zhang, T.; Low, J.; Huang, X.; Al-Sharab, J. F.; Yu, J.; Asefa, T. *ChemCatChem*, **2017**, *9*, 3054-3062.
8. Yan, K.; Wu. G. *ACS Sustainable Chem. Eng*., **2015**, *3*, 779-791.
9. Joo, J. B.; Zhang, Q.; Dahl, M.; Lee, I.; Goebl, J.; Zaera, F.; Yin, Y. *Energy Environ. Sci*., **2012**, *5*, 6321-6327.
10. Puddu, V.; Choi, H.; Dionysiou, D. D.; Puma, G. L. *Appl. Catal. B*, **2010**, *94*, 211-218.
11. Zhou, W.; Sun, F.; Pan, K.; Tian, G.; Jiang, B.; Ren, Z.; Tian, C.; Fu, H. *Adv. Funct. Mater*., **2011**, *21*, 1922-1930.
12. Saravanan, K.; Ananthanarayanan, K.; Balaya, P. *Energy Environ. Sci*., **2010**, *3*, 939-948.

13. Yue, W.; Randorn, C.; Attidekou, P. S.; Su, Z.; Irvine, J. T. S.; Zhou, W. *Adv. Funct. Mater*., **2009**, *19*, 2826-2833.

14. Li, W.; Wu, Z.; Wang, J.; Elzatahry, A. A.; Zhao, D. *Chem. Mater.*, **2014**, *26*, 287-298.

15. Jiang, X.; Herricks, T.; Xia, Y. *Adv. Mater*., **2003**, *15*, 1205-1209.

16. Zou, X.; Silva, R.; Huang, X.; Asefa, T. *Chem. Commun*., **2013**, *49*, 382-384.

17. Yu, J.; Low, J.; Xiao, W.; Zhou, P. *J. Am. Chem. Soc*., **2014**, *136*, 8839-8842.

18. Fu, J.; Cao, S.; Yu, J.; Low, J.; Lei, Y. *Dalton Trans.*, **2014**, *43*, 9158-9165.

19. Liu, S.; Xia, J.; Yu, J. *ACS Appl. Mater. Interfaces*, **2015**, *7*, 8166-8175.

20. Yang, X.; Fu, H.; Yu, A.; Jiang, X. *J. Colloid Interface Sci.*, **2012**, *387*, 74-83.

21. Zhong, L. S.; Hu, J. S.; Wan, L. J.; Song, W. G. *Chem. Commun*., **2008**, 1184-1186.

22. Zhang, H.; Banfield, J. F. *J. Phys. Chem. B*, **2000**, *104*, 3481-3487.

23. Zhang, H.; Banfield, J. F. *J. Mater. Chem*., **1998**, *8*, 2073-2076.

24. Tian, G.; Fu, H.; Jing, L.; Tian, C. *J. Hazard. Mater*., **2009**, *161*, 1122-1130.

25. Yaghoubi, H.; Li, Z.; Chen, Y.; Ngo. H. T.; Bhethanabotla, V. R.; Joseph, B.; Ma, S.; Schlaf, R.; Takshi, A. *ACS Catal.*, **2015**, *5*, 327-335.

26. Luttrell, T.; Halpegamage, S.; Tao. J.; Kramer, A.; Sutter, E.; Batzill, M. *Sci. Rep*., **2014**, *4*, 4043 (1-8).

27. Zhuang, H.; Zhang, Y.; Chu, Z.; Long, J.; An, X.; Zhang, H.; Lin, H.; Zhang, Z.; Wang, X. *Phys. Chem. Chem. Phys*., **2016**, 18, 9636-9644.

28. Xiao, F.; Wang, F.; Fu, X.; Zheng, Y. *J. Mater. Chem*., **2012**, *22*, 2868-2877.

29. Zhang, Y.; Zhang, N.; Tang, Z. R.; Xu, Y. J. *ACS Sustain. Chem. Eng*., **2013**, *1*, 1258-1266.

30. Park, H.; Kim, H.-I.; Moon, G.-H.; Choi, W. *Energy Environ. Sci*., **2016**, *9*, 411-433.

31. Zhang, Q.; Gao, L.; Guo, J. *Appl. Catal. B*, **2000**, *26*, 207-215.

32. Archana, P. S.; Jose, R.; Vijila, C.; Ramakrishna, S. *J. Phys. Chem. C*, **2009**, *113*, 21538-21542.

Chapter 3

Copper-Decorated Microsized Nanoporous TiO_2 Photocatalysts for CO_2 Reduction by H_2O

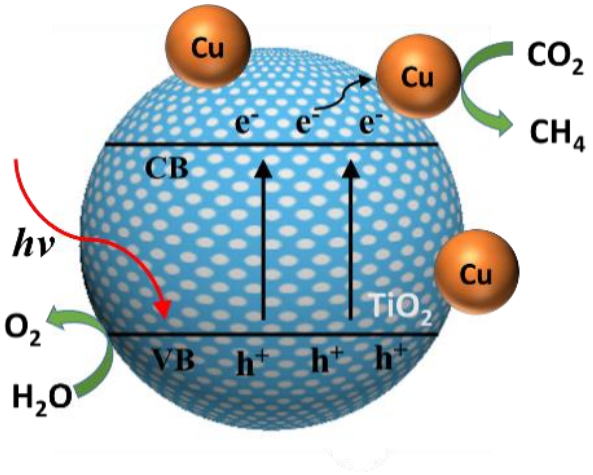

3.1. Overview

A series of metallic copper (Cu)-decorated microsized, nanoporous titanium dioxide (TiO_2) materials with different loadings of Cu were synthesized by in situ hydrolysis of Sn^{2+}-grafted titanium glycolate microspheres in the presence of Cu^{2+} ions. The resulting materials showed good photocatalytic activity for CO_2 reduction with water. In particular, the material prepared with an optimal loading of Cu (~0.4 wt%) exhibited the highest photocatalytic activity for the reduction of CO_2 to hydrocarbon fuel (CH_4), with an efficiency that was 21-fold higher than that of the most commonly studied and utilized commercial photocatalyst, Degussa P25 TiO_2, under similar reaction conditions.

3.2. Introduction

In light of the rapid depletion of conventional fuels and the rising level of atmospheric carbon dioxide (CO_2), the possible reduction of CO_2 with water into useful hydrocarbon fuels with the use of semiconductor materials as photocatalysts and abundant solar energy as an activator has attracted considerable attention. This is because the process can potentially provide a long-term solution to mitigate the greenhouse gas CO_2, and it can also serve as a route to recycle this relatively inert compound back into synthetic fuels, which would allow us to meet some of our growing needs for energy.[1-3] In this photoreduction process, as there is no involvement of fossil fuels or additional sources of carbon other than CO_2, the process is often referred to as "carbon neutral", and is, thus, quite appealing. To make this process a reality, a variety of semiconductor photocatalysts, including TiO_2, CdS, ZrO_2, ZnO, MgO, and WO_3, have been investigated over the last several years.[4,5] In particular, TiO_2 has garnered much attention, because it is inexpensive, chemically stable, harmless, and abundant.[6] However, TiO_2 is photoresponsive and photocatalytically active only under UV light owing to its relatively large band gap (3.2 eV). Besides, it suffers significantly from unwanted electron–hole recombination. Consequently, this otherwise interesting photocatalyst has limited ability to photoreduce CO_2. Thus, proper modification of its band gap and improvement of its ability to separate the charge carriers forming on it should bring about a major enhancement in its overall photocatalytic performances (e.g., catalytic conversion, product yield, selectivity, etc.) during CO_2 reduction.

One effective strategy that can improve the photoactivity of TiO_2 and other related semiconductor materials involves the incorporation of transition metals into the material, as the added metals can serve as "charge-carrier traps" and suppress electron-hole recombination processes within the material.[7] Furthermore, the added metals can serve as the actual catalytic or

co-catalytic sites that enable the entire photocatalytic processes. Noble metals such as In, Ru, Rh, Pd, Pt, and Au have been explored as part of this strategy or for the purpose of improving the ability of TiO2 to photocatalyze the conversion of CO_2 into hydrocarbon fuels,[8-13] but Cu deserves more attention because it is more earth abundant, inexpensive, and less toxic than these noble metals.[7,14-16] Besides, Cu is known for its broad range of applications as a catalyst and co-catalyst for various chemical transformations involving photocatalysis, electrocatalysis, and, more importantly, CO_2 reduction.[17-20]

Recently, our group reported the synthesis of TiO_2 materials functionalized with Ag nanoparticles by reducing Ag^+ ions with Sn^{2+}-grafted titanium glycolate microparticles and then letting the microparticles hydrolyze.[21] By using this method as a stepping board, herein we synthesized a series of new Cu-decorated nanoporous TiO_2 composite microparticles with different amounts of Cu (denoted as *x* wt% Cu-TiO_2, for which *x* is the weight percent of Cu^{2+} ions used to make the materials and is 0.04, 0.2, 0.3, 0.4, or 0.8 wt%). Whereas the materials all showed some photocatalytic activity toward CO_2 reduction with H_2O under illumination of simulated solar light, the one with an optimal amount of Cu (0.4 wt%) showed the best activity for the reaction. Besides being a better catalyst to reduce CO_2 than the other materials we investigated herein, this material showed activity that was 21-fold higher than that of commercial TiO_2 (P25, Degussa).

3.3. Experimental Section

3.3.1. Chemicals and reagents.

Titanium(IV) *n*-butoxide (TBO), ethylene glycol (EG), acetone, ethanol, tin(II) chloride ($SnCl_2$), and copper(II) sulfate ($CuSO_4$) were all purchased from Sigma-Aldrich. All reagents were

of analytical grade, and they were used without further purification. Distilled water was used throughout the experiments.

3.3.2. Synthesis of Sn^{2+}-grafted titanium glycolate microspheres (Sn^{2+}-TGMs).

Sn^{2+}-TGMs were synthesized at room temperature by following our previously reported synthetic method.[21] First, TBO (2 mL) and EG (50 mL) were mixed. The solution was stirred for 4h to let TBO and EG completely react to form titanium glycolate. The solution was then poured into another solution containing acetone (170mL) and water (2.7 mL). This solution was stirred for 60 min. A white solid product was collected by centrifugation of the solution, and this solid material was washed with ethanol (3×40 mL) and dried at 60 °C to give the TGMs. Then, the TGMs (0.1 g) were dispersed in distilled water (40 mL) containing $SnCl_2$ (0.1 g). The color of the dispersion slowly changed from white to yellow while stir-ring for 30 min, which indicated functionalization of the TGMs with Sn^{2+} ions. The mixture was centrifuged, and the yellow-colored solid product was recovered and washed with distilled water (6×40 mL) and then left to dry under ambient conditions. This finally gave Sn^{2+}-TGMs.

3.3.3. Synthesis of Cu-decorated nanoporous TiO_2 with different content of Cu (*x* wt% Cu-TiO_2).

A series of Cu-TiO_2 materials with various amounts of Cu were synthesized by mixing the above-obtained Sn^{2+}-TGMs with different concentrations of aqueous Cu^{2+} solutions (0.04, 0.2, 0.3, 0.4, and 0.8 wt% Cu^{2+}). For example, the Sn^{2+}-TGMs (0.1 g) were subjected to in situ hydrolysis and condensation in boiling water(40 mL) containing Cu^{2+} ions (0.04mg, 0.1 mg $CuSO_4$) for 24 h, and this produced a material labeled as 0.04 wt% Cu-TiO_2.The material was recovered by centrifugation, washed several times with water (40 mL) and ethanol (40 mL), and left to dry at

60 °C. Similarly, other Cu-TiO_2 samples, namely, 0.2 wt% Cu-TiO_2, 0.3 wt% Cu-TiO_2, 0.4 wt% Cu-TiO_2, and 0.8 wt% Cu-TiO_2, were obtained in the same way but by using the appropriate amount of $CuSO_4$. A control material was also synthesized by using the same procedure but without adding Cu^{2+} ions in the solution. Another control material was synthesized simply by mixing $SnCl_2$ (200mg) and $CuSO_4$ (40 mg) in water (40 mL) and letting the two react for 24 hat 100 °C. The solid product was collected by centrifugation, washed several times with water (40 mL) and ethanol (40 mL), and finally left to dry at 60 °C.

3.3.4. Characterization of the materials/catalysts.

Transmission electron microscopy (TEM) images of the materials were taken with a Topcon002B TEM microscope operating at 200 kV. High-resolution TEM (HRTEM) images and energy-dispersive spectroscopy (EDS) were obtained with a JEOL2010F TEM equipped with EDS. The surface areas and pore properties of the materials were determined from N_2 adsorption-desorption isotherms, which were measured at@196°C by using a Micromeritics Tristar-3000 instrument. Before each measurement, the samples were degassed at 353 K for 8h. By applying the Brunauer-Emmett-Teller (BET) and the Barrett-Joyner Halenda (BJH) methods on the adsorption/desorption data, the surface areas and pore-size distributions of the materials, respectively, were calculated. The chemical compositions of the materials were analyzed with a Thermo Scientific K-Alpha X-ray photo emission spectrometer (XPS) equipped with Al K_a radiation as the X-ray source ($h\nu$ = 1486.6 eV) and with an energy resolution of 0.1 eV for high resolution scans of the individual signals. All the binding energies in the X-ray photoemission spectra were calibrated by using a C1s peak (binding energy: 284.8 eV) of the adventitious hydrocarbon present on the materials. X-ray diffraction (XRD) patterns were obtained with a Philip XPert diffractometer operating with Cu K_a radiation as the X-ray source. The XRD

diffraction patterns were recorded in the 2θ range of 10 to 80° with a step size 2θ of 0.02° and a scanning rate of 0.6° min^{-1}. Field-emission scanning electron microscopy (FESEM) images were examined by using a Zeiss Sigma Field Emission SEM. The UV/Vis diffuse reflectance spectra (UV/Vis DRS) were acquired with a Lambda950 spectrophotometer (PerkinElmer) over the spectral range of λ = 250 to 800 nm.

3.3.5. Photocatalytic reduction of CO_2.

A 200 mL homemade Pyrex reactor was used to perform the photocatalytic CO_2 reduction at room temperature and atmospheric pressure, similar to a method reported previously.[22-25] Prior to the test, the sample (50 mg) was dissolved in deionized water (10 mL) and poured into the reactor. The photocatalyst was then ultrasonically dispersed for 30 min and then dried at 80 °C for 2h to form a thin film on the bottom of the reactor. After this step, the reactor was sealed. To create an aerobic condition in the reaction system, the photocatalytic reactor was blown with N_2 gas for 30 min to remove the air in the reactor. The sources of carbon (i.e., CO_2) and hydrogen (i.e., H_2O) were generated in situ by letting $NaHCO_3$ (0.1 g, introduced into the reactor before sealing) and 2M sulfuric acid (0.3 mL, introduced into the reactor using a syringe) react, before the light was turned on. A300 W simulated solar Xe arc lamp was positioned 10 cm above the photocatalytic reactor and was used as the light source to irradiate the reactor. A sample (1 mL) of gas was removed from the reactor 1h after the light was on and was analyzed by a gas chromatograph (GC-2014C, Shimadzu, Japan) equipped with a flame ionization detector (FID) and a methanizer. Blank experiments were also performed without CO_2 or irradiation to check whether or not the products were formed as a result of the photocatalytic reduction of CO_2.

3.4. Results and Discussion

Details of the synthetic procedures that led to the materials depicted in **Scheme 3.1** are provided in the Experimental Section. First, Sn^{2+}-grafted titanium glycolate microspheres (denoted Sn^{2+}-TGMs) were synthesized by mixing titanium glycolate microspheres (TGMs) with an aqueous solution of Sn^{2+} ions at room temperature. The Sn^{2+}-TGMs were then subjected to in situ hydrolysis and condensation reactions in the presence of different concentrations of aqueous $CuSO_4$ solutions in boiling water. With the surface-grafted Sn^{2+} ions serving as the reductant, different relative amounts of Cu^{2+} ions were then left to undergo reduction and to deposition to the surfaces of the products. This finally yielded the different Cu-modified TiO_2 materials, labeled *x* wt% Cu-TiO_2, for which *x* = 0.04, 0.2, 0.3, 0.4, and 0.8, or the weight percent of Cu^{2+} ions used to synthesize the materials.

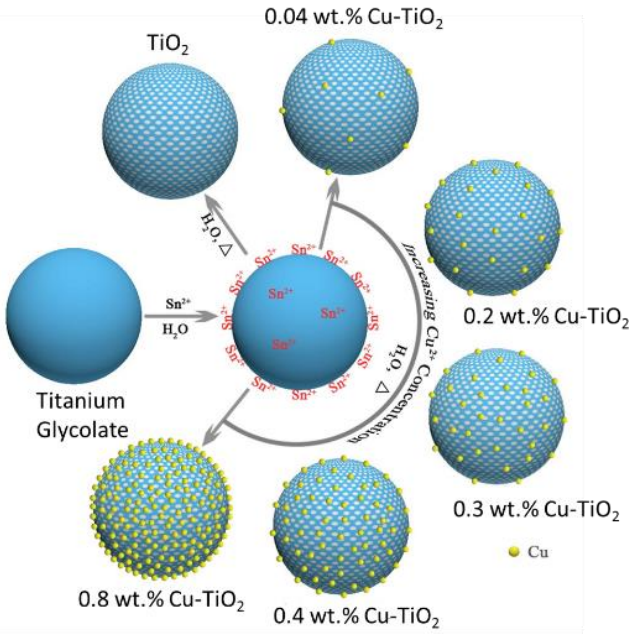

Scheme 3.1 An illustration of the synthesis of Cu-modified nanoporous TiO_2 photocatalysts (*x* wt% Cu-TiO_2; *x* = 0.04, 0.2, 0.3, 0.4, and 0.8 or the weight percent of Cu^{2+}ions used to synthesize the materials).

The morphology of the Cu-TiO_2 microparticles and their precursors (i.e., the TGMs) was analyzed with transmission electron microscopy (TEM). The images show that the TGM shave spherical morphology with sizes of approximately 500 nm (**Figure 3.1a**). The TiO_2 microparticles derived from the TGMs show a spherical morphology similar to that of the TGMs (**Figure 3.1b**). Although the Cu^{2+}-containing TiO_2 microparticles (Cu-TiO_2) derived from Cu^{2+}-TGMs also have spherical morphology (**Figures 3.1c-g**), their surfaces are rough and corrugated, especially as the amount of Cu^{2+} ions used to make the materials increases. More specifically, if the concentration of Cu^{2+} ions is relatively low, the surfaces of the microparticles appear only slightly rougher and have fewer dark spots associated with Cu species in the TEM images (see below) (**Figure 3.1c**). As the amount of Cu^{2+} ions are increased, Cu-enriched shells around the porous TiO_2 microparticles, which look dark in the TEM images, are increasingly formed (**Figures 3.1d-g**).

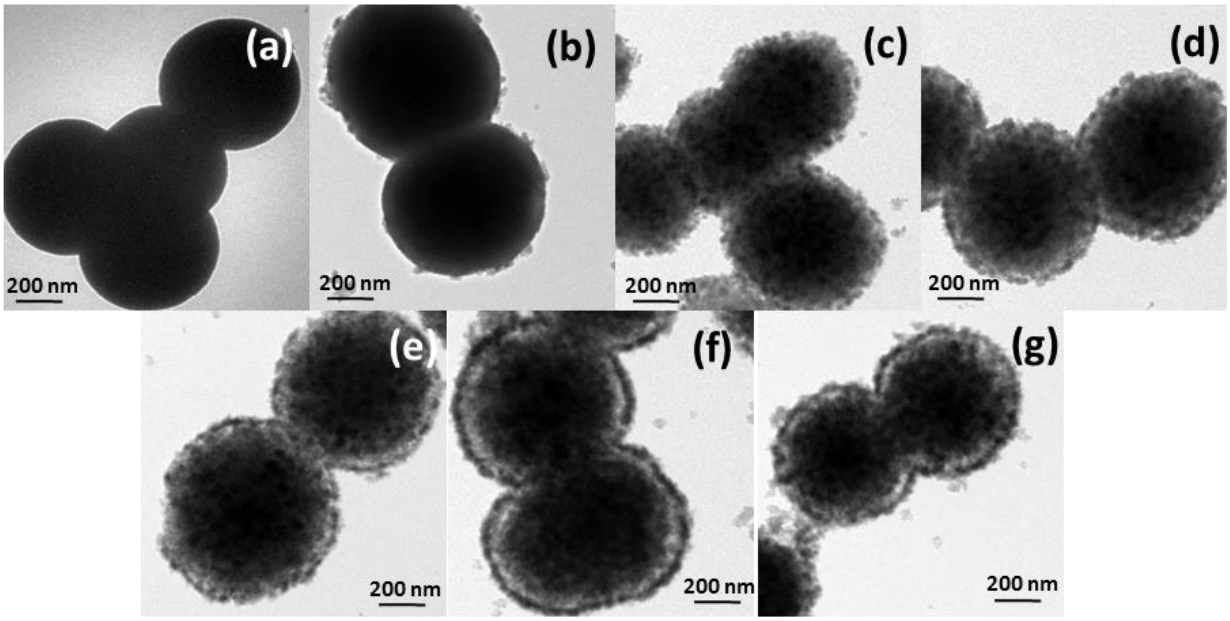

Figure 3.1. TEM images of a) TGMs and b) TiO_2, c) 0.04 wt% Cu-TiO_2, d) 0.2 wt% Cu-TiO_2, e) 0.3 wt% Cu-TiO_2, f) 0.4 wt% Cu-TiO_2, and g) 0.8 wt% Cu-TiO_2 microparticles.

Similarly, the field-emission scanning electron microscopy (FESEM) images of the as-obtained 0.4 wt% Cu-TiO_2 material (**Figure 3.2**) show uniform, spherical particles with an average

diameter of approximately 500 nm; this value is in agreement with the above TEM results. Furthermore, the images show that relative to the Cu-free TiO_2 microparticles (**Figure 3.3**), those containing Cu (*e.g.*, 0.4 wt% Cu-TiO_2 microparticles) have rougher surfaces and darker spots, which is again indicative of the successful functionalization of the nanoporous TiO_2 microparticles with Cu species.

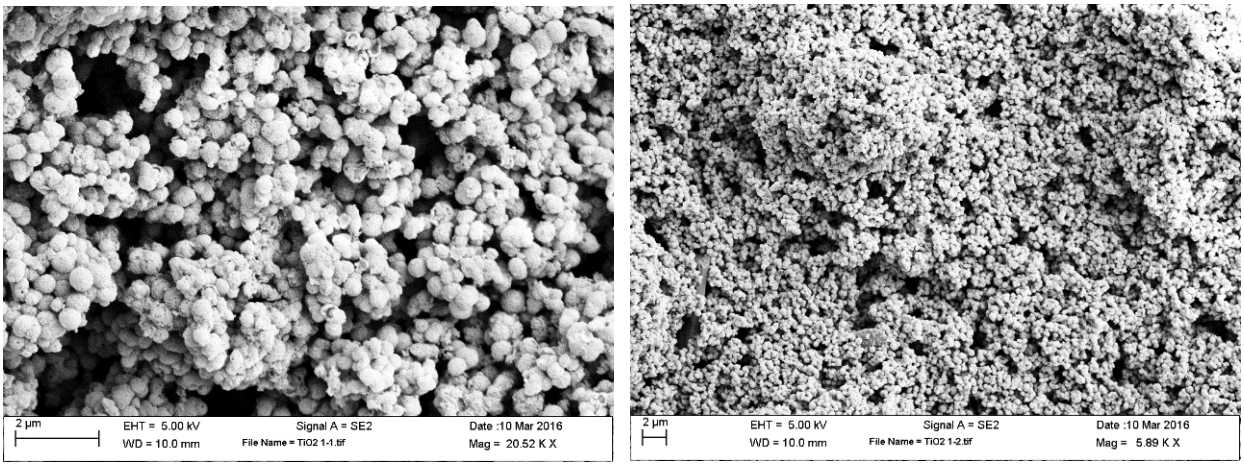

Figure 3.2. FESEM images of 0.4 wt.% Cu-TiO_2 at different magnification.

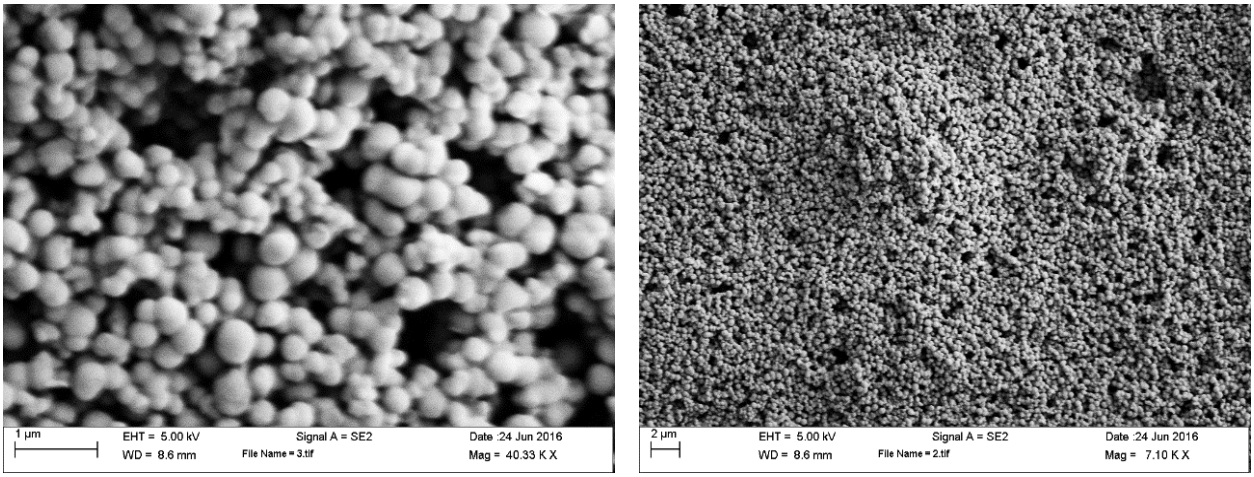

Figure 3.3. FESEM images of TiO_2 at different magnification.

To determine the distribution of Cu in the Cu-TiO_2 microparticles, a scanning transmission electron microscopy (STEM) image and an energy-dispersive spectroscopy (EDS) line profile of the 0.4 wt% Cu-TiO_2 microparticles were acquired, and the results are provided in **Figure 3.4**. The EDS line profile shows a signal corresponding to Cu mainly on the surfaces of the particles, which confirms that Cu is present predominantly around the outer shells of the microparticles (**Figure 3.4b**). From the high-resolution TEM (HRTEM) image of the edge of a microparticle in the sample (**Figure 3.5a**), a lattice fringe with an interplanar spacing of 0.36 nm that can be attributed to the (101) atomic plane of anatase with interplanar spacing values of 0.24 and 0.32 nm that can be ascribed to the (101) and (110) atomic planes of rutile TiO_2, respectively, are observed (**Figures 3.5b-d**).[26-28] These results are all in agreement with those obtained by X-ray diffraction (XRD) below.

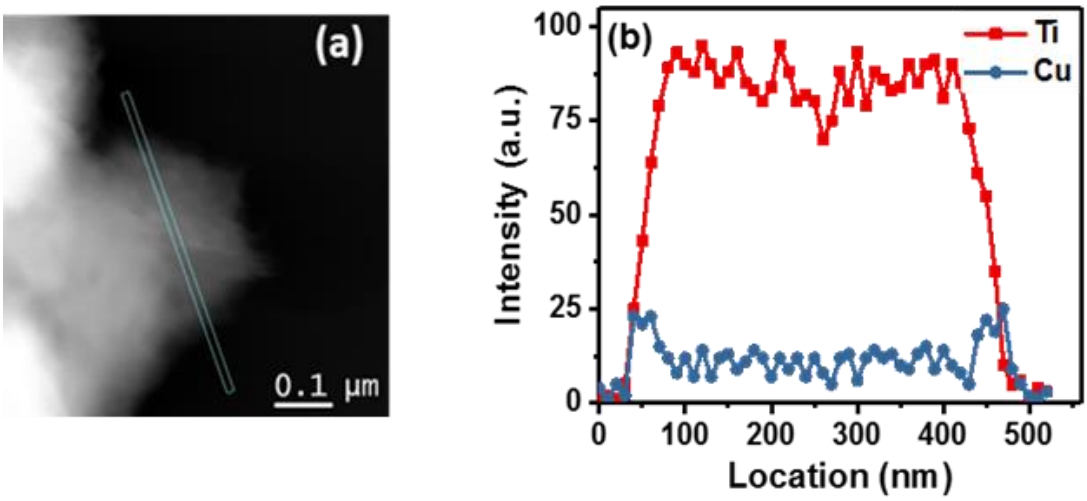

Figure 3.4. a) STEM image and b) the corresponding EDS line-scan profile of a microparticle in a sample of 0.4 wt% Cu-TiO_2.

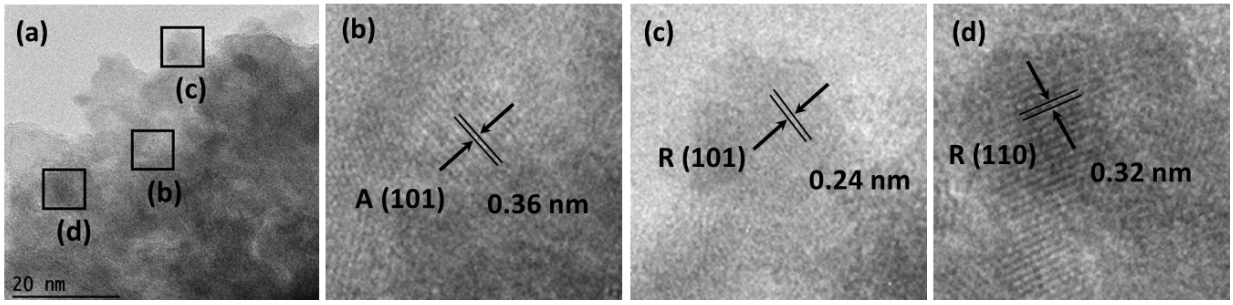

Figure 3.5. (a) HRTEM image of the edge of a typical 0.4 wt.% Cu-TiO_2 sample, (b) HRTEM lattice image of anatase (101), which is represented with A in the image, (c) HRTEM image indicating the lattice fringes of rutile (101), the latter is marked by R in the image, and (d) HRTEM lattice image of R (110).

Clearly, the Cu species formed in the materials are the result of the reduction of Cu^{2+} ions in the solution by the TGM-supported Sn^{2+} ions and subsequent deposition of the reduction product(s) onto the surfaces of the TGMs. To determine indirectly the possible oxidation state of the Cu species deposited on the materials after reduction (or to differentiate whether they are in the forms of Cu^0 or Cu^+ or still Cu^{2+}), a simple control experiment involving the reaction between Sn^{2+} ions and Cu^{2+} ions in solution and XRD analysis of the solid product obtained from the reaction was first performed. The XRD pattern of the product obtained after letting aqueous solutions of $SnCl_2$ and $CuSO_4$ react in boiling water is depicted in **Figure 3.6** (see also the Experimental Section for further details). The XRD pattern of the product shows diffraction peaks at 2θ = 43.41, 50.51, and 74.19°, which correspond to the (111), (200), and (220) planes of Cu^0 (JCPDS: 04-0836), respectively. This result strongly suggests that the Cu^{2+} ions can be fully reduced to Cu^0 by the Sn^{2+} ions.

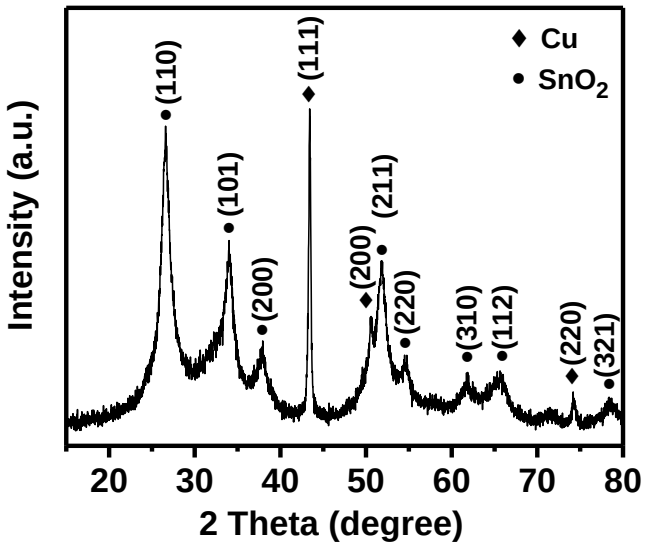

Figure 3.6. XRD patterns of the as-obtained SnO_2 (JCPDS: 41-1445) and metallic Cu (JCPDS: 04-0836) after mixing $CuSO_4$ with $SnCl_2$ in boiling water for 24 h and letting them react.

To identify further the oxidation state of Cu or the type of Cu species deposited on the nanoporous TiO_2 microparticles (i.e., whether they exist in the forms of Cu^0, Cu_2O, CuO, and/or $Cu(OH)_2$), the materials were analyzed by X-ray photoelectron spectroscopy (XPS). Specifically, the oxidation state of Cu was analyzed on the basis of the positions of the Cu $2p_{3/2}$ peaks in the spectra of the materials. Relative to the main Cu $2p_{3/2}$ peaks of Cu^0 and Cu_2O, which have similar binding energies, those of CuO and $Cu(OH)_2$ are both shifted to higher binding energies by (1.3 ± 0.2) and (2.5 ± 0.15) eV, respectively.[29] Besides, there is another major difference between the peaks associated with the Cu^0/Cu^{1+} and Cu^{2+} species in the X-ray photoelectron spectrum: a shake-up satellite peak at a binding energy of approximately 942 eV is observed for paramagnetic Cu^{2+} but not for the Cu^0 and Cu^{1+} species, which have completely filled 3d shells.[14-16,29,30] So, by monitoring the position of the 2p peak of Cu by XPS, the chemical compositions of the materials synthesized above can at least be partially assessed.

The high-resolution X-ray photoelectron spectra of the Cu 2p region of all the samples were also compared with one another (**Figure 3.7a**). The binding energies were all calibrated by using the C 1s peak at a binding energy of 284.8 eV as a reference for the adventitious hydrocarbon present on the surfaces of the materials. In the case of 0.2 wt% Cu-TiO_2, 0.3 wt% Cu-TiO_2, and 0.4 wt% Cu-TiO_2, a small peak at a binding energy of approximately 932.2 eV corresponding to Cu $2p_{3/2}$ of Cu^0 and/or Cu^{1+} is observed (**Figure 3.7b**). In the case of 0.8 wt% Cu- TiO_2, peaks at binding energies of approximately 932.2 and 952.2 eV, which correspond to Cu $2p_{3/2}$ and Cu $2p_{1/2}$ of Cu^0 and/or Cu^{1+}, respectively, are clearly observable (**Figure 3.7a**).[29] Furthermore, no shake-up peak at a binding energy of approximately 942 eV associated with Cu^{2+} is observed in the X-ray photoelectron spectrum of 0.8 wt% Cu-TiO_2.

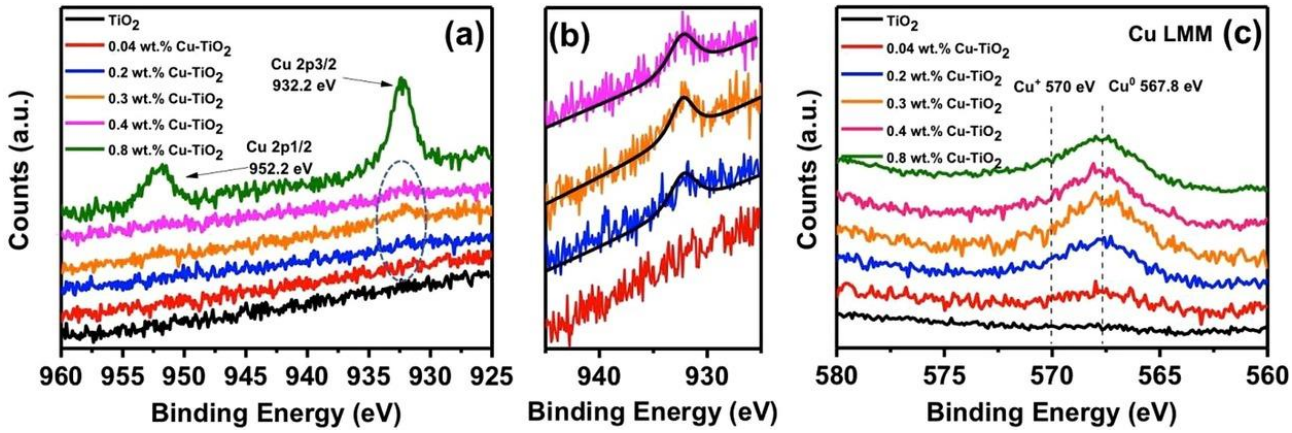

Figure 3.7. a) X-ray photoelectron spectra showing the Cu 2p peak region of Cu-modified nanoporous TiO_2 microparticles containing different loadings of Cu (x wt% Cu-TiO_2; x = 0.04, 0.2, 0.3, 0.4, and 0.8 of Cu^{2+} ions used to synthesize the materials) and Cu-free nanoporous TiO_2 microparticles (control materials). b) Enlarged X-ray photoelectron spectra showing the Cu $2p_{3/2}$ peak of the results in panel a. c) Cu LMM Auger transition of x wt% Cu-TiO_2 and plain TiO_2 microparticles.

As mentioned above, Cu^0 and Cu^{1+} have very similar Cu 2p peak positions in their X-ray photoelectron spectra; so, they are difficult to distinguish by simply monitoring their $2p_{3/2}$ peak positions. Thus, to determine the actual oxidation state of Cu in the materials, the peaks associated with Auger Cu LMM transitions in the spectra of the materials were analyzed. Given that the Auger Cu LMM peak positions for Cu^0 and Cu^{1+} show up at binding energies of approximately 567.9 and 570.0 eV, respectively, these two Cu species can be differentiated by using Auger peak analysis.[31-34] As depicted in **Figure 3.7c**, whereas no Auger peak is observed at a binding energy of approximately 570.0 eV, an Auger peak centered at a binding energy of approximately 567.8 eV is seen, which clearly confirms the presence of Cu^0 on the surfaces of copper-decorated TiO_2. On the basis of the Auger Cu LMM results and coupled with the XRD results discussed earlier, which indicate the existence of Cu^0, it is then clear that Cu^0 is the predominant, if not the only, Cu species in at least four of the Cu-loaded TiO_2 materials (i.e., 0.2 wt % Cu-TiO_2, 0.3 wt % Cu-TiO_2, 0.4 wt % Cu-TiO_2, and 0.8 wt % Cu-TiO_2).

Similar Auger peaks and XPS peaks corresponding to Cu $2p_{1/2}$ and Cu $2p_{3/2}$ are not observed in the spectra of the Cu-TiO_2 material that possesses the lowest amount of Cu (i.e., 0.04 wt % Cu-TiO_2). This is, however, most likely owing to the fact that the amount of Cu in this particular material is too small to be detected by XPS, which often has a detection limit of approximately 0.1 at % for most elements. Additionally, as photoelectrons are typically generated only from the top <5 nm layers of the sample during XPS, not enough or not a detectable amount of them can be generated in this case anyway. Hence, it is not possible directly to confirm the presence of surface Cu0 species in this material, which was synthesized with the lowest amount of Cu. Nevertheless, the fact that Cu^0 is the only oxidation state seen in the materials synthesized

from relatively higher amounts of Cu^{2+} (which gives XPS-detectable amounts of Cu species) in addition to the fact that the reactions used to make all of the materials were identical make us believe that Cu^0 is the major, if not the only, Cu species present in the entire series of materials synthesized herein.[35] Thus, on the basis of the Cu 2p, Cu LMM XPS scans, and the XRD results in **Figures 3.6** and **3.7**, it can be said that the Cu^{2+} ions added into the reaction mixtures must have been successfully reduced and ended up as Cu^0 in all of the Cu-TiO_2 materials reported herein.

The effects, if any, of the amount of Cu^{2+} ions used in the precursors on the crystal structures of the synthesized products were studied by XRD. The XRD patterns (**Figure 3.8**) show no Bragg reflections associated with Cu in any of the materials, possibly because of the low amount or the high dispersion/extremely small size of the Cu species formed in the materials.[7,36] Furthermore, no Bragg peaks associated with anatase or the rutile phase are seen in the XRD patterns of the control material (plain TiO_2) and 0.04 wt % Cu-TiO_2, which indicates the amorphous nature of these materials. Interestingly, on the other hand, the Cu-TiO_2 materials derived from the precursors containing increasingly higher amounts of Cu^{2+} ions show crystalline TiO_2 comprising both the anatase and rutile phases.[37] Specifically, Bragg reflections at 2θ = 25.29, 47.89, 55.35, 62.79, and 67.97°, which can be ascribed to the (101), (200), (211), (204), and (116) main crystal planes, respectively, of anatase (JCPDS: 21-1272) and Bragg reflections at 2θ = 27.07, 35.91, 41.05, and 53.71° owing to the (110), (101), (111), and (211) main crystal planes, respectively, of rutile (JCPDS: 21-1276) are observed.[26,38,39] The anatase-to-rutile ratio in the different materials was estimated by using the Spurr equation (1):[40]

$$F_A = 1/(1 + 1.26 \times I_R/I_A) \quad (1)$$

in which F_A is the mass fraction of anatase and IA and IR are the intensities of the strongest anatase (101) and rutile (110) diffraction peaks, respectively, in a given sample. A slight decrease in the anatase-to-rutile ratio is observed upon increasing the amount of Cu^{2+} ions used to make the Cu-TiO_2 materials (Table 3.1), which suggests that the addition of higher amounts of Cu^{2+} ions can promote the formation of the rutile phase at the expense of the anatase phase in the materials, a result that is in line with the literature.[15, 29]

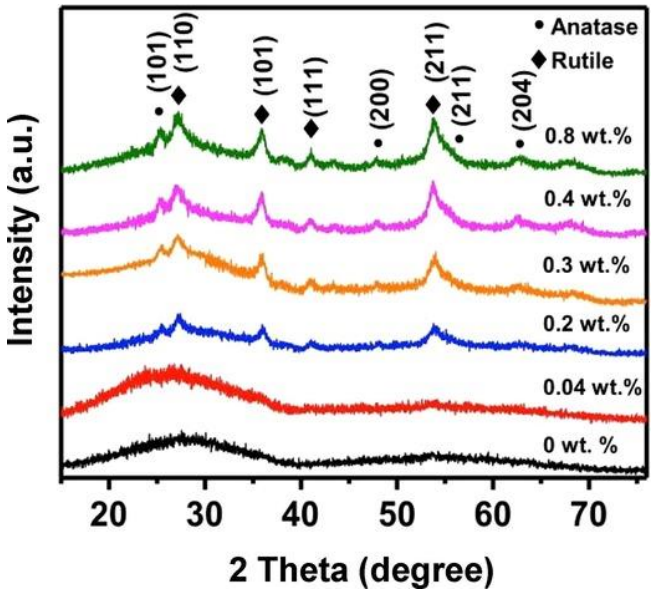

Figure 3.8. XRD patterns of Cu-modified TiO_2 photocatalysts prepared from precursors containing different amounts of Cu^{2+} (*x* wt % Cu-TiO_2; *x* = 0.04, 0.2, 0.3, 0.4, and 0.8) and the control material TiO_2.

Table 3.1. Anatase-to-Rutile ratio.[a]

Sample name	TiO_2	0.04 wt.% Cu-TiO_2	0.2 wt.% Cu-TiO_2	0.3 wt.% Cu-TiO_2	0.4 wt.% Cu-TiO_2	0.8 wt.% Cu-TiO_2
Anatase to Rutile ratio	-	-	30%	29%	28%	26%

[a] Estimated from Spurr equation

Generally, high surface areas, three-dimensional interconnected pores, and big pore volumes in solid-state photocatalysts endow the materials with enhanced photocatalytic activities. This is because these structural features provide more accessible catalytic active sites to the photocatalysts and improve the mass transport of the reactants, intermediates, and products through the structures of the photocatalysts during catalysis.[41] Hence, these types of structural features are often deliberately introduced into solid-state photocatalysts by various methods, and their effects on the catalytic activities of the materials are investigated.

On the basis of the TEM images, it was already established above that as more Cu^{2+} ions are used during the synthesis of the nanoporous Cu-TiO_2 microparticles, the surfaces of the particles become increasingly decorated by Cu and become rougher. N_2 porosimetry was additionally used to investigate the effects of the amount of Cu loaded in the materials on the surface areas and pore structures of the materials. The N_2 adsorption-desorption isotherms of all the materials give a type IV isotherm with a type H3 hysteresis loop (**Figure 3.9**), which suggests the presence of mesoporous structures (2-50 nm) in the materials.[7, 14, 42] Furthermore, the capillary condensation step occurs at a higher partial pressure (P/P_0) for the Cu-loaded nanoporous TiO_2 microparticles (or Cu-TiO_2), in the range of 0.8 to 1.0, than for the plain nanoporous TiO_2 microparticles. This indicates that the Cu-TiO_2 materials have a substantial amount of macropores (>50 nm) in addition to mesopores.[7,14] Similarly, the pore-size distribution (PSD) of the pores in the Cu-modified materials, which were determined by using the Barret-Joyner-Halenda (BJH) method, also show a bimodal pore distribution, the first with a mean pore size of approximately 3.6 nm (mesopores) and the second with a mean pore size of approximately 38 nm (**Figures 3.9b,c**). The latter constitute some mesopores and some macropores, most of which likely have to do with interparticle pores/void spaces.[43,44]

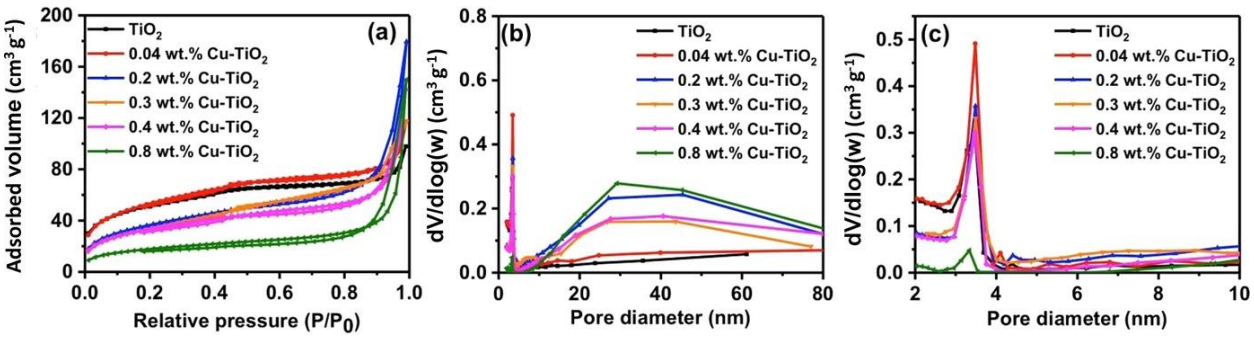

Figure 3.9. a) N_2 adsorption-desorption isotherms of Cu-modified nanoporous TiO_2 microparticles containing different loadings of Cu (*x* wt % Cu-TiO_2; *x* = 0.04, 0.2, 0.3, 0.4, and 0.8) and plain TiO_2 microparticles and b, c) the corresponding pore-size distributions.

Furthermore, a gradual decrease in the surface area of the Cu-TiO_2 materials is observed upon increasing the amount of Cu^{2+} ions used to synthesize the materials. For example, the surface area of 0.04 wt % Cu-TiO_2 is approximately 187 $m^2\ g^{-1}$, but that of 0.8 wt % Cu-TiO_2 is only 60 $m^2\ g^{-1}$. This result suggests the formation of a more compacted shell and a less porous structure in the materials as more Cu is used to make the materials. This is supported by the gradual disappearance of the mesopores (a reduction in the peak at $\approx$3.6 nm in the pore-size distribution graph) upon increasing the amount of Cu in the materials (**Figure 3.9c**). The values of the BET surface area, average pore size, and pore volume of all the materials are all compiled in **Table 3.2**.

Table 3.2. BET surface area, BJH pore volume and pore size summary for different samples.[a]

Sample name	BET surface area (m^2/g)	Average BJH pore size (nm)	BJH pore volume (cm^3/g)
TiO_2	179	3.5	0.11
0.04 wt.% Cu-TiO_2	187	3.5	0.14
0.2 wt.% Cu-TiO_2	132	3.5	0.25
0.3 wt.% Cu-TiO_2	124	3.5	0.21
0.4 wt.% Cu-TiO_2	119	3.5	0.20
0.8 wt.% Cu-TiO_2	60	2.8	0.22

[a] Pore size distribution (PSD) are calculated from the desorption branches of the isotherms using the Barrett-Joyner-Halenda (BJH) method

The digital image and UV/Vis diffuse reflectance spectroscopy (DRS) results of the materials measured in the range of λ = 250 to 800 nm are provided in **Figures 3.10** and **3.11**. The colors of the samples slowly change from light yellow to dark green upon increasing the amount of Cu^{2+} ions used to make the Cu-TiO_2 materials (**Figure 3.10**). The absorbance of the materials in the visible region also continuously changes upon increasing the concentration of Cu^{2+} ions used to make the materials, which suggests that the materials have different light-absorption properties.[45] Furthermore, the diffuse reflectance spectrum shows a redshift in the onset values of the absorption band and higher absorption in the visible region upon incorporating more Cu into the TiO_2 microparticles.[46] The band-gap (E_g) energies of the materials were calculated by using the reflectance data with the transformed Kubelka-Munk equation (2):[26]

$$[F(R) \cdot hv]^{0.5} = A(hv - E_g) \quad (2)$$

in which $F(R) = (1 - R)^2/2R$, hv is the incident photon energy; E_g is the band-gap energy; A is a constant, the value of which depends on the transition probability; and R is the percentage of reflected light. The values of E_g are found to be in the range of 2.03 to 2.34 eV (**Table 3.3**). These values are consistent with those reported in the literature, for which a slight but steady decrease in the band gap of the materials is reported upon increasing the loading of the metal on TiO_2. The results also indirectly imply that the metal (i.e., Cu in this case) is homogeneously distributed on the surfaces of the material (i.e., TiO_2).[15,45,46]

Figure 3.10. Physical appearance of the various Cu-TiO_2 materials/photocatalysts (from left to right: TiO_2, 0.04 wt.% Cu-TiO_2, 0.2 wt.% Cu-TiO_2, 0.3 wt.% Cu- TiO_2, 0.4 wt.% Cu- TiO_2, and 0.8 wt.% Cu-TiO_2).

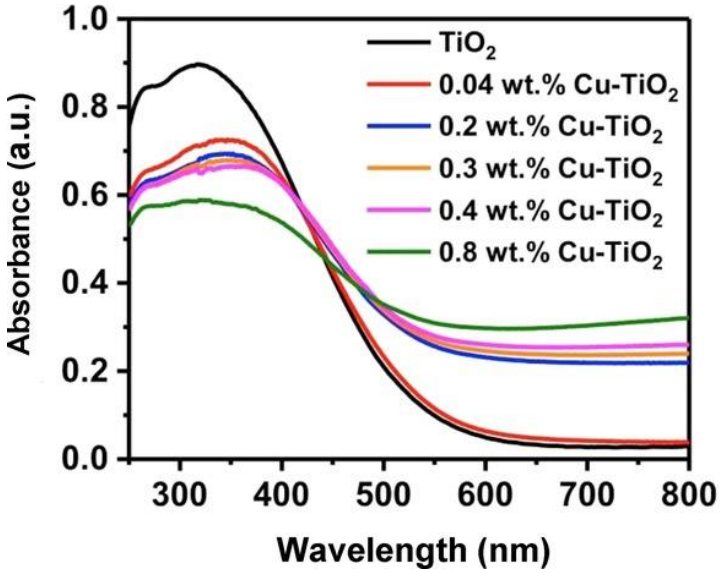

Figure 3.11. UV/Vis diffuse reflectance spectra of Cu-modified TiO_2 containing different loadings of Cu (*x* wt % Cu-TiO_2; x is the amount of Cu^{2+} ions used to make the materials and has values of 0.04, 0.2, 0.3, 0.4, and 0.8) and the Cu-free control material, TiO_2.

Table 3.3. Band gap values of different materials studies.[a]

Sample name	TiO_2	0.04 wt.% Cu-TiO_2	0.2 wt.% Cu-TiO_2	0.3 wt.% Cu-TiO_2	0.4 wt.% Cu-TiO_2	0.8 wt.% Cu-TiO_2
Band gap	2.34	2.33	2.29	2.26	2.19	2.03

[a] Estimated from Kubelka-Munk equation

Considering the unique structures of the materials, the presence of the semiconducting TiO_2 material, and the presence of Cu, a metal known for its catalytic activity toward CO_2 reduction, the materials were expected to serve as photocatalysts for CO_2 reduction. Hence, the photocatalytic activities of the materials and the corresponding control materials for CO_2 reduction with H_2O were investigated under illumination of solar simulated light (see the Experimental Section for details). Upon using the Cu-containing TiO_2 materials as photocatalysts, the reaction yielded methane (CH4) as the only hydrocarbon product. However, in the absence of either CO_2 or light irradiation, the reaction did not give any detectable hydrocarbon product. These experiments suggest that CH_4 is the result of the photocatalytic reduction of CO_2 over the Cu-TiO_2 materials. Notably, CH_4 is the product of complete CO_2 reduction. Consequently, the photocatalytic reduction of CO_2 with water over the materials reported herein to produce CH_4 rather than possible partially reduced products, such as CO, is of great significance for making high-energy synthetic fuel from CO_2.[7,47]

In **Figure 3.12**, comparative results for the photocatalytic activities of the different Cu-TiO_2 materials containing different loadings of Cu towards the reduction of CO_2 to CH_4 are presented. Upon using P25, one of the most commonly studied and utilized commercial TiO2 materials obtained from Degussa P25, as a photocatalyst or as a reference, the rate of production of CH_4 was only 0.38 $\mu mol\, g^{-1}\, h^{-1}$. Plain TiO_2, which was prepared and used as the second reference material, barely showed photocatalytic activity toward CO_2 reduction to CH_4 with H_2O.

On the contrary, The TGM-derived TiO_2 microparticles containing a small amount of Cu exhibited significant catalytic activity toward the photoreduction of CO_2 to CH_4. Among the materials we investigated, the one with 0.4 wt % Cu (or the material denoted as 0.4 wt % Cu-TiO_2) gave the highest photocatalytic activity. This material produced CH_4 at a rate of 8.04 μmol g^{-1} h^{-1}, a rate that is 21-fold higher than that of P25 TiO_2 (Degussa).

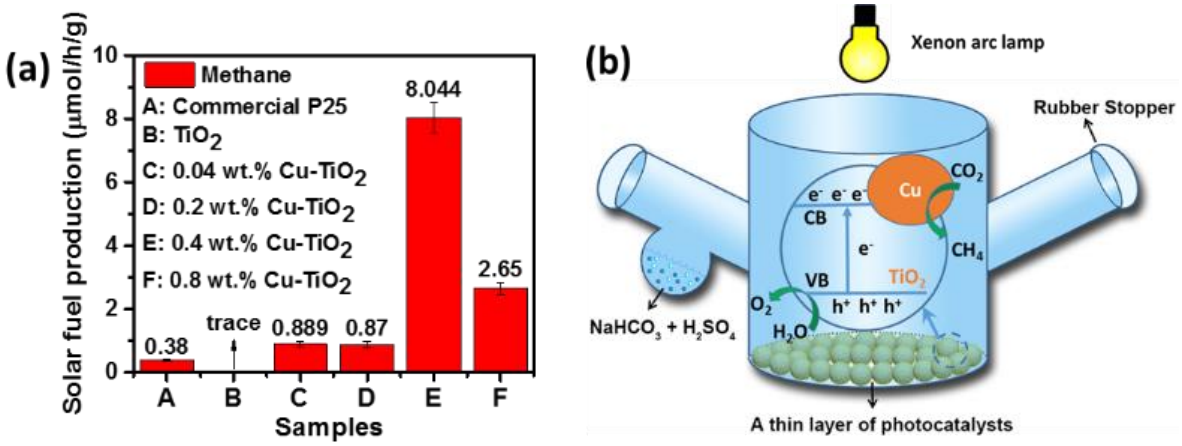

Figure 3.12. a) Effect of amount of Cu in Cu-TiO_2 on the catalytic yield of methane from CO_2 in the presence of water under solar simulator irradiation and b) schematic illustration of the photoreactor and the possible reaction mechanism responsible for the photocatalytic processes.

As mentioned above, plain TiO_2 often suffers from a rapid electron-hole recombination process and, thus, shows negligible photocatalytic activity.6a Hence, the catalytic activity of many such photocatalysts can potentially be improved by inhibiting possible recombination of the charge carriers, that is, electrons and holes, forming in the conduction and valence bands, respectively, of the photocatalysts upon excitation with light. In the presence of metals such Cu, which can serve as trapping sites for the photogenerated electrons, the chance of an electron–hole recombination process can be significantly minimized. In such systems, the trapped electrons can easily migrate to the surfaces of the materials and are able to reduce CO_2 molecules first to intermediates such as

$\cdot CO_2^-$ and ultimately to the CH_4 end product through multielectron transfer processes.[15,30,48] This is why higher rates of photoreduction of CO_2 can be achieved by Cu-TiO_2 materials.

Besides inhibiting charge recombination, the Cu species serve as the actual catalytic sites for the CO_2 reduction reaction in such systems. So, not surprisingly, the yield of the reaction initially increases upon increasing the amount of Cu species loaded onto Cu-TiO_2 until the optimal loading of 0.4 wt % is reached. In the materials possessing loadings of Cu lower than this value, the photoreduction of CO_2 to CH_4 takes place at slower rates. For example, whereas 0.4 wt % Cu-TiO_2 gives the best catalytic output (8.04 μmol g^{-1} h^{-1} of CH_4 from CO_2), 0.04 wt % Cu-TiO_2, 0.2 wt % Cu-TiO_2, and 0.3 wt % Cu-TiO_2 give lower catalytic outputs and rates (0.89, 0.87 μmol g^{-1} h^{-1} and 1.77 μmol g^{-1} h^{-1}, respectively). The relatively lower rates in the latter cases can be attributed to the lower density of metallic or Cu sites present in these materials to perform charge trapping as well as catalysis. However, increasing the density of Cu further, that is, higher than 0.4 wt %, also gives lower rates in the production of CH_4. For example, 0.8 wt % Cu-TiO_2 gave CH_4 only at a lower rate of 2.65 μmol g^{-1} h^{-1}. In this case, the excess Cu sites are likely to serve as recombination centers for the photogenerated electrons–hole pairs, which compromises the catalytic reduction of CO_2.[4,7,30]

Moreover, as shown in **Figure 3.9** and **Table 3.2**, the presence of Cu significantly affects the structural features of the materials as well. As the amount of Cu increases, the surface areas and the porosity of the samples slowly decrease. Nevertheless, below the optimal loading of Cu on TiO_2 (≈ 0.4 wt %), the rate of production of CH_4 generally increases as the amount of Cu loaded in the materials increases. This can be attributed to the fact that the greater the amount of Cu species placed on the TiO_2 microparticles, the greater the number of available catalytic sites for CO_2 reduction. However, 0.04 wt % Cu-TiO_2 and 0.2 wt % Cu-TiO_2 give similar rates for the

production of CH_4 (0.89 and 0.87 μmol g^{-1} h^{-1}, respectively). This unusual trend in similar photocatalytic activity exhibited by these two materials can be partly explained based on their relative surface areas. Relative to the surface area of 0.04 wt % Cu-TiO_2 (187 m^2 g^{-1}), that of 0.2 wt % Cu-TiO_2 is substantially lower (132 m^2 g^{-1}). Consequently, although the amount of Cu loaded in TiO_2 is higher in 0.2 wt % Cu-TiO_2 than in 0.04 wt % Cu-TiO_2, the former material has a lower surface area and fewer exposed catalytic active sites and thereby a more compromised photocatalytic activity. This conclusion is supported by comparing the rates of CH_4 production over 0.2 wt % Cu-TiO_2, 0.3 wt % Cu-TiO_2, and 0.4 wt % Cu-TiO_2. The surface areas of these three materials are very close (132, 124, and 119 m^2 g^{-1}, respectively); however, their rates of production of CH_4 substantially increase upon increasing the weight percent of Cu (i.e., 0.87, 1.77, and 8.04 μmol g^{-1} h^{-1}, respectively).

On the other hand, compared with 0.4 wt % Cu-TiO_2 (the BET surface area of which is 119 m^2 g^{-1}), 0.8 wt % Cu-TiO_2 (the BET surface area of which is 60 m^2 g^{-1}) shows lower photocatalytic activity. This can also be partly explained by the lower porosity and lower surface area of the latter, which give rise to a smaller density of exposed surface active sites and a slower mass-transfer rate for the reactants and products. So, overall, the surface area of these materials (expectedly) plays an important role and partly explains the trends in the relative photocatalytic activities of the different Cu-TiO_2 materials reported here.

An additional plausible reason that can partly account for 0.4 wt % Cu-TiO_2 having the best photocatalytic activity is the presence of anatase and rutile phases. These two crystalline phases of titania are known to lead to so-called “phase junctions” and synergistic processes that help catalysis.[49] More specifically, after the generation of electron-hole pairs by the photoenergy, the photogenerated electrons in the conduction band of anatase/rutile can be trapped in the

material's conduction band edge, which prevents them from recombining with the holes.[50] As seen in the HRTEM image and XRD pattern (**Figures 3.5** and **3.8**, respectively), upon adding more Cu, the materials become more crystalline, and more importantly, they contain both anatase and rutile phases. In particular, 0.4 wt % Cu-TiO_2 and 0.8 wt % Cu-TiO_2 have the highest proportions of these two crystalline phases of titania. The mixed-phase structure can, in turn, facilitate charge separation, which increases the lifetime of the photoexcited charge–hole pairs and improves the overall photocatalytic activity of the material.[51,52] Although a similar, or even greater, effect might be present in the 0.8 wt % Cu-TiO_2 material, its significantly low surface area, coupled with its excess amount of Cu, which can promote charge recombination, might ultimately lower its photocatalytic output relative to that of 0.4 wt % Cu-TiO_2.

3.5 Conclusions

In summary, we successfully synthesized a series of novel Cu-decorated nanoporous TiO_2 photocatalysts containing various loadings of Cu, denoted as *x* wt% Cu-TiO_2 by using 0 to 0.8 wt% Cu^{2+} ions in the precursors, for the efficient photocatalytic reduction of CO_2 with water into hydrocarbon fuels. An optimal amount of deposited Cu species rendered the greatest photocatalytic activity to the materials toward CO_2 reduction because they increased the visible-light absorption, helped with the formation of the right types of TiO_2 crystals, and served as an electron traps, suppressing unwanted photo generated electron-hole recombinations, in the materials. Thanks to these as well as their structural features (high surface area and three-dimensional pore structures), the nanoporous TiO_2-supported Cu nanoparticles could function as effective co-catalyst photocatalysts toward CO_2 reduction. The optimal amount of Cu^{2+} that gave the best catalytic performance was found to be approximately 0.4 wt%. This material produced CH_4 at a rate of 8.04

μmol g^{-1} h^{-1}; this rate is 21-fold higher than that of the commercial TiO_2 photocatalyst (P25 obtained from Degussa).

3.6 Reference

1. Su, J.; Vayssieres, L. *ACS Energy Lett.*, **2016**, *1*, 121-135.
2. Neatu, Ş.; Maciá-Agulló, J. A.; Concepción, P.; Garcia, H. *J. Am. Chem. Soc.*, **2014**, *136*, 15969-15976.
3. Yadav, D.; Yadav, R. K.; Kumar, A.; Park, N.; Baeg, J. *ChemCatChem*, **2016**, *8*, 3389-3393.
4. Li, Y.; Wang, W.; Zhan, Z.; Woo, M.; Wu, C. *Appl. Catal. B*, **2010**, *100*, 386-392.
5. Jin, J.; Yu, J.; Guo, D.; Cui, C.; Ho, W. *Small*, **2015**, *11*, 5262-5271.
6. Li, X.; Yu, J.; Low, J.; Fang, Y.; Xiao, J.; Chen, X. *J. Mater. Chem. A,* **2015**, *3*, 2485-2534.
7. Fang, B.; Xing, Y.; Bonakdarpour, A.; Zhang, S.; Wilkinson, D. P. *ACS Sustainable Chem. Eng.*, **2015**, *3*, 2381-2388.
8. Habisreutinger, S. N.; Schmidt-Mende, L.; Stolarczyk, J. K. *Angew. Chem. Int. Ed.*, **2013**, *52*, 7372-7408.
9. Kar, P.; Farsinezhad, S.; Mahdi, N.; Zhang, Y.; Obuekwe, U.; Sharma, H.; Shen, J.; Semagina, N.; Shankar, K. *Nano Res.*, **2016**, *9*, 3478-3493.
10. Kohno, Y.; Hayashi, H.; Takenaka, S.; Tanaka, T.; Funabiki, T.; Yoshida, S.; *J. Photochem. Photobiol. A*, **1999**, *126*, 117-123.
11. Yui, T.; Kan, A.; Saitoh, C.; Koike, K.; Ibusuki, T.; Ishitani, O. *ACS Appl. Mater. Interfaces*, **2011**, *3*, 2594-2600.
12. Wang, W.; An, W.; Ramalingam, B.; Mukherjee, S.; Niedzwiedzki, D. M.; Gangopadhyay, S.; Biswas, P. *J. Am. Chem. Soc.*, **2012**, *134*, 11276-11281.
13. Zhang, Z.; Wang, Z.; Cao, S.; Xue, C. *J. Phys. Chem. C*, **2013**, *117*, 25939-25947.

14. Yu, J.; Ran, J. *Energy Environ. Sci.*, **2011**, *4*, 1364-1371.

15. Ola, O.; Maroto-Valer, M. M. *Catal. Sci. Technol.*, **2014**, *4*, 1631-1637.

16. Yin, G.; Nishikawa, M.; Nosaka, Y.; Srinivasan, N.; Atarashi, D.; Sakai, E.; Miyauchi, M. *ACS Nano*, **2015**, *9*, 2111-2119.

17. He, Z.; Fu, J.; Cheng, B.; Yu, J.; Cao, S. *Appl. Catal. B*, **2017**, *205*, 104-111.

18. Solomon, E. I.; Heppner, D. E.; Johnston, E. M.; Ginsbach, J. W.; Cirera, J.; Qayyum, M.; Kieber-Emmons, M. T.; Kjaergaard, C. H.; Hadt, R. G.; Tian, L. *Chem. Rev.*, **2014**, *114*, 3659-3853.

19. Gawande, M. B.; Goswami, A.; Felpin, F. X.; Asefa, T.; Huang, X.; Silva, R.; Zou, X.; Zboril, R.; Varma, R. S. *Chem. Rev.*, **2016**, *116*, 3722-3811.

20. Low, J.; Cheng, B.; Yu, J. *Appl. Surf. Sci.*, **2017**, *392*, 658-686.

21. Zou, X.; Silva, R.; Huang, X.; AI-Sharab, J. F.; Asefa, T. *Chem. Commun.*, **2013**, *49*, 382- 384.

22. Xu, Q. Yu, J.; Zhang, J.; Zhang, J.; Liu, G. *Chem. Commun.*, **2015**, *51*, 7950-7953.

23. Yu, J.; Low, J.; Xiao, W.; Zhou, P. *J. Am. Chem. Soc.*, **2014**, *136*, 8839-8842.

24. Fu, J.; Cao, S.; Yu, J.; Low, J.; Lei, Y. *Dalton Trans.*, **2014**, *43*, 9158-9165.

25. Liu, S.; Xia, J.; Yu, J. *ACS Appl. Mater. Interfaces*, **2015**, 7, 8166-8175.

26. Yaghoubi, H.; Li, Z.; Chen, T.; Ngo, H. T.; Bhethanabotla, V. R.; Joseph, B.; Ma, S.; Schlaf, R.; Takshi, A. *ACS Catal.*, **2015**, *5*, 327-335.

27. Li, H.; Bian, Z.; Zhu, J.; Huo, Y.; Li, H.; Lu, Y. *J. Am. Chem. Soc.*, **2007**, *129*, 4538-4539.

28. Wang, G.; Wang, H.; Ling, Y.; Tang, Y.; Yang, X.; Fitzmorris, R. C.; Wang, C.; Zhang, J. Z.; Li, Y. *Nano Lett.*, **2011**, *11*, 3026-3033.

29. Colón, G.; Maicu, M.; Hidalgo, M. C.; Navío, J. A.; *Appl. Catal. B*, **2006**, *67*, 41-51.

30. Liu, L.; Gao, F.; Zhao, H.; Li, Y. *Appl. Catal. B*, **2013**, *134-135*, 349-358.

31. Zhang, L.; Han, L.; Zhao, G.; Chai, R.; Zhang, Q.; Liu, Y.; Lu, Y. *Chem. Commun.*, **2015**, *51*, 10547-10550.

32. Crêpellière, J.; Popa, P. L.; Bahlawane, N.; Leturcq, R.; Werner, F.; Siebentritt, S.; Lenoble, D. *J. Mater. Chem. C*, **2016**, *4*, 4278-4287.

33. Poulose, A. C.; Veeranarayanan, S.; Mohamed, M. S.; Aburto, R. R.; Mitcham, T.; Bouchard, R. R.; Ajayan, P. M.; Sakamoto, Y.; Maekawa, T.; Kumar, D. S. *Sci. Rep.*, **2016**, *6*, 35961-35974.

34. Pan, L.; Zou, J.; Zhang, T.; Wang, S.; Li, Z.; Wang, L.; Zhang, X. *J. Phys. Chem. C*, **2014**, *118*, 16335-16343.

35. Liu, D.; Fernández, Y.; Ola, O.; Mackintosh, S.; Maroto-Valer, M.; Parlett, C. M. A.; Lee, A. F.; Wu, J. C. S. *Catal. Commun.*, **2012**, *25*, 78-82.

36. Tseng, I.; Chang, W.; Wu, J. *Appl. Catal. B*, **2002**, *37*, 37-48.

37. Poliah, R.; Sreekantan, S. *J. Nanomater.*, **2011**, 239289.

38. Xu, Q.; Yu, J.; Zhang, J.; Zhang, J.; Liu, G. *Chem. Commun.*, **2015**, *51*, 7950-7953.

39. Miao, X.; Pan, K.; Liao, Y.; Zhou, W.; Pan, Q.; Tian, G.; Wang, G. *J. Mater. Chem. A*, **2013**, *1*, 9853-9861.

40. Spurr, R. A.; Myers, H. *Anal. Chem.*, **1957**, *29*, 760-762.

41. Yu, J.; Su, Y.; Cheng, B. *Adv. Funct. Mater.*, **2007**, *17*, 1984-1990.

42. Zhang, T.; Huang, X.; Asefa, T. *Chem. Commun.*, **2015**, *51*, 16135-16138.

43. Chen, J.; Hua, Z.; Yan, Y.; Zakhidov, A. A.; Baughman, R. H.; Xu, L. *Chem. Commun.*, **2010**, *46*, 1872-1874.

44. Amoli, V.; Bhat, S.; Maurya, A.; Banerjee, B.; Bhaumik, A.; Sinha, A. K. *ACS Appl. Mater. Interfaces*, **2015**, *7*, 26022-26035.

45. Xin, B.; Wang, P.; Ding, D.; Liu, J.; Ren, Z.; Fu, H. *Appl. Surf. Sci.*, **2008**, *254*, 2569-2574.

46. Gonell, F.; Puga, A. V.; Julián-López, B.; García, H.; Corma, A. *Appl. Catal. B*, **2016**, *180*, 263-270.

47. Fang, B.; Bonakdarpour, A.; Reilly, K.; Xing, Y.; Taghipour, F.; Wilkinson, D. P. *ACS Appl. Mater. Interfaces*, **2014**, *6*, 15488-15498.

48. Jeong, S.; Kim, W. D.; Lee, S.; Lee, K.; Lee, S.; Lee, D.; Lee, D. *ChemCatChem*, **2016**, *8*, 1641-1645.

49. Zhang, J.; Xu, Q.; Feng, Z.; Li, M.; Li, C. *Angew. Chem. Int. Ed.*, **2008**, *47*, 1766-1769.

50. Ma, Y.; Wang, X.; Jia, Y.; Chen, X.; Han, H.; Li, C. *Chem. Rev.*, **2014**, *114*, 9987-10043.

51. Wang, W.; Dong, J.; Ye, X.; Li, Y.; Ma, Y.; Qi, L. *Small*, **2016**, *12*, 1469-1478.

52. Cao, F.; Xiong, J.; Wu, F.; Liu, Q.; Shi, Z.; Yu, Y.; Wang, X.; Li, L. *ACS Appl. Mater. Interfaces*, **2016**, *8*, 12239-12245.

Chapter 4

Mesoporous TiO_{2-x} Composed of Nanosized Anatase with Unusual Long-Lived Excitons for Efficient Photocatalysis of CO_2 Reduction

4.1. Overview

A nanoporous TiO_{2-x} material that is comprised of small yet stable, vacancy-rich anatase nanoparticles that are necked together and show unique optical, thermal and electronic properties is synthesized using a mesoporous carbon template. When they are within the mesoporous carbon template, the nanoparticles display an unprecedented charge/discharge-like property, "blinking" under an electron beam without decaying for an extended period of time. This indicates the presence of robust electron-trapping conduction band(s) in the particles. After being extracted from the template, they show long-lived charge carriers (electrons and holes) at room temperature in the dark, long after (at least, 30 min) exposure to UV irradiation. The material is synthesized by taking advantage of the pores (ca. 50 nm) of polymer-derived mesoporous carbon as hard templates to hydrolyze and condense a titania precursor into small, isolated TiO_2 nanoparticles. During a subsequent calcination step, the mesoporous carbon template serves as a barrier isolating the nanoparticles from each other and preventing them from growing beyond ca. 10 nm in size and form TiO_{2-x}. Unlike most titania nanomaterials, the ones formed inside the controlled volume pores remain in anatase phase and undergo no phase transition to rutile phase despite their treatment at high temperature (800 °C). The material maintains the same anatase structure even at 1200 °C in a transmission electron microscope (TEM). To the best of our knowledge, such exceptionally stable, catalytically-competent (reduced) anatase nanoparticles, with long lived charge carriers, the

unusual “blinking” property under electron beam and with a 50 nm red-shift in UV absorption, have never been reported before. These properties promise a greatly enhanced quantum efficiency in photo- and electrocatalytic activity for environmental remediation, solar-electricity conversion, etc. Catalytic potentials of the new anatase material are demonstrated using a reaction of UV-driven conversion of the greenhouse gas CO_2 into synthetic hydrocarbons (CH_4).

4.2. Introduction

Nanostructured materials have interesting electronic, optical and magnetic properties that are often drastically different from their bulk counterparts.[1,2] Furthermore, many have catalytic activities for various reactions, and their catalytic properties can be tuned/improved by changing their size, shape and compositions.[3,4] Their catalytic properties can be optimized or tailored for a specific reaction, for example, by doping the material with other elements (metals, heteroatoms and metal oxides), by conjugating them with other materials and forming heterojunctions, and by introducing nanopores and high surface area into their structures.[5-8]

With the global production of over 10 million metric tons, TiO_2 is one of the most widely used materials for various applications. TiO_2 is commonly used in commercial sunscreens, self-cleaning materials, printing inks, cosmetic products, paints and varnishes.[9-11] It also finds important applications in paper, plastics, fiber, rubber, food, glass and ceramic industries.[12] Moreover, nanosized TiO_2 is one of the most investigated semiconductor materials for photocatalytic reactions, including water splitting and CO_2 reduction.[13,14] TiO_2 is attractive for these as well as many other applications because it is inexpensive, easily scalable and stable under various conditions. However, TiO_2 is not very efficient in driving photocatalytic reactions for the following two major reasons. 1) TiO_2 has a large band gap (3.2 eV) and thus capable of absorbing

light only in the UV region of solar spectrum, which is a very small fraction (*ca*. 3%) of solar energy.[15] In other words, photons from the visible region of sunlight do not have enough energy to surmount the band gap in in to be exploited in photocatalysis. 2) TiO_2 forms photoexcited electrons and holes that have fast recombination times, making the material inefficient in photocatalysis.[16] This means, the charge carriers that TiO_2 forms would quickly recombine and be lost, rather than getting involved in redox reactions.

Fortunately, these problems can be overcome by doping it with elements such as nitrogen or carbon, by functionalizing it with *ca*. 0.1 - 2% metals (also known as metallization), or by creating vacancy/defect sites in it.[17,18] The first two entail the introduction of heteroatoms or metals into the TiO_2 structure, which often leads to higher quantum efficiency and thereby good photocatalytic activity in the material.[19] For example, a TiO_2 material possessing <5 mol % of Ag NPs was reported to exhibit a better photocatalytic activity toward oxidation of rhodamine B than a pure TiO_2 because the Ag NPs could readily trap photoexcited electrons and inhibit their recombination with the holes.[20] By taking advantage of the surface-plasmon resonance (SPR) properties of SPR-active metallic NPs using metals such as Ag NPs, the ability of TiO_2 to absorb sunlight or to inhibit the recombination of charge carriers can be achieved.[21] In this case, the Ag NPs serve as nano-antennas and allow TiO_2 to indirectly receive visible light. However, not all metal-doped TiO_2 materials show improved photocatalytic activity. For example, TiO_2 containing 1% Pt was reported to show less activity towards various photocatalytic reactions than plain TiO_2.[22] This is because the metals facilitate charge recombination by building up excess negative charges and attracting the holes from the valence bands. Additionally, at relatively higher metal loadings, the metals can block a significant portion of the photocatalyst from being illuminated.[23]

Another approach involves the introduction of oxygen vacancies in the TiO_2 lattice.[24] This can, in fact, be viewed as the alternative of doping heteroatomic or metallic species into TiO_2, which is discussed earlier. Besides creating good adsorption and catalytically active sites, the oxygen vacancies can change the electronic structure, charge transport, and surface properties of TiO_2. The oxygen vacancies can also reduce the electron-hole recombination processes, thereby improving the photocatalytic reaction rates over the TiO_2 material. Despite this, methods that lead to catalytically active, stable oxygen vacancy-rich TiO_2 have been hard to come by. Moreover, many of the materials are unstable under ambient conditions and light illumination, and their photogenerated electrons and holes tend to recombine and not last more than a few minutes. Consequently, they often show low photocatalytic activity.[25]

While TiO_2 has a long history in catalysis, its catalytic properties for energy applications has recently been drawing increasing interest. For example, TiO_2's photocatalytic properties can be exploited for the hydrogen evolution reaction (HER) to produce hydrogen (H_2), a clean energy carrier, from water.[26-28] Furthermore, by introducing dopants or creating vacancies in it, its electronic properties and quantum efficiency (*i.e.*, the proportion of light the material converts into charge carriers), which help it to photocatalyze reactions, can be improved, and its band positions can be realigned to match with the potentials of the half reactions involved in such reactions as water splitting and CO_2 reduction.[17,29] This is, in fact, currently one of the most promising approaches to enhance the overall photocatalytic activity of TiO_2 and other related semiconductor materials for various renewable energy-pertinent reactions.

The greenhouse gas CO_2 in the atmosphere, which is largely due to the consumption of fossil fuels, continues to rise and pose a danger of global warming. Thus, converting CO_2 into valuable chemicals is one promising route to reduce the amount of CO_2 present in the atmosphere.

Moreover, CO_2 reduction reaction can serve as a means to store intermittent energy from sources such as wind and solar power in the form of chemical energy (*e.g.*, by producing H_2 with solar-powered electrolysis and converting the H_2 into easily portable light fuels such as HCOOH using CO_2). The process can also help with the production of useful chemical feedstocks and synthetic fuels (such as CH_4, CH_3OH, HCOOH, carbonates, carbamates and urea) at the expense of CO_2.[30] Recently, electrochemical and photochemical reduction of CO_2 with water or H_2 have also been demonstrated, allowing the use of CO_2 as a relatively stable and a safe and an abundant source of carbon in chemical synthesis. However, the large-scale applications of all these processes have been limited by the unavailability of efficient and sustainable catalysts to formulate CO_2, which is inherently too stable to activate at low energy. Thus, the rational design and synthesis of advanced catalysts for transformations of CO_2 to value-added chemicals with the help of H_2 or, preferably, H_2O, at less energy expense is currently a major interest. In particular, catalysts that work with sustainable energy sources such as sunlight are of paramount importance to scale up the process for a broad range of applications.[31,32]

In this work, we report a unique type of photoactive nanoporous TiO_2 comprised of small anatase nanoparticles by using a polymer-derived nanoporous carbon as a template. The material and its nanoparticles show unusual photophysical and electronic properties both under light and under electron beam. When they are within the carbon template, the anatase nanoparticles show charge/discharge properties, lighting up and fading for an extended time during imaging under an electron beam. When exposed to UV-light, the nanoporous TiO_2 and its nanoparticles exhibit long lived excitons for, at least, the duration of the measurement (30 min) in electron paramagnetic resonance (EPR) measurements. Both results indicate the exceptional electron trapping ability of the conduction bands in the anatase nanoparticles in the materials. We also show that the

nanoporous TiO_2 displays excellent photocatalytic properties for reduction of CO_2, producing CH_4 (a synthetic fuel) from the greenhouse gas CO_2. Given TiO_2's versatile photocatalytic properties and proven commercial applications, the material reported herein can also be expected to find lots of other practical applications in environmental remediation and decontamination, in sunscreen products, and in electronic and photonic heterojunction devices.

4.3. Experimental Section

4.3.1. Chemicals and reagents.

Aniline (≥99.5%), ammonium persulfate (≥98.0%), sodium hydroxide (≥97.0%), hydrochloric acid (37%), titanium(IV) *n*-butoxide (TBO) (97%), ethylene glycol (EG) (anhydrous, 99.8%), ammonium persulfate (≥98.0%) and acetone (HPLC Plus grade, >99,9%) were purchased from Sigma-Aldrich. Colloidal silica (SNOWTEX®) with nominal particle size of 47 nm was obtained from Nissan Chemical America Corporation. Anhydrous ethanol was obtained from Fisher Scientific. The chemicals and reagents were all used as received without further purification. Distilled water was used throughout the experiments.

4.3.2. Synthesis of Polyaniline (PANI)-derived Mesoporous Carbons (PDMCs).

PDMC was synthesized by following the synthetic route previously reported by our group, with a slight modification.[33,34] First, a composite material composed of PANI and silica nanoparticles was synthesized *via* polymerization of aniline with the help of ammonium persulfate in the presence of colloidal silica templates. Typically, colloidal silica (30 g) was mixed with aqueous HCl solution (1 M, 120 mL) containing aniline (2 mL). The solution was stirred for 30 min in a water bath with a temperature between 0 and 5 °C. Then, aqueous HCl solution (1 M, 20

mL) containing ammonium persulfate (5 g) was added drop-wise into the above solution under stirring. The solution was further stirred for 24 h between 0 and 5 °C. The solution was kept in oven at 100 °C to let the solvent in the solution evaporate. The resulting green-colored solid material was then subjected to pyrolysis under Ar atmosphere at 800 °C for 2 h, after raising the temperature from room temperature to 800 °C at a rate of 5 °C min^{-1}. The black powdered product (800 mg) was subsequently treated with aqueous NaOH solution (2 M, 54 mL) in an autoclave at 100 °C for 24 h to remove the silica templates in it. Finally, the mixture was filtered, and the solid product was washed with water (80 mL, 4 times) and then EtOH (20 mL, 2 times), and then dried at 50 °C. This produced PDMC.

4.3.3 PDMCs-Assisted Synthesis of Nanosized TiO_{2-x} Material.

First, TBO (1 mL) was mixed with ethylene glycol (20 mL), and the two were stirred together for 4 h to form titanium glycolate solution (TGS). Then, using a MilliporeSigma™ Glass Vacuum Filter Assembly, in which a Pall Universal Membrane Disc Filter (0.45 µm, 25 mm) containing PDMC (300 mg) was placed, the TGS was slowly poured under vacuum pumping to infiltrate the TGS into the pores of PDMC. The TGS-loaded PDMC were then dispersed in a solution containing acetone (20 mL) and water (320 µL) and stirred for 12 h and then collected via centrifugation and dried at 60 °C. The resulting material, titanium glycolate-PDMC (or TG-PDMC), was then placed on a ceramic combustion boat in a temperature-programmable tube furnace and pyrolyzed under Ar atmosphere as follows. The temperature was raised from room temperature to 800 °C at a rate of 5 °C min^{-1} and then kept at 800 °C for 2 h. The furnace was was then let to cool down to room temperature naturally. During this pyrolysis step, TG-PDMC was converted to TiO_{2-x}-PDMC. Finally, the PDMC template in TiO_{2-x}-PDMC was removed by

calcining the material at 550 °C in air for 30 min. This resulted in a nanoporous TiO_2 material that is compositionally found to be TiO_{2-x} (*vide infra*); thus, hereafter it is referred to as such.

4.3.4 Synthesis of TiO_2 (Control) Materials *via* Calcination or Hydrolysis + Calcination.

For comparative studies, two control TiO_2 materials were synthesized by following a modified method previously reported by our group.[29] First, TBO (2 mL) and EG (50 mL) were mixed and stirred together for 4 h to produce TGS. The TGS was then poured into another solution containing acetone (170 mL) and water (2 mL). After stirring for 60 min, the solution was centrifuged and the precipitate was washed with ethanol and dried at 60 °C. The resulting white solid product, which contained titanium glycolate microspheres (TGMs), was then calcined in air at 800 °C for 2 h, after raising the temperature from room temperature to 800 °C at a rate of 5 °C min^{-1}. This gave a TiO_2 material that is denoted as TiO_2-(C), where "C" represents "synthesized by calcination".

In another experiment, the TGMs were refluxed in a boiling water for 24 h. The solution was centrifuged, and the precipitate was washed with ethanol and dried at 60 °C. The resulting material, dubbed TiO_2-(H), where "H" represents "TiO_2 synthesized by Hydrolysis", was then calcined at 500 ° C. This gave another TiO_2 material that is named as TiO_2-(H+C).

4.3.5 Characterizations.

Transmission electron microscope (TEM) images of the materials were taken with a Topcon 002B TEM instrument operating at 200 kV. Low energy electron beam S(T)EM images were performed using FEI Magellan microscope operating with a beam deceleration mode and equipped with a home-designed sample holder suitable for scanning low energy electron

microscopy (SLEEM). The instrument could operate with electron energy in the range of 0 eV to 30 keV. The beam deceleration was achieved with a relatively simple method, by applying of negative bias on the sample holder, and this was done in order to improve both the resolution and the contrast of the images. The energy of the beams could be as small as units of eV and be adjusted until a good image was obtained. While using a beam with energy of 500 eV for reflection mode and 10 keV for transmission mode (STEM), the spots where the TiO_{2-x} nanoparticles underwent continuous brightening and fading, presumably due to charging and discharging. The videos of the process was also taken with the same instrument.

The surface areas and pore properties of the materials were investigated by N_2 porosimetry using a Micromeritics Tristar-3000 instrument (Micromeritics, USA). Before each measurement, the sample was degassed at 80 °C for 8 h under a flow of N_2 gas to remove any possible guest species adsorbed on the samples' surfaces. The surface areas and pore size distributions of the materials were calculated using the Brunauer-Emmett-Teller (BET) method and the Barrett-Joyner-Halenda (BJH) method, respectively. The pore volumes of the materials were determined based on the amount of N_2 adsorbed at a relative pressure of 0.99. X-ray diffraction (XRD) patterns of the materials were obtained using a Philip XPert diffractometer operating with Cu Kα radiation as the X-ray source. The XRD diffraction patterns were recorded in a 2θ range between 10 and 80° with a step size (2θ) of 0.02° and at a scanning speed of 0.6° min^{-1}. The UV-Vis diffuse reflectance spectra (UV-Vis DRS) of the materials were acquired with a Lambda 950 spectrophotometer (PerkinElmer) in a spectral range of 250 to 800 nm. Thermogravimetric analyses (TGA) of the materials were carried out using a PerkinElmer TGA7 instrument by heating the samples at a rate of 5 °C min^{-1} under air that was flowing at a rate of 20 mL min^{-1}. Elemental

compositions of the materials were probed with a Thermo Scientific K-Alpha X-ray photoemission spectrometer (XPS) equipped with an Al Kα radiation as the X-ray source (hυ = 1486.6 eV).

Electron paramagnetic resonance (EPR) experiments were performed using an Elexsys E580e spectrometer (Bruker), that is operating at X-band (9.5 GHz) and utilizing a standard TE_{102} resonator with an ESR900 flow cryostat (Oxford Instruments). For the EPR samples, the weighted quantities of TiO_{2-x} and TiO_2-(H+C) powders were placed in quartz EPR tubes (OD 4 mm) and then flame sealed under atmospheric air. UV irradiation of the samples was done in a separate finger Dewar at liquid nitrogen temperature (77 K) using a 4 W split-tube lamp (UVGL-15, 254/365 nm). The UV exposure time was about 25-30 min, and the samples were periodically rotated to allow more uniform light exposure. Concentrations of EPR-visible defects in each sample were determined by comparing the measured EPR signal intensities to the EPR standard with a known number of spins (a $CuSO_4 \cdot 5H_2O$ crystal of known weight in mineral oil).

4.4. Results and Discussion

The synthetic procedure that was employed to prepare the TiO_{2-x} material is depicted in **Scheme 4.1** and also described in detail in the Experimental Section above. The procedure comprises four steps: a) synthesis of PANI-derived mesoporous carbons (PDMC), b) loading of a TGS precursor within the mesopores of PDMC to form TGS/PDMC, c) conversion of TGS/PDMC into TGM/PDMC, d) conversion of TGM/PDMC into TiO_{2-x}/PDMC by pyrolysis, and e) removal of the PDMC templates from TiO_{2-x}/PDMC.

In the first step, aniline is polymerized in the presence of colloidal silica templates using ammonium persulfate as oxidant. The resulting PANI-SiO_2 composite material is treated at 800 °C for 2 h under Ar atmosphere to pyrolyze the PANI. When the SiO_2 templates are subsequently

etched away with an aqueous alkaline solution, PDMCs are formed. Into the mesopores of the PDMCs, titanium glycolate solution (TGS) is infiltrated, and the resulting TGS-loaded PDMCs are subjected to pyrolysis at 800 °C. This generates TiO_{2-x}-PDMCs. Finally, the PDMC template was burned away at 550 °C in air for 30 min, leaving behind nanoporous TiO_{2-x}.

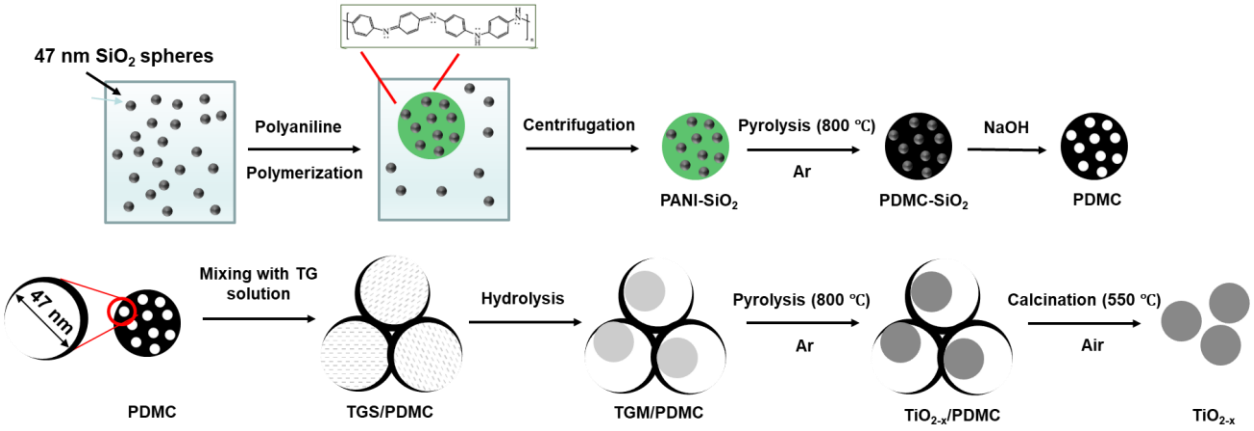

Scheme 4.1. Schematic illustration of the synthetic procedure leading to TiO_{2-x}. First, PANI-derived mesoporous carbons (PDMCs) are synthesized by polymerizing PANI in the presence of colloidal SiO_2, then pyrolyzing the PANI/SiO_2 under Ar atmosphere and finally etching away the SiO_2. This produces PDMCs, which is used as a template for the synthesis of TiO_{2-x} in the next steps. In this case, TGS is loaded in the pores of PDMCs, the TGS/PDMCs is then pyrolyzed, and finally the PDMC template is removed by calcination. This finally results in the TiO_{2-x} material.

The morphologies of PDMC, TiO_{2-x}-PDMC and TiO_{2-x} were first examined by a TEM. The TEM images of PDMC reveal that the material possesses highly mesoporous structures with an average pore size of *ca*. 47 nm (**Figures 4.1a** and **4.1b**). The images of TiO_{2-x}-PDMC show the formation of TiO_{2-x} nanoparticles with an average size of *ca*. 8 nm inside the pores of PDMCs (**Figures 4.1c** and **4.1d**). Furthermore, the results reveal that the TiO_{2-x} nanoparticles maintain

their shape and size, without severe aggregation, even after the removal of PDMC template by calcination at 550 °C (see **Figures 4.1e** and **4.1f**).

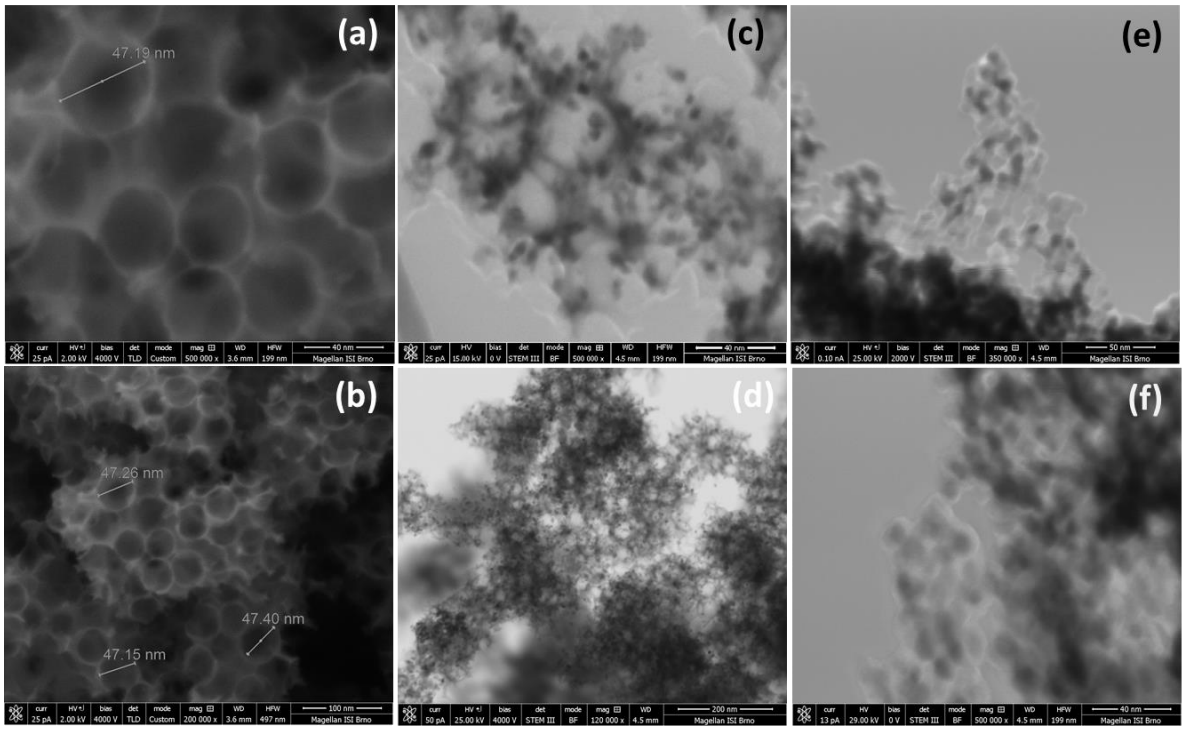

Figure 4.1. TEM images of (a,b) PDMC, (c,d) TiO_{2-x}-PDMC, and (e,f) TiO_{2-x} materials.

For comparison, the structures of single particles of TGM, TiO_2-(C), TiO_2-(H), and TiO_2-(H+C) were imaged by a TEM (**Figure 4.2**).[29] The image of TiO_2-(C) shows a microparticle with nonporous structure (**Figure 4.2b**), similar to its parent material TGM (**Figures 4.2a**). However, the latter does not have the same spherical shape as the former, and the particle appears a bit deformed. This deformation from spherical shape is seen in all of the particles of TiO_2-(C) material. Meanwhile, TiO_2-(H), which is prepared by hydrolyzing TGM in a boiling water, shows porous structures composed of closely packed nanosized grains of *ca*. 6-9 nm in size (**Figure 4.2c**). Furthermore, after treatment at 500 °C for 2 h, and becoming TiO_2-(H+C), not only it shows microparticles but also nanoporous structure composed of nanoparticles with an average size of

ca. 8 nm in each microparticle. Interestingly, the microparticles maintain the original spherical morphology after calcination (compare the image in **Figure 4.2c** versus that in **Figure 4.2d**), which is unlike those of TiO_2-(C) (i.e., the images in **Figure 4.2b**).

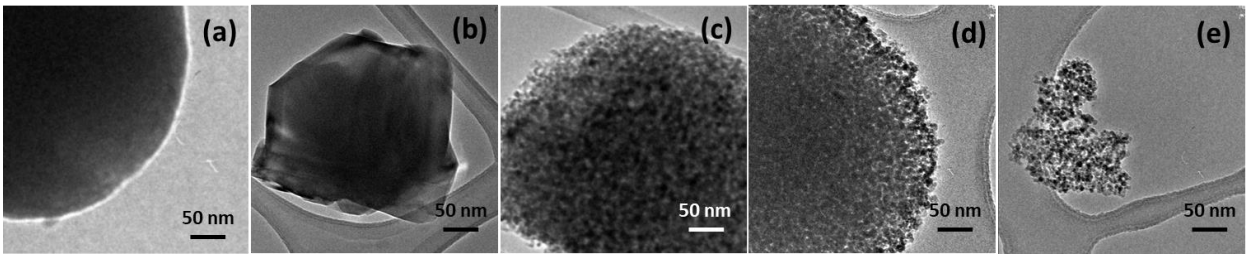

Figure 4.2. TEM images of single particles of (a) TGM, (b) TiO_2-(C), (c) TiO_2-(H), (d) TiO_2-(H+C) and TiO_{2-x}.[29]

Thermogravimetric analysis (TGA) was carried out under air to figure out the temperature that would be required to remove the PDMC templates as well as to determine the amount of TiO_{2-x} loaded in the PDMC (**Figure 4.3** and **Figure 4.4**). The TGA curves were run from room temperature to 500, 550 or 600 °C at a rate of 5 °C min^{-1} and then held at each temperature for 30 min. The results indicate that PDMC cannot be completely removed by holding the temperature at 550 °C for 30 min. On the other hand, nearly 100 % of the PDMC is removed by holding the temperature at 550 °C or 600 °C for 30 min. The latter results also indicate that no SiO_2 template is present in the PDMC, or the complete removal of SiO_2 during the treatment of PDMC/SiO_2 materials in alkaline solution. In other words, *ca*. 100 % weight loss would not have occurred in the TGA traces had there been some residual SiO_2. The TGA results also indicate that PDMC can be completely removed by calcining the TiO_{2-x}-PDMC at or above 550 °C for 30 min. This is how the calcination temperature and time to remove PDMC were ultimately chosen for the synthesis of TiO_{2-x}.

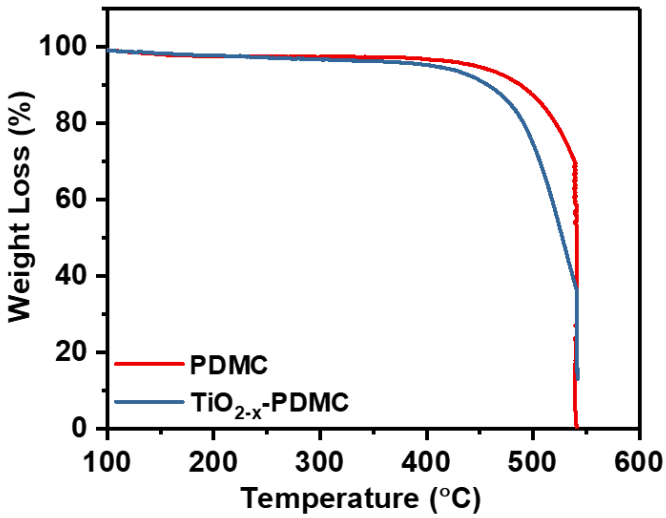

Figure 4.3. TGA curves obtained in air atmosphere for PDMC and TiO_{2-x}-PDMC materials by holding the temperature at 550 °C for 30 min.

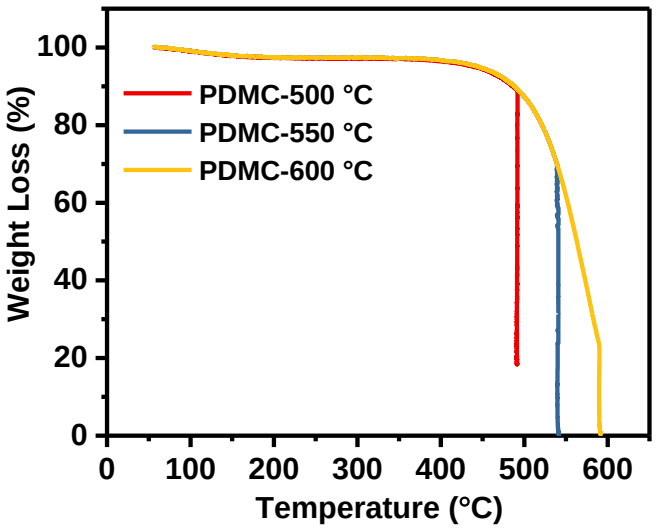

Figure 4.4. TGA curves of PDMC obtained by holding at 500, 550 and 600 °C under air for 30 mins, respectively.

The amount of TiO_{2-x} in the PDMC was determined by comparing the TGA curve of TiO_{2-x}/PDMC with that of PDMC (**Figure 4.3**). The TGA curve of TiO_{2-x}/PDMC shows a total residue of *ca*. 14% after calcination at 550 °C for 30 min, and this weight can be exclusively attributed to

the TiO_{2-x} material. It is also worth noting that the decomposition of TiO_{2-x}/PDMC starts at *ca*. 430 °C, which is *ca*. 30 °C lower than that of PDMC. This indicates that the presence of TiO_{2-x} facilitates the thermal decomposition of PDMC, perhaps by facilitating the heat transfer in the PDMC nanoparticles and thus promoting the combustion of the carbon material. It also indirectly corroborates that titania is successfully loaded in TiO_{2-x}/PDMC.

N_2 porosimetry is used to investigate the pore structures and determine the surface areas and pore sizes of PDMC, TiO_{2-x}-PDMC, TiO_{2-x} and TiO_2-(H+C) (**Figures 4.5**). The N_2 adsorption/desorption isotherm of PDMC is Type IV with type H2 hysteresis loop, which is characteristic of mesoporous materials. Its BET surface area is 708 m^2 g^{-1} and its BJH pore size distribution curve shows pores predominantly centered at *ca*. 43 nm, which correspond to the sizes of the colloidal silica templates. Like that of PDMC, the N_2 adsorption/desorption isotherm of TiO_{2-x}-PDMC is found to be type IV with type H2 hysteresis loop. The surface area and pore size of TiO_{2-x}-PDMC are slightly lower, with a value of 440 m^2 g^{-1} and 34 nm, respectively. In addition, the pore volume of TiO_{2-x}-PDMC is lower (1.63 m^3 g^{-1}), compared with that of PDMC (2.00 cm^3 g^{-1}). These must have been due to the presence of titania nanoparticles in the former. These results indirectly confirm that the formation and presence of titania inside the pores of PDMC, just like the TEM images indicated earlier. It is worth adding here that a substantial amount of small mesopores and micropores (near 2 nm in size) are also found in both materials (see Figure 4b and S2). In the case of TiO_{2-x}, the surface area is 99 m^2/g, the pore volume is 0.23 cm^3/g and the average pore diameter is 8.6 nm. The surface area and porosity of the corresponding control titania material, TiO_2-(H+C), is also obtained and compared with those of the other materials in **Table 4.1** below.

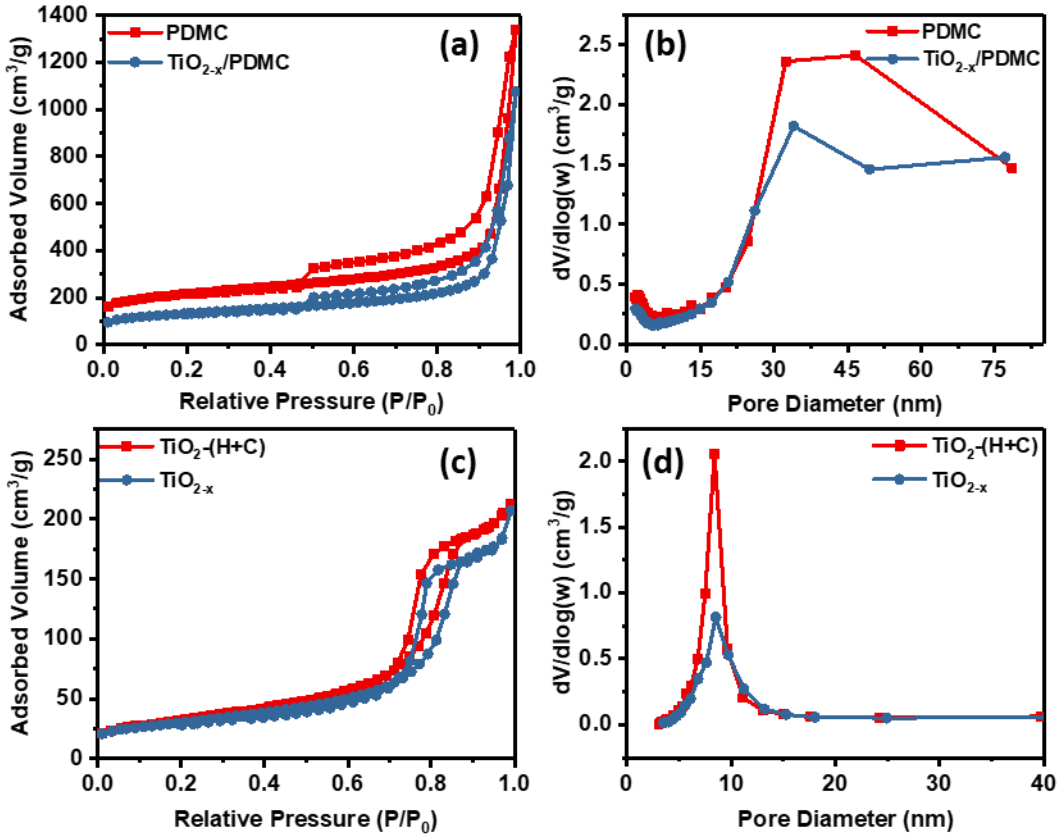

Figure 4.5. (a) N_2 adsorption/desorption isotherms of PDMC and TiO_{2-x}/PDMC, (b) their corresponding pore size distribution, (c) N_2 adsorption/desorption isotherms of TiO_2-(H+C) and TiO_{2-x}, and (d) their corresponding pore size distributions.

Table 4.1 Structural properties of PDMC, TiO_{2-x}-PDMC, TiO_{2-x} and TiO_2-(H+C).[a)]

Material	BET surface area/(m^2 g^{-1})	Average pore size/(nm)	Pore volume/(cm^3 g^{-1})
PDMC	708	43	2.00
TiO_{2-x}-PDMC	440	34	1.63
TiO_{2-x}	99	8.6	0.23
TiO_2-(H+C)	116	8.3	0.31

[a)] Calculated based on the data in the adsorption branch of N_2 adsorption/desorption isotherms.

The images and UV/Vis diffuse reflectance spectra of TiO_{2-x} and TiO_2-(H+C) are provided in **Figure 4.6**. While TiO_2-(H+C) has a white color, TiO_{2-x} has a yellowish color, which indicate that the two materials have different light-absorption properties. The results also indicate that, unlike most traditional TiO_2 materials, which are photoactive only under UV light, TiO_{2-x} is responsive to visible light. This visible light absorption character of TiO_{2-x} is further confirmed from the diffuse reflectance spectra. While TiO_2-(H+C) shows absorption edge at *ca*. 390 nm (in the UV region), the diffuse reflectance spectrum of TiO_{2-x} is red-shifted with the onset value of the adsorption band appearing at approximately 500 nm, indicating the presence of optically-active mid-gap states related to oxygen vacancies, interstitial Ti^{3+} and undercoordinated O^-.[35,36] This indicates that TiO_{2-x} has a better ability to absorb visible light than TiO_2-(H+C), for example.

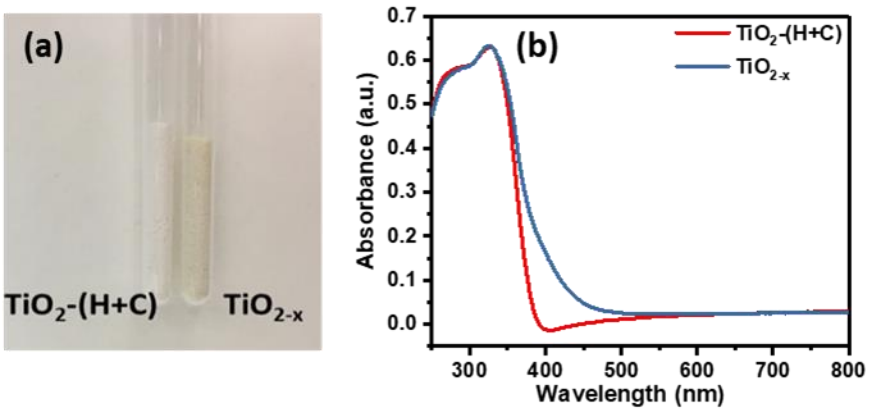

Figure 4.6. (a) Physical appearance of TiO_{2-x} and TiO_2-(H+C) and (b) UV-vis diffuse reflectance spectra of TiO_2-(H+C) and TiO_{2-x} materials.

X-ray photoelectron spectroscopy (XPS) was carried out to determine the chemical composition of the materials (Figure 4.7). The XPS survey spectra of TiO_2-(H+C) and TiO_{2-x} reveal that both materials are composed mainly of Ti, O and C. Peaks corresponding to N are not seen in the survey spectrum of TiO_{2-x}, indicating the absence of N dopants in this material. The presence of C in both materials is mainly contributed to the adventitious hydrocarbon species

present in their surfaces (**Figures 4.7c** and **4.7f**). The binding energy positions of Ti $2p_{3/2}$ and Ti $2p_{1/2}$ are observed at 458.2 and 463.9 eV, respectively. The splitting-value between Ti $2p_{3/2}$ and Ti $2p_{1/2}$ is *ca*. 5.7 eV (**Figures 4.7b** and **4.7e**), which corresponds to the characteristic value of TiO_2. This results rule out the possibility of C and N dopants causing the yellowish color in the TiO_{2-x} material, as is the case in many colorful TiO_2 materials.[37]

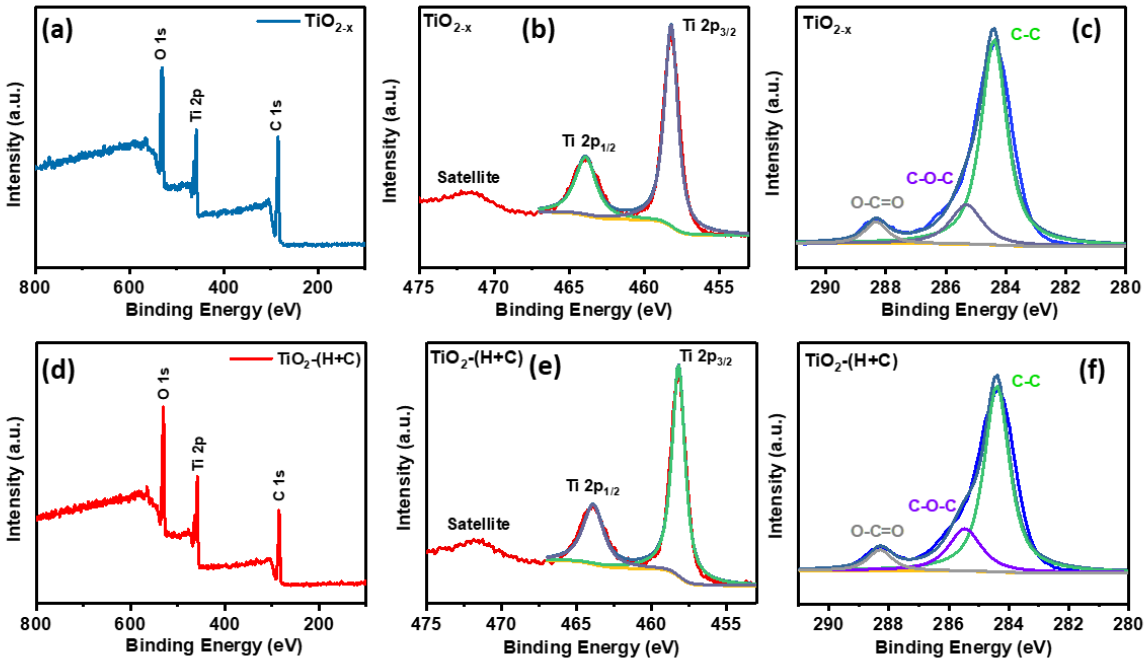

Figure 4.7. (a) XPS survey spectrum of TiO_2-(H+C) and TiO_{2-x}. High-resolution XPS spectra of (b,c) C-1s peaks and (d,e) Ti-2p peaks of TiO_2-(H+C) and TiO_{2-x} materials.

X-ray diffraction (XRD) is used to characterize the crystalline phase and crystallite sizes of the TiO_{2-x} material. In our previous study, we observed that treating TGM or TiO_2-(H) at 800 °C led to the expected phase transformation from anatase to rutile, accompanied by the growth in sizes of the TiO_2 nanocrystals.[29] In marked contrast, here we find that both TiO_{2-x} and TiO_2-(H+C) preserve their anatase phases and show no evidence of a rutile phase (**Figure 4.8**). The crystal size in both materials are estimated based on the strongest anatase (101) peaks using Scherrer equation

($d = 0.89\,\lambda/\beta\cos\theta$, where d, λ, β and θ are the crystallite size, the wavelength of the X-ray radiation, the full width at half-maximum of the peaks in radians and the diffraction angle, respectively). Accordingly, the average crystallite size of TiO_{2-x} and TiO_2-(H+C) are found to be 8.2 and 7.9 nm, respectively. For TiO_{2-x}, the measured crystallite size is perfectly consistent with the expected size of 7 nm assuming that each 47 nm nanopore in the PDMC template was fully preloaded with TGS precursors before converting it to TiO_{2-x}. Thus, it appears that the presence of the PDMC templates plays a crucial role both in controlling the size of synthesized TiO_{2-x} nanoparticles and also in maintaining their anatase phase. The PDMC template works as a physical barrier preventing the TiO_2 nanoparticles from growing beyond a certain size during the TGM pyrolysis step and also during the high-temperature (800 °C) activation step when converting TiO_2 to a catalytically-active TiO_{2-x}. The size of TiO_2 nanoparticles is then simply defined by the amount of TGS precursor preloaded in each nanopore in PDMC. Despite being small in size, the TiO_{2-x} nanoparticles do not convert to a rutile phase, even after high temperature treatment, because an anatase phase is known to be more stable for small TiO_2 particles (<10 nm).[38,39]

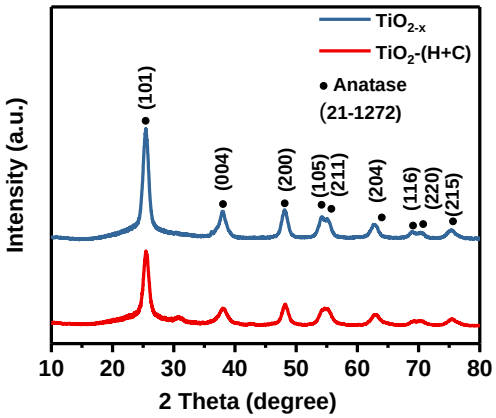

Figure 4.8. XRD patterns of TiO_2-(H+C) and TiO_{2-x} materials.

Electron paramagnetic resonance (EPR) is used to further clarify the difference between TiO_2-(H+C) and TiO_{2-x} and to determine the nature of mid-gap defect states responsible for the observed UV-Vis absorption edge shift in TiO_{2-x} (and for its yellowish color appearance). Both samples are measured several times: before and after UV irradiation, and then after dark adaptation at room temperature following up the UV irradiation (**Figure 4.9**). Several peaks resolved in the EPR spectra are identified based on their g-factor values. The signal at g = 2.017 is believed to be from holes trapped at undercoordinated oxygen atoms (O^- centers) and possibly hydroxy groups at TiO_2 surface.[40] The signal at g = 2.000 has several overlapping contributions, including electrons trapped at oxygen vacancies and also weakly-localized electrons (polarons) associated with Ti^{3+} centers in crystallite bulk and at surface.[40-42] The signals at g = (1.990, 1.962) correspond to bulk Ti^{3+} centers,[40,43,44] and the broad signal at g = 1.945 is from surface Ti^{3+} centers.[40,43,45]

As seen in **Figure 4.9a**, all EPR signals in TiO_2-(H+C) are weak before the UV exposure, and the signals are further suppressed after the UV exposure. Based on the signal intensity at g = 2.000, and considering the average crystallite grain size of ca. 8 nm as determined from our XRD experiments, we estimate on average 0.02-0.04 spin defects per crystallite in TiO_2-(H+C) before the UV exposure. This defect count includes ionized oxygen vacancy centers and also weakly-localized electrons (polarons) in bulk and at surface of TiO_2-(H+C) crystallites. After the UV exposure the spin defect number in TiO_2-(H+C) reduces to essentially zero, indicating that all paramagnetic defects are now fully ionized by trapping electrons or holes generated during the UV illumination, being converted to their EPR-invisible states.

The EPR signals are noticeably stronger in TiO_{2-x} (**Figure 4.9b**). Note that the vertical (intensity) scale in **Figure 4.9b** is ten times larger than that for TiO_2-(H+C) in **Figure 4.9a**. When measured in the dark, the spin count numbers, for the g = 2.000 line, gives on average 0.2 spin

defects per crystallite grain in TiO_{2-x}, a remarkable 5-10 increase over what was seen in TiO_2-(H+C). After the UV exposure the defect number in TiO_{2-x} increases even further to about 0.85 spin defects per crystallite, again in marked contrast to TiO_2-(H+C) where the number of spin defects decreased after the UV exposure. The high density of spin defects in the dark TiO_{2-x}, and its additional four times increase after the UV exposure (almost to the level of one defect per crystalline), point out to greatly increased concentrations of oxygen vacancies and shallow-trap defects (e.g. undercoordinated Ti^{3+} and O^- atoms) in reduced TiO_{2-x}. A small fraction of these defects (0.2 defects per crystallite) is already ionized and EPR-visible in the sample kept in the dark; even larger fraction (0.85 defects per crystallite) is converted to the ionized, EPR-visible states, by trapping photogenerated electrons and holes, after the UV exposure. These mid-gap defects, including oxygen vacancies and undercoordinated Ti^{3+} and O^- in bulk and at surface, are the most probable cause of the red shift in the absorption spectra in of TiO_{2-x} and also its yellowish color.[41, 42]

To test the stability of photogenerated electron/hole charge defects in TiO_{2-x}, the UV-irradiated samples were warmed up and kept in the dark at room temperature for varied periods of time, before freezing them again and remeasuring their EPR spectra. Notably, the room temperature dark adaptation for 25 min (the green trace in **Figure 4.9b**) did not produce any visible changes in the EPR spectrum as compared to what measured immediately after the UV irradiation (the red trace in **Figure 4.9b**). This indicates that all photogenerated electron/hole charge states are stable on that time scale even at room temperature and no charge recombination occurs. However, the dark adaptation for 72 h (the purple trace) results in a complete recovery of the spectrum to what is originally obtained for this sample before any UV exposure (the blue trace in **Figure 4.9b**), with all photogenerated charge states being fully recombined to their original dark

states. The long lifetimes of photogenerated electron/hole traps in our TiO_{2-x} and their slow recombination rate even at room temperature could be one of the crucial factors explaining the enhanced photocatalytic activity of TiO_{2-x} toward CO_2 reduction as discussed below.

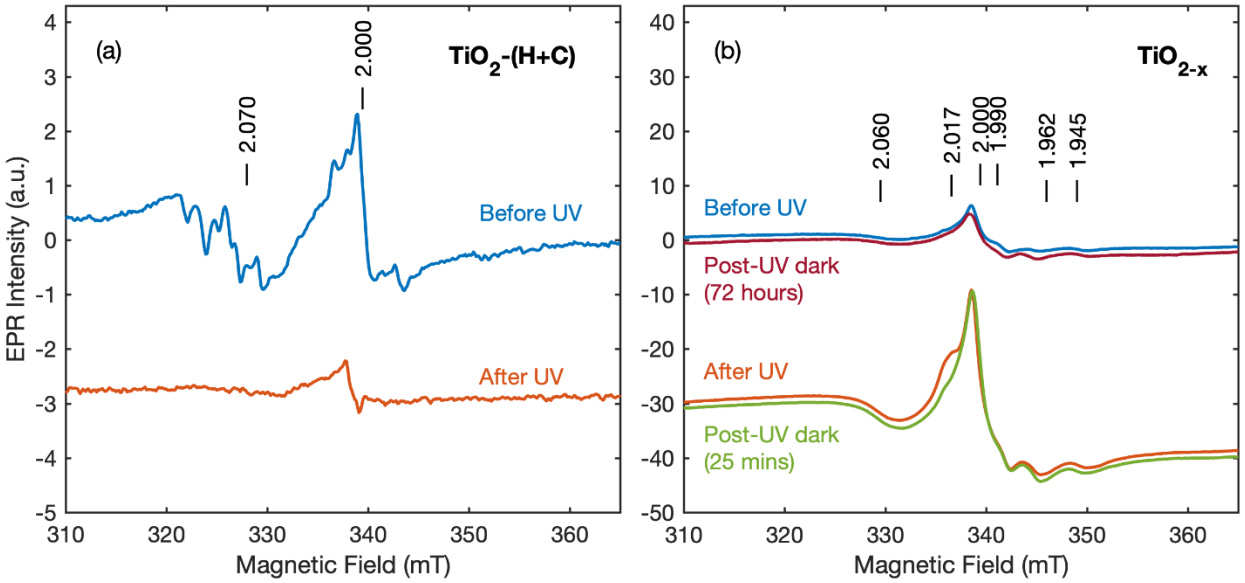

Figure 4.9. EPR spectra of (a) TiO_2-(H+C) and (b) TiO_{2-x}, measured before (blue trace) and after (red trace) UV irradiation. Two additional spectra shown in (b) are for TiO_{2-x} that is dark adapted for 25 min (green trace) or 72 h (purple trace) at room temperature after UV illumination. The spectra are vertically shifted for clarity. Vertical lines, marked with their g-factor values, identify the main peaks resolved in the EPR spectra: (2.06-2.07) Cu^{2+} impurities; (2.017) holes trapped on (undercoordinated) oxygen atoms; (2.000) negatively-charged oxygen vacancies and weakly-localized electrons (polarons); (1.990 and 1.962) bulk Ti^{3+} centers; and (1.945) surface Ti^{3+} centers.[40-45] Notice a 10x difference in the vertical scales between (a) and (b). EPR experimental conditions: temperature, 20 K; microwave frequency, 9.5 GHz; microwave power, 0.2-2 mW; modulation amplitude, 0.5-1 mT.

In addition to the EPR signals around g-factor 2 as discussed above, TiO_{2-x} after UV irradiation also develops a broad baseline signal spanning from 100 to 1000 mT as shown in **Figure 4.10**. This broad signal was not observed in TiO_2-(H+C), neither before nor after UV irradiation. Notably, the intensity of this broad signal increases when temperature increases from 20 to 50 K; the behavior is opposite to what would be expected from a conventional EPR signal. Indeed, all other peaks seen in the same EPR spectra in **Figure 4.10** show a consistent **decrease** in their intensities by ~2.5x, when temperature changes from 20 to 50 K. The broad linewidth, the significant signal intensity and the atypical temperature dependence, all taken together point out to the unconventional origin of this broad baseline signal in TiO_{2-x}. We speculate that this broad signal originates from weakly-localized electrons (polarons), produced during UV irradiation and trapped in bulk and at surface of TiO_{2-x}, and from electrically-driven spin resonance of these electron/holes due to their conductive coupling to a microwave electrical field. Recent DFT calculations have shown that electron/hole states with shallow trap potentials, and with low energy hopping barriers, may indeed exist in reduced TiO_{2-x}.[42] At low temperatures (below 20 K) these shallow electron/hole states remain fully localized and their conductive coupling to microwave electric fields is mostly suppressed. However, at higher temperatures exceeding the electron confining energy (above 10 K in our case), the shallow electrons/holes become mobile, being involved in a charge hoping and a cyclotron motion, and through this motion they conductively couple to electric microwave field causing strong microwave absorption and resulting in a broad spectral baseline signal as that observed in the EPR spectra in **Figure 4.10**. Broad baseline EPR signals with similar spectral line shapes have been previously reported for conduction and weakly-localized electrons in Si/SiGe heterostructures where these signals were ascribed to the cyclotron resonance microwave absorption.[46] We have not been able to find any reports on this broad

baseline signal in other TiO_2 structures, including anatase and rutile nanoparticles. The stability of this broad baseline EPR signal in our TiO_{2-x} was also tested by warming the UV-irradiated sample to room temperature and by observing that the signal remained stable for the first 30 minutes, and it completely decayed down only after 72 hours in the dark at room temperature.

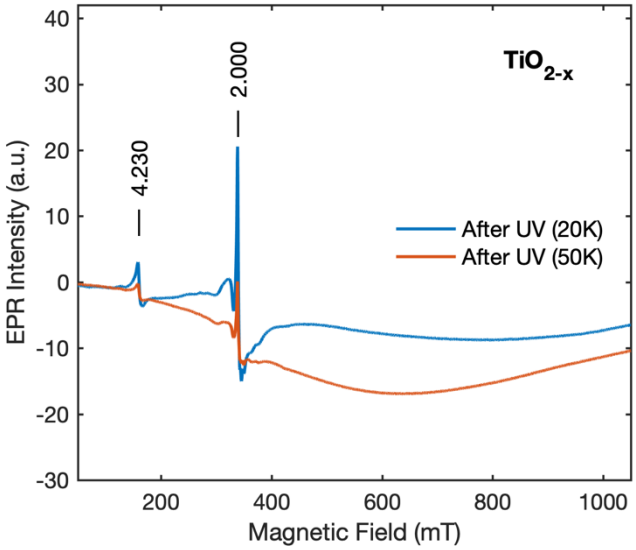

Figure 4.10. Broad field-range EPR spectra of TiO_{2-x} after UV irradiation, measured at two temperatures: 20 K (blue trace) and 50 K (red trace). The broad baseline signal spanning from 100 to 1100 mT is due to weakly-localized electrons/holes and their conductive coupling to electric microwave field through charge hopping and cyclotron motion.

Interestingly also, the TiO_{2-x} material shows unique blinking properties under exposure to slow electron beam during TEM imaging (**Figures 4.11** and Movies S1 and 4.13). This properties, which appeared initially to be due to charge-discharge processes, remain intact indefinitely as long as the sample is under electron beam. This is an unusual phenomenon, because most materials which charge/discharge during TEM imaging lose the charging property quickly and go dark. However, the TiO_{2-x} nanoparticles in TiO_{2-x}/PDMC light up and go dark under a beam of slow energy electron beams indefinitely. The lighting and darkening take places in 5-10 seconds

intervals and takes place in the same spots where were the TiO_{2-x} particles are observed. The carbon material remain to have the same feature during this time (see the movies, Movie S1 and 4.13).

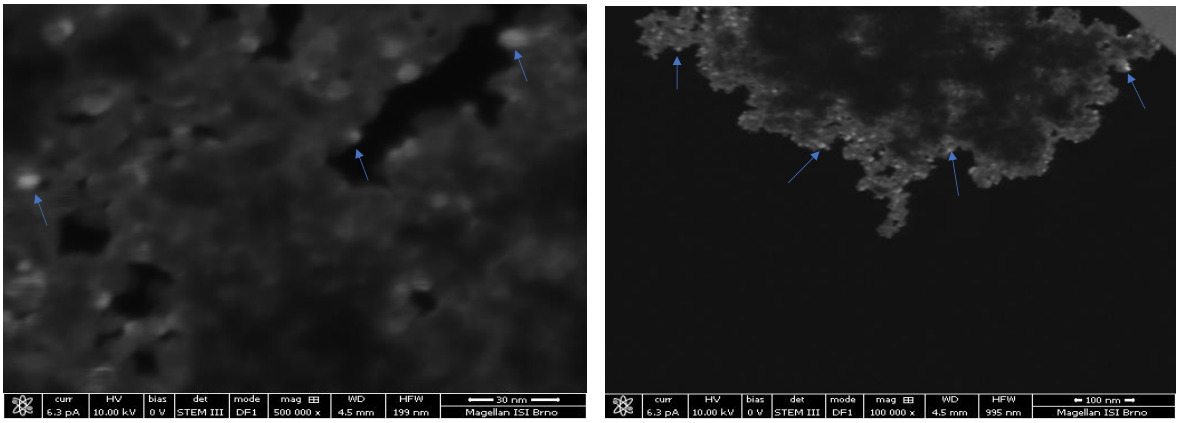

Figure 4.11. The lighting up of the TiO_{2-x} nanoparticles in TiO_{2-x}/PDMC under a beam of slow energy electrons in the dark field detector segment (to highlight the material contrast) in a high-resolution STEM at 10 keV. The lighter spots indicated by blue arrows are captured while the particles are lighting up under electron beam. Within 2-5 second, they go dark and come back again after another 10 seconds or more. They keep doing this as long as they are under electron beam. Usually, the charging effects induced by impacted electrons in insulators take μs to ms. For better viewing of this process, see the movie, Movie 1 and 2 included herein.

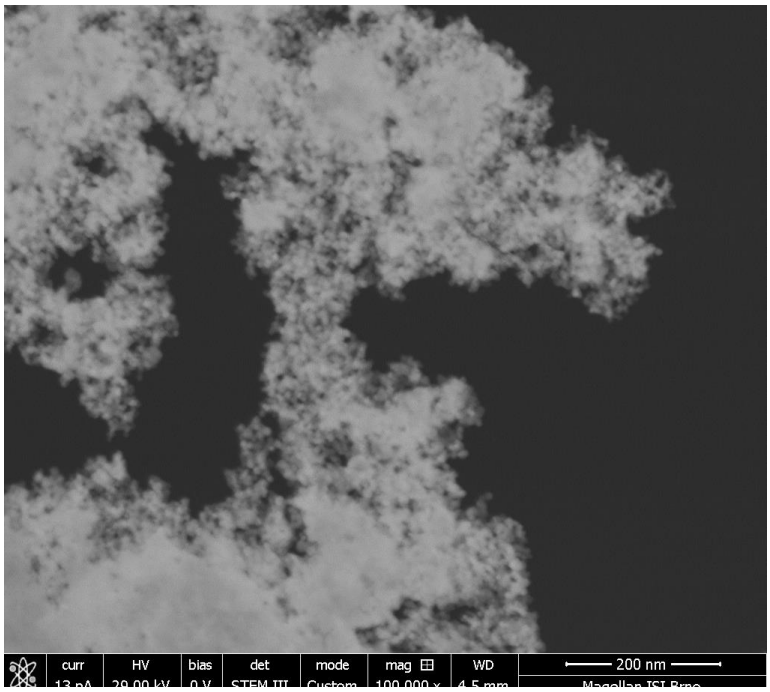

Figure 4.12. Dark field STEM image of TiO_{2-x} obtained using 29 KeV electron beams.

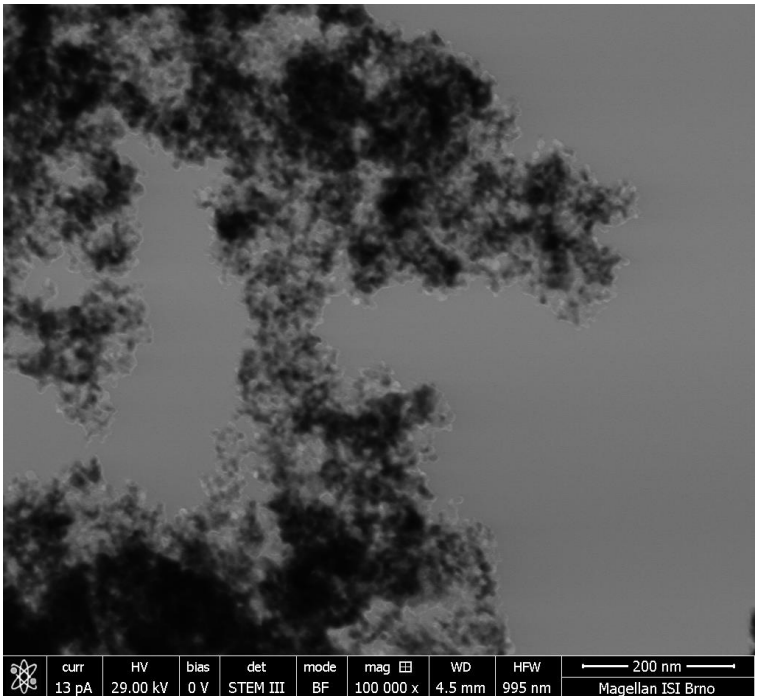

Figure 4.13. SEM image obtained using low energy electron beams (500 eV) of TiO_{2-x}.

Considering their high surface area, nanopores and nanocrystallites, as well as their unique optical properties, we had expected that these materials would photocatalyze various reactions. With this in mind, the photocatalytic properties of TiO_{2-x} as well as the control material TiO_2-(H+C) are investigated (**Figure 4.14**). The experimental set-up we used for the experiment is similar to the one in our previous reports.[29] As expected, no hydrocarbon products are detected in the reaction mixture in the absence of CO_2, even under irradiation of light and in the presence of the TiO_2 materials. However, in the presence of CO_2, H_2O and light, both materials yielded a hydrocarbon product (CH_4). The rate of production of CH_4 was 26.12 µmol h^{-1} g^{-1} and 14.75 µmol h^{-1} g^{-1} for TiO_{2-x} and TiO_2-(H+C), respectively. This result indicates that the photocatalytic performance is highly dependent on the materials. Since both materials possess similar surface area, porosity, phase composition, crystallinity and crystal size, the significantly enhanced photocatalytic activity of TiO_{2-x} can be most likely due to presence of high concentrations of oxygen vacancies and Ti^{3+} associated shallow electron traps, that can serve as photoelectron trapping sites and also as catalytical binding centers at the TiO_2 surface, thus enhancing the charge separation efficiency (as confirmed with our EPR results). The photocatalytic activity of the materials are compared with other recently reported materials (see **Table 4.2**). Their performances are comparable and better than many.

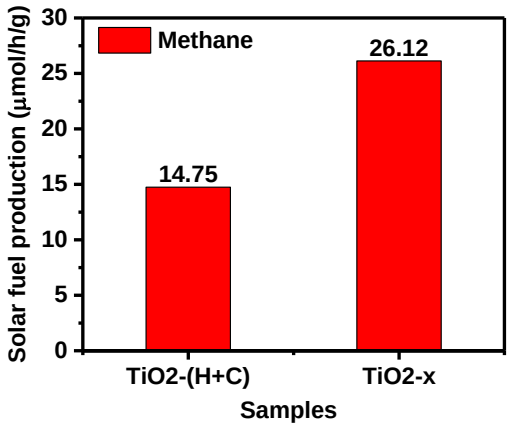

Figure 4.14. Rates of photocatalytic production of CH_4 from CO_2 and H_2O over TiO_2-(H+C) and TiO_{2-x}.

Table 4.2. Recent advances in photocatalytic systems for CO_2 reduction by TiO_2 based catalysts and comparisons of the performances of different notable catalysts with that our catalyst.

Photocatalyst	Light Source	Major Products	Yield (μmol h^{-1} g^{-1})	Refs
TiO_2 nanoparticles	8 W Hg lamp	CH_4, CH_3OH	*ca*. 0.4, 0.05	47
Fluorinated TiO_{2-x}	300W Xenon lamp with an AM 1.5 filter	CH_4	1.63	48
Pd_7Cu_1-loaded TiO_2	300 W Xenon lamp with a 400 nm short-wave-pass cutoff filter	CH_4	19.6	49
3 wt.% CuO-TiO_2 hollow sphere	40 W Hg UV lamp	CH_4	2.1	50
1.5 wt% Ag-TiO2	300 W Xenon lamp	CH_4	11.2	51
Au-Cu-TiO_2	1000 W Xe lamp	CH_4	44	52
N-doped TiO_2	Compact fluorescent integrated bulbs	CH_4	0.16	53
N-TiO_2	Full spectrum light irradiation	CH_3OH	20	54
45% CdS/TiO_2	Hg lamp	CH_4	*ca*. 0.5	55
TiO_{2-x}	**300 W Xenon lamp**	**CH_4**	**26.12**	**This work**

4.5. Conclusion

In summary, we have developed oxygen vacancy-rich, nanoporous TiO_{2-x} containing small anatase nanoparticles with high surface area using a polymer-derived mesoporous carbon (PDMC) as a template. The presence of PDMC template during the high temperature pyrolysis was found to be crucial for both maintaining the anatase phase and creating oxygen vacancies in the titania materials. The resulting material showed unusual photophysical and optical properties when it was interacting with light or electron beam. When they were within the PDMC template and under electron beam, the titania nanoparticles charged/discharged, lighting up and fading for as long us they were under the beam. After being extracted from the PDMC, TiO_{2-x} showed long-lived excitons and charge carriers that remained separated and stable many minutes after exposure to light, as observed with EPR studies. Both of these properties are unusual, and they have never been reported for TiO_2 nor for any other material, to the best of our knowledge. More importantly, these properties can be taken advantage of to use this material for various light-related applications, *e.g.*, photocatalysis and light harvesting for solar cells. To this end, we have demonstrated one photocatalytic experiment using this material as a photocatalyst. The TiO_{2-x} has been demonstrated to have efficient photocatalytic properties for reduction of CO_2 with H_2O under simulated solar light producing CH_4 with high rates.

4.6. Reference

1. Roduner, E. *Chem. Soc. Rev.,* **2006,** *35*, 583-592.

2. Guo, Y. G.; Hu, J. S.; Wan, L. J. *Adv. Mater*., **2008**, *20*, 2878-2887.

3. Gong, M.; Zhou, W.; Tsai, M.-C.; Zhou, J.; Guan, M.; Lin, M.-C.; Zhang, B.; Hu, Y.; Wang, D.-Y.; Yang, J.; Pennycook, S. J.; Hwang, B. J.; Dai, H., *Nat. Commun*., **2014**, *5*, 4695-4700.
4. Zaera, F., Chem. *Soc. Rev.,* **2013,** *42*, 2746-2762
5. Kumar, S. G.; Devi, L. G., J. *Phys. Chem.,* **2011**, 115, 13211-13241.
6. Sathish, M.; Viswanathan, B.; Viswanath, R. P.; Gopinath, C. S., *Chem. Mater.,* **2005**, 17, 6349-6353.
7. Fu, J.; Yu, J.; Jiang, C.; Cheng, B., *Adv. Energy. Mater*., **2018,** *8*, 1701503.
8. Meek, S. T.; Greathouse, J. A.; Allendorf, M. D., *Adv. Mater,* **2011,** *23*, 249-267.
9. Chen, X.; Selloni, A., *Chem. Rev.,* **2014**, *114*, 9281-9282.
10. Braun, J. H.; Baidins, A.; Marganski, R. E., *Prog. Org. Coat.,* **1992,** *20*, 105-138.
11. Banerjee, S.; Dionysiou, D. D.; Pillai, S. C., *Appl. Catal. B-Environ.,* **2015,** *176-177*, 396-428.
12. Zhou, J. J.; Wang, S. Y.; Gunasekaran, S., J. *Food Sci.,* **2009,** 74, N50-N56.
13. Xie, S.; Zhang, Q.; Liu, G.; Wang, Y., *Chem. Comm.,* **2016,** *52*, 35-59.
14. Ramesha, G. K.; Brennecke, J. F.; Kamat, P. V., *Acs. Catal.,* **2014,** *4*, 3249-3254.
15. Cheng, X.; Yu, X.; Xing, Z., *Appl. Surf. Sci.,* **2012,** 258, 3244-3248.
16. Kudo, A.; Miseki, Y., Chem. *Soc. Rev.* **2009,** *38*, 253-27.
17. Low, J.; Cheng, B.; Yu, J., *Appl. Surf, Sci.,* **2017,** *392*, 658-686.
18. Gordon, T. R.; Cargnello, M.; Paik, T.; Mangolini, F.; Weber, R. T.; Fornasiero, P.; Murray, C. B., *J. Am. Chem. Soc.,* **2012,** *134*, 6751-6761.
19. Adachi, K.; Ohta, K.; Mizuno, T., *Sol. Energy.,* **1994,** *53*, 187-190.
20. Xin, B.; Jing, L.; Ren, Z.; Wang, B.; Fu, H., *J. Phys. Chem. B.,* **2005,** *109*, 2805-2809.
21. Shuang, S.; Lv, R.; Xie, Z.; Zhang, Z., *Sci. Rep.* **2016**, 6, 26670.

22. Linsebigler, A.; Rusu, C.; Yates, J. T., J. *Am. Chem. Soc.,* **1996,** *118*, 5284-5289.

23. Bouras, P.; Stathatos, E.; Lianos, P., *Appl. Catal. B-Environ.,* **2007,** *73* (1), 51-59.

24. Pan, X.; Yang, M.-Q.; Fu, X.; Zhang, N.; Xu, Y.-J., *Nanoscale*, 2013, 5 (9), 3601-3614.

25. Choi, W.; Termin, A.; Hoffmann, M. R., *J. Phys. Chem. A.,* **1994,** *98* (51), 13669-13679.

26. Ni, M.; Leung, M. K. H.; Leung, D. Y. C.; Sumathy, K., *Renew. Sustain. Energy Rev.,* **2007,** *11*, 401-425.

27. Chu, J.; Sun, Y.; Han, X.; Zhang, B.; Du, Y.; Song, B.; Xu, P., *ACS Appl. Mater. Interfaces*., **2019,** *11*, 18475-18482.

28. Zhou, W.; Li, W.; Wang, J.-Q.; Qu, Y.; Yang, Y.; Xie, Y.; Zhang, K.; Wang, L.; Fu, H.; Zhao, D., *J. Am. Chem. Soc.,* **2014,** *136*, 9280-9283.

29. Zhang, T.; Low, J.; Koh, K.; Yu, J.; Asefa, T., *ACS Sustain. Chem. Eng.,* **2018,** *6*, 531-540.

30. Ola, O.; Maroto-Valer, M. M., *J. Photochem. Photobiol.,* **2015,** *24*, 16-42

31. Schultz, D. M.; Yoon, T. P., Science., **2014,** *343* , 1239176.

32. Asahi, R.; Morikawa, T.; Ohwaki, T.; Aoki, K.; Taga, Y., *Science* **2001,** *293*, 269.

33. Huang, X.; Zhou, L.-J.; Voiry, D.; Chhowalla, M.; Zou, X.; Asefa, T., *ACS Appl. Mater. Interfaces*., **2016**, *8*, 18891-18903.

34. Zhang, T.; Asefa, T., **2018**, *12* (3), 329-338.

35. Feng, N.; Liu, F.; Huang, M.; Zheng, A.; Wang, Q.; Chen, T.; Cao, G.; Xu, J.; Fan, J.; Deng, F., *Sci. Rep.,* **2016,** *6*, 34765.

36. Zhu, M.; Mi, Y.; Zhu, G.; Li, D.; Wang, Y.; Weng, Y., *J. Phys. Chem. C.,* **2013,** *117*, 18863-18869.

37. Asahi, R.; Morikawa, T.; Irie, H.; Ohwaki, T., *Chem. Rev.,* **2014,** *114*, 9824-9852.

38. De Angelis, F.; Di Valentin, C.; Fantacci, S.; Vittadini, A.; Selloni, A., *Chem. Rev.,* **2014,** *114*, 9708-9753.

39. Zhang, H.; F. Banfield, J., *J. Mater. Chem.,* 1998, *8*, 2073-2076.

40. Howe, R. F.; Gratzel, M., *J. Phys. Chem. A.,* **987,** *91*, 3906-3909.

41. Nakamura, I.; Negishi, N.; Kutsuna, S.; Ihara, T.; Sugihara, S.; Takeuchi, K., J. *Phys. Chem. A.,* **2000**, *161*, 205-212.

42. Di Valentin, C.; Pacchioni, G.; Selloni, A., *J. Phys. Chem. C.,* **2009,** *113*, 20543-20552.

43. Howe, R. F.; Gratzel, M., ., *J. Phys. Chem. A.,* **1985,** *89*, 4495-4499.

44. Sekiya, T.; Yagisawa, T.; Kamiya, N.; Das Mulmi, D.; Kurita, S.; Murakami, Y.; Kodaira, T., *J. Phys. Soc. Jpn.,* **2004,** *73*, 703-710.

45. Serwicka, E.; Schlierkamp, M. W.; Schindler, R. N., *Zeitschrift für Naturforschung A*, **1981**, *36*, 226-232

46. Jantsch, W.; Wilamowski, Z.; Wilamowski, Z.; Sandersfeld, N.; Schäffler, F., Phys. Status Solidi B, **1998,** *210*, 643-648.

47. Koci, K.; Obalova, L.; Matejova, L.; Placha, D.; Lacny, Z.; Jirkovsky, J.; Solcova. O., *Appl. Catal. B-Environ*., **2009**, *89*, 494-502.

48. Xing, M.; Zhou, Y.; Dong, C.; Cai, L.; Zeng, L.; Shen, B.; Pan, L.; Dong, C.; Chai, Y.; Zhang, J., Yin, Y., *Nano Lett.,* **2018**, *18*, 3384-3390.

49. Long, R.; Liu, Y.; Chen, S.; Zheng, X.; Gao, C.; He. C.; Chen, N.; Qi, Z.; Song, L.; Jiang, J.; Zhu, J.; Xiong, Y., *J. Am. Chem. Soc*., **2017**, *139*, 4486−4492.

50. Fang, B.; Xing, Y.; Bonakdarpour, A.; Zhang, S.; Wilkinson, D. P., *ACS Sustain. Chem. Eng.*, **2015**, *3*, 2381-2388.

51. Yu, B.; Zhou, Y.; Li, P.; Tu, W.; Li, P.; Tang, L.; Ye, J.; Zou, Z., *Nanoscale*, **2016**, *8*, 11870-11874.

52. Neatu, S.; Macia-Agullo, J. A.; Concepcion, P.; Garcia, H., *J. Am. Chem. Soc*., **2014**, *136*, 15969-15976.

53. Phongamwong, T.; Chareonpanich, M.; Limtrakul, J., *Appl. Catal. B-Environ*., **2015**, *168-169*, 114-124.

54. Michalkiewicz, B.; Majewska, J.; Kadziolka, G.; Bubacz, K.; Mozia, S.; Morawski, A. W., *J. CO_2 Util*., **2014**, *5*, 47-52.

55. Beigi, A. A.; Fatemi, S.; Salehi, Z., *J. CO_2 Util*., **2014**, *7*, 23-29.

Chapter 5

Copper Nanoparticles/Polyaniline-derived Mesoporous Carbon Electrocatalysts for Hydrazine Oxidation

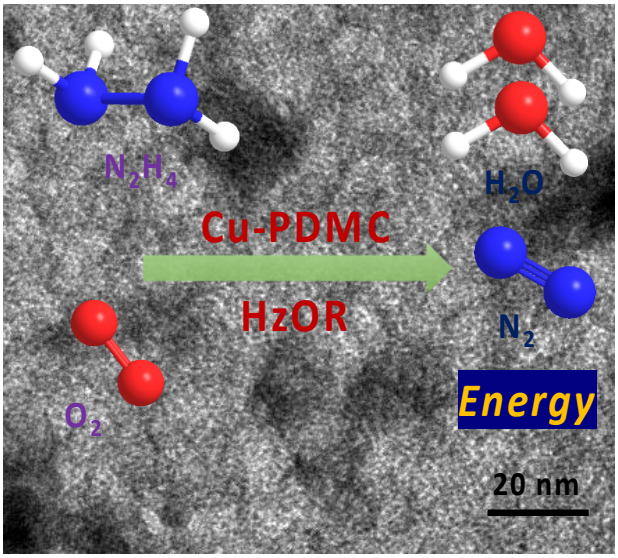

5.1. Overview

Copper nanoparticles-decorated polyaniline-derived mesoporous carbon (Cu-PDMC) that can serve as noble metal-free electrocatalyst for the hydrazine oxidation reaction (HzOR) is synthesized *via* a facile synthetic route. The material exhibits excellent electrocatalytic activity toward HzOR with low overpotential and high current density. The material also remains stable during the electrocatalytic reaction for long time. Its good electrocatalytic performance makes this material a promising alternative to conventional noble metal-based catalysts (*e.g.*, Pt) that are commonly used in HzOR-based fuel cells.

5.2. Introduction

Owing to the continued depletion of fossil fuels and the rapidly growing demand for alternative energy sources worldwide, direct liquid fuel cells, which can convert chemical energy sources (*e.g*., ethanol, methanol and hydrazine) into electrical energy, have been attracting considerable attention.[1-3] Among fuels that are applicable to and used in direct liquid fuel cells, hydrazine has some unique advantages, namely: it has high theoretical cell voltage, it produces high power density and it causes no greenhouse gas emission or harmful byproducts when used as a fuel in fuel cells.[2,4] However, to efficiently and sustainably convert chemical fuels such as hydrazine into electrical energy using direct liquid fuel cells, efficient, sustainable and inexpensive catalysts are required. Conversely, it is important to develop efficient, noble metal-free catalysts that can replace the less earth-abundant, precious metal-based catalysts that are currently used in hydrazine-based and other fuel cells.[5-9] Supporting the catalytically active metallic species onto suitable, high surface area porous materials can also render the metals larger accessible surface and thereby improved electrocatalytic activity per unit mass during their operations in fuel cells.[2,10,11]

Recently, our group reported the synthesis of heteroatom-doped mesoporous carbon nanoparticles with high porosity, large surface area, and good conductivity.[12-14] They were made via a facile, hard template-based synthetic route and using polymer/colloidal silica self-aggregates as precursor. We here show that the resulting nanoporous carbon material can be used as a good support material for Cu nanoparticles (Cu NPs) and we then demonstrate that the Cu NPs-loaded nanoporous carbon can effectively electrocatalyze HzOR. The electrocatalytic performance and stability of the material in the reaction are also investigated, and comparative results with respect

to the performances of other metal-based catalytic materials for HzOR reported in the literature are discussed.

5.3. Experimental Section

5.3.1. Materials, chemicals and reagents

Colloidal silica dispersion (Ludox HS-40, 40 wt. % suspension in water), aniline, ammonium persulfate, hydrochloric acid (37%), Nafion perfluorinated resin solution, 2-propanol, hydrazine monohydrate (98%), copper(II) nitrate hemi(pentahydrate) and phosphate buffer saline (10X PBS, pH 6.8) were obtained from Sigma-Aldrich. Sodium hydroxide was purchased from Fisher Scientific. All the chemicals and reagents were of analytical grade and used as received without further purification. Distilled water was used throughout the experiments.

5.3.2. Synthesis of polyaniline-derived mesoporous carbon (PDMC)

First, a nanocomposite material composed of polyaniline (PANI) and silica nanoparticles (PANI-SiO_2) was synthesized with oxidative polymerization of aniline in the presence of ammonium persulfate (oxidant) and colloidal silica templates.[12-13] Typically, colloidal silica (15 g or 11.5 mL) and aniline (1 mL or 10.5 mmol) were mixed with aqueous HCl solution (60 mL, 1 M). The solution was stirred in a temperature range between 0 and 5 °C for 10 min. Then, while still being stirred, aqueous HCl solution (12 mL, 1 M) containing ammonium persulfate (2.5 g or 11.0 mmol) was added drop-wise into the solution. After stirring it further for 8 h, the solution was centrifuged. The solid product was washed 3 times with water and ethanol, and then kept at 60 °C to dry. The resulting PANI-SiO_2 nanocomposite material was subjected to pyrolysis under argon atmosphere in a temperature-programmable tube furnace as follows. The temperature of the furnace was raised from 25 to 300 °C at a heating rate of 1 °C min^{-1} and kept at 300 °C for 3 h.

The temperature was then increased to 800 °C at a heating rate of 10 °C min^{-1} and kept at 800 °C for 2 h. After letting the furnace cool down to room temperature, the resulting black powdered product (270 mg) was taken out and treated with 1.0 M NaOH solution (18 mL) in an autoclave at 100 °C for 18 h to remove the silica templates in it. A solid product was recovered *via* filtration, washed with copious amount of water and then ethanol, and finally kept at 60 °C to dry. The resulting PANI-derived mesoporous N-doped carbon nanoparticles were denoted as PDMCs.

5.3.3. Synthesis of Cu NPs-Loaded PDMC (Cu-PDMC)

To generate PDMC-supported Cu NPs, 150 mg of PDMC was dispersed in a Cu(II) solution containing 54 mg $Cu(NO_3)_2 \cdot 2.5H_2O$ in distilled water (20 mL). The mixture was stirred for 4 h at room temperature and then kept at 100 °C to let the solvent evaporate. The resulting Cu(II)-loaded PDMC material was thermally treated under argon atmosphere as follows. The temperature was raised from room temperature to 100 °C at a ramp of 1 °C min^{-1} and kept at 100 °C for 1 h. The temperature was then raised from 100 to 250 °C at a ramp of 2 °C min^{-1} and kept at 250 °C for 1 h. Finally, it was let to cool down to room temperature. The resulting product, which was found to have *ca.* 7.5% Cu by weight, was denoted as Cu-PDMC.

5.3.4. Characterization

Transmission electron microscope (TEM) images of the materials were taken with a Topcon 002B TEM instrument operating at 200 kV. The surface areas and pore properties of the materials were determined by N_2 porosimetry (at -196 °C) using a Tristar-3000 instrument (Micromeritics, USA). Before each measurement, the samples were degassed at 80 °C for 8 h under a flow of N_2 gas to remove any possible gas impurities adsorbed on the samples' surfaces. Based on the adsorption-desorption data (isotherm), the surface areas were calculated with the

Brunauer-Emmett-Teller (BET) method and the pore size distributions and average pore sizes of the materials were determined by the Barrett-Joyner-Halenda (BJH) method. A linear fit of the adsorption isotherm data in the relative pressure range (P/P_0) of 0.05-0.3 was used for the surface area calculation. X-ray diffraction (XRD) patterns of the materials were obtained using a Philip XPert diffractometer operating with Cu Kα radiation as the X-ray source. The XRD diffraction patterns were recorded in a 2θ range between 15 and 80 ° with a step size (2θ) of 0.02° and a scan rate of 0.6° min^{-1}. Thermogravimetric analyses of the materials were conducted with a TGA7 instrument (PerkinElmer) at a heating rate of 10 °C min^{-1} under a flow of air at a rate of 20 mL min^{-1}. The surface chemical compositions of the materials were analyzed with a Thermo Scientific K-Alpha X-ray photoemission spectrometer (XPS) operating with Al Kα X-ray source ($h\nu$ = 1486.6 eV). For high resolution spectra of individual peaks, an energy resolution of 0.1 eV was employed for the scans. All the binding energies in the XPS spectra were calibrated using C1s peak (binding energy: 284.8 eV) associated with adventitious hydrocarbons present on the materials.

5.3.5. Electrochemical and electrocatalytic studies

5.3.5.1. Preparation of electrodes

The electrochemical and electrocatalytic properties of the materials toward HzOR were evaluated with a VersaSTAT 3 potentiostat (Princeton Applied Research, PAR) using a three-electrode electrochemical cell. The cell consisted of a saturated calomel electrode (SCE) as a reference electrode, a carbon rod (diameter: 6 mm) as a counter electrode, and a glassy carbon electrode (GCE, diameter: 3 mm) coated with the catalysts as a working electrode. To prepare the working electrode, 2 μL of a homogeneous suspension of catalyst (PDMC or Cu-PDMC) with a concentration of 10 g L^{-1} in 2-proponal was drop-casted onto the surface of a freshly polished GCE.

After letting the catalyst-coated GCE dry under ambient condition, 2 μL of Nafion solution (5% in 2-propanol) was drop-casted on the top of the electrode. The electrode was then dried completely under ambient condition, and it finally became ready to use for the tests.

5.3.5.2. Cyclic voltammetry and stability test

The cyclic voltammograms (CVs) of HzOR over the materials synthesized above were acquired and analyzed in a phosphate buffered saline (PBS) solution (0.1 M, pH 7.4). In the CV measurements, the potential was scanned from -0.6 to +0.6 V (*vs*. SCE) with different scan rates (ranging from 10 to 100 mV/s) and using different hydrazine concentrations (ranging from 10 to 100 mM). Before acquiring the cyclic voltammogram for it, the electrode was stabilized by chronoamperometrically running the electrocatalysis for 30 min. All the electrochemical measurements were carried out at room temperature and under ambient pressure. Furthermore, chronoamperometric measurement was performed over the material at a potential of 0 V (*vs*. SCE) in 50 mM hydrazine in 0.1 M PBS solution. Additionally, the CV of HzOR in 50 mM hydrazine over the Cu-PDMC after being used in chronoamperometric test was measured in 0.1 M PBS.

5.4. Results and Discussion

The synthetic procedure used to make Cu-PDMC consisted of three steps, as illustrated in **Scheme 5.1**. First, PANI-silica composite material was synthesized by *in-situ* polymerization of aniline in the presence of 12 nm-sized colloidal silica nanoparticles (templates). The resulting material was pyrolyzed under argon atmosphere at 300 °C for 3 h, and then at 800 °C for 2 h. The carbonized product was treated with aqueous NaOH solution to remove the silica templates in it or to produce the PANI-derived mesoporous carbon (PDMC). Finally, the PDMC was immobilized with Cu(II) ions, and the Cu(II)-PDMC was pyrolyzed at 250 °C for 1 h to produce

Cu-PDMC. Since PDMC inherently contain N dopants or moieties,[12,13] a large amount of Cu(II) ions could easily be immobilized into PDMC by the virtue of the favorable interactions between N moieties and Cu(II) ions. As a result, a large amount of Cu NPs could be produced in the material

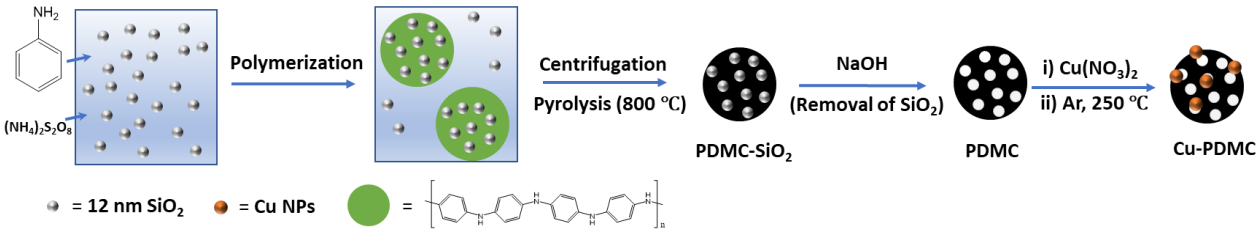

Scheme 5.1. Schematic illustration of the synthetic procedure applied to make polyaniline (PANI)-derived mesoporous carbon-supported Cu NPs (Cu-PDMC) material.

The structures of PDMC and Cu-PDMC were examined with transmission electron microscope (TEM). The PDMC material showed nanoporous structure with an average pore size of *ca*. 11 nm (**Figure. 5.1a** and **Figure 5.1b**), suggesting that the colloidal silica nanoparticles successfully served as templates and helped create the porous structure inside the material. In the corresponding images of Cu-PDMC, dark spots corresponding to Cu NPs were additionally observed (**Figure. 5.1c**). This suggested that Cu NPs were successfully formed or present in Cu-PDMC. From the HRTEM image (**Figure 5.1d**), the lattice fringes were found to have an interplanar spacing of 0.21 nm, which corresponds to the (111) lattice plane of metallic copper.[15]

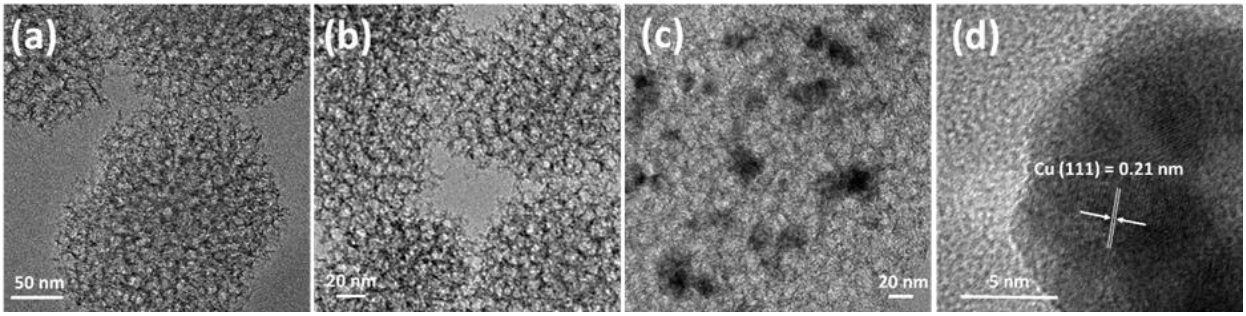

Figure 5.1. TEM images of (a, b) PDMC and (c) Cu-PDMC. (d) HRTEM image of Cu-PDMC.

N_2 porosimetry was used to investigate if and how the synthesis of Cu NPs within the pores of PDMC could affect the surface areas and the pore structures of the material (**Figure. 5.2a** and **Figure 5.2b**). The N_2 adsorption/desorption isotherm of PDMC was found to be type IV with type H2 hysteresis loop, which is characteristic of mesoporous materials. The BET surface area of the material was found to be 712 m^2/g and its BJH pore size distribution was centered at *ca*. 10.6 nm, which is comparable to the size of colloidal silica nanoparticles used as templates for the synthesis of the materials. Just like PDMC, the N_2 adsorption/desorption isotherm of Cu-PDMC was also type IV with type H2 hysteresis loop. The surface area and pore size of Cu-PDMC were slightly lower (695 m^2/g and 9.7 nm, respectively) compared with those of PDMC, indirectly indicating that some of the Cu NPs were formed/present within PDMC's pore structure. This result was further corroborated by TEM (Fig. 1c), which showed the presence of Cu NPs within the structures of Cu-PDMC. Quantitative results of N_2 porosimetry analyses of both materials are compiled in **Table 5.1**.

Table 5.1. Structural properties of PDMC and Cu-PDMC.[a]

Material	**BET surface area /(m^2/g)**	**Average pore size /(nm)**	**Pore volume /(cm^3/g)**
PDMC	712	10.6	1.33
Cu-PDMC	695	9.7	1.24

[a] Calculated based on the data in the adsorption branch of N_2 adsorption/desorption isotherms.

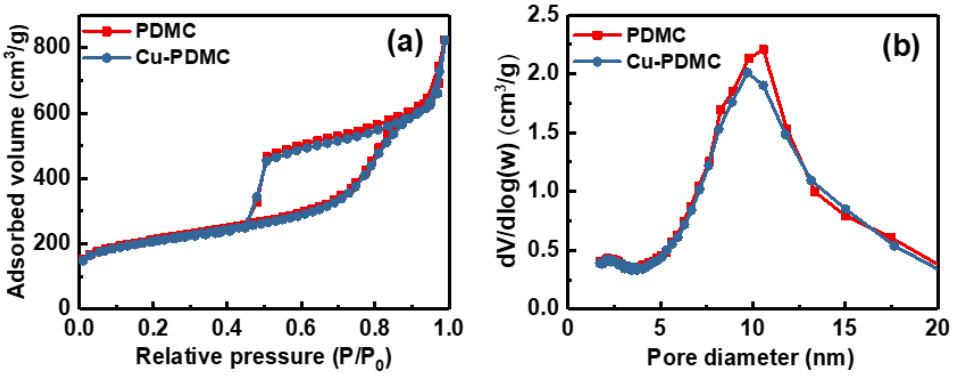

Figure 5.2. (a) N_2 adsorption/desorption isotherms of PDMC and Cu-PDMC and (b) their corresponding pore size distributions.

The crystal phases and structures of the materials were identified with X-ray diffraction (XRD) (Figure. 5.3). The XRD patterns of PDMC displayed a broad diffraction peak at 2θ of 24°, which could be ascribed to the (002) crystalline lattice of graphitic (sp^2-hybridized) carbon.[12,16] The XRD patterns of Cu-PDMC showed an additional peak centered at 2θ of 43.4°, corresponding the (111) plane of the face-centered cubic (fcc) lattice of metallic Cu (JCPDS: 04-0836).[17-19] No characteristic diffraction peaks associated with Cu_2O and CuO were seen in the XRD patterns. Overall, the XRD results revealed that metallic Cu was the predominant Cu species in the Cu-PDMC material. Metallic Cu was formed in the material because the PDMC forming during pyrolysis can reduce the Cu(II) species loaded in PDMC through the reactions shown in Eqs. (1) and (2) below.[20-23]

$$2Cu(NO_3)_2 \xrightarrow{\Delta} 2CuO + 4NO_2 + O_2 \quad (1)$$

$$2CuO + C \xrightarrow{\Delta} 2Cu + CO_2 \quad (2)$$

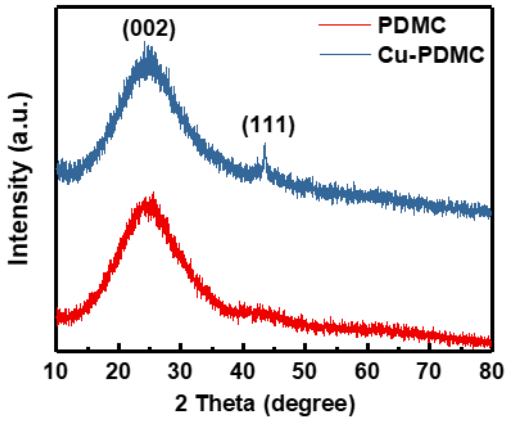

Figure 5.3. XRD patterns of PDMC and Cu-PDMC.

The surface chemical composition of Cu-PDMC was studied using X-ray photoelectron spectroscopy (XPS). The XPS survey spectrum showed the presence of C, N, O and Cu in the material (**Figure. 5.4a**). To determine the chemical states with which these different elements exist in the materials, the N 1s, C 1s and Cu 2p peaks were further analyzed by high-resolution XPS (**Figure. 5.4b-d**). The N 1s peak in the spectrum was deconvoluted into four distinct peaks with different binding energy values of 398.3, 400.1, 400.9 and 403.5 eV, corresponding to pyridinic-N, pyrrolic-N, quaternary-N and pyridinic N^{+}-O^{-} species, respectively.[12,13,24] The presence of nitrogen dopants in the material could be further seen in the deconvoluted C 1s peak (**see Figure. 5.4c**).[13,25] The oxidation state of Cu was determined based on the positions of the Cu $2p_{3/2}$ and Cu $2p_{1/2}$ peaks.[16,26-28] Two peaks at binding energies of *ca*. 932.3 and 952.1 eV, which correspond to Cu $2P_{3/2}$ and Cu $2p_{1/2}$ of Cu^{0} and/or Cu^{1+}, respectively, were observed. Two additional small peaks (Cu $2p_{3/2}$ at 934 eV and Cu $2p_{1/2}$ at 952 eV), along with the characteristic satellite peaks (at 940.1 eV and 943.6 eV) corresponding to Cu^{2+} species, were also seen. The appearance of Cu^{2+} signal is most likely associated with the oxidation of Cu^{0} to Cu^{2+} during the exposure of the surface of Cu NPs to air or humidity.[29,30] On the basis of the XPS peaks of Cu 2p, coupled with the TEM and

XRD results discussed earlier, which indicated the existence of Cu^0, it was clear that Cu^0 was the dominant Cu species in Cu-PDMC material.

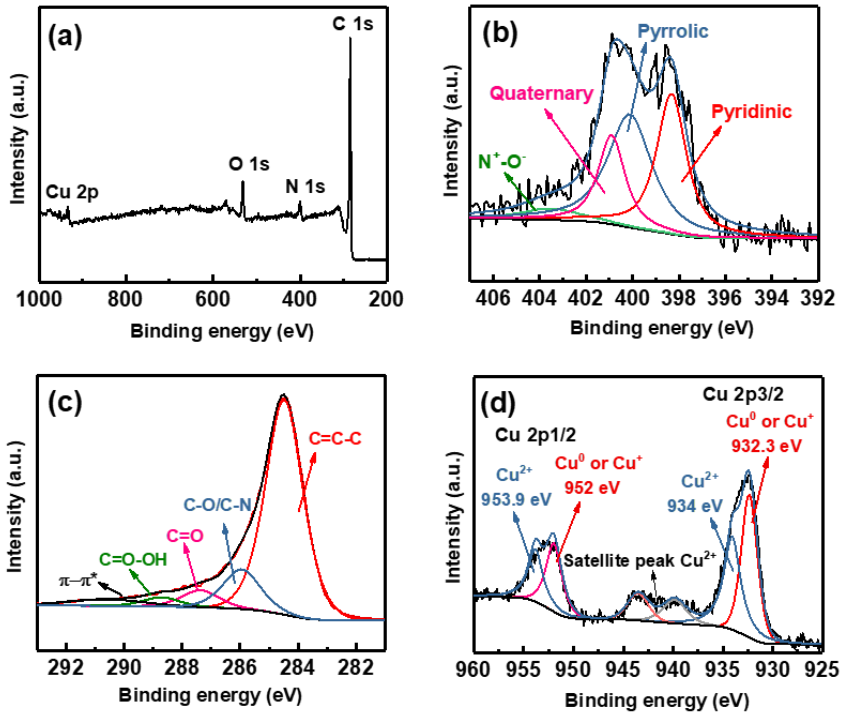

Figure 5.4. (a) XPS survey spectra of Cu-PDMC. High-resolution XPS spectra of (b) N 1s peak, (c) C 1s peak and (d) Cu 2p peak of Cu-PDMC.

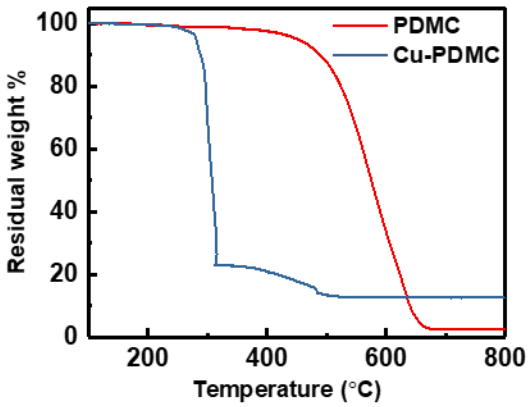

Figure. 5.5. TGA curves obtained under air for PDMC and Cu-PDMC materials.

By comparing the weight of the residue after TGA in air of Cu-PDMC with that of PDMC, the amount of Cu NPs in PDMC was estimated (**Figure. 5.5**). While PDMC gave *ca*. 2.6 wt. % residue, which is due to the residual silica templates, Cu-PDMC gave *ca*. 12.6 wt. % residue, which is largely due to CuO as the PDMC should be lost in form of CO_2 during calcination. Based on these, the amount of Cu NPs in Cu-PDMC was determined to be *ca*. 7.5 wt. %. The TGA results also indirectly corroborated that Cu NPswere successfully loaded in Cu-PDMC. It is worth adding that the presence of Cu NPs was found to facilitate the material's thermal decomposition. While the decomposition of PDMC started at *ca*. 450 °C and completed at *ca*. 650 °C, the initial and final decomposition temperatures of PDMC decreased by *ca*. 150 °C in the presence of Cu NPs (*i.e*., in the case of Cu-PDMC). This is because Cu NPs help the transfer of heat to PDMC in Cu-PDMC and promote the oxidation/combustion of the carbon material.[31-33]

To evaluate the electrocatalytic performance of PDMC and Cu-PDMC for HzOR, cyclic voltammograms (CVs) over the materials in the presence of 50 mM hydrazine solution in PBS (pH 7.4) at a scan rate of 10 mV s^{-1} were first recorded, and the results were compared with one another (**Figure. 5.6**). In the presence of 50 mM hydrazine, PDMC showed a peak at *ca*. 0.18 V vs. saturated calomel electrode (SCE), indicating that the material had electrocatalytic activity toward HzOR. Cu-PDMC did this too, but its onset and peak potentials shifted to negative values compared with those of PDMC. The onset potential of HzOR reaction over Cu-PDMC was found to be -0.31 V *vs*. SCE, which was much lower than that over PDMC (E = -0.15 V), and its peak potential was found to be at 0.04 V vs. SCE. In other words, Cu-PDMC required a much lower overpotential to realize the same level of catalytic activity toward HzOR than PDMC did. This indicates that Cu-PDMC has higher and better electrocatalytic activity toward HzOR compared with PDMC. Additionally, the peak current density during HzOR (2.45 mA cm^{-2}) over Cu-PDMC

was higher than the one over PDMC, whose corresponding value was only 1.54 mA cm^{-2}. The above results clearly demonstrate that Cu-PDMC shows a much higher electrocatalytic activity for HzOR than PDMC does.[1,34,35] In fact, Cu-PDMC's electrocatalytic activity toward HzOR is comparable with those of many recently reported metal-based electrocatalysts (see **Table 5.2**). Considering Cu-PDMC's superior electrocatalytic performance, the remaining studies were carried out only for Cu-PDMC.

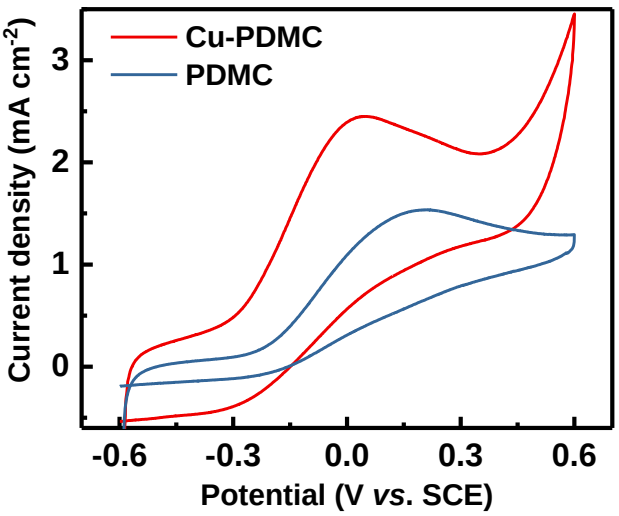

Figure 5.6. Cyclic voltammograms of HzOR over PDMC and Cu-PDMC materials obtained using 50 mM hydrazine in PBS (pH 7.4) at a scan rate of 10 mV s^{-1}.

Table 5.2. Comparison of the electrocatalytic activity toward HzOR of different metal-based electrocatalysts.

Electrocatalyst	**Reaction medium**	**Scan rate /(mV s^{-1})**	**[NH_4] /(mM)**	**Onset/Peak potential /(V *vs.* SCE)[a]**	**Reference**
Cu-GP	0.1 M KOH	100	10	-0.1/0.3	34
S-RGO/Cu	0.1 M KOH	100	10	NA/0.26	35
Flower-shaped CuO	0.1 M KOH	50	100	-0.18/NA	36
Cu (hydr)oxide/Cu electrode	0.1 M NaOH	50	10	NA/0.21	37
Cu metal electrode	1 M NaOH	20	5 wt.%	-0.87/NA	38
CeO_2-RGO	3 M NaOH	50	22	0.1/0.5	39
Ag/CFC	1 M KOH	10	20	-0.54/-0.24	40
Au/TiO_2-NTs/Ti	0.1 M PBS	100	0.85	-0.1/0.24	41
Pd/C	0.05 M H_2SO_4	20	10	-0.05/0.1	42
Nanoporous gold	0.1 M PBS	20	10	-0.4/NA	43
AuPd DANCs	0.1 M $HClO_4$	50	10	-0.11/0.1	44
Cu-PDMC	**0.1 M PBS**	**10**	**50**	**-0.31/0.04**	**This work**

[a] NA means not available.

The CVs of HzOR over Cu-PDMC at different concentrations of hydrazine (ranging from 10 mM to 100 mM) were then acquired. The shapes of the CV curves showed only oxidation peaks and no cathodic peaks (during the reverse scan), demonstrating that hydrazine is oxidized irreversibly (**Figure 5.7a**).[1] Furthermore, a linear relationship between peak current density and hydrazine concentration was observed (**Figure 5.7b**).

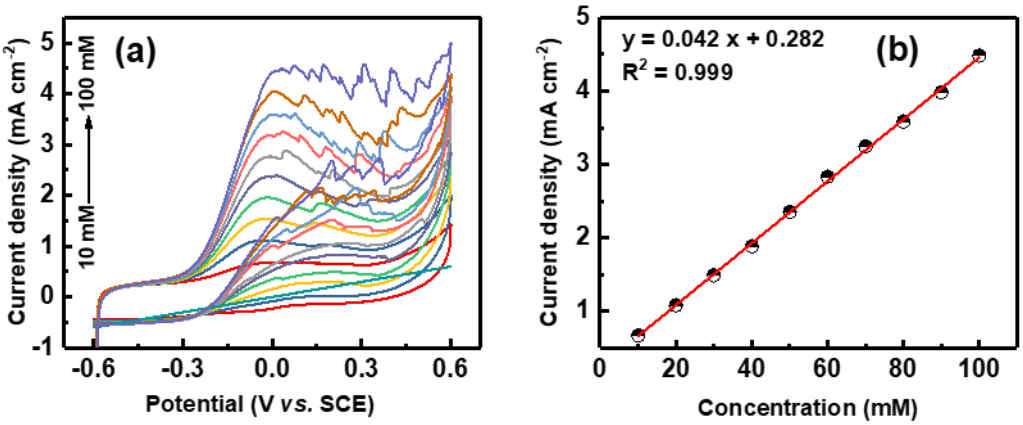

Figure 5.7 (a) Cyclic voltammograms (CVs) of HzOR obtained for different hydrazine concentrations at a scan rate of 10 mV s^{-1} in a 0.1 M PBS solution (pH 7.4) over Cu-PDMC and (b) the linear dependence of current density of HzOR with respect to the concentration of hydrazine.

The electron transfer number (n) involved in HzOR over the catalysts was determined from the slope of the linear plot of current density (I/A) versus square root of scan rate ($v^{1/2}$) using the equation:

$$\mathrm{I}/A = 3.01 \times 10^{-5} n[(1-\alpha)n_\alpha]^{1/2} c D^{-1/2} v^{1/2} \quad (3)$$

where I is current, A is the surface area of the working electrode ($A = 0.071$ cm^2), n is the total number of electrons involved in the oxidation of hydrazine, n_α is the number of electrons involved in the rate-determining step ($n_\alpha = 1$), c is the concentration of hydrazine ($c = 50$ mM), and v is the scan rate. The electron transfer coefficient (α) can be determined from the linear relationship between peak potential (E_p) and the natural logarithm of scan rate ($\log(v)$) using the equation:

$$E_p = k + [0.03/\alpha n_\alpha] \log v \quad (4)$$

where k is a constant and $n_\alpha = 1$.

The diffusion coefficient (D) was determined based on the linear correlation between current density (I/A) and inverse square root of time ($t^{-1/2}$) and using the Cottrell equation [2,4]:

$$I/A = nFCD^{1/2}\pi^{-1/2}t^{-1/2} \quad (5)$$

where F is Faraday constant ($F = 96496$ C mol^{-1}).

Next, the CVs of HzOR over Cu-PDMC at different scan rates were obtained. Increasing the scan rate ($\log v$) led to more positive peak potential value (E_p) for the reaction (**Figure 5.8a**). Current density (I/A) was found to vary linearly with square root of scan rate ($v^{1/2}$), suggesting a typical diffusion-controlled electrochemical process (**Figure 5.8b**).[3,34,35] Furthermore, a linear relationship between E_p and $\log v$ was observed (**Figure 5.8c**). The total number of electrons (n) involved in the reaction was calculated using equations (3) - (5) above and found to be 4.05, demonstrating that the anodic oxidation of hydrazine over Cu-PDMC proceeded through a four-electron process or *via* complete oxidation to dinitrogen (N_2) and water. Accordingly, the net reaction for the reaction can be written as: $N_2H_4 + 4OH^- \rightarrow N_2 + 4H_2O + 4e^-$.

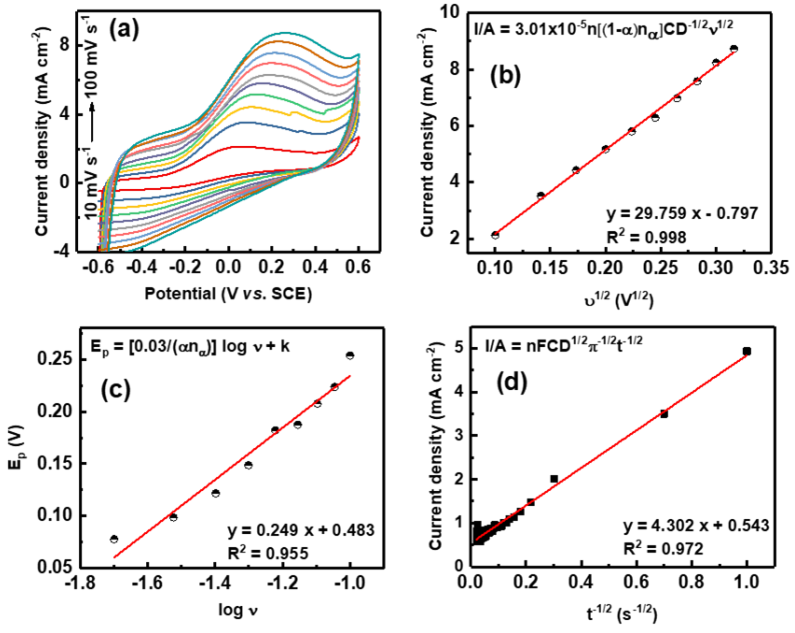

Figure 5.8 Electrochemical analysis used to determine the electron transfer number of HzOR over Cu-PDMC material. (a) Cyclic voltammograms of HzOR obtained with 50 mM hydrazine in a 0.1 M PBS solution (pH 7.4) at different scan rates, (b) the linear dependence of current density (I/A) *vs.* square root of scan rate $(v^{1/2})$, (c) the linear dependence of peak potential (E_p) *vs.* log of scan rate $(\log v)$, and d) a plot of current density (I/A) *vs.* square root of time $(t^{-1/2})$ obtained from chronoamperometric analysis.

The long-term stability of a catalyst is crucial for its use in fuel cells. Thus, the stability of Cu-PDMC during electrocatalysis of HzOR was evaluated by monitoring the possible change in current density (I/A) in successive detection of 50 mM hydrazine at its near-peak potentials (0 V *vs.* SCE) for 8500 s (the bubbles forming on the working electrode were removed between each scans) (**Figure 5.9**). The chronoamperometry analysis showed that there was no significant change in the current density after running the reaction for 8500 s, indicating the high stability of Cu-PDMC as electrocatlayst during HzOR. Furthermore, the performance of Cu-PDMC was checked after being used in chronoamperometric test, it showed only a very slight loss in catalytic activity (**Figure 5.10**). This corroborates its stability during the electocatalytic HzOR.

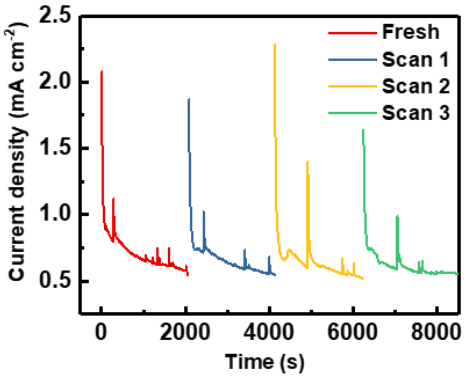

Figure 5.9 Chronoamperometric stability test of Cu-PDMC in 50 mM hydrazine in a 0.1 M PBS solution (pH 7.4) during electrocatalytic HzOR.

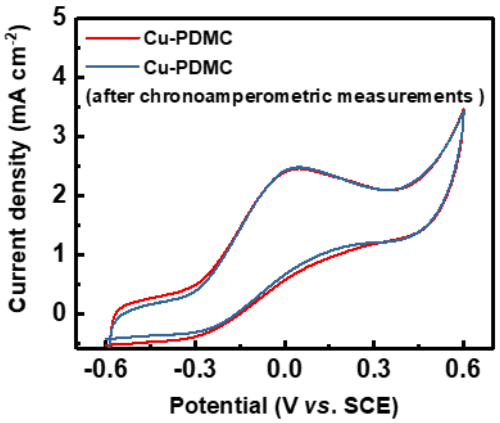

Figure 5.10 Cyclic voltammograms of HzOR obtained with a scan rate of 10 mV s^{-1} in 50 mM hydrazine in PBS (pH 7.4) over Cu-PDMC material before and after being used in a chronoamperometric test.

5.5. Conclusions

In summary, Cu nanoparticles-loaded polymer-derived mesoporous carbon (Cu-PDMC) that shows very good electrocatalytic activity for HzOR has been successfully synthesized. The inclusion of Cu nanoparticles into nanoporous carbon has been found to reduce the overpotential and increase the current density of the reaction. The resulting material has the potential to serve as non-noble metal-based electrocatalyst for HzOR, and the synthetic method can be extended for the development of other non-noble metal-based electrocatalysts for HzOR and other reactions.

5.6. Reference

1. Cazetta, A. L.; Zhang, T.; Silva, T. L.; Almeida, V. C.; Asefa, T. *Appl. Catal. B: Environ.*, **2018**, *225*, 30-39.
2. Martins, A. C.; Huang, X.; Goswami, A.; Koh, K.; Meng, Y.; Almeida, V. C.; Asefa, T. *Carbon*, **2016**, *102*, 97-105.
3. Koh, K.; Meng, Y.; Huang, X.; Zou, X.; Chhowalla, M.; Asefa, T. *Chem. Commun.*, **2016**, *52*, 13588-13591.
4. Meng, Y.; Zou, X.; Huang, X.; Goswami, A.; Liu, Z.; Asefa, T. *Adv. Mater*., **2014**, *26*, 6510-6516.
5. Huang, J.; Zhao, S.; Chen, W.; Zhou, Y.; Yang, X.; Zhu, Y.; Li, C. *Nanoscale*, **2016**, *8*, 5810-5814.
6. Yu, D.; Wei, L.; Jiang, W.; Wang, H.; Sun, B.; Zhang, Q.; Goh, K.; Si, R.; Chen, Y. *Nanoscale*, **2013**, *5*, 3457-3464.
7. Ma, Y.; Li, H.; Wang, R.; Wang, H.; Lv, W.; Ji, S. *J. Power Sources*, **2015**, *289*, 22-25.
8. Yang, G. W.; Gao, G. Y.; Wang, C.; Xu, C. L.; Li, H. L. *Carbon*, **2008**, *46*, 747-752.
9. Asefa, T. *Acc. Chem. Res*., **2016**, *49*, 1873-1883.
10. White, R. J.; Luque, R.; Budarin, V. L.; Clark, J. H.; Macquarrie, D. J. *Chem. Soc. Rev.*, **2009**, *38*, 481-494.
11. Wildgoose, G. G.; Banks, C. E. *Small*, **2006** *2*, 182-193.
12. Huang, X.; Zhou, L. J.; Voiry, D.; Chhowalla, M.; Zou, X.; Asefa, T. *ACS Appl. Mater. Inter.*, **2016**, *8*, 18891-18903.
13. Koh, K.; Jeon, M.; Chevrier, D. M.; Zhang, P.; Yoon, C. W.; Asefa, T. *Appl. Catal. B: Environ.*, **2017**, *203*, 820-828.
14. Meng, Y.; Voiry, D.; Goswami, A.; Zou, X.; Huang, X.; Chhowalla, M.; Liu, Z.; Asefa, T. *J. Am. Chem. Soc*., **2014**, *136*, 13554-13557.
15. Zhang, Q.; Qin, Z.; Wu, Z.; Liu, L.; Shen, B.; Hu, W. *Sci. Rep*., **2017**, *7*, 1338-1349.
16. Chaudhari, N. K.; Song, M. Y.; Yu, J. S. *Sci. Rep*., **2014**, *4*, 5221-5230.
17. Zhang, T.; Low, J.; Huang, X.; Al-Sharab, J. F.; Yu, J.; Asefa, T. *ChemCatChem*, **2017**, *9*, 3054-3062.

18. Sugano, Y.; Shiraishi, Y.; Tsukamoto, D.; Ichikawa, S.; Tanaka, S.; Hirai, T. *Angew. Chem. Int. Ed*., **2013**, *52*, 5295-5299.
19. Jiang, D.; Liu, Q.; Wang, K.; Qian, J.; Dong, X.; Yang, Z.; Du, X.; Qiu, B. *Biosens. Bioelectron*., **2014**, *54*, 273-278.
20. Ryu, S. K.; Lee, W. K.; Park, S. J. *Carbon Sci.*, **2004**, *5*, 180-185.
21. Bhaduri, B.; Verma, N. *J. Colloid Interface Sci*., **2015**, *457*, 62-71.
22. Shiota, K.; Matsunaga, H.; Miyake, A. *J. Therm. Anal. Calorim*., **2015**, *121*, 281-286.
23. Morales, M. V.; Asedegbega-Nieto, E.; Bachiller-Baeza, B.; Cuerrero-Ruiz, A. *Carbon*, **2016**, *102*, 426-436.
24. Pels, J. R.; Kapteijn, F.; Moulijn, J. A.; Zhu, Q.; Thomas, K. M. *Carbon*, **1995**, *33*, 1641-1653.
25. Matter, P. H.; Zhang, L.; Ozkan, U. S. *J. Catal.*, **2006**, *239*, 83-96.
26. Colón, G.; Maicu, M.; Hidalgo, J. A.; Navío, J. A. *Appl. Catal. B: Environ.*, **2006**, *67*, 41-51.
27. Liu, L.; Gao, F.; Zhao, H.; Li, Y. *Appl. Catal. B: Environ.*, **2013**, *134-135*, 349-358.
28. Ola, O.; Maroto-Valer, M. M. Catal. Sci. Technol., **2014**, *4*, 1631-1637.
29. Qin, L.; Xu, H.; Zhu, K.; Kang, S. Z.; Li, G.; Li, X. *Catal. Lett*., **2017**, *147*, 1315-1321.
30. Park, B. K.; Jeong, S.; Kim, D.; Moon, J.; Lim, S.; Kim, J. S. *J. Colloid Interface Sci.*, **2007**, *311*, 417-424.
31. Fard, A. K.; Rhadfi, T.; Mckay, G.; Al-marri, M.; Abdala, A.; Hilal, N.; Hussien, M. A. *Chem. Eng. J.*, **2016**, *293*, 90-101.
32. Xiong, H.; Moyo, M.; Motchelaho, M. A.; Tetana, Z. N.; Dube, S. M. A.; Jewell, L. L.; Covile, N. *J. Catal.*, **2014**, *311*, 80-87.
33. Zou, X.; Silva, R.; Goswami, A.; Asefa, T. *Appl. Surf. Sci.*, **2015**, *357*, 221-228.
34. Gao, H.; Wang, Y.; Xiao, F.; Ching, C. B.; Duan, H. *J. Phys. Chem. C*, **2012**, *116*, 7719-7725.
35. Liu, C.; Zhang, H.; Tang, Y.; Luo, S. *J. Mater. Chem. A*, **2014**, *2*, 4580-4587.
36. Ma, Y.; Wang, H.; Key, J.; Ji, S.; Lv, W.; Wang, R. *J. Power Sources*, **2015**, *300*, 344-350.
37. Karim-Nezhad, G.; Jafarloo, R.; Dorraji, P. S. *Electrochim. Acta*, **2009**, *54*, 5721-5726.
38. Asazawa, K.; Yamada, K.; Tanaka, H.; Taniguchi, M,; Oguro, K. *J. Power Sources*, **2009**, *191*, 362-365.
39. Srivastava, M.; Das, A. K.; Khanra, P.; Uddin, M. E.; Kim, N. H.; Lee, J. H. *J. Mater. Chem. A*, **2013**, *1*, 9792-9801.

40. Liu, R.; Ye, K.; Gao, Y.; Zhang, W.; Wang, G.; Gao, D. *Electrochim. Acta*., **2015**, *186*, 239-244.
41. Hosseini, M.; Momeni, M. M.; Faraji, M. *J. Mol*. *Catal. A: Chem.*, **2011**, *335*, 199-204.
42. Liang, Y.; Zhou, Y.; Ma, J.; Zhao, J.; Chen, Y.; Tang, Y.; Lu, T. *Appl. Catal. B: Environ.*, **2011**, *103*, 388-396.
43. Yan, X.; Meng, F.; Cui, S.; Liu, J.; Gu, J.; Zou, Z. *J. Electroanal. Chem.*, **2011**, *661*: 44-48.
44. Chen, L. X.; Jiang, L. Y.; Wang, A. J.; Chen, Q. Y.; Feng, J. J. *Electrochim. Acta*, **2016**, *190*, 872-878.

Chapter 6

Mesoporous Graphitic Carbon Nitrides Decorated with Cu Nanoparticles: Efficient Photocatalysts for Degradation of Tartrazine Yellow Dye

6.1. Overview

A series of mesoporous graphitic carbon nitride (mpg-C_3N_4) materials are synthesized by directly pyrolyzing melamine in the presence of different colloidal silica nanoparticles serving as hard templates, and then etching the silica templates from the carbonized products. The mass ratio of melamine-to-silica templates and the size of the silica nanoparticles are found to dictate whether or not mpg-C_3N_4 with large surface area and desirable, high porosity form. The surfaces of the mpg-C_3N_4 materials are then decorated with copper (Cu) nanoparticles, producing Cu-decorated mpg-C_3N_4 composite materials that show excellent photocatalytic activity for degradation of tartrazine yellow dye. Their excellent photocatalytic performance is attributed to the high surface area of the mpg-C_3N_4 and the catalytically relevant synergistic effects created by mpg-C_3N_4 and Cu nanoparticles, including the Cu nanoparticles' greater ability to separate photogenerated charge carriers. This work has been published in *Nanomaterials* (Reproduced with permission from *Nanomaterials* **2018**, *8*, 636. https://doi.org/10.3390/nano8090636).

6.2. Introduction

The fast-growing global economy is currently accompanied by various environmental pollutants, which have been causing serious threats to society's well-being and the development of sustainable future.[1] So, there is no question that these pollutants must be tackled to overcome

their many undesirable consequences. Among many remediation strategies to address environmental pollutants, semiconductor-based solar photocatalysis, which utilizes the abundant solar energy to decompose environmentally polluting organic and inorganic species via various light induced redox reactions over semiconductor materials, is quite promising.[2] Many semiconducting materials, such as TiO_2, ZnO, and SnO_2, have been extensively studied for these purposes. However, their large band gap energy hinders the absorption of visible light, resulting in inefficient utilization of solar energy to photocatalyze reactions over these materials.

Graphitic carbon nitride (g-C_3N_4), a low-cost metal-free polymeric semiconductor with great thermal and chemical stability and good electronic structure and light sensitivity that are suited for visible light photocatalysis, has recently emerged as a promising material for various solar-based pollutant photodegradation applications and stimulated intensive research works.[2,3] However, pure g-C_3N_4 materials synthesized via high-temperature thermal condensation of several types of nitrogen-rich precursors (*e.g.*, cyanamide, dicyandiamide, melamine, thiourea and urea) generally possess non-porous structure and relatively low surface area because of the high degree of polycondensation that these precursors tend to undergo during synthesis.[4,5] Thus, finding synthetic methods and/or precursors that can lead to advanced g-C_3N_4 materials with high surface area and large porosity are of importance, since such structural features provide the materials with more accessible catalytically active sites and better pathways for mass transport of reactants and products and thus improved photocatalytic performances for decontamination of pollutants, water splitting, carbon dioxide reduction, etc.[2,6,7]

Meanwhile, although g-C_3N_4 has a reasonably good band gap energy (2.7 eV) for visible-light photocatalysis, with conduction band (CB) and valence band (VB) potentials located at *ca.* -1.1 eV and *ca.* +1.6 eV vs normal hydrogen electrode (NHE), respectively,[5] the photo-induced

electron-hole pairs still suffer from rapid recombination even when high surface area and large porosity are introduced into the material. The charge carriers are thus unable to participate in many photocatalytic reactions making the material show poor photocatalytic activity.[1] In order to improve the charge separation efficiency as well as the light absorption of g-C_3N_4, many strategies have been developed. For example, the optical properties and electronic structures of g-C_3N_4 have been improved by depositing metal particles[8] and doping or co-doping heteroatoms (metals or nonmetals) on it,[6,9,10] by combining it with carbon materials and forming hybrid photoactive materials[11] and by constructing heterojunctions over its structures.[12] In the case of metal deposition, the immobilized metal particles on the surfaces of g-C_3N_4 improve charge separation efficiency often by capturing the photogenerated electrons and preventing them from combining with holes. In this strategy, noble metals such as Au,[13] Pt,[14] Pd[15] and Ag[16] have particularly been used to produce hybrid materials with g-C_3N_4 that have superior photocatalytic performances. Compared with noble metals, non-noble metals such as Cu may be better to use for these purposes because they are more earth abundant and can ultimately constitute low-cost g-C_3N_4-based materials for a broad range of applications.[17,18] In terms of the potential applications of g-C_3N_4-based semiconductor composites, pollutant degradation is of particular interest. Up to date, g-C_3N_4-based materials have been utilized to efficiently degrade a various of organic contaminants, including methyl orange, methylene blue and rhodamine B.[5]

In the past few years, melamine, which is nontoxic and inexpensive, has been explored as precursor to synthesize g-C_3N_4 materials by thermal condensation.[19,20] Melamine may provide some more advantages over cyanamide precursors, which are commonly used to make g-C_3N_4, especially when the precursor is used along with rigid template materials (such as mesoporous or

colloidal SiO_2) to create nanopores in g-C_3N_4, because melamine is less likely to produce toxic and flammable byproducts during the solution phase nanocasting synthetic steps.[4]

Herein, we show that melamine and colloidal silica nanoparticles with different sizes can be used as precursor and hard templates, respectively, to produce mesoporous g-C_3N_4 materials with three-dimensionally interconnected frameworks, large surface areas and high porosities. The mass ratio of melamine-to-silica nanoparticles is found to be crucial in the formation of high surface area and desirable pore sizes in the final g-C_3N_4 materials. The pore size of the materials was easily tailored (to 12, 22, 47 or 79 nm) by changing the sizes of the silica nanoparticles used as templates during the synthesis. By functionalizing the surfaces of the materials with Cu nanoparticles, mesoporous g-C_3N_4 composite materials decorated with Cu nanoparticles are produced. The resulting Cu-decorated mesoporous g-C_3N_4 are then shown, for the first time, to serve as efficient photocatalysts for degradation of tartrazine yellow, a colorful azo-dye that is widely used as a colorant in various food and pharmaceutical products in many countries but is also implicated in causing allergies, hyperactivity and even cancer if consumed in excess, and is banned in many other countries as a result.[21]

6.3. Experimental Section

6.3.1. Materials, chemicals and reagents

Colloidal silica dispersions (12 nm, Ludox TM-40, 40 wt. % suspension in water and 22 nm, Ludox HS-40, 40 wt. % suspension in water), copper(II) nitrate hemi(pentahydrate) and sodium borohydride were obtained from Sigma-Aldrich. Colloidal silica dispersions (47 nm, SNOWTEX-30LH, 30 wt. % suspension in water and 79 nm, SNOWTEX-ZL, 40 wt. % suspension in water) were purchased from Nissan Chemical America Corporation. Melamine

(99%) and ammonium hydrogen difluoride (95%) were acquired from Alfa Aesar. Tartrazine yellow was obtained from Duas Rodas Company. All the chemicals and reagents were of analytical grade and used as received without further purification. Distilled water was used throughout the experiments.

6.3.2. Synthesis of melamine-derived mesoporous g-C_3N_4 (mpg-C_3N_4)

First, melamine (1 g, 7.92 mmol) and different amounts of 12 nm colloidal silica (0.25, 1, 2 or 4 g) were mixed with hot water (80 °C, 80 mL), and the solution was stirred for 1 h at 80 °C in a closed beaker. The beaker was then left open and the solution was kept at 100 °C to let the solvent evaporate completely. The resulting composite materials comprising melamine-silica nanoparticles were pyrolyzed in a semi-closed or a partially covered combustion boat in a tube furnace under Argon atmosphere at 550 °C for 3 h at a ramp of 20 °C min^{-1}. In order to create nanoporous structures in the materials by removing the silica templates, the resulting yellow powders were treated in 4 M ammonium hydrogen difluoride solution for 24 h at room temperature. The solid products were recovered via filtration, washed with copious amount of water and then ethanol, and finally kept at 60 °C to dry. The resulting materials were denoted as 12-mpg-C_3N_4-*x*, where *x* represents the initial mass ratio of melamine-to-colloidal silica templates, which is 0.25, 1, 2 or 4. As a control material for the studies, bulk g-C_3N_4 was prepared without including 12 nm silica nanoparticles templates in the precursor. Similarly, by using colloidal silica templates with sizes of 22, 47 or 79 nm, but keeping the melamine-to-silica nanoparticles ratio as 1 and the synthetic procedures and conditions the same, three other mesoporous g-C_3N_4 materials, named *y*-mpg-C_3N_4-1, where *y* represents the size of colloidal silica templates (22, 47 or 79 nm), were also synthesized.

6.6.3. Synthesis of Cu nanoparticles-decorated 22-mpg-C_3N_4-1 materials

Two Cu-decorated 22-mpg-C_3N_4-1 materials containing different amounts of Cu nanoparticles were synthesized by mixing two different concentrations of aqueous Cu^{2+} solutions (5 or 10 wt. % Cu^{2+}) with 22-mpg-C_3N_4, followed by the reduction of the Cu^{2+} ions with $NaBH_4$ solution. For example, 22-mpg-C_3N_4-1 (300 mg) was first dispersed in water (40 mL) containing Cu^{2+} ions (15 mg, 0.23 mmol), and then a desired amount of $NaBH_4$ (50 mg, 1.32 mmol) was added dropwise into the above mixture. The mixture was stirred for 4 h at room temperature and then filtered. The solid product was washed with water and ethanol and dried in an oven at 60 °C overnight. The final product, which has 5 wt. % Cu was named as 5Cu-22-mpg-C_3N_4-1, and the corresponding material containing 10 wt. % Cu, which was obtained in a similar manner but by using higher amount of Cu^{2+} ions (30 mg, 0.47 mmol), was named 10Cu-22-mpg-C_3N_4-1.

6.3.4. Characterization

The BET surface areas and pore properties of the materials were analyzed by N_2 porosimetry (at -196 °C) using a Tristar-3000 instrument (Micromeritics Instrument Corporation, USA). The samples were degassed at 80 °C for 12 h under a flow of N_2 gas to remove any possible gas impurities adsorbed on the samples' surfaces before each measurement. Based on the adsorption-desorption isotherm data, the surface areas and the pore size distributions were calculated with the Brunauer-Emmett-Teller (BET) method and the Barrett-Joyner-Halenda (BJH) method, respectively. Transmission electron microscope (TEM) images of the materials were taken with a JEOL 1200EX transmission electron microscope. The powder X-ray diffraction (XRD) patterns of the materials were recorded with a Philips X'Pert XRD diffractometer operating with Cu Kα radiation as the X-ray source. The XRD patterns were recorded in a 2θ range between 10 and 80 ° with a step size (2θ) of 0.02° and a scan rate of 0.6° min^{-1}. Thermogravimetric analyses of the materials were conducted with a TGA7 instrument (PerkinElmer) with a heating rate of 5

°C min^{-1} under a flow of air at a rate of 20 mL min^{-1}. The UV-Vis diffuse reflectance spectra (UV−Vis DRS) of the materials in a spectral range of 250 to 800 nm were obtained with a Lambda 950 spectrophotometer (PerkinElmer). Small angel X-ray scattering (SAXS) were obtained using a Bruker HiStar area detector and an Enraf-Nonius FR571 rotating anode X-ray generator equipped with a graphite monochromator (Cu Kα; λ= 1.5418 Å). The surface chemical compositions of the materials were analyzed with a Thermo Scientific K-Alpha X-ray photoemission spectrometer (XPS) operating with Al Kα X-ray source (hv = 1486.6 eV). For high resolution spectra of individual peaks, an energy resolution of 0.1 eV was employed for the scans. Energy dispersive X-ray fluorescence (EDXRF) was performed on an EDAX (EDAX International) DX-95 EDXRF spectrometer equipped with Rh tube.

6.3.5. Photocatalytic degradation of tartrazine yellow dye

The photocatalytic performances of the as-prepared mpg-C_3N_4 materials containing different loadings of Cu nanoparticles and the control material (bulk C_3N_4) for degradation of tartrazine dye in solutions were evaluated by subjecting the samples to UV light emitted by a Germicide lamp (Osram, German, 18 W) in a jacketed beaker at room temperature, as in our previous report.[21] Blank experiments were also performed without putting the photocatalysts in the solution. Typically, prior to the test, 100 mg of the catalyst (with a concentration of 0.5 g L^{-1}) was mixed with 200 mL tartrazine yellow dye solution (with a concentration of 10 mg L^{-1}). The mixture was stirred for 30 min in the dark to let the solution and the catalyst reach adsorption-desorption equilibrium, and the light irradiation was then turned on. During photocatalytic reaction, 4.0 mL of a suspension was sampled every 30 min using 0.45 μm syringe filters (Millipore) and the concentration of tartrazine yellow in the supernatant was measured and quantified using UV-Vis spectrophotometer (Agilent, Cary 50).

6.4. Results and Discussion

The synthetic procedures that were employed to make the set of mesoporous C_3N_4 and Cu-decorated mesoporous C_3N_4 materials (denoted as *y*-mpg-C_3N_4-*x* and Cu-22-mpg-C_3N_4 respectively) is illustrated in **Scheme 6.1** and also described in the Experimental section above. First, an optimal mass ratio of melamine-to-silica nanoparticles that can render the material with high surface area and desired pore size was determined. Briefly, melamine was mixed with different amounts of 12 nm colloidal silica templates to form composite materials. After thermal condensation of melamine and removal of the silica templates from the carbonized composite material, a set of 12-mpg-C_3N_4-*x* was obtained, in which *x* represents the mass ratio of melamine-to-silica nanoparticles (0.25, 0.5, 1, or 4). Another set of materials, *y*-mpg-C_3N_4-1, where *y* represents the size of colloidal silica templates, was synthesized by using 22, 47 or 79 nm silica nanoparticles as templates with an optimized *x* value (*x* = 1). Different relative amounts of Cu^{2+} (5 or 10 wt. %) were then deposited onto the surface of 22-mpg-C_3N_4-1 using $NaBH_4$ as reductant and finally photocatalytically active materials labeled as 5Cu-22-mpg-C_3N_4-1 and 10Cu-22-mpg-C_3N_4-1, respectively, were obtained.

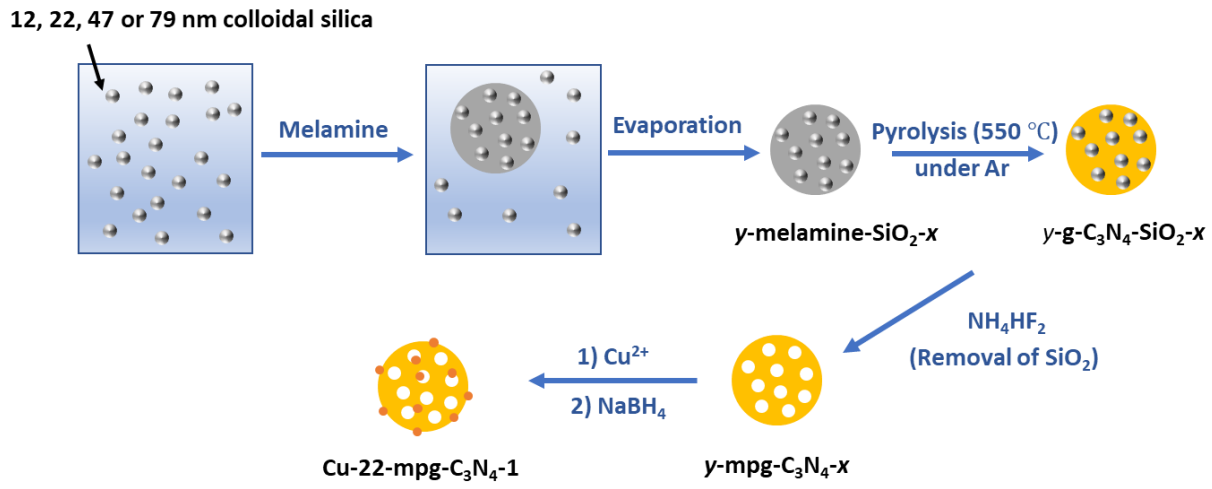

Scheme 6.1. Schematic illustration of the procedure used to synthesize *y*-mpg-C_3N_4-*x* and Cu-22-mpg-C_3N_4 materials, where *y* and *x* represent the size of the silica nanoparticles used as templates and the initial mass ratio of melamine-to-silica nanoparticles, respectively.

The structures of 12-mpg-C_3N_4-*x* were first investigated by N_2 porosimetry. The results showed that the surface area and porosity of the materials depended on the initial mass ratio of melamine-to-colloidal silica (12 nm) templates used to synthesize the materials (**Figure 6.1**). Bulk g-C_3N_4, which was synthesized without using colloidal silica templates, exhibited low surface area (3 m^2/g) and non-porous structure (0.04 cm^3/g). When colloidal silica nanoparticles templates were used, the surface area of the materials first increased, from 7 m^2/g for 12-mpg-C_3N_4-0.25 (which was synthesized using melamine-to-silica nanoparticles mass ratio of 0.25) to 136 m^2/g for 12-mpg-C_3N_4-1 (which was synthesized using melamine-to-silica nanoparticles mass ratio of 1), but then decreased to 9 m^2/g for 12-mpg-C_3N_4-4 (which was synthesized using the highest ratio of melamine-to-silica nanoparticles of 4). The pore volume of the materials exhibited a similar trend, namely, it first increased from 0.06 cm^3/g (for the material made from the precursor with melamine-to-silica nanoparticles mass ratio of 0.25) to 0.27 cm^3/g (for the one made from a precursor with melamine-to-silica nanoparticles mass ratio of 1), but then decreased to 0.05 cm^3/g (for the one made from a precursor with melamine-to-silica nanoparticles mass ratio of 4). It is also worth noting that only 12-mpg-C_3N_4-1 (which was synthesized using melamine-to-silica nanoparticles mass ratio of 1) showed a pore size centered at *ca.* 11.7 nm, a pore size that is comparable to the size of colloidal silica templates used to synthesize the material. Lower or higher melamine-to-silica mass ratio (where $x = 0.25$, 0.5 or 4) did not result in materials whose pore size directly correspond to each silica nanoparticle; in the former case (where the amount of silica nanoparticles with respect to that of melamine is relatively high), the pores corresponded rather to

aggregates of multiple silica nanoparticles due to the possible necking of silica nanoparticles in the precursors, and in the latter case, not enough carbon formed by pyrolysis to form structures all around the silica nanoparticles.

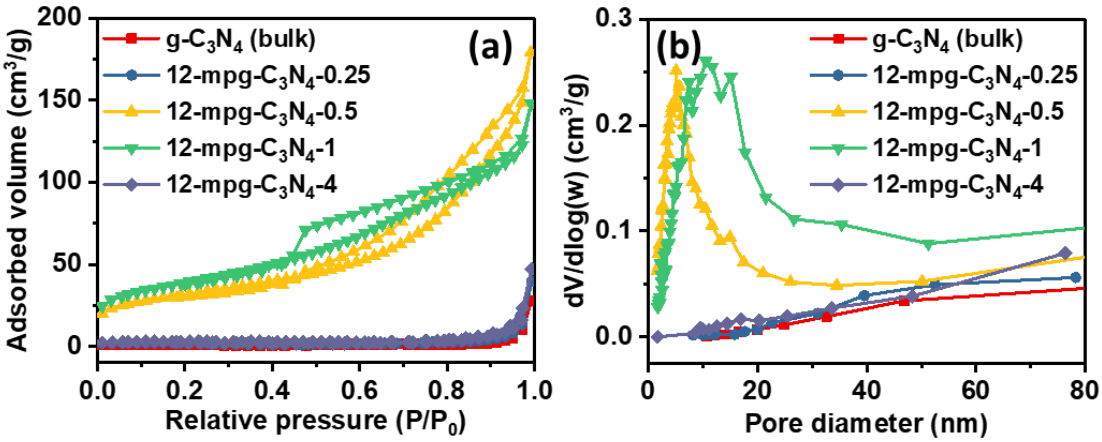

Figure 6.1. (a) N_2 adsorption-desorption isotherms of 12-mpg-C_3N_4-*x* materials synthesized by using different ratios of melamine-to-silica nanoparticles and (b) their corresponding pore size distributions.

Based on N_2 porosimetry results presented above, the mechanism leading to mpg-C_3N_4 and Cu-loaded mpg-C_3N_4 was proposed, as illustrated in **Scheme 6.2**. At the lowest melamine-to-silica mass ratio (x = 0.25), the material did not maintain its porous structure after removal of silica due to the insufficient amount of melamine used and the small amount of carbon product forming from it. When the highest melamine-to-silica nanoparticles mass ratio (x = 4) was used, the lack of silica nanoparticles templates may also adversely affect the formation of porous structure in the material, generating less porosity compared with that in 12-mpg-C_3N_4-1 (whose melamine-to-silica nanoparticles mass ratio is much lower, x = 1) (**Figure 6.1b**). In addition, the formation of compact g-C_3N_4 shells around the silica spheres templates due to the relatively higher amount of melamine used may have prevented ammonium hydrogen difluoride from reaching the silica templates and

etching them all. As a result, the silica templates could not all be removed from the carbonized product, leaving non-porous structure in the material. This was actually corroborated by thermogravimetric analysis (TGA) (**Figure 6.2**), which clearly revealed that 12-mpg-C_3N_4-4 had higher amount of residue associated with silica (*ca.* 6.79 wt. %) compared with 12-mpg-C_3N_4-1 (*ca.* 1.12 wt. %). However, the low surface area in the former was also likely to be caused by the lack of porous structure in the material since most of the silica was still removed despite a relatively large amount of it was also left behind. Based on the above results, the optimal mass ratio of melamine-to-silica nanoparticles for the synthesis of high surface area mpg-C_3N_4 materials with desired pore sizes was determined to be 1.

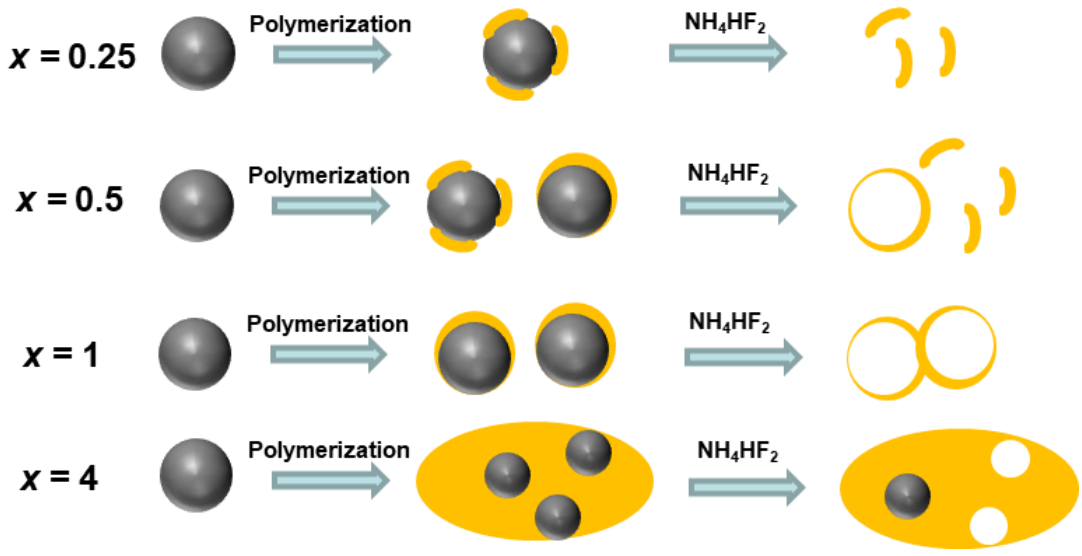

Scheme 6.2. Proposed mechanism of the formation of different 12-mpg-C_3N_4-*x* materials by using different mass ratios of melamine-to-silica nanoparticles.

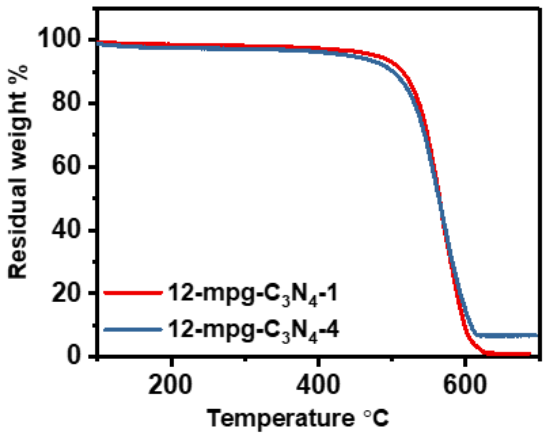

Figure 6.2. TGA curves obtained under air for 12-mpg-C_3N_4-1 and 12-mpg-C_3N_4-4 materials.

The synthetic procedure was easily extended to produce a series of *y*-mpg-C_3N_4-1 materials with different pore sizes (with *y* = 12, 22, 47 or 79 nm, representing the different pore sizes), by using colloidal silica nanoparticles with sizes of 22, 47 or 79 nm as templates (**Figure 6.3**). When the size of the silica nanoparticles templates used to synthesize the materials was increased, the surface areas of the *y*-mpg-C_3N_4-1 materials slightly decreased from 136 m^2/g to 73 m^2/g, but their corresponding pore volume increased from 0.27 cm^3/g to 1.05 cm^3/g. Quantitative results of N_2 porosimetry analyses of all materials are compiled in **Tables 6.1 and 6.2**.

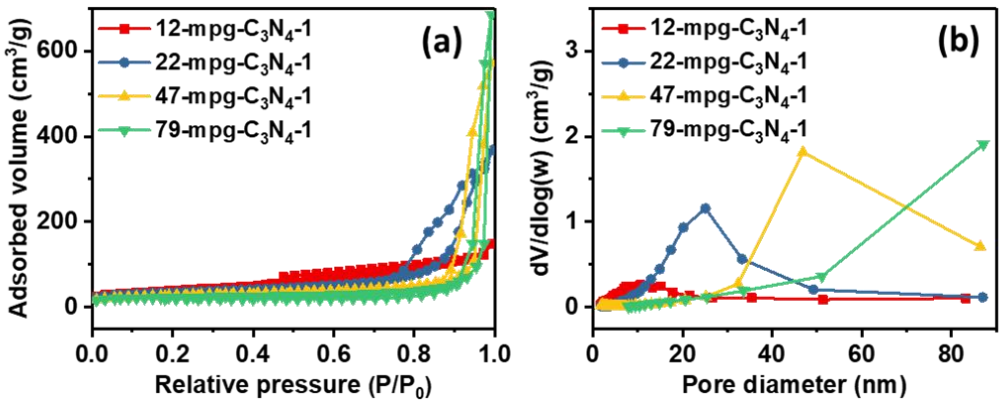

Figure 6.3. (a) N_2 adsorption-desorption isotherms of different *y*-mpg-C_3N_4-1 materials synthesized using different mass ratios of melamine-to-silica nanoparticles in the precursors and (b) their corresponding pore size distributions.

Table 6.1. BET surface area, average BJH pore size, and pore volume of different 12-mpg C_3N_4-*x* materials.

Size of SiO_2 nanoparticles	Mass ratio of melamine-SiO_2 nanoparticles	BET surface area (m^2/g)	Average pore size (nm) [a]	Pore volume (cm^3/g)
12	-	3	-	0.04
12	0.25	7	-	0.06
12	0.5	110	6.2	0.22
12	1	136	11.7	0.27
12	4	9	-	0.05

[a] Pore size is measured based on the adsorption data.

Table 6.2. BET surface area, average BJH pore size, and pore volume of different *y*-mpg-C_3N_4-1 materials.

Size of SiO_2 nanoparticles	Mass ration of melamine-SiO_2 nanoparticles	BET surface area (m^2/g)	Average pore size (nm) [a]	Pore volume (cm^3/g)
12	1	136	11.7	0.27
22	1	118	22.5	0.56
47	1	92	43.6	0.88
79	1	73	*ca.* 80	1.05

[a] Pore size is measured based on the adsorption data.

The structures of the *y*-mpg-C_3N_4-1 materials were further examined by transmission electron microscope (TEM) (**Figures 6.4a-4c**). When $x = 1$, the material showed pores with sizes of 12 nm (Figure 3a), corroborating the pore size obtained by N_2 porosimetry for this material earlier (which is 12-mpg-C_3N_4-1) (**Table 6.1**). The TEM images of the *y*-mpg-g-C_3N_4-1 materials, which were synthesized by keeping the same *x* value but by changing the sizes of the silica

nanoparticles templates, clearly showed that the materials all possessed nanoporous structures. However, their pore sizes were highly dependent on the sizes of the silica templates used to synthesize them, which increased from *ca.* 12 nm to *ca*. 79 nm as the sizes of colloidal silica templates were increased from 12 nm to 79 nm. In addition, TEM images were also acquired for 5Cu-22-mpg-C_3N_4-1 and 10Cu-22-mpg-C_3N_4-1 (**Figure 6.4e** and **Figure 6.4f**). The images of these materials showed many dark spots and areas associated with Cu species. Overall, the N_2 porosimetry and TEM results above clearly indicated that mesoporous g-C_3N_4 materials with high surface area and desired pore sizes could be produced by a facile synthetic method using melamine as precursor and a proper amount of silica nanoparticles as templates. Furthermore, the porosity of the materials could be tuned by varying the sizes of the silica particles used as templates to make the materials.

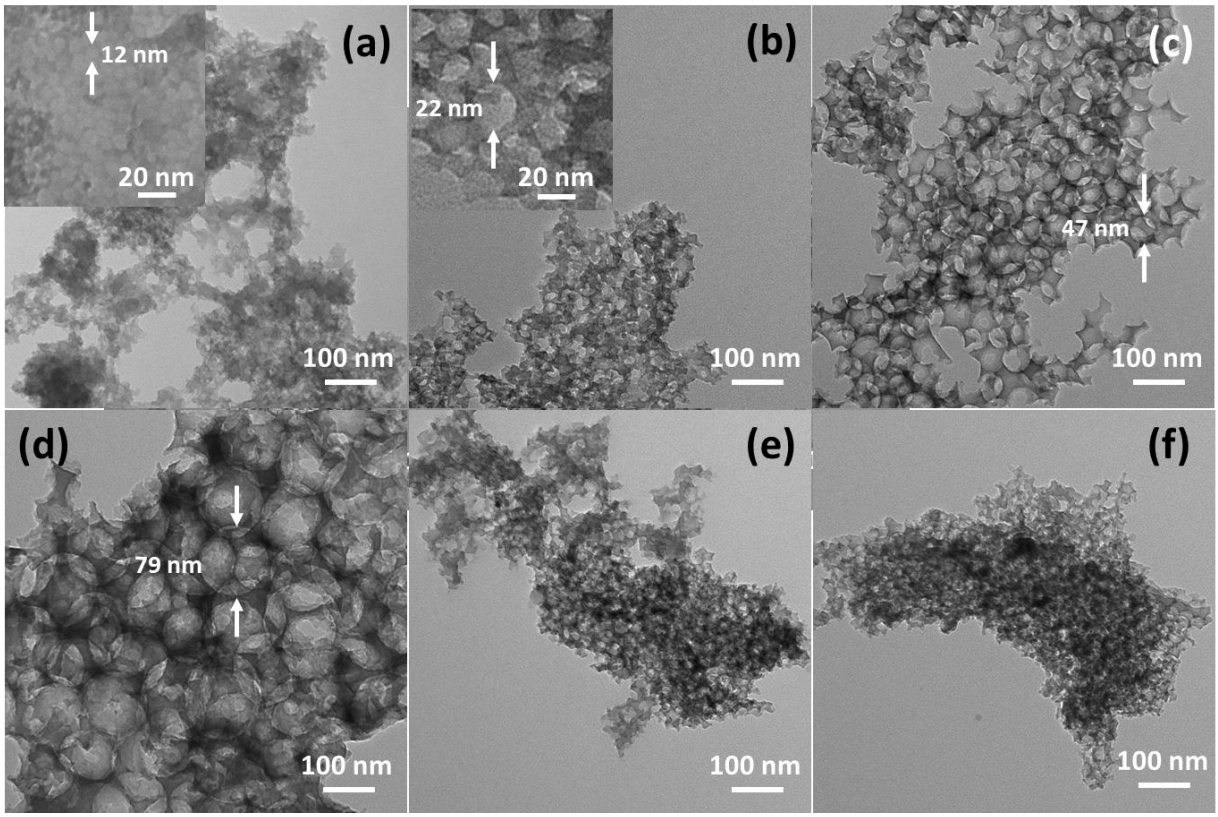

Figure 6.4. TEM images of the different *y*-mpg-C_3N_4-1 and Cu-22-mpg-C_3N_4-1 materials synthesized using different sizes of silica nanoparticles templates and different amount of Cu, respectively: (a) 12-mpg-C_3N_4-1, (b) 22-mpg-C_3N_4-1, (c) 47-mpg-C_3N_4-1, (d) 79-mpg-C_3N_4-1, (e) 5Cu-22-mpg-C_3N_4-1, and (f) 10Cu-22-mpg-C_3N_4-1.

Since 22-mpg-C_3N_4-1 and Cu-22-mpg-C_3N_4-1 materials were used as representative materials to evaluate the photodegradation performances of Cu-doped mpg-C_3N_4 materials toward tartrazine yellow dye, the following characterizations were carried out only for these materials. The colors of the samples slowly changed from yellow to light green upon increasing the relative amount of Cu^{2+} ions used to synthesize the different Cu-22-mpg-C_3N_4-1 materials (**Figure 6.5a**). UV-Vis diffuse reflectance spectroscopy (DRS) was used to determine the optical properties of these materials in the range from 250 nm to 800 nm (**Figure 6.5b**). The intrinsic absorption edge of the 22-mpg-C_3N_4-1 was found to be *ca.* 459 nm, which is in line with the value reported for g-C_3N_4 materials in the literature and indicates the formation of g-C_3N_4.[22] After decorating its surfaces with 5 wt. % and 10 Wt. % of Cu (producing 5Cu-22-mpg-C_3N_4-1 and 10Cu-22-mpg-C_3N_4-1 materials), the absorption edge of the materials shifted to higher wavelengths, to *ca.* 498 nm and *ca.* 514 nm, respectively, and their intensities have increased; this suggests that the Cu-modified mpg-C_3N_4 materials have enhanced light absorbance in the visible range as the amount of Cu is increased, up to, at least, 10 wt.%.[23]

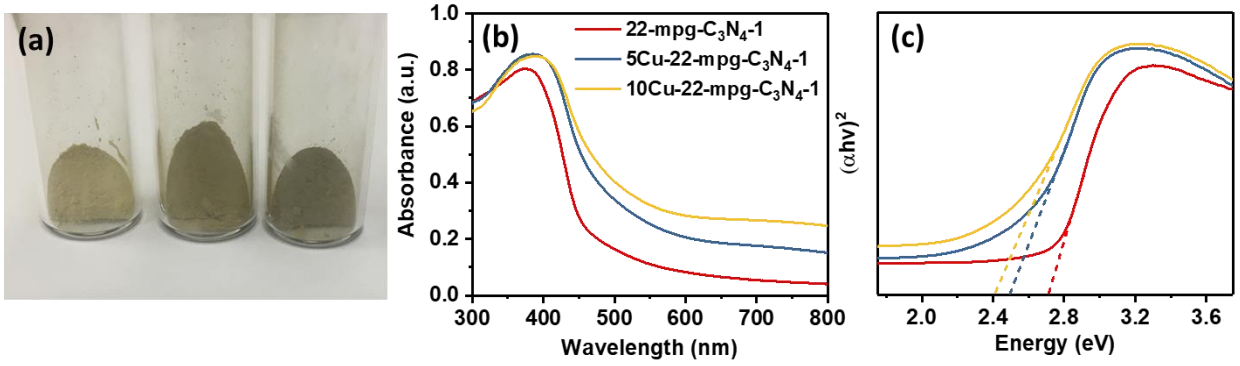

Figure 6.5. (a) Physical appearance of 22-mpg-C_3N_4-1, 5Cu-22-mpg-C_3N_4-1, and 10Cu-22-mpg-C_3N_4-1 materials (from left to right). (b) UV-Vis diffuse reflectance spectra (DRS) of 22-mpg-C_3N_4-1, 5Cu-22-mpg-C_3N_4-1, and 10Cu-22-mpg-C_3N_4-1 and (c) the corresponding plots of transformed Kubelka-Munk function versus the energy of the light.

The band gap energy (E_g) of the materials were calculated based on the spectra obtained with UV-Vis DRS using the transformed Kubelka-Munk equation (Figure 4b): $[F(R) \cdot \mathrm{h}v]^2 = \alpha = \mathrm{A}(\mathrm{h}v - E_g)$, where $F(R) = (1-R)^2/2R$, hv is the incident photon energy, R is the percentage of reflected light, E_g is the band gap energy and A is constant, whose value depends on the transition probability.[24,25] The E_g value of 22-mpg-C_3N_4-1 was 2.71 eV, whereas the E_g values of 5Cu-22-mpg-C_3N_4-1 and 10Cu-22-mpg-C_3N_4-1 were 2.49 and 2.41 eV, respectively, indicating that the value of E_g decreased as the amount of Cu mpg-C_3N_4-1 increased. These results are consistent with those reported for g-C_3N_4 in the literature, where a steadily decrease in band gap energy has been observed as more metal has been loaded on it.[26-28] Overall, the DRS results suggested that Cu/mpg-C_3N_4 composite materials have significantly improved light absorption, and thus potentially better photocatalytic activity, compared with pure g-C_3N_4.

The amount of Cu in Cu-22-mpg-C_3N_4-1 was estimated by comparing the weight of the residue remained in Cu-mpg-C_3N_4 at the end of thermogravimetric analysis (TGA) in air with respect to that of 22-mpg-C_3N_4-1 (**Figure 6.6**). While 22-mpg-C_3N_4-1 gave *ca*. 1.12 wt. % residue associated with residual silica, since the C_3N_4 in it should be lost in the form of CO_2 and NO_2 during calcination, 5Cu-22-mpg-C_3N_4-1 and 10Cu-22-mpg-C_3N_4-1 gave *ca*. 6.07 wt. % and 12.24 wt. % residue, which should be largely due to CuO. From these numbers, the amounts of Cu in 5Cu-22-mpg-C_3N_4-1 and 10Cu-22-mpg-C_3N_4-1 were determined and found to be *ca*. 3.73 wt. % and 8.68 wt. %, respectively. In addition, it is worth noting the TGA curves indicated that the

presence of Cu NPs in mpg-C_3N_4 facilitated the materials' thermal decomposition. While 22-mpg-C_3N_4-1 was stable up to *ca.* 480 °C in air and decomposed in the range of 480 to 625 °C, the Cu-functionalized counterparts, 5Cu-22-mpg-C_3N_4-1 and 10Cu-22-mpg-C_3N_4-1, decomposed in lower temperature ranges of 440 to 575 °C and 390 to 560 °C, respectively. The decreased thermal stability of Cu-22-mpg-C_3N_4-1 materials indirectly indicated the successful decoration of the surfaces of mpg-C_3N_4 with Cu nanoparticles, because the presence of Cu (metallic) particles has been reported to facilitate the heat transfer during calcination and promote the combustion of mpg-C_3N_4.[29]

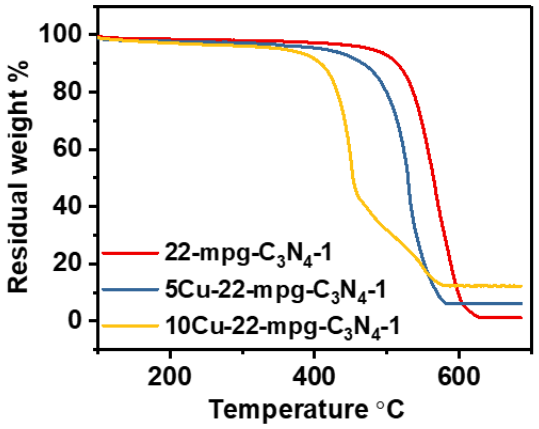

Figure 6.6. TGA curves obtained in air for 22-mpg-C_3N_4-1, 5Cu-22-mpg-C_3N_4-1 and 10Cu-22-mpg-C_3N_4-1 materials.

X-ray diffraction (XRD) patterns were obtained to determine the phase structure of 22-mpg-C_3N_4-1 and Cu-22-mpg-C_3N_4-1 materials (**Figure 6.7**). The XRD patterns of 22-mpg-C_3N_4-1 showed two pronounced diffraction peaks centered at *ca.* 27.5° and 13.0°, corresponding to the (002) and (100) planes of the interlayer stacking of conjugated aromatic systems and the interplanar separation, respectively,[5,30] of g-C_3N_4, indirectly confirming the formation of g-C_3N_4. While the XRD patterns of both Cu-22-mpg-C_3N_4-1 materials showed the prominent peak

associated with C_3N_4, they did not show any diffraction peak associated with Cu species, due possibly to either the low content or the high dispersion of Cu nanoparticles.[28] The latter seems to be a good possibility, based on TEM images (**Figure 6.4e** and **Figure 6.4f**). Energy dispersive X-ray fluorescence (EDXRF) was further carried out to determine the Cu content in 10Cu-22-mpg-C_3N_4-1 material (**Figure 6.8**). The result showed that the Cu content in 10Cu-22-mpg-C3N4-1 was *ca.* 14.1 wt. %.

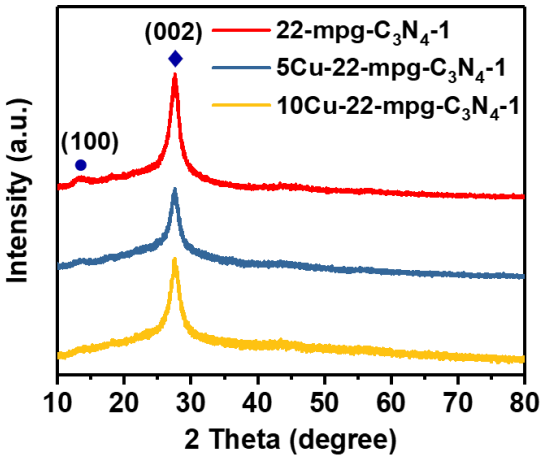

Figure 6.7. XRD patterns of 22-mpg-C_3N_4-1, 5Cu-22-mpg-C_3N_4-1 and 10Cu-22-mpg-C_3N_4-1 materials.

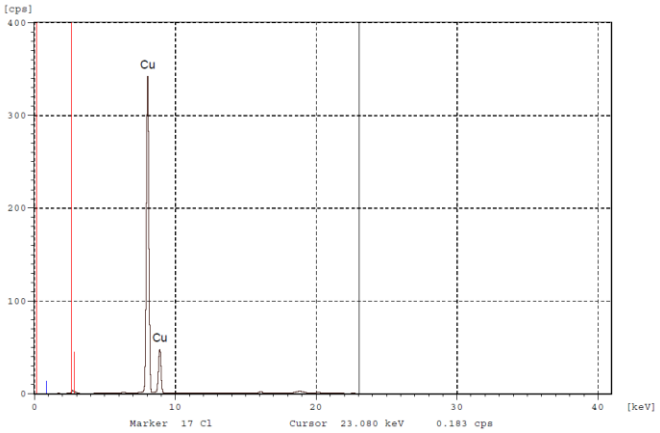

Figure 6.8. EDXRF results of 10Cu-22-mpg-C_3N_4-1.

X-ray photoelectron spectroscopy (XPS) analysis was further performed to determine the composition of 10Cu-22-mpg-C_3N_4-1 material as well as the chemical states of C, N and Cu exist in 10Cu-22-mpg-C_3N_4-1 material. The survey spectrum showed that only C, O, N and Cu were present in the material (**Figure 6.9a**). The C 1s peak in the spectrum showed two peaks centered at *ca*. 284.3 eV and 288.0 eV, corresponding to sp^2-boned carbon in C-C and N-C=N (**Figure 6.9b**).[5] The N 1s peak in the spectrum was deconvoluted into four peaks with binding energy values of 398.5, 399.9, 401.1 eV and 404.1 eV, which can be ascribed to sp^2-bonded nitrogen in C-N=C, the nitrogen in tertiary N-$(C)_3$ groups, the N-H structure and π excitation, respectively (**Figure 6.9c**).[5,31] The oxidation state of Cu was determined on the basis of the position of the Cu $2p_{3/2}$ peak (Figure 7d). Two peaks at binding energies of *ca*. 932.4 and 952.2 eV were observed, corresponding to Cu $2p_{3/2}$ and Cu $2p_{1/2}$ of Cu^0 and/or Cu^{1+}. The additional small peaks at *ca*. 933.9 and 954.0 eV were also observed, corresponding to Cu^{2+} species. The presence of Cu^{2+} signal is most likely due to the oxidation of Cu^0/Cu^+ to Cu^{2+} when the surface of Cu nanoparticles is exposed to air or humidity.[32]

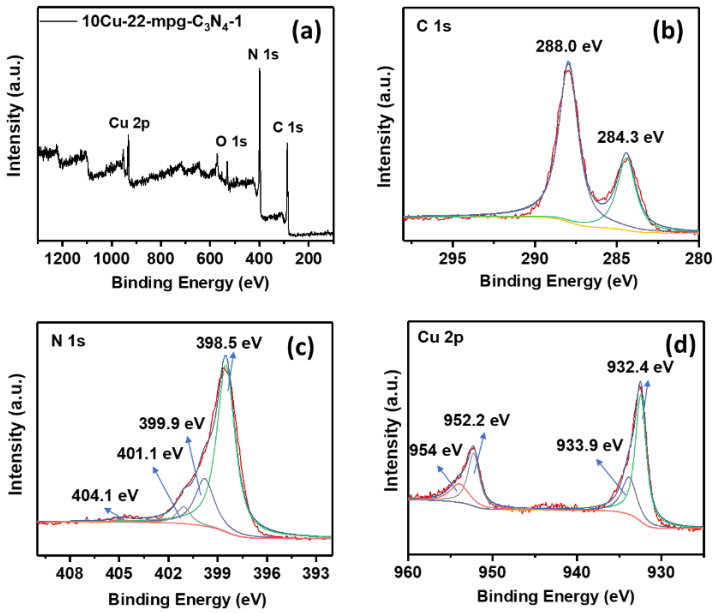

Figure. 6.9. (a) XPS survey spectra of 10Cu-22-mpg-C_3N_4-1; High-resolution XPS spectra of (b) C 1s peak, (b) N 1s peak and (d) Cu 2p peak of 10Cu-22-mpg-C_3N_4-1.

The photocatalytic activities of the materials for the degradation of tartrazine yellow dye in solutions, a colorful additive that is widely used in various consumer products worldwide but is also often regarded as a cause of allergies, hyperactivity and even cancer, were evaluated (**Figure 6.10**). The necessary comparative and control experiments were also performed. In one control experiment, the extent of photolysis of tartrazine yellow without catalysts over an irradiation period of 240 min was found to be only *ca.* 5.3%, demonstrating that the photodegradation of this dye is slow in the absence of catalyst. A sample of 22-mpg-C_3N_4-1 also did not function well as photocatalyst either, as it resulted in the photodegradation of only *ca.* 18.8% tartrazine yellow over the same time period. However, the photocatalytic performance of the material was significantly improved after its surfaces were decorated with Cu nanoparticles, and the degradation rates of tartrazine yellow dye in solutions in the presence of Cu-22-mpg-C_3N_4-1 materials depended on the amount of Cu nanoparticles they contained. For example, the extent of photodegradation of tartrazine yellow dye within 240 min in the presence of 5Cu-22-mpg-C_3N_4-1 and 10Cu-22-mpg-C_3N_4-1 were *ca.* 32.8% and *ca.* 81.9%, respectively, which were significantly higher than the one in the presence of 22-mpg-C_3N_4-1. For comparison, the performance of 10Cu-47-mpg-C_3N_4-1 (a material containing 10% Cu nanoparticles in 47-mpg-C_3N_4-1, which is synthesized using 47 nm silica nanoparticles as templates) was also evaluated, and this material led to *ca.* 42.5% photodegradation of tartrazine yellow in the same time period. The former had a surface area is 87 m^2/g, which is lower than that of 10Cu-22-mpg-C_3N_4-1, which is 97 m^2/g. These results suggest that the surface-deposited Cu nanoparticles as well as the surface area of the materials played major

roles in the enhanced photodegradation of tartrazine yellow dye over Cu-doped mpg-C_3N_4 materials.

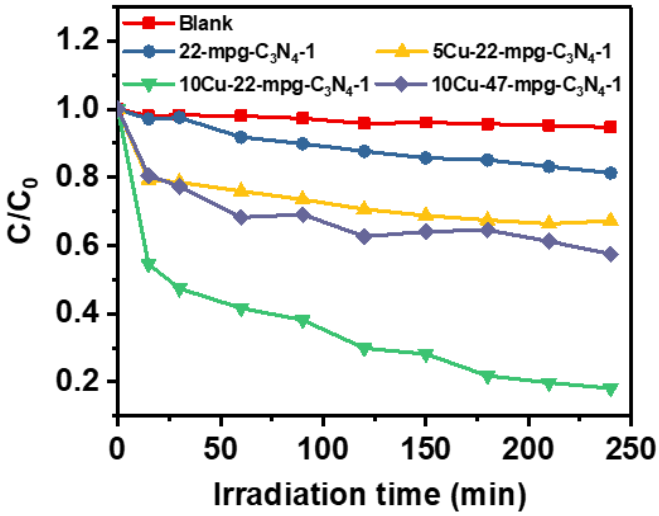

Figure 6.10. Degradation rate of tartrazine yellow over the as-prepared mpg-C_3N_4 and Cu-mpg-C_3N_4 photocatalysts.

In photodegradation systems, efficient charge separation is important, because it leaves the charges available for various redox reactions not to be compromised to undesirable charge recombination processes. The photogenerated electrons on the conduction band often react with O_2 and form superoxide radicals ($O_2^{\bullet-}$). The resulting superoxide radicals as well as the photogenerated holes are generally responsible for photo-oxidative degradation of various compounds.[2,33,34] Unfortunately, plain g-C_3N_4 often suffers from rapid electron-hole recombination and gives negligible photocatalytic activity. However, in the presence of metals such as Cu, which can trap the photogenerated electrons, the recombination rate of the photogenerated electron-hole pairs in g-C_3N_4 can be significantly minimized. Hence, not surprisingly, the decoration of mpg-C_3N_4 with Cu nanoparticles facilitated the photodegradation of tartrazine yellow over the materials, making the 10Cu-22-mpg-C_3N_4 materials to show superior

photocatalytic activity compared with plain 22-mpg-C_3N_4-1. Compared with 10Cu-22-mpg-C_3N_4-1 (whose surface area is 97 m^2/g), 10Cu-47-mpg-C_3N_4-1 exhibited inferior photocatalytic activity, most likely due to its lower surface area (87 m^2/g), which resulted in less exposed active sites.[35] So, in addition to decorating its surfaces with Cu nanoparticles, introducing high surface area in mpg-C_3N_4 can improve its photocatalytic activity toward degradation of tartrazine yellow dye.

6.5. Conclusions

A facile synthetic route that produces highly photocatalytically active Cu nanoparticles-loaded mesoporous g-C_3N_4 by using melamine as a precursor and colloidal silica nanoparticles as hard templates has been developed. The synthetic conditions that produce mesoporosity in the materials have been investigated and the mechanisms that lead to mesoporosity in the materials have been proposed. The surface area, pore size and pore volume of mpg-C_3N_4 could be tuned by changing the size of the silica nanoparticles templates used to synthesize the materials. The Cu nanoparticles decorating the surface of mpg-C_3N_4 improved the light absorption, enhanced the charge separation efficiency, and increased the photocatalytic activity of the materials. The resulting Cu-decorated mpg-C_3N_4 were found to photocatalytically degrade tartrazine yellow for the first time and their catalytic activity was better than that of pure mpg-C_3N_4. In particular, the material that was synthesized from using melamine-to-silica nanoparticles mass ratio of 1 and contained 10 wt.% Cu showed superior photocatalytic activity toward the photodegradation of tartrazine yellow dye. The photocatalytic performance of the materials also depended on their specific surface area, besides the amount of Cu loaded on them. The present work can provide a new synthetic strategy to prepare three-dimensionally interconnected porous g-C_3N_4 materials

with large surface area and high porosity and also demonstrates their potential applications for remediation of common environmental pollutants.

6.6. Reference

1. Jiang, L.; Yuan, X.; Pan, Y.; Liang, J.; Zeng, G.; Wu, Z.; Wang, H. *Appl. Catal. B Environ.*, **2017**, *217*, 388-406.
2. Mamba, G.; Mishra, A.K. *Appl. Catal. B Environ.*, **2016**, *198*, 347-377.
3. Zhang, L.; Chen, X.; Guan, J.; Jiang, Y.; Hou, T.; Mu, X. *Mater. Res. Bull.*, **2013**, *48*, 3485-3491.
4. Cui, L.; Song, J.; McGuire, A.F.; Kang, S.; Fang, X.; Wang, J.; Yin, C.; Li, X.; Wang, Y.; Cui, B. *ACS Nano*, **2018**, *12*, 5551-5558.
5. Cao, S.; Low, J.; Yu, J.; Jaroniec, M. *Adv. Mater.*, **2015**, *27*, 2150-2176.
6. Ran, J.; Ma. T.Y.; Gao, G.; Du, X.-W.; Qiao, S.Z. *Energy Environ. Sci.*, **2015**, *8*, 3708-3717.
7. Ye, S.; Wang, R.; Wu, M.Z.; Yuan, Y.-P. *Appl. Surf. Sci.*, **2015**, *358*, 15-27.
8. Li, Z.; Wang, J.; Zhu, K.; Ma, F.; Meng, A. *Mater. Lett.*, **2015**, *145*, 167-170.
9. Hu, S.; Li. F.; Fan, Z.; Wang, F.; Zhao, Y.; Lv, Z. *Dalton Trans*., **2015**, *44*, 1084-1092.
10. Lu, C.; Chen, R.; Wu, X.; Fan, M.; Liu, Y.; Le. Z.; Jiang, S.; Song, S. *Appl. Surf. Sci.*, **2016**, *360*, 1016-1022.
11. Zheng, Y.; Jiao, Y.; Chen, J.; Liu, J.; Liang, J.; Du, A.; Zhang, W.; Zhu, Z.; Smith, S.C.; Jaroniec, M.; Lu, G.Q.; Qiao, S.Z. *J. Am. Chem. Soc*., **2011**, *133*, 20116-20119.
12. Shi, H.; Chen, G.; Zhang, C.; Zou, Z. *ACS Catal.*, **2014**, *4*, 3637-3643.
13. Samanta, S.; Martha, S.; Parida, K. *ChemCatChem*, **2014**, *6*, 1453-1462.
14. Zhang, G.; Lan, Z.-A.; Lin, L.; Lin, S.; Wang, X. *Chem. Sci*., **2016**, *7*, 3062-3066.
15. Jiang, F.; Tan, W.; Chen, H.; Tan, L.; Liu, J. *RSC Adv*., **2015**, *5*, 51841-51851.
16. Fu, Y.; Huang, T.; Zhang, L.; Zhu, J.; Wang, X. *Nanoscale*, **2015**, *7*, 13723-13733.
17. Zhang, T.; Low, J.; Huang, X.; Al-Sharab, J.F.; Yu, J.; Asefa, T. *ChemCatChem*, **2017**, *9*, 3054-3062.
18. Le, S.; Jiang, T.; Zhao, Q.; Liu, X.; Li, Y.; Fang, B.; Gong, M. *RSC Adv*., **2016**, *6*, 38811-38819.

19. Yan, S.C.; Li, Z.S.; Zou, Z.G. *Langmuir*, **2009**, *25*, 10397-10401.

20. Li, X.; Zhang, J.; Shen, L.; Ma, Y.; Lei, W.; Cui, Q.; Zou, G. *Appl. Phys. A: Mater. Sci. Process*., **2009**, *94*, 387-392.

21. Souze, I.P.A.F.; Pezoti, O.; Bedin, K.C.; Cazetta, A.L.; Melo, S.A.R.; Souza, L.S.; Silva, M.C.; Almeida, V.C. *Ceram. Int.*, **2018**, *44*, 12292-12300.

22. Hong, J.; Xia, X.; Wang, Y.; Xu, R. *J. Mater. Chem.*, **2012**, *22*, 15006-15012.

23. Gao, J.; Wang, J.; Qian, X.; Dong, Y.; Xu, H.; Song, R.; Yan, C.; Zhu, H.; Zhong, Q.; Qian, G.; Yao, J. *J. Solid State Chem.*, **2015**, *228*, 60.

24. Zhang, T.; Low, J.; Koh, K.; Yu, J.; Asefa, T. *ACS Sustainable Chem. Eng*., **2018**, *6*, 531-540.

25. Dong, G.; Zhang, L. *J. Mater. Chem.*, **2012**, *22*, 1160-1166.

26. Min, C.; Shen, C.; Li. R.; Li, Y.; Qin, J.; Yang, X. *Ceram. Int.*, **2016**, *42*, 5575-5581.

27. Li, K.; Zeng, Z.; Yan, L.; Luo, S.; Luo, X.; Huo, M.; Guo, Y. *Appl. Catal. B Environ.*, **2015**, *165*, 428-437.

28. Ge, L.; Han, C.; Liu, J.; Li, Y. *Appl. Catal. A*, **2011**, *409-410*, 215-222.

29. Zou, X.; Silva, R.; Goswami, A.; Asefa, T. *Appl. Surf. Sci.*, **2015**, *357*, 221-228.

30. Liao, G.; Chen, S.; Quan, X.; Yu, H.; Zhao, H. *J. Mater. Chem*., **2012**, *22*, 2721-2726.

31. Zang, Y.; Li, L.; Li, X.; Lin, R.; Li, G. *Chem. Eng. J*., **2014**, *246*, 277-286.

32. Zhang, T.; Asefa, T. *Front. Chem. Sci. Eng*., **2018**, *12*, 329-338.

33. Cheng, N.; Tian, J.; Liu, Q.; Ge, C.; Qusti, A.H.; Asiri, A.M.; Al-Youbi, A.O.; Sun, X. *ACS Appl. Mater. Interfaces*, **2013**, *5*, 6815-6819.

34. Xu, M.; Han, L.; Dong, S. *ACS Appl. Mater. Interfaces*, **2013**, *5*, 12533-12540.

35. Zheng, Y.; Lin, L.; Wang, B.; Wang, X. *Angew. Chem. Int. Ed.*, **2015**, *54*, 12868-12884.

Chapter 7

Nanostructuring Polymers with High Surface Area Using Inorganic Templates for Efficient Extraction of Anionic Dyes from Solutions

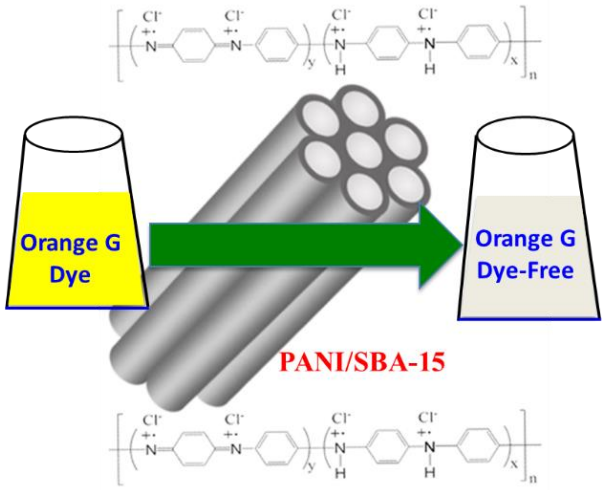

7.1. Overview

A protonated polyaniline-functionalized SBA-15 mesoporous silica nanomaterial (H^+-PANI/SBA-15) with high surface area and ideal surface properties for the adsorption of anionic dyes is synthesized. Compared with the conventional emeraldine salt of polyaniline (H^+-PANI), H^+-PANI/SBA-15 has a significantly higher adsorption capacity for the anionic dye Orange G and is a more effective sorbent for the removal of anionic pollutants from wastewater. This work has been published in *Chem. Commun.* (Reproduced with permission from *Chem. Commun.*, **2015**, *51*, 16315. **DOI:** 10.1039/C5CC06816A. Copyright Royal Society of Chemistry).

7.2. Introduction

Organic dyes are a class of important organic compounds that are widely used in the textile, wood and food industries, but often find their way into industrial effluents.[1,2] Besides their unwanted colors in water systems, many of them can undergo degradation and produce toxic products that can contaminate both surface and ground water systems, and cause adverse biological activity.[2,3] So, if not treated or removed properly from industrial wastewater discharges, these colorful compounds can cause severe environmental problems. Hence, several methods have been developed to remove such dyes from industrial effluents;[2,4] the methods include coagulation-flocculation,[5] biodegradation,[6] membrane-based separation,[7] ionexchange,[8] electrochemical treatment,[9] oxidation[10] and adsorption.[11] Among them, the adsorption method remains the most feasible and appealing method to remove dyes from various water systems due to its ease of operation, its inexpensiveness, the low residue formation, and the possibility of recycling the adsorbent materials.[1,2]

Recently, polymers such as polyaniline (PANI) have attracted great interest as adsorbent materials for dye adsorption applications because of their numerous advantages, including their ability to easily transform between protonated and deprotonated forms using a simple procedure, and thus adsorb and desorb various agents, and their excellent environmental stability.[12] Notably, the protonated form of PANI (emeraldine salt or H^+-PANI) has recently been demonstrated to have the ability to selectively adsorb an anionic dye from solutions.[13] However, H^+-PANI suffers from a relatively low surface area and limited adsorption capacity due to its closely compacted polymeric chains that is typical to polymeric materials.[14]

To overcome this problem and improve the properties of PANI for various applications, some synthetic strategies have been adopted, including (1) doping of the polymer with acids

containing bulky counterions to increase the polymer's interchain spaces[13] and (2) making PANI a nanostructured material, *e.g.*, in the form of nanotubes,[15] nanofibers[16] or microspheres.[17] However, the resulting materials still possess a relatively low surface area, with the highest value reported being 80 m^2 g^{-1} for PANI having a microsphere morphology.[17]

It has also been demonstrated that the synthesis of polymers using porous inorganic support materials as hard templates and the production of polymer/inorganic type composite materials can result in the formation of polymers with a high surface area. In particular, SBA-15 mesoporous silica,[18] which possesses a large surface area, nanosized pores, and good stability, can serve as an ideal porous material for hosting polymers such as PANI to produce PANI/inorganic type composite materials with high surface area.[19] However, unsurprisingly the major research studies on the application of such types of composite nanomaterials have focused only on electrochemical areas, as the main, unique properties of PANI include conductivity and electroactivity.[20,21] Conversely, to the best of our knowledge, the adsorption properties of mesoporous silica-supported PANI for dyes in solutions has never been reported before.

7.3. Experimental Section

7.3.1. Materials and reagents

Poly(ethylene glycol)-*block*-poly(propylene glycol)-*block*-poly(ethylene glycol) ($(PEG)_{20}(PPG)_{70}(PEG)_{20}$ or Pluronic® 123) was obtained from BASF. Tetraethyl orthosilicate (TEOS), aniline, ammonium persulfate, hydrochloric acid (ACS Reagent, 37%), ammonium hydroxide, and Orange G (OG) were purchased from Sigma-Aldrich. Anhydrous ethanol was received from Fischer Scientific. Deionized water was used in all the experiments.

7.3.2. Synthesis of SBA-15 mesoporous silica

First, 4 g Pluronic® 123 was mixed with a solution containing 20 mL concentrated hydrochloric acid and 130 mL deionized water, and the solution was stirred at 45 °C. After the Pluronic® 123 was dissolved completely, 8.5 g TEOS was added drop-wise into the solution. The solution was vigorously stirred at 45 °C for 20 h, and then kept in oven at 80 °C for 24 h under static condition. The solution was filtered, and the resulting white precipitate was washed copiously with deionized water and dried at 60 °C in oven, giving the as-synthesized SBA-15. The as-synthesized SBA-15 was then calcined at 550 °C for 5 h to remove the Pluronic®123 templates in it. This finally resulted in the desired mesoporous SBA-15 material.

7.3.3. Synthesis of H^+-PANI/SBA-15 and PANI/SBA-15

First, 150 mg SBA-15 was dispersed uniformly in 30 mL deionized water by sonication. Then, 0.3 mL (3.28 mmol) of aniline was added to the above suspension, and the mixture was stirred for 4 h at room temperature. After adjusting the suspension's pH to 4 by adding some hydrochloric acid (1 M), the mixture was stirred for another 4 h in an ice bath (0-5 °C) to let the protonated aniline disperse uniformly. Into the above suspension, a solution prepared by dissolving 750 mg ammonium persulfate (3.28 mmol) in 1 mL deionized water was slowly added drop-wise. The polymerization of aniline, forming polyaniline (PANI), then started to take place immediately, as indicated by the change in color of the dispersion from white to dark green. The polymerization was let to go for 10 h. The solid product (H^+-PANI/SBA-15) was then collected by centrifugation and washed with copious amount of deionized water and ethanol until the supernatant became clear. The resulting solid product was the emeraldine salt form of PANI supported onto SBA-15, named H^+-PANI/SBA-15.

For comparative studies, PANI/SBA-15 (the emeraldine base form of PANI supported onto SBA-15) was also synthesized. This was done by stirring 20 mg H^+-PANI/SBA-15 in 40 mL

aqueous ammonia solution (0.01 M) for 4 h, and then centrifugation of the suspension and washing the recovered precipitate *via* sonication with ethanol, followed by centrifugation and decantation. The color of the sample changed from dark green to dark blue, indicating the transformation of H^+-PANI/SBA-15 to PANI/SBA-15.

7.3.4. Synthesis of H^+-PANI and PANI

To synthesize H^+-PANI, 1 mL (11 mmol) of aniline was mixed with 100 mL deionized water and the solution was stirred for 4 h at room temperature. The pH of the solution was adjusted to 4 by adding some hydrochloric acid (1 M) into it. The solution was further stirred for another 4 h in an ice bath (0-5 °C) to let the protonated aniline disperse uniformly. Then, 2.5 g ammonium persulfate (11 mmol) was dissolved in 1 mL deionized water and slowly added, drop-wise, to the above suspension, to initiate the polymerization of aniline. The polymerization reaction was let to go for 10 h. The green solid product, which was recovered *via* centrifugation, was washed with deionized water, followed by ethanol. This resulted in the hydrochloric acid-doped PANI, or H^+-PANI.

For comparative studies, the undoped form of H^+-PANI (or PANI) was also synthesized by treating 20 mg H^+-PANI with 40 mL ammonia solution (0.01 M) for 4 h, and then washing the resulting polymer with ethanol and recovering it from the solution *via* centrifugation, followed by decantation.

7.3.5. Standard curves for concentration of Orange G (OG) versus absorbance

The absorbance of different concentrations (2, 4, 5, 10, 15, 20, 30, and 40 μg/mL) of OG in both PBS and deionized water was measured by UV-Vis spectroscopy in the range of 300 nm to 800 nm. The absorption maximum for OG occurs at 480 nm, and by using the band's intensity

at this wavelength, the correlation between intensity and concentration of OG with the Beer-Lambert equation was determined. Specifically, two equations, one for water and another for PBS, were obtained and then used to calculate the amount of OG adsorbed by the materials in the adsorption experiments.

7.3.6. Characterizations and instrumentations

Transmission electron microscope (TEM) images were taken with a Topcon 002B TEM microscope operating at 200 KV. Scanning electron microscopic (SEM) images were obtained using a Zeiss Sigma field emission scanning electron microscope (FESEM). UV-Vis spectra (including solid UV-Vis) were acquired with a Lambda 950 spectrophotometer (PerkinElmer). Nitrogen adsorption-desorption isotherms were performed using a Micromeritics Tristar-3000 instrument. The sample was degassed at 333 K for 8 h under a flow of nitrogen gas before each measurement. From the adsorption isotherms and data, the surface area and pore size distributions of the materials were determined by Brunauer-Emmett-Teller (BET) method and Barrett-Joyner-Halenda (BJH) method, respectively. pH values of solutions were determined with Accumet pH meter 915 (Fisher Scientific). FTIR spectra were recorded using a Thermo Nicolet Avatar 360 FTIR spectrometer. Thermogravimetric analyses (TGA) of the materials were performed on PerkinElmer TGA7 instrument.

7.4. Results and Discussion

In this communication, we report the synthesis of SBA-15- supported hydrochloric acid-doped PANI/SBA-15 (H^+-PANI/SBA-15) with high surface area and the ability of the material to remove the anionic dye OG from aqueous solution (**Figure 7.1**). We also show that the adsorption capacity of H^+-PANI/SBA-15 for OG is much higher than that of hydrochloric acid-doped PANI

(conventional emeraldine salt or H^+-PANI). The significantly improved adsorption capacity of H^+-PANI/SBA-15, compared with H^+-PANI, is made possible by the high surface area generated in H^+-PANI with the aid of the inorganic porous support material SBA-15.

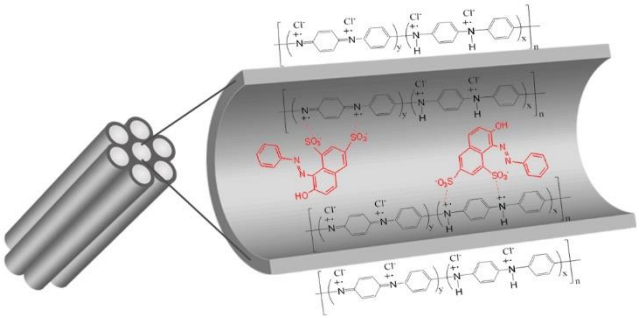

Figure 7.1. Schematic representation of the adsorption process of OG in H^+-PANI/SBA-15.

Details of the synthetic procedures that we employed to make SBA-15, H^+-PANI/SBA-15, and H^+-PANI are provided below. First, SBA-15 whose surfactant templates were removed by calcination was synthesized. Using $NH_4S_2O_8$ as the oxidizing agent, aniline was then polymerized on the walls of the SBA-15 at pH = 4, as illustrated in **Figure 7.2**.[20] This finally led to the formation of the desired material, H^+-PANI/SBA-15. By following a similar procedure but without using SBA-15 as the template, the reference material H^+-PANI was also synthesized. For comparative studies, the deprotonated counterparts, PANI/SBA-15 and PANI, were obtained by treating the H^+-doped materials (*i.e.*, H^+-PANI/SBA-and H^+-PANI, respectively) with dilute aqueous NH_4OH solution. The structures of all the materials were then characterized, and their adsorption properties were evaluated in phosphate buffered saline (PBS) and distilled water.

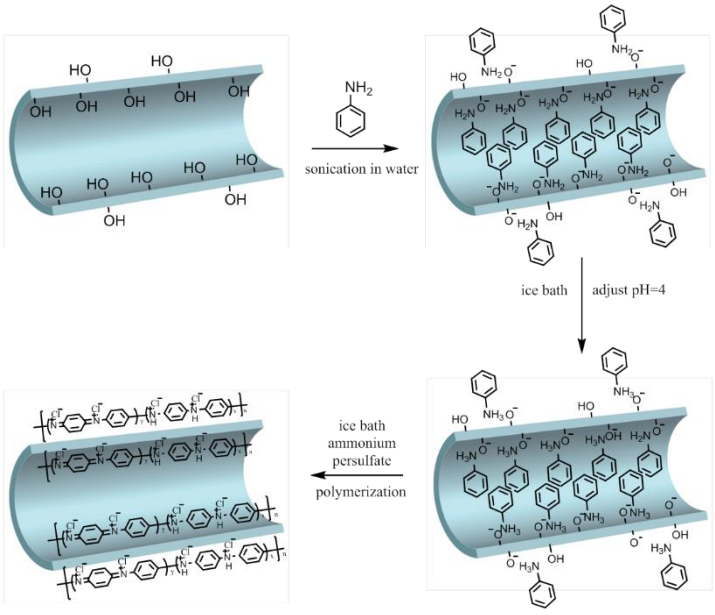

Figure 7.2. Schematics of the synthesis of H^+-PANI/SBA-15 material.[21]

The formation of H^+-PANI on SBA-15, or the presence H^+-PANI in H^+-PANI/SBA-15 after the polymerization process, was qualitatively discerned from the change in the SBA-15 color from white to the characteristic dark green color of the emeraldine salt (H^+-PANI). Moreover, upon treatment with NH_4OH solution, the dark green color of H^+-PANI/SBA-15 turned dark blue, indicating its transformation to the emeraldine base (PANI/SBA-15) (**Figure 7.3**). This was further confirmed from the diffuse UV-Vis spectra of H^+-PANI/SBA-15 and PANI/ SBA-15 (**Figure 7.4**), which showed the typical absorption bands as well as corresponding shifts associated with PANI and H^+-PANI as reported in a previous work.[21]

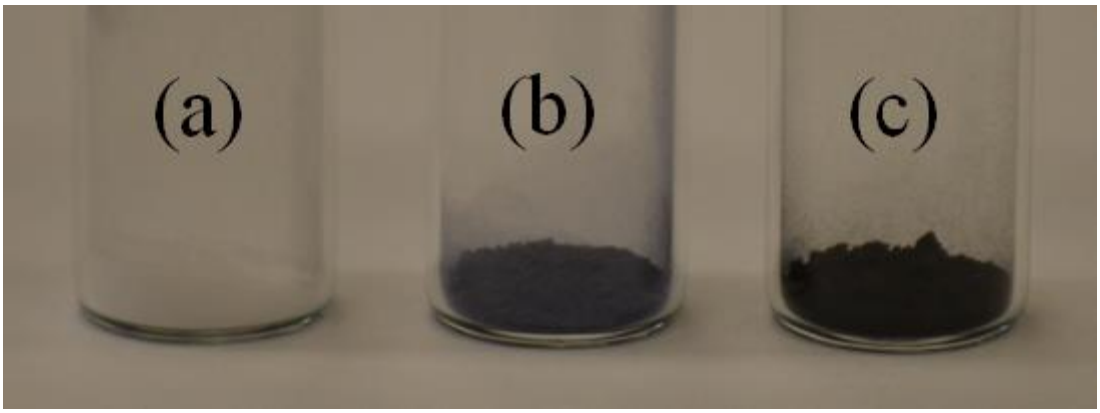

Figure 7.3. Photographs of SBA-15 (white color) (a), PANI/SBA-15 (dark blue) (b), and H^+-PANI/SBA-15 (dark green) (c).

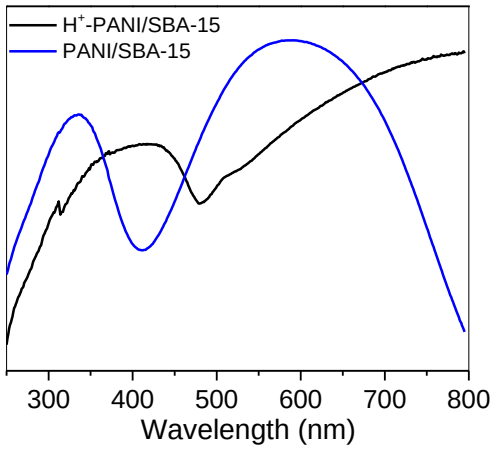

Figure 7.4. Diffuse UV-Vis spectra of H^+-PANI/SBA-15 and PANI/SBA-15.

The morphologies of SBA-15, H^+-PANI and H^+-PANI/SBA-15 materials were investigated by transmission electron microscopy (TEM). The representative TEM images of SBA-15 (**Figure 7.5a** and **Figure 7.6a**) showed particles with rod-like morphology and hexagonally ordered channel pores. The TEM images of H^+-PANI/SBA-15 revealed similar ordered channel pore structures, except that the structures looked smeared, presumably due to the encapsulation of PANI in the pores of the material (**Figure 7.5b** and **Figure 7.6b**). Nevertheless,

this result indicated that the original structure of SBA-15 remained intact after the polymerization process.[22] Additionally, dark layers and dots could be seen along the outer surfaces of H^+-PANI/ SBA-15, concomitant with the formation/presence of the polymer. On the other hand, the TEM image of H^+-PANI (**Figure 7.7**) showed some particles, without apparent pores revealing the compact structure of the polymer, as expected.[23]

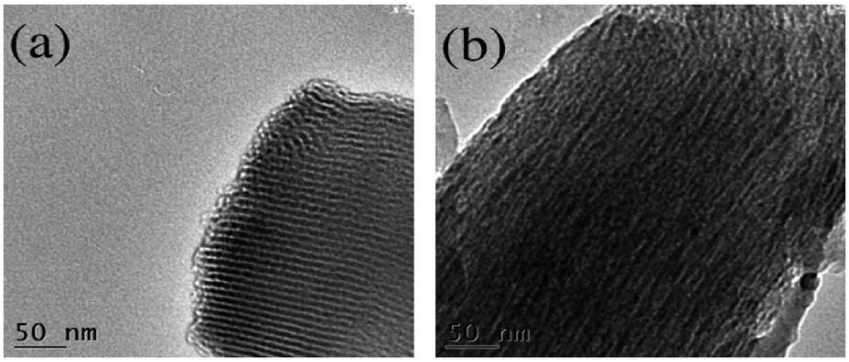

Figure 7.5. TEM images of SBA-15 (a) and H^+-PANI/SBA-15 (b).

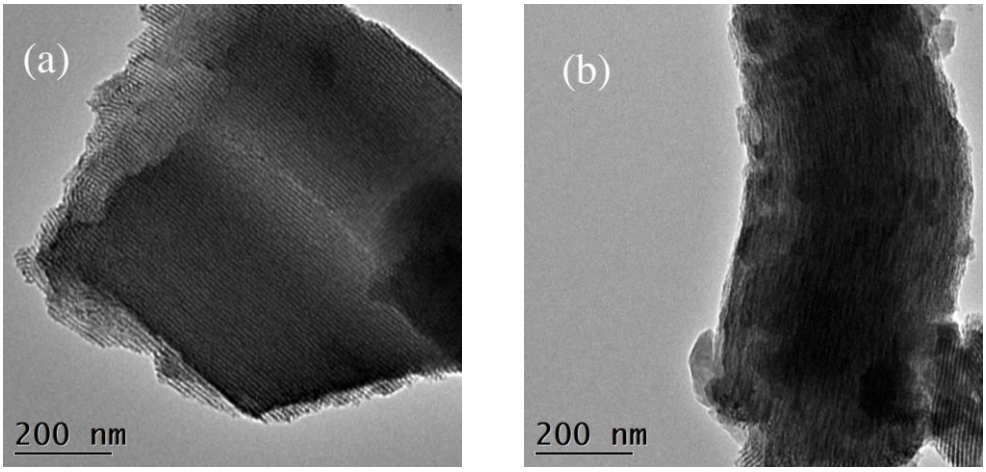

Figure 7.6. TEM images of SBA-15 (a) and H^+-PANI/SBA-15 (b).

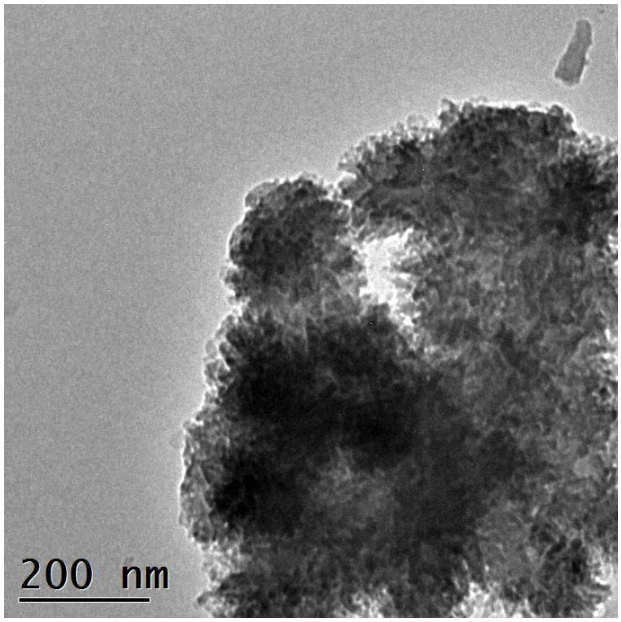

Figure 7.7. TEM image of H^+-PANI.

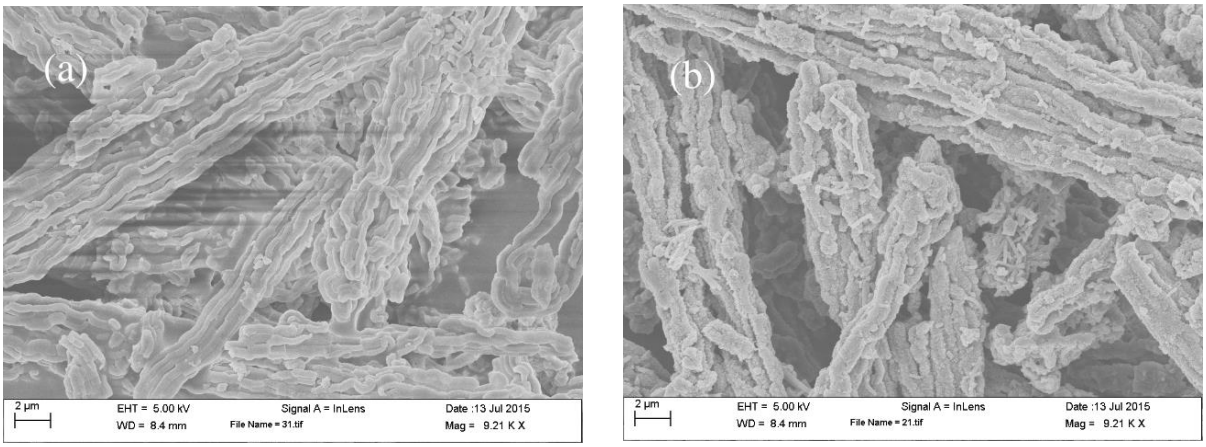

Figure 7.8. SEM images of SBA-15 (a) and H^+-PANI/SBA-15 (b). The SEM images of H^+-PANI/SBA-15 show rod-like morphology akin to that of SBA-15, the material used as a template. Moreover, the surfaces of H^+-PANI/SBA-15 appear rougher than those of SBA-15, suggesting that the outer surfaces of the SBA-15 particles in the former most likely possess PANI.

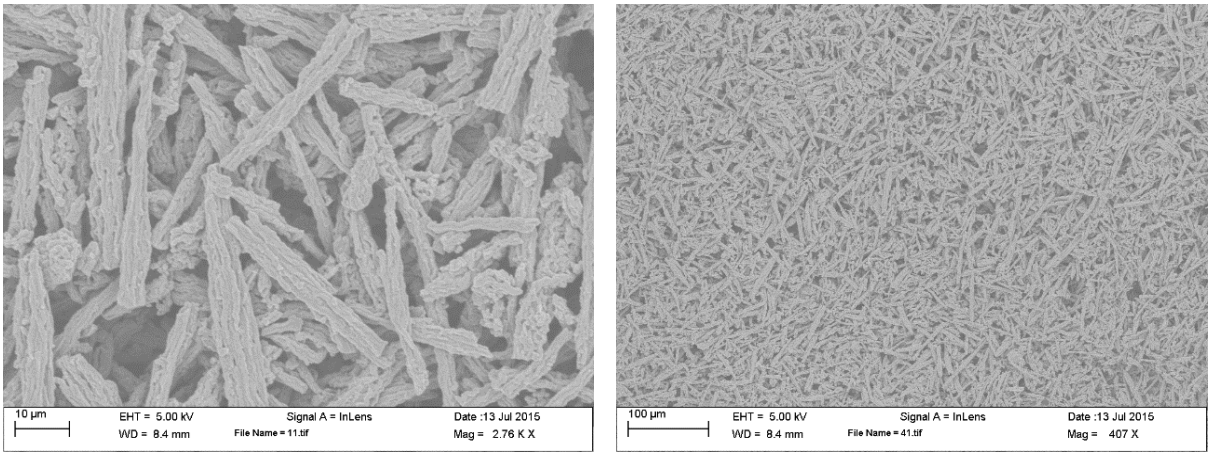

Figure 7.9. Lower magnification SEM images of H^+-PANI/SBA-15. The particles were recovered after centrifugation and washing (similar procedure was used to collect H^+-PANI in Figure 7.8). As no isolated polymeric particles were observed in the images, the images confirm that the polymerization process has occurred mainly on the surfaces of SBA-15, or barely in the solution.

The polymerization of PANI inside the pores of SBA-15 was further confirmed from the changes in the porous properties of the materials, as measured with N_2 adsorption/desorption (**Figure 7.10**). Both SBA-15 and H^+-PANI/SBA-15 showed the type IV isotherm with the H1 type hysteresis loop, the characteristic isotherm for mesoporous materials. This suggested that the inclusion of PANI in the pores of SBA-15 did not compromise the mesoporous structure of SBA-15. Moreover, the capillary condensation step of H^+-PANI/SBA-15 shifted to a lower relative pressure (P/P_0) compared with that of SBA-15, indicating that H^+-PANI/SBA-15 possessed smaller pores than SBA-15. Similarly, the pore volume of H^+-PANI/SBA-15 (0.4 $cm^3\ g^{-1}$) was lower than that of SBA-15 (0.7 $cm^3\ g^{-1}$). (As can be expected, the as-synthesized SBA-15, whose pores were completely filled with surfactant, had a much smaller pore volume of 0.19 $cm^3\ g^{-1}$). These results were all indicative of the presence of PANI in the inner pore walls of H^+-PANI/SBA-15.

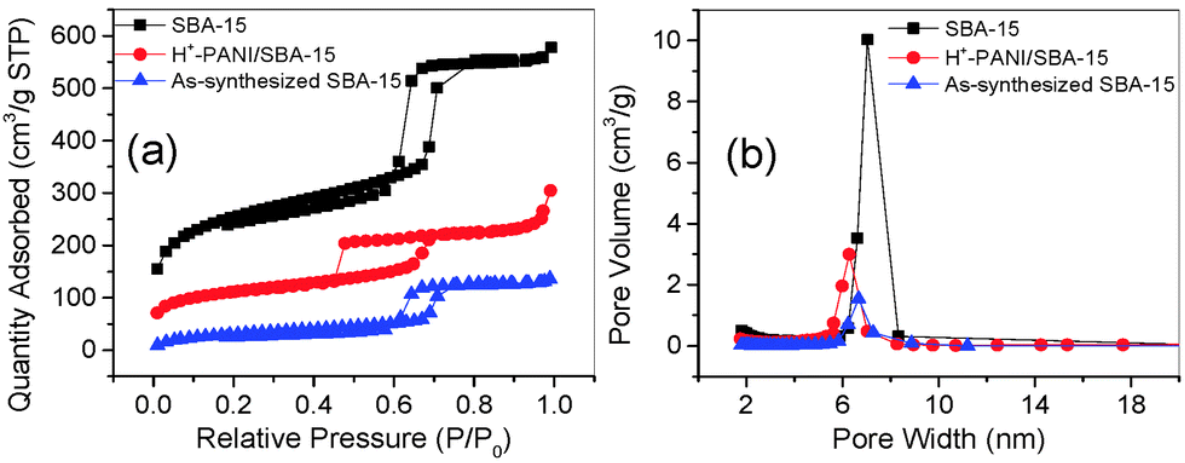

Figure 7.10. (a) N_2 adsorption/desorption isotherms and (b) pore size distributions of as-synthesized SBA-15, SBA-15 and H^+-PANI/SBA-15. The pore size distribution graphs are obtained using the data in the adsorption branches of the isotherms.

Meanwhile, the pore size distributions of H^+-PANI/SBA-15 SBA-15, determined by the Barrett-Joyner-Halenda (BJH) method (**Figure 7.10b**), showed that the former had a slightly lower average pore size (6.27 nm) than SBA-15 whose average pore size was 7.03 nm. This relatively insignificant change in pore size suggested that the polymerization of PANI occurred only along the cylindrical pore surfaces of SBA-15. The surface areas of SBA-15 and H^+-PANI/ SBA-15 were found to be 849 $m^2\ g^{-1}$ and 373 $m^2\ g^{-1}$, respectively (for comparison, the surface area of as-synthesized SBA-15 was 111 $m^2\ g^{-1}$). These results clearly suggested that the polymerization of PANI took place within the pores of SBA-15, with the structures being predominantly formed on the pore walls of SBA-15. On the other hand, N_2 adsorption/desorption porosimetry of H^+-PANI showed a type II isotherm, which corresponds to a non-porous or low surface area material (**Figure 7.11**). Moreover, the surface area of H^+-PANI was only around 35 $m^2\ g^{-1}$, indicating its low porosity, in line with its TEM image as discussed above.

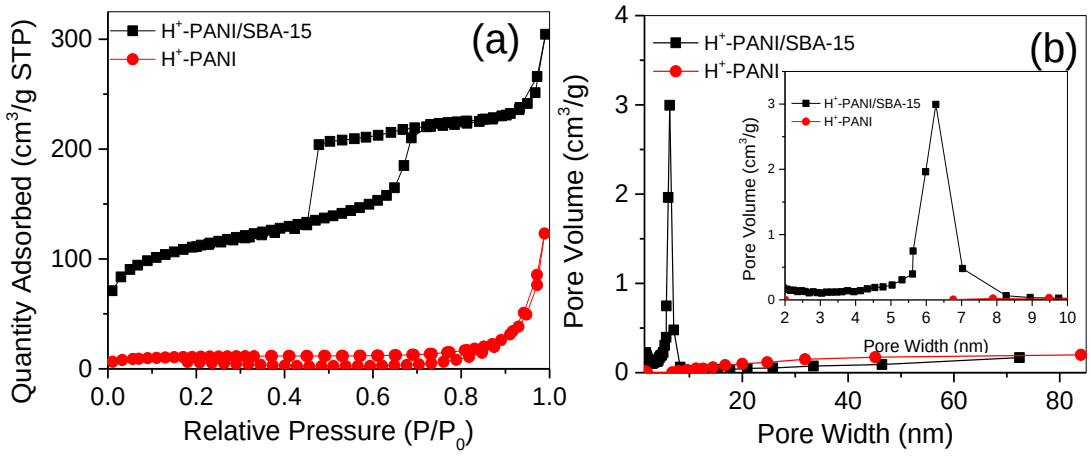

Figure 7.11. (a) N_2 adsorption/desorption isotherms and (b) pore size distributions of H^+-PANI/SBA-15 and H^+-PANI materials.

Using thermogravimetric analysis (TGA) (**Figure 7.12**), the successful synthesis of PANI on SBA-15 was further deduced and the amount of PANI was quantitatively determined. While the as-made SBA-15 showed 47.9% weight loss from 100 to 700 °C. SBA-15 showed only 2.2% weight loss. This indicated that the latter had almost no surfactant (note that even the 2.2% weight loss from it was most likely only due to the condensation surface silanol groups). The weight loss from H^+-PANI/SBA-15 in the same temperature range was, however, higher (39.2%), and it could be attributed to PANI. It is also worth noting that compared with H^+-PANI, whose decomposition started at *ca*. 250 °C, the decomposition of the nanocomposite material H^+-PANI/ SBA-15 started at *ca*. 350 °C. This indicates that the covalent attachment of PANI with the SBA-15 host material enhances the thermal stability of PANI, as documented for similar materials before.[20]

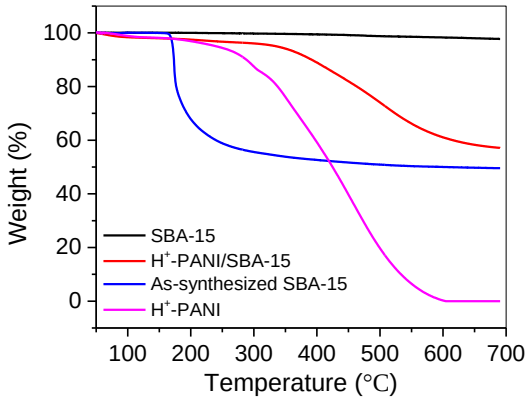

Figure 7.12. TGA curves of as-synthesized SBA-15, SBA-15, H^+-PANI, and H^+-PANI/SBA-15.

Further evidence of the presence of PANI on the SBA-15 was confirmed by FTIR spectroscopy (**Figure 7.13**). The FTIR spectrum of SBA-15 showed absorption bands at 1078, 812, and 460 cm^{-1} , which correspond to the characteristic asymmetric and symmetric Si-O-Si stretching and Si-O-Si bending modes, respectively, of the silica material.[24,25] The typical adsorption bands of H^+-PANI were also observed in the spectrum. In particular, peaks at 1570 and 1492 cm^{-1}, which correspond to C-N and, C=C stretching of the quinoid and benzenoid rings, respectively; a peak at 1299 cm^{-1}, which can be assigned to the C-N stretching mode of the benzenoid ring; and a peak at 1140 cm^{-1}, due to aromatic C-H in-plane bending,[26] have been observed. The spectrum of H^+-PANI/SBA-15, the one obtained after polymerization, showed the typical peaks expected for both SBA-15 and H^+-PANI, except that some of the peaks were slightly shifted to a higher wavenumbers (including the C=N stretching peak of quinoid rings at 1578 cm^{-1}, the C=C stretching peak of the benzenoid rings at 1500 cm^{-1}, and the C-N stretching mode of benzene ring at 1316 cm^{-1}). The shifts of these peaks are not totally unprecedented considering that the polymer has limited flexibility as a result of its covalent bonding and hydrogen bonding interactions with the SBA-15.[27] Nevertheless, overall, the FTIR results corroborated that the polymerization of aniline took place in SBA-15 and that PANI was present in H^+-PANI/SBA-15.

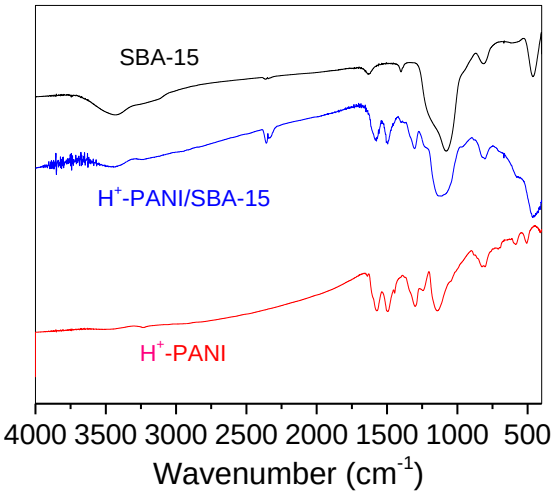

Figure 7.13. FTIR spectra of SBA-15, H^+-PANI, and H^+-PANI/SBA-15.

As mentioned above, the positively charged backbone of PANI has the ability to adsorb anionic dyes from aqueous solutions.[14] Hence, in this work the adsorption properties of the high surface area containing composite nanomaterial we synthesized (H^+-PANI/SBA-15) and its reference materials were tested using the anionic dye OG. To study the role of the positively charged backbone of PANI for adsorption of OG, additionally the adsorption properties of the control samples (emeraldine base of PANI and PANI/SBA-15) were evaluated.

OG, which is an organic dye that contains two sulfonate groups ($-SO_3Na$), dissociates and remains ionized in PBS and distilled water. Thus, OG can serve as a good model anionic pollutant. More importantly though, OG is widely used as dying agent in wool, silk, paper, leather, and wood industries, but finds its way into water systems and causes mutagenesis, cancer, allergy, and other harmful effects in animals.[2,3] So, the removal of OG and similar anionic dyes from contaminating wastewater systems and industrial effluents to ameliorate their harmful effects on living organisms is critically important.[2]

To this end, the adsorption properties of H^+-PANI/SBA-15 were evaluated in PBS (pH 7.4) and distilled water (pH 5.6). Before the adsorption tests, standard curves of absorbance (at 480 nm) *vs*. concentration of OG in both types of solutions were plotted using the Beer-Lambert law (**Figure 7.14**), from which two linear equations were obtained: (for OG concentration between 2 and 40 ug mL^{-1}), "concentration (ug mL^{-1}) = (absorbance 0.0297)/0.0343" in PBS and "concentration (ug mL^{-1}) = (absorbance 0.0197)/0.0344" in distilled water. The equations were then applied to determine the amount of OG removed from the solutions. Before the actual adsorption experiments were carried out, the stability of OG was tested by measuring the absorbance of 25 ug mL^{-1} of OG at 480 nm for 6 h at room temperature (**Figure 7.15**). The results showed that the absorbance barely changed, confirming that OG is stable in both PBS and distilled water.

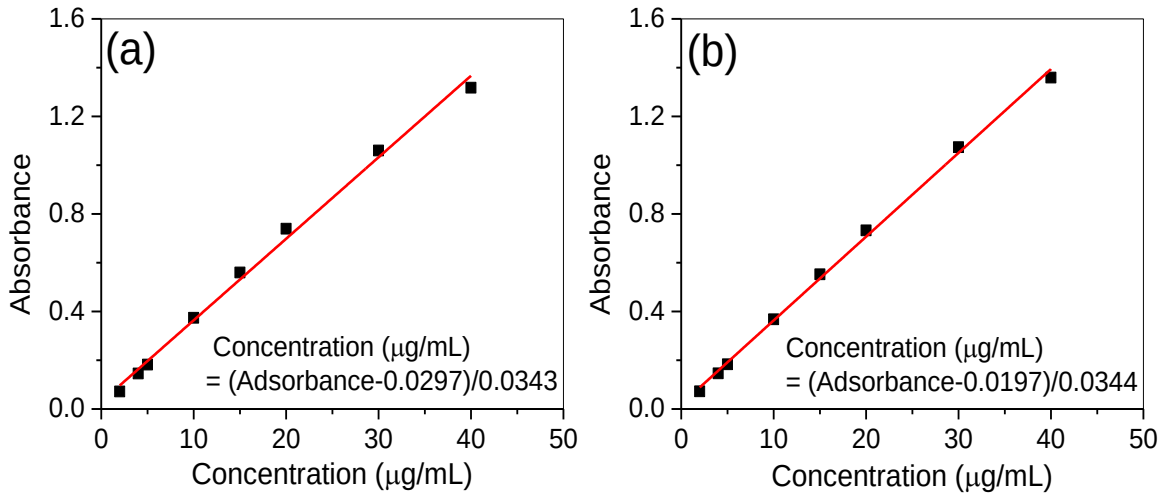

Figure 7.14. Standard curves based on the absorbance of the absorption maximum of OG at 480 nm versus concentration of OG in PBS (a) and distilled water (b).

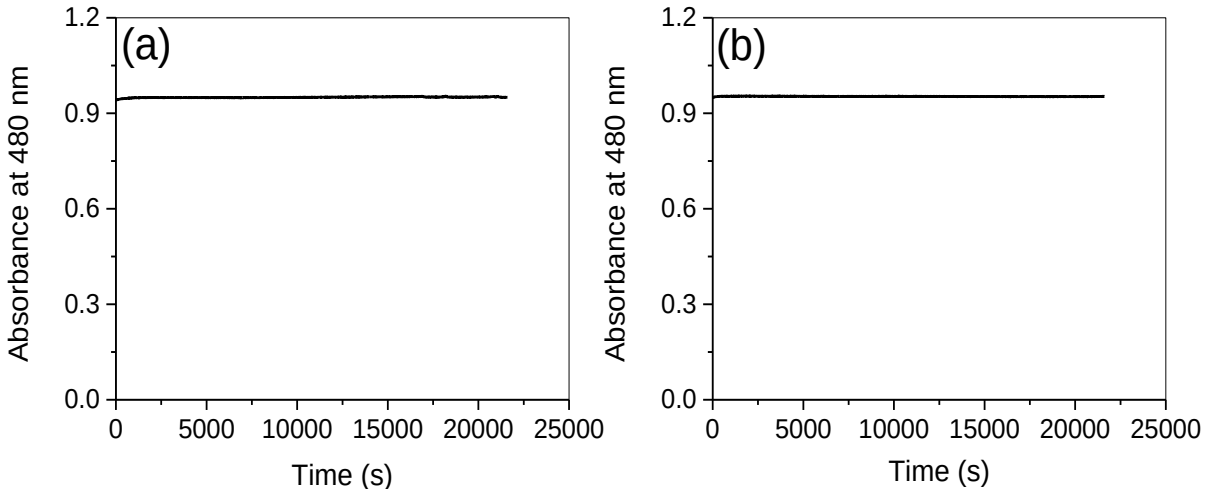

Figure 7.15. Absorbance of 25 μg/mL OG at 480 nm in PBS (a) and distilled water (b) measured for 6 h.

The actual adsorption results in PBS at pH 7.4 are displayed in **Figure 7.16**. The results showed that SBA-15 exhibited barely any adsorption toward OG. This is most likely because at pH 7.4, some of the -OH groups on the surface of SBA-15 get ionized, making the material negatively charged, and thus unable to attract the negatively charged OG molecules.[28,29] However, thanks to its positively charged backbone and thus its ability to electrostatically interact with the negatively charged sulphonate groups of OG, H^+-PANI showed good adsorption capacity, giving a value of 130 ug OG per mg of the material. More interestingly though, H+ -PANI/SBA-15 showed an even significantly higher adsorption capacity than H^+-PANI, giving a value of 241 ug OG per mg. When normalized with respect to the amount of PANI in the materials, this value actually amounted to 615 ug mg^{-1} of PANI. This result clearly proves that the nanoporous SBA-15 support material in H^+-PANI/SBA-15 improved PANI's adsorption capacity toward the anionic dye OG, by increasing the PANI surface area. On the other hand, the control materials SBA-15, PANI and PANI/SBA-15 were all found to barely adsorb or remove the OG from solutions (**Figure**

7.17). This result suggests that the positively charged backbone of H^+-PANI/SBA-15 is equally important in the adsorption capacity of the material.

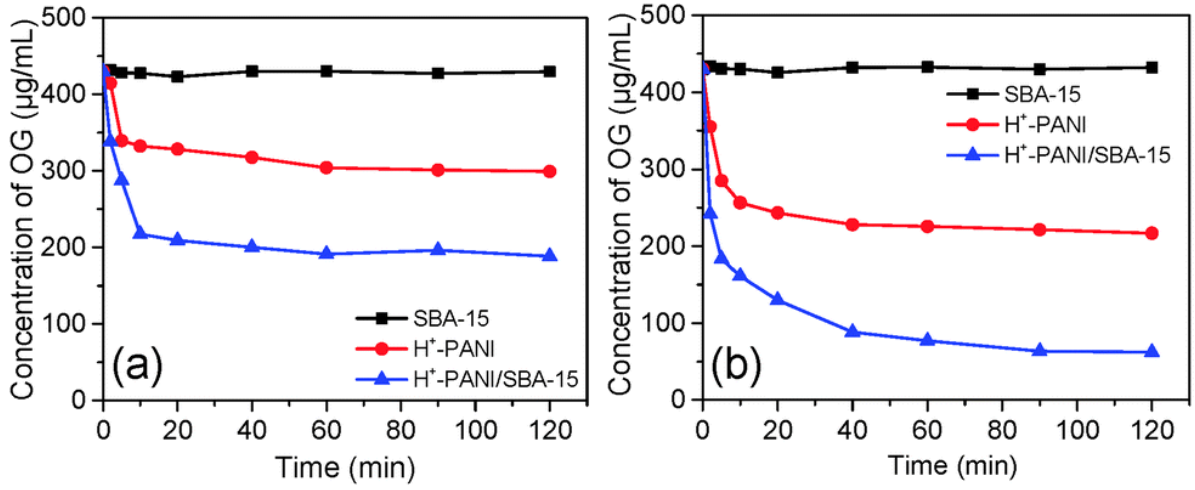

Figure 7.16. Concentration profiles of OG in the presence of SBA-15, H^+-PANI, H^+-PANI/SBA-15 in (a) PBS and (b) distilled water at the initial OG concentration of 420 ug mL^{-1}.

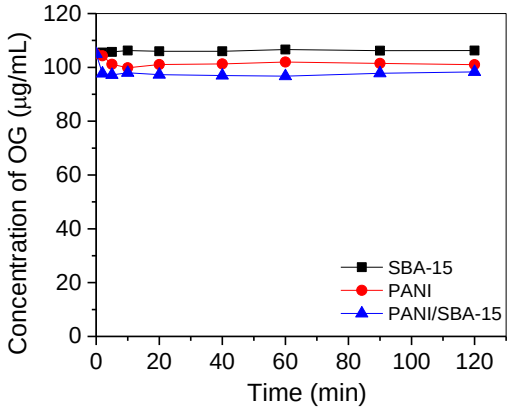

Figure 7.17. Concentration profiles of OG over 2 h in the presence of SBA-15, PANI and PANI/SBA-15 in PBS.

Additional adsorption experiments were performed in distilled water (pH 5.6), and the results are displayed in **Figure 7.16b**. In distilled water, the adsorption capacity of both H^+-PANI and H^+-PANI/SBA-15 was higher, reaching values of 210 ug mg^{-1} (which is similar to what has

been reported for a similar material before[13]) and 368 ug mg^{-1}, respectively. The latter value is actually 939 ug mg^{-1} when it is normalized to the amount of PANI in the material. The generally higher adsorption capacity of the materials in water than in PBS is because distilled water has lower pH and makes the PANI backbone in H^+-PANI and H^+-PANI/ SBA-15 more positively charged and more favorable to interact with the anionic species of OG. Nevertheless, H^+-PANI/SBA-15 still showed much higher adsorption capacity for OG than H^+-PANI did in water too, proving again that the increased surface area in the former was responsible for the higher adsorption capacity of the material.

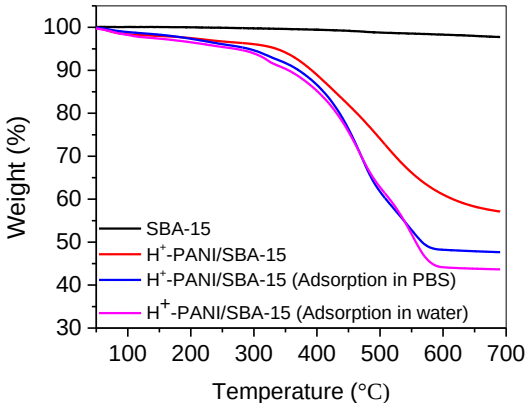

Figure 7.18. Thermogravimetric analysis (TGA) curves of OG-saturated SBA-15, H^+-PANI/SBA-15, OG-saturated H^+-PANI/SBA-15 in PBS, and OG-saturated H^+-PANI/SBA-15 in water.

Using the results in the TGA traces in **Figure 7.18**, the amount of OG in OG-saturated H^+-PANI/SBA-15 from PBS or aqueous OG solutions was determined. The TGA traces display that the weight loss from OG-saturated H^+-PANI/SBA-15 in PBS is 52.34%, whereas that from OG-saturated H^+-PANI/SBA-15-OG in water is slightly higher (56.34%). Further calculations show that the amount of OG adsorbed in PBS and distilled water is 201 μg/mg and 310 μg/mg, respectively. The results clearly confirmed that the adsorption capacity of H^+-PANI/SBA-15 is

higher in water than in PBS, most likely due to the fact that the PANI backbone remains H^+-doped and more positively charged in former than in the latter.

To get a better understanding of the adsorption processes, the adsorption data for H^+-PANI and H^+-PANI/SBA-15 toward OG were fitted with pseudo-first order,[1,30] pseudo-second order[30] and intraparticle diffusion models.[1,31] More detailed information is provided below and the fitting results for pseudo-first order and second order are shown in **Figure 7.19**, **Figure 7.20** and **Table 7.1**. The pseudo-second order model was found to best fit the results obtained for both PBS and distilled water solutions, as the corresponding R^2 values were close to 1 and the calculated adsorption capacity was similar to those obtained from experiments. Moreover, intraparticle diffusion model (**Figure 7.21**) gave linear plots that did not pass through the origin; this indicated that intraparticle diffusion was involved in the adsorption process, but it was not the only rate limiting process. The results (**Figure 7.21**) further suggested that the adsorption process involved two steps.[32] In the first step, OG molecules adsorbed on the exterior surfaces of H^+-PANI and H^+-PANI/SBA-15. This process was fast and completed within 10 min. As the outer surfaces of the material got saturated quickly, the OG molecules continued to enter the spaces between H^+-PANI backbones and within the channel pores of H^+-PANI/SBA-15 in the course of 10 to 90 min time period. So, overall, the results indicated that adsorption process of OG on the adsorbent occurs likely via both external and intraparticle diffusion. More experimental results on mechanistic, equilibrium, kinetic, thermodynamic and regeneration studies of the adsorption of OG on H^+-PANI/SBA-15 are described and discussed below.

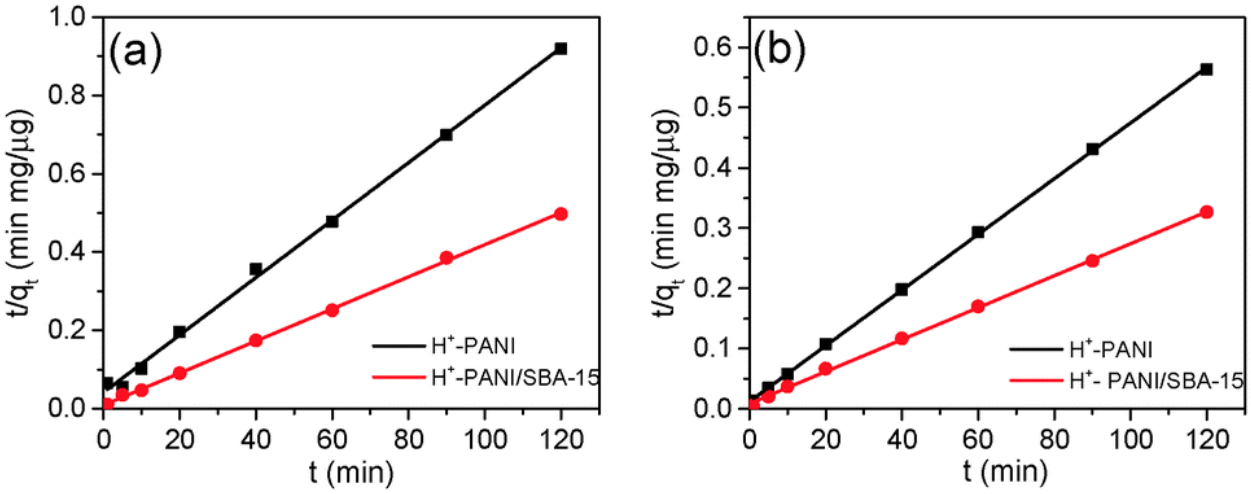

Figure 7.19. Plots based on pseudo-second order model of the data of adsorption of OG by H^+-PANI and H^+-PANI/SBA-15 in PBS (a) and distilled water (b).

7.5. Details of Kinetic and Modeling Studies and Results and Discussions

To study the kinetic behavior of the adsorption of OG in H^+-PANI and H^+-PANI/SBA-15 in both PBS and distilled water, the amount of adsorbent was set at 1 mg/mL in the initial OG concentration of 430 μg/mL at room temperature.

The amount of OG adsorbed at equilibrium q_e (μg/mg) on the adsorbents was then calculated with the following equation:

$$q_e = \frac{(C_0 - C_e)V}{W} \quad (1)$$

where C_0 and C_e (μg/mL) are the liquid phase adsorbate concentration at initial time and at equilibrium, respectively, V is the volume of the solution (mL) and W is the mass of adsorbent used (mg).

The amount of adsorbate in the adsorbent at time t, q_t was calculated by:

$$q_t = \frac{(C_0 - C_t)V}{W} \quad (2)$$

where C_0 and C_t (μg/mL) are the liquid phase adsorbate concentration at initial time and at time t, respectively, V is the volume of the solution (mL) and W is the mass of adsorbent used (mg).

To determine the process by which OG is adsorbed in the materials, pseudo-first order, pseudo-second order and intraparticle diffusion models were tested on the adsorption data obtained for OG on the H^+-PANI/SBA-15 as well as the control materials, and the validity of the models was checked by linear equation analysis of $log(q_e - q_t)\ vs\ t$, $t/q_t\ vs\ t$, and $q_t\ vs\ t^{0.5}$ and their corresponding correlation coefficients, R^2.

7.5.1. Pseudo-first order

The pseudo-first order rate expression can be given by Lagergren equation[1] in the form of:

$$\frac{dq_t}{dt} = k_1(q_e - q_t) \quad (3)$$

where q_e and q_t (μg/mg) refer to the solid phase adsorbate concentration at equilibrium and at time t (min), respectively, and k_1 is the rate constant of pseudo-first order adsorption (min^{-1}). Integrating equation (3) with boundary conditions at $t = 0$, $q_t = 0$ and $t = t$, $q_t = q_t$, results in:

$$\log(q_e - q_t) = logq_e - \frac{k_1 t}{2.303} \quad (4)$$

7.5.2. Pseudo-second order

The pseudo-second order kinetic rate equation is expressed as:[31]

$$\frac{dq_t}{dt} = k_2(q_e - q_t)^2 \quad (5)$$

where q_e and q_t (μg/mg) have the same meaning as in equation (3), and k_2 is the rate constant of pseudo-second order adsorption (mg/μg min). After integrating and rearranging equation (5) using the boundary conditions $t = 0$ to $t = t$ and $q_t = 0$ to $q_t = q_t$, the following equation (Eqn. 6) can be obtained:

$$\frac{t}{q_t} = \frac{1}{k_2 q_e^2} + \frac{t}{q_e} \tag{6}$$

If pseudo-second order kinetics is applicable, the plot of $t/q_t \; vs \; t$ should give a linear relationship, and there is no need to know any parameter beforehand to determine q_e and k_2 (or they can be determined from the slope and intercept of the plot, respectively).

7.5.3. Intraparticle diffusion model

The third model, intraparticle diffusion model, which was designed by Weber and Morris, is shown in equation (7), and it was also tested on our data.[1,32]

$$q_t = k_i t^{0.5} + C \tag{7}$$

where k_i is the intraparticle diffusion rate constant in μg/mg $min^{0.5}$ and C is a y-intercept (μg/mg), which is proportional to the boundary layer thickness. If the intraparticle diffusion is the rate-controlling factor, then the plot of $q_t \; vs \; t^{0.5}$ should be linear. Moreover, if the plot passes through the origin, then the intraparticle diffusion can be said to be the only rate-limiting factor.

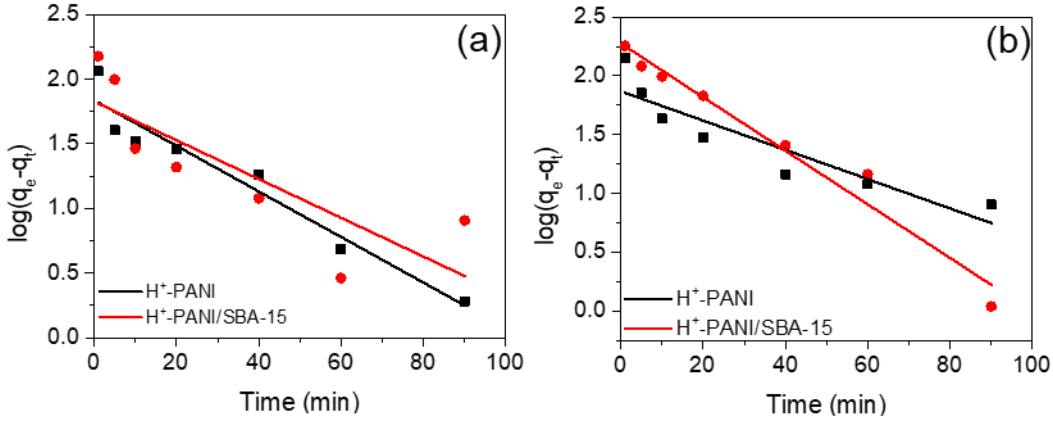

Figure 7.20. Pseudo-first order model-based plots of the adsorption of OG in H^+-PANI and H^+-PANI/SBA-15 in PBS (a) and distilled water (b).

Table 7.1. Comparison of the pseudo first and second order adsorption rate constants (k_1 and k_2) and experimental and calculated values of q_e for adsorption of OG by H^+-PANI and H^+-PANI/SBA15 in PBS and distilled water.

	First order kinetic model				Second order kinetic model		
	q_e (exp) (µg/mg)	k_1 (min^{-1})	q_e (cal) (µg/mg)	R^2	k_2 (mg/µg min)	q_e (cal) (µg/mg)	R^2
Adsorption in PBS							
H^+-PANI	130.61	4.06×10^{-2}	68.64	0.930	1.28×10^{-3}	136.42	0.998
H^+-PANI/SBA-15	241.60	3.45×10^{-2}	67.17	0.611	1.81×10^{-3}	243.90	0.999
Adsorption in water							
H^+-PANI	216.72	2.87×10^{-2}	73.96	0.810	1.75×10^{-3}	216.45	1
H^+-PANI/SBA-15	367.68	5.26×10^{-2}	188.54	0.962	8.08×10^{-4}	377.36	0.999

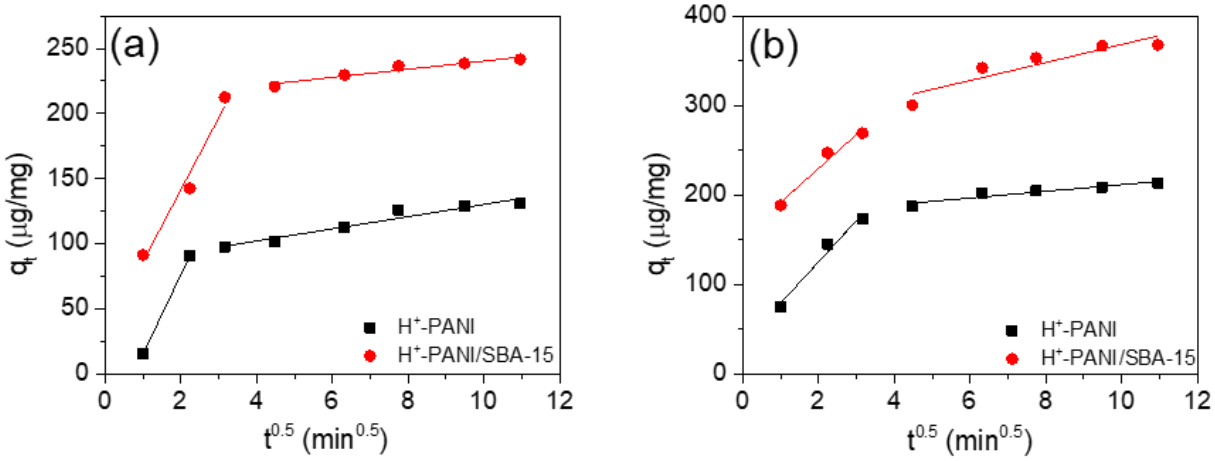

Figure 7.21. Intraparticle diffusion model-based plots of adsorption of OG by H^+-PANI and H^+-PANI/SBA-15 in PBS (a) and distilled water (b).

Table 7.2. Kinetic data of intraparticle diffusion model of OG adsorption by H^+-PANI and H^+-PANI/SBA15 in PBS and distilled water.

	Intraparticle diffusion model			
	k_{i1} (μg/mg $min^{0.5}$)	R_{i1}^2	k_{i2} (μg/mg $min^{0.5}$)	R_{i2}^2
Adsorption in PBS				
H^+-PANI	60.74	----	4.68	0.939
H^+-PANI/SBA-15	55.26	0.971	3.15	0.926
Adsorption in water				
H^+-PANI	46.19	0.976	3.73	0.896
H^+-PANI/SBA-15	37.94	0.97	10.03	0.855

7.6. Further Study of Adsorption Properties of OG in H^+-PANI/SBA-15

The equilibrium and kinetic adsorption experiments were performed with initial OG concentration ranging from 50-500 μg/mL and adsorbent concentration of 1 mg/mL at room temperature. The results are compiled below.

7.6.1. Effect of initial concentration and contact time

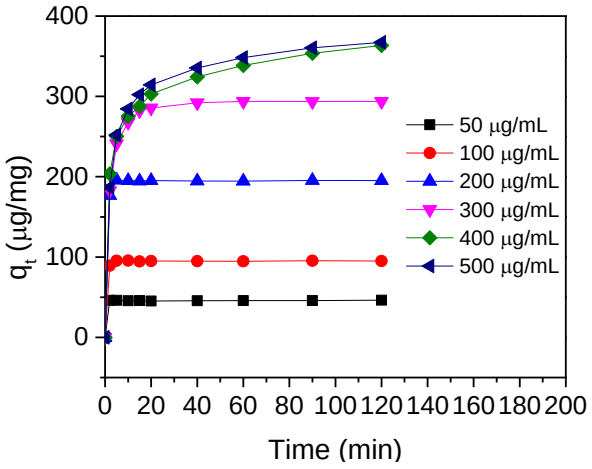

Figure 7.22. Amount of OG adsorbed per unit mass of H^+-PANI/SBA-15 from solutions with different initial concentrations of OG.

Figure 7.22 shows the variation of the amount of OG adsorbed on H^+-PANI/SBA-15 versus time from solutions with different initial concentrations of OG. It was observed that for OG solutions with initial concentrations between 50-200 μg/mL, the time needed to reach equilibrium was less than 10 min, while for higher initial OG concentration of 300-500 μg/mL, equilibrium could take as much as 2 h. To make sure that the full equilibrium was attained, the adsorption experiments were run for 6 h. This adsorption process can be explained as follows. First, the dye molecules encounter the outer surfaces of H^+-PANI/SBA-15 and get adsorbed there. They then get increasingly diffused into the pores of the adsorbent. Thus, OG with higher initial concentration will take relatively longer contact time to reach an equilibrium point, as there are more molecules to diffuse into the pores, in a process that takes relatively longer time.

It can also been seen that the amount of OG adsorbed in H^+-PANI/SBA-15 expectedly increases with time; however, at some point it reaches a constant value where no additional OG

can be adsorbed by the material. At this point, the amount of OG adsorbing into the material and desorbing from the material are said to be in a state of dynamic equilibrium. Similar phenomena are reported for the adsorption of other dyes and molecules, such as methylene blue on activated carbon prepared from coconut husk and tetracycline on NaOH-activated carbon produced from macadamia nut shells.[34,35]

7.6.2. Effect of pH

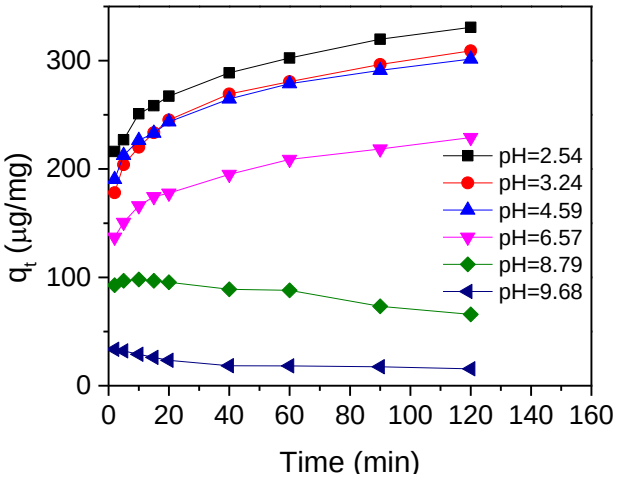

Figure 7.23. Adsorption profiles of OG dye in the presence of H^+-PANI/SBA-15 at different pH values.

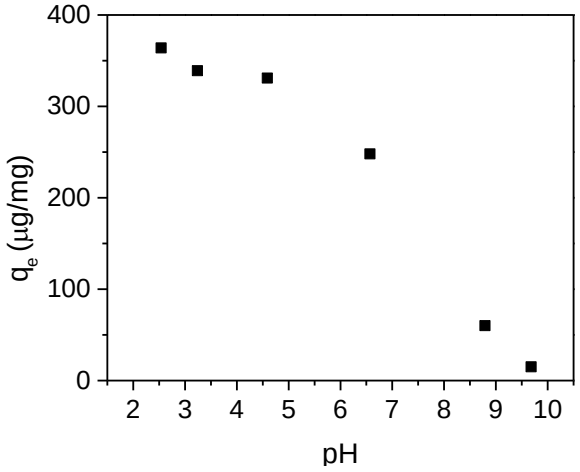

Figure 7.24. The amount of OG adsorbed in H^+-PANI/SBA-15 at equilibrium versus the pH of the solution.

The pH of the solution plays an important role in the adsorption of OG, as shown in **Figure 7.23** and **Figure 7.24**. The experiments were performed with a constant initial concentration of OG of 500 μg/mL. As can be seen in the results, the amount of OG adsorbed in the material decreases as the pH value of the solution increases (or vice versa). This phenomenon can be explained by the fact that lower pH makes the backbone of H^+-PANI/SBA-15 more positively charged, enhancing its ability to exert electrostatic attractions toward the negatively charged anionic OG adsorbate molecules. On the other hand, at higher pH (*e.g.*, pH 9.68), the amount of OG adsorbed in the material is negligible, which means most of the adsorbent is transformed to its emeraldine base form at this pH and is no longer able to pick up the OG molecules.[14]

7.6.3. Adsorption isotherms

Adsorption isotherms describe how the adsorbate molecules distribute between the liquid and solid phase when the system reaches equilibrium. Fitting experimental data into different

isotherm models can give information about how adsorbate molecules interact with adsorbent surfaces.

The equilibrium adsorption isotherm of OG on H^+-PANI/SBA-15 is shown in **Figure 7.25**. At low OG concentrations, the graph shows a steep increase, indicating H^+-PANI/SBA-15' strong affinity toward OG molecules. However, at higher OG concentrations, the graph plateaus and the material is able to no longer adsorb more OG after a certain point (which means it reaches its adsorption capacity).

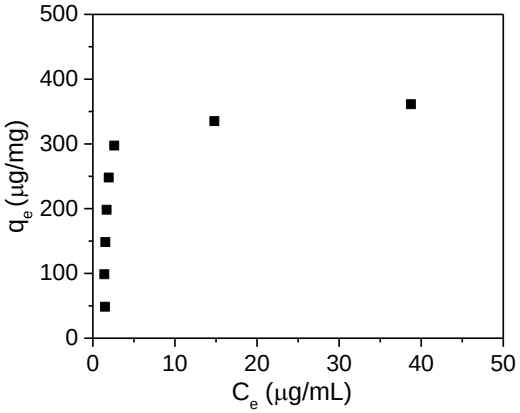

Figure 7.25. Equilibrium adsorption isotherm of OG on H^+-PANI/SBA-15.

The isotherm models of Langmuir, Freundlich and Temkin were applied on the data, and the applicability of each model to describe the adsorption process is then judged by the value of its correlation coefficient values (R^2).

7.6.3.1. Langmuir isotherm

The Langmuir isotherm is given as following:[35]

$$q_e = \frac{q_m K_L C_e}{1 + K_L C_e} \quad (8)$$

where q_e is the equilibrium solid phase adsorbate concentration (μg/mg), q_m is the maximum adsorption capacity (μg/mg), C_e is the equilibrium liquid phase adsorbate concentration (μg/mL), and K_L is the Langmuir adsorption constant (mL/μg). Equation (8) can be rearranged to the following linear form:

$$\frac{C_e}{q_e} = \frac{C_e}{q_m} + \frac{1}{K_L q_m} \tag{9}$$

Thus, if the adsorption follows Langmuir isotherm, the plot of C_e/q_e versus C_e should be linear and the values of q_m and K_L can be determined from the slope and the intercept of the graph, respectively.

The dimensionless separation factor, R_L, is also an important parameter, which can indicate the favorability of the adsorption process. R_L is defined as:[35]

$$R_L = \frac{1}{1 + K_L C_0} \tag{10}$$

where C_0 is the highest initial dye concentration (μg/mL) and K_L is the Langmuir constant. Based on the value of R_L, the adsorption process can be said to be irreversible ($R_L = 0$), favorable ($0 < R_L < 1$), linear ($R_L = 1$) or unfavorable ($R_L > 1$).

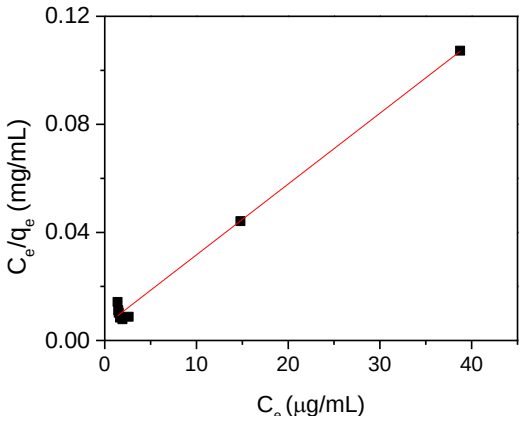

Figure 7.26. A plot based on Langmuir isotherm of adsorption of OG on H^+-PANI/SBA-15.

As shown in **Figure 7.26**, when C_e/q_e was plotted against C_e, a straight line was obtained, and the correlation coefficient R^2 was found to be 0.99, indicating the adsorption of OG on H^+-PANI/SBA-15 can be fitted well with the Langmuir isotherm. The corresponding values of q_m and K_L are calculated from equation (9) and compiled in Table S3. The separation factor R_L was found to be 0.004, which is in the range of 0 - 1; so, this again confirms the favorable uptake of OG by H^+-PANI/SBA-15.

7.6.3.2. Freundlich isotherm

The Freundlich model, which is an empirical model that describes heterogeneous surfaces with sites of different affinities, can be written as:[35]

$$q_e = K_F C_e^{1/n} \tag{11}$$

where q_e is the equilibrium solid phase adsorbate concentration (µg/mg), C_e is the equilibrium liquid phase adsorbate concentration (µg/mL), K_F is the Freundlich constant (µg/mg)(mL/μg)$^{1/n}$ and n is the heterogeneity factor giving an indication of how favorable the adsorption process is.

By taking the logarithm of equation 11, a linear form of Freundlich expression can be obtained as follows:

$$ln\ q_e = ln\ K_F + \frac{1}{n} ln C_e \quad (12)$$

A linear plot of $ln\ q_e$ versus $ln\ C_e$ enables the constant K_F and n to be determined. The ratio of $1/n$ is a measure of surface heterogeneity, and as its value gets closer to zero, the material surface is said to be more heterogeneous.

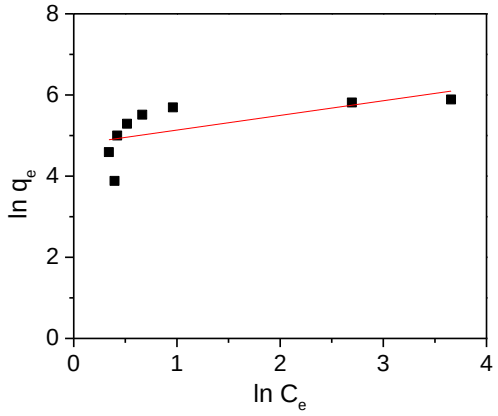

Figure 7.27. Freundlich isotherm of OG on H^+-PANI/SBA-15

The plot of lnq_e versus lnC_e gave a straight line with a slope of 0.43, see **Figure 7.27**, from which the values of K_F and n were determined and compiled in **Table 7.3**.

7.6.3.3. Temkin isotherm

The Temkin model assumes that the heat of adsorption of all the molecules on the layer of the adsorbent would decrease linearly with the surface coverage due to adsorbate/adsorbent interactions.[5] The Temkin model can be used in the following form:

$$q_e = \frac{RT}{b} lnK_T + \frac{RT}{b} lnC_e \quad (13)$$

where b is the Temkin constant related to the heat of adsorption (J/mol), K_T is the Temkin isotherm constant (L/g), R is the gas constant (8.314 J/mol K) and T the absolute temperature (K). Thus, a plot of q_e versus $ln\ C_e$ can be used to determine the values of b and K_T, from the slope and intercept of the graph, respectively, see **Figure 7.28** and **Table 7.3**.

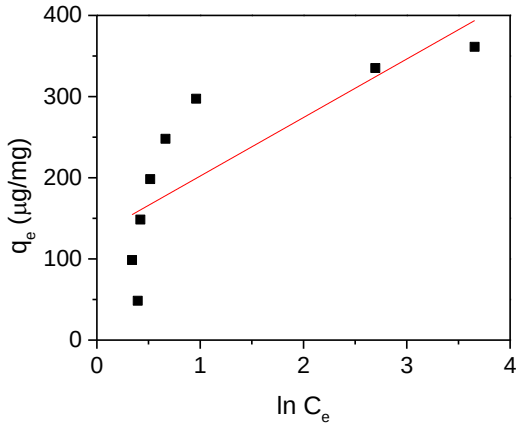

Figure 7.28. Temkin isotherm of OG on H^+-PANI/SBA-15.

Table 7.3. Parameters obtained based on the Langmuir, Freundlich, and Temkin isotherm models.

Isotherm model	Parameters
Langmuir	Q_m = 384.61 µg/mg
	K_L = 0.47 mL/µg
	R^2= 0.99
Freundlich	K_F= 118.32 (µg/mg)(mL/µg)$^{1/n}$
	n = 2.766
	R^2= 0.43
Temkin	K_T = 6.06 L/g
	b= 34.61 J/mol
	R^2 = 0.64

Table 7.3 summarized all the constants and their corresponding correlation coefficients, R^2 for the three isotherm models. Among the three models, the Langmuir model was found to best fit the experimental data, giving R^2 = 0.99. Conformation of the experimental data into Langmuir isotherm equation indicates the homogeneous nature of H^+-PANI/SBA-15 surface and also that the OG molecule are distributed on the surface of H^+-PANI/SBA-15 in monolayers.

Table 7.4. Comparisons based on q_m values (the maximum adsorption capacity of adsorbents) of different adsorbents applied for removal of OG from solutions.

Material (Adsorbent)	q_m (mg/g)	Reference
PVA@SiO1.5-hPEA-1/2-Gel [a]	4.57 (ca.)	36
rGO [b]	5.98	37
Activated carbon from Thespesia populnea pods	9.129	38
BFA [c]	18.796	39
MAMPS, MAMMS [d]	48.98; 61.33	40
DTCSCu [e]	53.38	41
Nano zirconia	54.31±1.573 (ca.)	42
LDH, CLDH [f]	76.4; 378.8	43
HDTMAB [g]	101.42 (ca.)	44
Chitosan (ungrafted), ChgPHMA, ChgPBMA, ChgPEMA, ChgPMMA [h]	95; 265; 290; 360; 435	45
H^+-PANI/SBA-15	***384.61***	***Present work***
Chitosan	922.9	46
Chitosan/DTAC [i]	1452.07	47

[a] PVA@SiO1.5-hPEA-1/2-Gel = Poly(vinyl alcohol) (PVA)-enhanced hybrid hydrogels of hyperbranched poly(ether amine) ($SiO_{1.5}$-hPEA-Gels). [b] rGO = Reduced graphene oxide. [c] BFA = Bagasse fly ash. [d] MAMMS = Monoamine-modified magnetic silica and MAMMS = Magnetite-free MAMMS. [e] DTCSCu = Copper**(**II**)** complex of dithiocarbamate-modified starch. [f] LDH = Layered double hydroxide; CLDH = Mg–

Fe layer double hydroxide. [g] HDTMAB = Na-bentonite modified with hexadecyltrimethylammonium bromide. [h] ChgPHMA = Chitosan grafted poly(hexyl methacrylate); ChgPBMA = Chitosan grafted poly(butyl methacrylate); ChgPEMA = Chitosan grafted poly(ethyl methacrylate); ChgPMMA = Chitosan grafted poly(methyl methacrylate). [i] Chitosan/DTAC = Chitosan/Dodecyltrimethylammonium chloride.

7.6.4. Adsorption kinetics

To get a further understanding of the adsorption processes, the data for the adsorption of OG on H^+-PANI/SBA-15 obtained at different initial OG concentration were fitted with pseudo-second order and intraparticle diffusion models (**Figure 7.29** and **Figure 7.30**), and the corresponding fitting values are compiled in **Table 7.5** and **Table 7.6**.

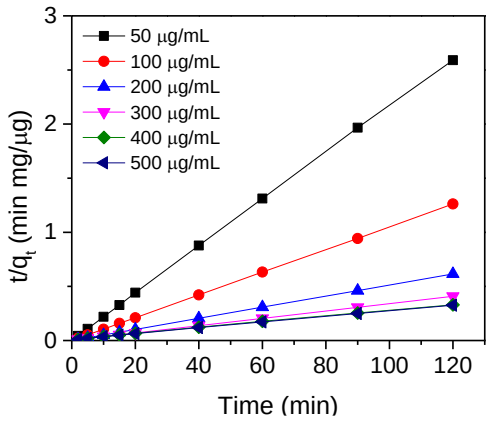

Figure 7.29. Plots based on pseudo-second order model of the adsorption of OG by H^+-PANI/SBA-15 from solutions with different initial OG concentrations.

Table 7.5. Kinetic data of Pseudo-second order model of OG adsorption by H^+-PANI/SBA15 with different initial OG concentrations.

OG Concentration (μg/mL)	Second order kinetic model			
	q_e (exp) (μg/mL)	k_2 (mg/μg min)	q_e (cal) (μg/mL)	R^2

50	46.33	9.42×10^{-2}	46.08	1
100	95.09	1.84×10^{-1}	95.24	1
200	195.19	6.5×10^{-2}	196.08	1
300	293.71	3.61×10^{-3}	294.12	0.999
400	363.48	7.44×10^{-4}	370.3	0.999
500	367.18	8.38×10^{-4}	377.36	1

From **Figure 7.29** and **Table 7.5**, for initial OG concentration varied from 50-500 μg/mL, pseudo-second order kinetic model all showed great agreement between the experimental and the calculated q_e values. In addition, the correlation coefficient, R^2, was found to be greater than 0.999 for all these cases, confirming that the pseudo-second order kinetic model was applicable to describe the adsorption behavior of OG on H^+-PANI/SBA-15.

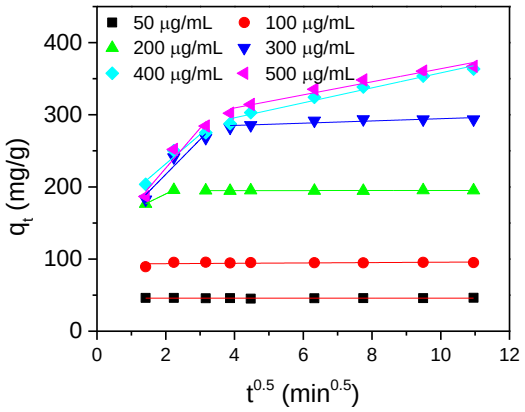

Figure 7.30. Plots based on intraparticle diffusion model of the data of adsorption of OG by H^+-PANI/SBA-15 from solutions with different initial OG concentrations.

Table 7.6. Kinetic data obtained based on intraparticle diffusion model of the data of adsorption of OG by H^+-PANI/SBA15 in distilled water.

OG Concentration (μg/mL)	Intraparticle diffusion model			
	k_{i1} (µg/mg min$^{0.5}$)	R^2	k_{i2} (µg/mg min$^{0.5}$)	R^2
50	0.01	0.22	----	----
100	0.25	0.38	----	----
200	0.84	0.4	----	----
300	48.44	0.941	1.56	0.751
400	40.63	0.957	10.38	0.975
500	55.43	0.949	9.07	0.965

It can be observed from **Figure 7.30** and **Table 7.6** that at lower initial OG concentration, only one adsorption step on the plot of q_t versus $t^{0.5}$ was observed. However, at higher initial OG concentration, the plot of q_t versus $t^{0.5}$ was not linear in the whole range, and it could be separated into two linear sections, indicating the presence of multistage adsorption process. The first linear region was attributed to the diffusion of OG on the external surfaces of H^+-PANI/SBA-15, and its high k_{i1} value demonstrated that the processes were fast due to the strong electrostatic interaction. The second portion could be ascribed to the gradual adsorption of OG, controlled by the intraparticle diffusion, and in this stage, the OG molecules entered the porous structure of the adsorbents. Furthermore, the linear plots did not pass through the origin, suggesting that the adsorption process was not only controlled by intraparticle diffusion, but instead was dictated by both external mass diffusion and intraparticle diffusion processes.[34,35,47,48]

7.6.5. Thermodynamic studies

The effect of temperature on OG adsorption on H^+-PANI/SBA-15 was studied at 20, 30 and 40 °C with constant initial OG concentration of 500 µg/mL and an adsorbent concentration of 1 mg/mL, see **Figure 7.31**. From the results, the activation energy (E_a), Gibbs free energy (ΔG°), enthalpy (ΔH°) and entropy (ΔS°) of the adsorption processes were also calculated (see below).

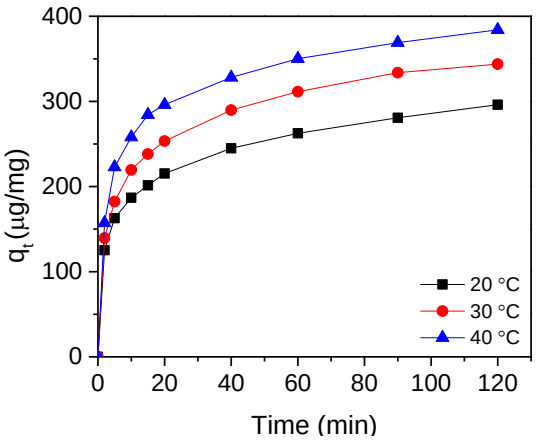

Figure 7.31. Effect of temperature on removal of OG by H^+-PANI/SBA-15.

From **Figure 7.31**, it can be seen that an increase in temperature causes a slight increase in the amount of OG adsorbed by H^+-PANI/SBA-15, suggesting the adsorption process of OG on H^+-PANI/SBA-15 is endothermic.

7.6.5.1. Activation energy (E_a)

The magnitude of activation energy can be used to determine whether the adsorption of a given compound on a given adsorbent takes place *via* physical or chemical process. Physisorption process has usually activation energy values ranging from 5-40 kJ/mol, whereas chemisorption has a relatively higher activation energy range between 40-800 kJ/mol.[48] To get the value of the activation energy, Arrhenius equation was used:

$$ln\, k_2 = ln\, A - \frac{E_a}{RT} \qquad (14)$$

where k_2 is the pseudo second order rate constant of OG adsorption, E_a is the Arrhenius energy (kJ/mol), A is the Arrhenius factor, R is the gas constant (8.314 J/mol K) and T is the absolute temperature of the solution (K). A straight line with slope $-E_a/R$ was obtained upon plotting $ln\ k_2$ versus $1/T$ (see **Figure 7.32**). The activation energy (5.55 kJ/mol) is tabulated with other thermodynamic parameters in **Table 7.7**. The result confirms that the adsorption of OG on H^+-PANI/SBA-15 occurs *via* physisorption.

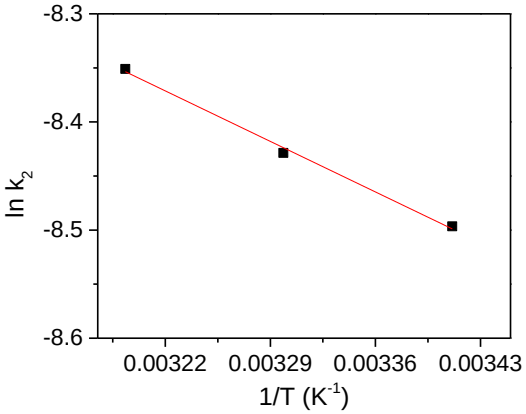

Figure 7.32. A plot of ln k_2 vs. $1/T$ for the data of adsorption of OG on H^+-PANI/SBA-15.

7.6.5.2 Gibbs free energy (ΔG°), enthalpy (ΔH°) and entropy (ΔS°)

Thermodynamic parameters, namely ΔG°, ΔH° and ΔS°, for the adsorption processes of OG on H^+-PANI/SBA-15 were determined from equation (15), (16) and (17):

$$k_c = \frac{q_e}{C_e}\ and\ \Delta G^\circ = -RT ln\ k_c \tag{15}$$

$$\Delta G^\circ = \Delta H^\circ - T\Delta S^\circ \tag{16}$$

$$lnk_c = -\frac{\Delta H^\circ}{RT} + \frac{\Delta S^\circ}{R} \tag{17}$$

where k_c is the standard thermodynamic equilibrium constant (mL/mg), q_e is the equilibrium solid phase adsorbate concentration (µg/mg), C_e is the equilibrium liquid phase adsorbate concentration (µg/mL), R is the gas constant (8.314 J/mol K), and T is the absolute temperature of the solution

(K). The values of ΔH° and ΔS° can be estimated from the slope and intercept after plotting $ln\ k_c$ versus $1/T$ (**Figure 7.33**). The values of thermodynamic parameters are listed in Table S7. The positive value ΔH° indicates that the adsorption process of OG on H^+-PANI/SBA-15 is endothermic while the negative value of ΔG°, which decreased with an increase of temperature, reveals the spontaneity of the adsorption process. The value of ΔG°, which ranged from -1.88 to -4.51 kJ/mol, once again confirming the physisorption process (-20 to 0 kJ/mol).[49] Similar results have been reported for the adsorption of other dyes such as acid green 25 and brilliant blue R on adsorbents such as activated palm ash[20] and organo-attapulgite (ATPOC) and organo-bentonite (BNTOC) clay-based materials.[21] The positive value of ΔS°suggests the increased randomness at the solid-solution interface during the adsorption process, and this phenomenon has also been described by other researchers.[34,48,49]

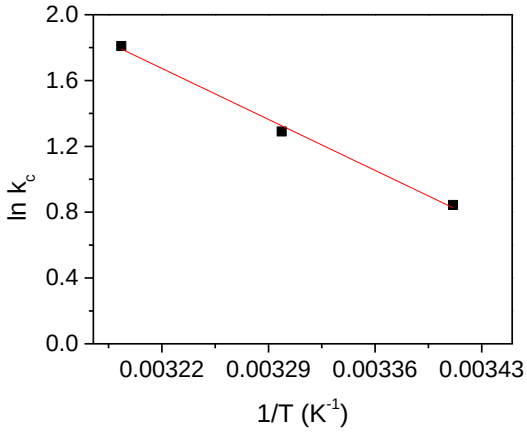

Figure 7.33. A plot of ln k_c vs. $1/T$ for the data of adsorption of OG on H^+-PANI/SBA-15.

Table 7.7. Thermodynamic data for adsorption of OG on H^+-PANI/SBA-15.

E_a	ΔH°	ΔS°	ΔG° (kJ/mol)		
kJ/mol	kJ/mol	kJ/mol	20 ℃	30 ℃	40 ℃
5.55	36.82	0.132	-1.88	-3.2	-4.51

7.6.6. Regeneration

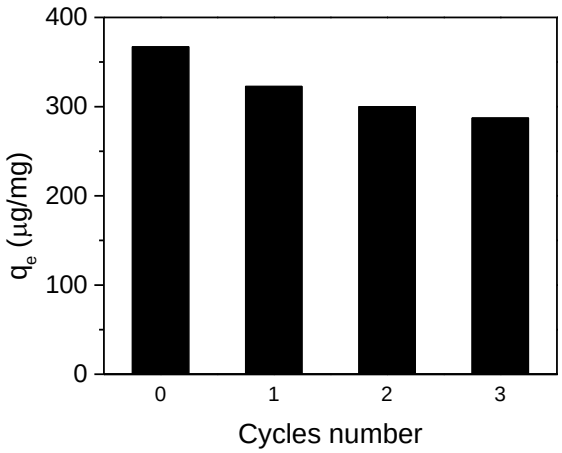

Figure 7.34. Adsorption amount of OG on H^+-PANI/SBA-15 and on recovered and regenerated H^+-PANI/SBA-15 materials. In the experiments, the initial concentration of OG was 500 μg/mL and the adsorbent concentration was 1 mg/mL.

As shown in **Figures 7.23** and **Figure 7.24**, the amount of OG adsorbed on H^+-PANI/SBA-15 decreased as the pH of the solutions increased, implying that the adsorbate molecules loaded on the adsorbent can be desorbed. To perform the regeneration test, the pre-loaded adsorbent was re-dispersed into $NaHCO_3$ solution and stirred vigorously for 30 min, this washing process was repeated twice to make sure that most of the adsorbed OG was desorbed from the adsorbent. The desorbed PANI/SBA-15 was then centrifuged and washed three times with water and re-doped with hydrochloric acid. The regenerated adsorbent was used again in the subsequent experiments of OG adsorption. From **Figure 7.34**, it was observed that at first cycle, the OG adsorption amount reduced from 367.17 μg/mg to 322.78 μg/mg, but in the next two adsorption-desorption cycles, there was only slight decrease in the final adsorbed amount of OG. This proved that H^+-PANI/SBA-15 could be used repeatedly without significantly losing its adsorption properties and adsorption capacity.

7.7. Conclusions

In summary, we have synthesized SBA-15-supported H^+-PANI that has a high surface area and ideal surface properties for the adsorption of anionic organic dyes from wastewater. We have described detailed experimental and modeling results about the adsorption properties of the materials. Our results could encourage further research on porous inorganic/polymer hybrid nanomaterials for the removal of ubiquitous anionic dyes from various water systems and industrial effluents.

7.8. Reference

1. Ayad, M. M.; El-Nasr, A. A. *J. Phys. Chem. C*, **2010**, *114*, 14377-14383.
2. Okesola, B. O.; Smith, D. K. *Chem. Commun.*, **2013**, *49*, 11164-11166.
3. Ahmad, A.; Mohd-Setapar, S. H.; Chuong, C. S.; Khatoon, A.; Wani, W. A.; Kumar, R.; Rafatullah, M. *RSC Adv.*, **2015**, *5*, 30801-30818.
4. Yu, H.; Fugetsu, G. *J. Hazard. Mater*., **2010**, *177*, 138-145.
5. Crini, G. *Bioresour. Technol.*, **2006**, *97*, 1061-1085.
6. Lau, Y. Y.; Wong, Y. S.; Teng, T. T.; Morad, N.; Rafatullah, M.; Ong, S. A. *RSC Adv.*, **2015**, *5*, 34206-34215.
7. Kurade, M. B.; Waghmode, T. R.; Jadhav, M. U.; Jeon, B. H.; Govindwar, S. P. *RSC Adv*., **2015**, *5*, 23046-23056.
8. Fu, G.; Su, Z.; Jiang, X.; Yin, J. *Polym. Chem.*, **2014**, *5*, 2027-2034.
9. Greluk, M.; Hubicki, Z. *Chem. Eng. J.*, **2013**, *215-216*, 731-739.
10. Duan, T.; Chen, Y.; Wen, Q.; Duan, Y. *RSC Adv*., **2014**, *4*, 57463-57475.

11. Ajmal, A.; Mageed, I.; Malik, R. N.; Idriss, H.; Nadeem, M. A. *RSC Adv.*, **2014**, 4, 37003-37026.

12. Geng, Z.; Lin, Y.; Yu, Y.; Shen, Q.; Ma, L.; Li, Z.; Pan, N.; Wang, X. *J. Mater. Chem.*, **2012**, *22*, 3527-3535.

13. Ansari, R; Mosayebzadeh, Z. *Chem. Pap.*, **2011**, *65*, 1-8.

14. Mahanta, D.; Madras, G.; Radhakrishnan, S.; Patil, S. *J. Phys. Chem. B*, **2009**, *113*, 2293-2299.

15. Mohamad, A.; Sawsan, Z. *Chem. Eng. J.*, **2012**, *204-206*, 79-86.

16. Trchova, M.; Konyushenko, E. N.; Stejskal, J.; Kovarova, J.; Ciric-Marjanovic, G. *Polym. Degrad. Stab.*, **2009**, *94*, 929-938.

17. Huang, J.; Virji, S.; Weiller, B. H.; Kaner, R. B. *J. Am. Chem. Soc.*, **2003**, *125*, 314-315.

18. Du, J. M.; Liu, Z. M.; Han, B. X.; Li, Z. H.; Zhang, J. L. Microporous Mesoporous Mater., *2005*, **84**, 254-260.

19. Zhao, D.; Feng, J.; Huo, Q.; Melosh, N.; Fredrickson, G. H.; Chmelka, B. F.; Stucky, G. D. *Science*, **1998**, *279*, 548-552.

20. Sasidharan, M.; Mal, N. K.; Bhaumik, A. *J. Mater. Chem.*, **2007**, *17*, 278-283.

21. Weng, S. H.; Lin, Z. H.; Zhang, Y.; Chen, L. X.; Zhou, J. Z. *React. Funct. Polym.*, **2009**, *69*, 130-136.

22. Silva, R.; Asefa, T. *Adv. Mater.*, **2012**, *24*, 1878-1883.

23. Cho, M. S.; Choi, H. J.; Kim, K. Y.; Ahn, W. S. Macromol. *Rapid Commun.*, **2002**, *23*, 713-716.

24. Kulkarni, M. V.; Viswanath, A. K.; Aiyer, R. C.; Khanna, P. K. *J. Polym. Sci., Part B: Polym. Phys.*, **2005**, *43*, 2161-2169.

25. Chaudhary, Y. S.; Ghatak, J.; Bhattab, U. M.; Khushalani, D. *J. Mater. Chem.*, **2006**, *16*, 3619-3623.

26. Jain, R. N.; Huang, X.; Das, S.; Silva, R.; Ivanova, v.; Minko, T.; Asefa, T.; Anorg. Z. *Allg. Chem.*, **2014**, *640*, 616.

27. Cui, Z.; Guo, C. X.; Yuanb, W.; Li, C. M. *Phys. Chem. Chem. Phys.*, **2012**, *14*, 12823-12828.

28. Li, N.; Li, X. T.; Geng, W. C.; Zhang, T.; Zuo, Y.; Qiu, S. L. J. *Appl. Polym. Sci.*, **2004**, *93*, 1597-1601.

29. Huang, X.; Tao, Z.; Praskavich, J. C. Jr.; Goswami, A.; Al-Sharab, J. F.; Minko, T.; Polshettiwar, V.; Asefa, T. *Langmuir*, **2014**, *30*, 10886-10898.

30. Huang, X.; Zhang, T.; Goswami, A.; Luo, F.; Asefa, T. *RSC Adv.*, **2015**, *5*, 28836-28839.

31. Namasivayam, C.; Kavitha, D. *Dyes Pigm.*, **2002**, *54*, 47-58.

32. Weber, W. J.; Morris, J. C. *J. Sanit, Eng. Div., Am. Soc. Civ. Eng.*, **1963**, *89*, 31-60.

33. Salem, M. A. *React. Funct. Polym.*, **2010**, *70*, 707-714.

34. Tan, I. A. W.; Ahmad, A. L.; Hameed, B. H. *J. Hazard. Mater.*, **2008**, *154*, 337-346.

35. Martins, A. C.; Pezoti, O.; Cazetta, A. L.; Bedin, K. C.; Yamazaki, D. A. S.; Bandoch, G. F. G.; Asefa, T.; Visentainer, J. V.; Almeida, V. C. *Chem. Eng. J.*, **2015**, *260*, 291-299.

36. Deng, S. J.; Xu, H. J.; Jiang, X. S.; Yin, J. *Macromolecules*., **2013**, *46*, 2399-2406.

37. Ramesha, G. K.; Vijaya Kumara, A.; Muralidhara, H. B.; Sampath, S. *J. Colloid Interface Sci.*, **2011**, *361***,** 270-277.

38. Arulkumar, M.; Sathishkumar, P.; Palvannan, T. *J. Hazard. Mater.*, **2011**, *186*, 827-834.

39. Mall, I. D.; Srivastava, V. C.; Agarwal, N. K. *Dyes and Pigments.*, **2006**, *69*, 210-223.

40. Atia, A. A.; Donia, A. M.; Amrani, W. A. A. *Chem. Eng. J.*, **2009**, *150*, 55-62.

41. Cheng, R. M.; Ou, S. J.; Xiang, B.; Li, Y. J.; Liao, Q. Q. *Langmuir.*, **2010**, *26*, 752-758.

42. Sharma, Y. C.; Gusain, D.; Upadhyay, S. N. *RSC. Adv.*, **2014**, *4*, 18755-18762.

43. Abdelkader, N. B. H.; Bentouami, A.; Derrichea, Z.; Bettahar, N.; Ménorval, L.-C. *Chem. Eng. J.*, **2011**, *169*, 231-238.

44. Jović-Jovičić, N.; Milutinović-Nikolić, A.; Banković, P.; Mojović, Z.; Žunić, M.; Gržetić, I.; Jovanović, D. *Appl. Clay Sci.*, **2010**, *47*, 452-456.

45. Konaganti, V. K.; Kotaa, R.; Patil, S.; Madras, G. *Chem. Eng. J.*, **2010**, *158*, 393-401.

46. Wong, Y. C.; Szeto, Y. S.; Cheung, W. H.; McKay, G. *Langmuir.*, **2003**, *19*, 7888-7894.

47. Zhang, L.; Cheng, Z.; Guo, X.; Jiang, X.; Liu, R. *J. Mol. Liq.*, **2014**, *197*, 353-367.

48. Hameed, B. H.; Ahmad, A. A.; Aziz, N. *Chem. Eng. J.*, **2007**, *133*, 195-203.

49. Bhatt, A. S.; Sakaria, P. L.; Vasudevan, M.; Pawar, R. R.; Sudheesh, N.; Bajaj, H. C.; Mody, H. M. *RSC Adv.*, **2012**, *2*, 8663-8671.

Chapter 8

Summary

My PhD research involves design and synthesis of *i*) highly crystalline porous anatase TiO_2 microparticles containing large surface area for photocatalytic CO_2 reduction, where the hydrolysis treatment is critical for the formation of nanoporous structure and small anatase grains, *ii*) oxygen vacancy-rich, nanoporous TiO_{2-x} containing small anatase nanoparticles with high surface area using a polymer-derived mesoporous carbon as a template for photocatalytic CO_2 reduction, where the presence of PDMC template during the high temperature pyrolysis is crucial for both maintaining the anatase and creating oxygen vacancies in the titania materials, *iii*) Cu-decorated TiO_2 for photocatalytic CO_2 reduction, where the optimal loading of Cu species is necessary for achieving the desired CO_2 reduction activity, *iv*) Cu nanoparticles-loaded polymer-derived mesoporous carbon for efficient electrocatalytic hydrazine oxidation reaction, *v*) Cu nanoparticles-loaded mesoporous g-C_3N_4 developed by using melamine as a precursor and colloidal silica nanoparticles as hard templates for photocatalytic tartrazine yellow degradation, where the mass ratio of melamine-to-silica templates and the size of the silica nanoparticles are found to dictate whether or not mpg-C_3N_4 with large surface area and high porosity form, and *vi*) SBA-15-supported H^+-PANI with high surface area and ideal surface properties for the adsorption of anionic organic dyes from wastewater. Their outstanding performance toward photocatalytic CO_2 reduction, photocatalytic tartrazine yellow degradation, electrocatalytic hydrazine oxidation and environmental remediation are closely related their synthetic strategies, which render the materials with desired structure and optimized physical and chemical properties. These materials deserve further investigations for achieving a sustainable future.

Appendices

Copyright and Permissions

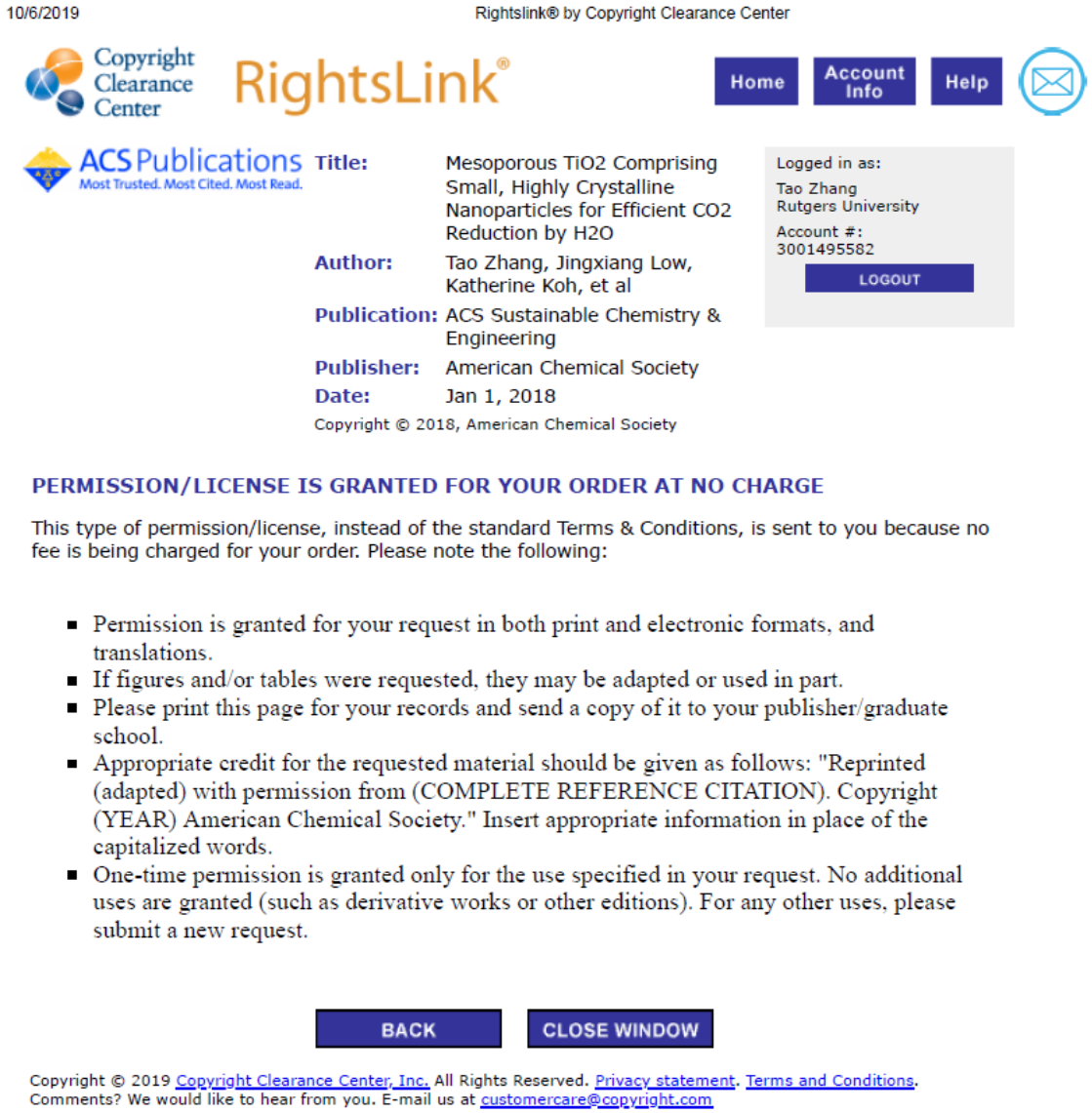

10/6/2019 Rightslink® by Copyright Clearance Center

Copyright Clearance Center RightsLink® Home Account Info Help

ACS Publications Most Trusted. Most Cited. Most Read.

Title: Mesoporous TiO2 Comprising Small, Highly Crystalline Nanoparticles for Efficient CO2 Reduction by H2O

Author: Tao Zhang, Jingxiang Low, Katherine Koh, et al

Publication: ACS Sustainable Chemistry & Engineering

Publisher: American Chemical Society

Date: Jan 1, 2018

Copyright © 2018, American Chemical Society

Logged in as:
Tao Zhang
Rutgers University
Account #:
3001495582
LOGOUT

PERMISSION/LICENSE IS GRANTED FOR YOUR ORDER AT NO CHARGE

This type of permission/license, instead of the standard Terms & Conditions, is sent to you because no fee is being charged for your order. Please note the following:

- Permission is granted for your request in both print and electronic formats, and translations.
- If figures and/or tables were requested, they may be adapted or used in part.
- Please print this page for your records and send a copy of it to your publisher/graduate school.
- Appropriate credit for the requested material should be given as follows: "Reprinted (adapted) with permission from (COMPLETE REFERENCE CITATION). Copyright (YEAR) American Chemical Society." Insert appropriate information in place of the capitalized words.
- One-time permission is granted only for the use specified in your request. No additional uses are granted (such as derivative works or other editions). For any other uses, please submit a new request.

BACK CLOSE WINDOW

Copyright © 2019 Copyright Clearance Center, Inc. All Rights Reserved. Privacy statement. Terms and Conditions.
Comments? We would like to hear from you. E-mail us at customercare@copyright.com

Title: Copper-Decorated Microsized Nanoporous Titanium Dioxide Photocatalysts for Carbon Dioxide Reduction by Water

Author: Tewodros Asefa, Jiaguo Yu, Jafar F. Al-Sharab, et al

Publication: ChemCatChem

Publisher: John Wiley and Sons

Date: Jun 26, 2017

Order Completed

Thank you for your order.

This Agreement between Rutgers University -- Tao Zhang ("You") and John Wiley and Sons ("John Wiley and Sons") consists of your license details and the terms and conditions provided by John Wiley and Sons and Copyright Clearance Center.

Your confirmation email will contain your order number for future reference.

printable details

License Number	4683131250601
License date	Oct 06, 2019
Licensed Content Publisher	John Wiley and Sons
Licensed Content Publication	ChemCatChem
Licensed Content Title	Copper-Decorated Microsized Nanoporous Titanium Dioxide Photocatalysts for Carbon Dioxide Reduction by Water
Licensed Content Author	Tewodros Asefa, Jiaguo Yu, Jafar F. Al-Sharab, et al
Licensed Content Date	Jun 26, 2017
Licensed Content Volume	9
Licensed Content Issue	15
Licensed Content Pages	9
Type of use	Dissertation/Thesis
Requestor type	Author of this Wiley article
Format	Print and electronic
Portion	Full article
Will you be translating?	No
Title of your thesis / dissertation	DESIGN AND SYNTHESIS OF NOVEL POROUS TITANIA AND SILICA NANOMATERIALS FOR SUSTAINABLE PHOTOCATALYSIS AND ENVIRONMENTAL APPLICATIONS
Expected completion date	Nov 2019
Expected size (number of pages)	200
Requestor Location	Rutgers University 98 Brett Rd PISCATAWAY, NJ 08854 United States Attn: Tao
Publisher Tax ID	EU826007151
Total	0.00 USD

RightsLink®

Home | Account Info | Help

Title:	Copper nanoparticles/polyaniline-derived mesoporous carbon electrocatalysts for hydrazine oxidation
Author:	Tao Zhang, Tewodros Asefa
Publication:	Frontiers of Chemical Science and Engineering
Publisher:	Springer Nature
Date:	Jan 1, 2018

Logged in as:
Tao Zhang
Rutgers University
Account #:
3001495582
LOGOUT

Order Completed

Thank you for your order.

This Agreement between Rutgers University -- Tao Zhang ("You") and Springer Nature ("Springer Nature") consists of your license details and the terms and conditions provided by Springer Nature and Copyright Clearance Center.

Your confirmation email will contain your order number for future reference.

printable details

License Number	4683131479772
License date	Oct 06, 2019
Licensed Content Publisher	Springer Nature
Licensed Content Publication	Frontiers of Chemical Science and Engineering
Licensed Content Title	Copper nanoparticles/polyaniline-derived mesoporous carbon electrocatalysts for hydrazine oxidation
Licensed Content Author	Tao Zhang, Tewodros Asefa
Licensed Content Date	Jan 1, 2018
Licensed Content Volume	12
Licensed Content Issue	3
Type of Use	Thesis/Dissertation
Requestor type	non-commercial (non-profit)
Format	print and electronic
Portion	full article/chapter
Will you be translating?	no
Circulation/distribution	5000 - 9999
Author of this Springer Nature content	yes
Title	DESIGN AND SYNTHESIS OF NOVEL POROUS TITANIA AND SILICA NANOMATERIALS FOR SUSTAINABLE PHOTOCATALYSIS AND ENVIRONMENTAL APPLICATIONS
Institution name	n/a
Expected presentation date	Nov 2019
Requestor Location	Rutgers University 98 Brett Rd PISCATAWAY, NJ 08854 United States Attn: Tao

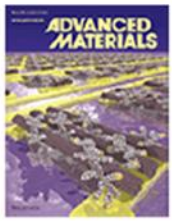

Title: Heteroatom-Doped Carbon Materials for Hydrazine Oxidation
Author: Tewodros Asefa, Tao Zhang
Publication: Advanced Materials
Publisher: John Wiley and Sons
Date: Nov 16, 2018

Order Completed

Thank you for your order.

This Agreement between Rutgers University -- Tao Zhang ("You") and John Wiley and Sons ("John Wiley and Sons") consists of your license details and the terms and conditions provided by John Wiley and Sons and Copyright Clearance Center.

Your confirmation email will contain your order number for future reference.

printable details

License Number	4683150023156
License date	Oct 06, 2019
Licensed Content Publisher	John Wiley and Sons
Licensed Content Publication	Advanced Materials
Licensed Content Title	Heteroatom-Doped Carbon Materials for Hydrazine Oxidation
Licensed Content Author	Tewodros Asefa, Tao Zhang
Licensed Content Date	Nov 16, 2018
Licensed Content Volume	31
Licensed Content Issue	13
Licensed Content Pages	17
Type of use	Dissertation/Thesis
Requestor type	Author of this Wiley article
Format	Print and electronic
Portion	Full article
Will you be translating?	No
Title of your thesis / dissertation	DESIGN AND SYNTHESIS OF NOVEL POROUS TITANIA AND SILICA NANOMATERIALS FOR SUSTAINABLE PHOTOCATALYSIS AND ENVIRONMENTAL APPLICATIONS
Expected completion date	Nov 2019
Expected size (number of pages)	200
Requestor Location	Rutgers University 98 Brett Rd PISCATAWAY, NJ 08854 United States Attn: Tao
Publisher Tax ID	EU826007151
Total	0.00 USD